University of Southampton

Faculty of Engineering and Physical Sciences

School of Chemistry

Synthesis of Complex Transition Metal Nitrides and their Ammonia Synthesis Activity

Samia Ibrahim Al Sobhi

Thesis for the degree of the degree of Doctor of Philosophy

November 2019

Dedication

To my parents
To my husband, Nawaf, and my two sons Ibrahim and Elyas
And to my brothers and sisters

Abstract

In this study, some nanocrystalline quaternary interstitial nitrides adopting the filled β-Mn and the η-6 carbide type structures have been synthesised using a modified Pechini method. This method, which involves dissolving metal salts with citric acid followed by the evaporation and ammonolysis of the resulting oxide precursors, has resulted in the nanoparticle materials. It has been shown to be a useful tool for producing homogenous quaternary nitrides in a fast and simple way. The structural properties of the samples were examined by powder X-ray diffraction and the data was further analysed and quantitatively refined using Rietveld refinement methods. Other characterisation techniques such as SEM, TEM, TGA and elemental analysis of carbon, hydrogen and nitrogen content were also undertaken. The surface areas of the materials were measured by the Brunauer- Emmett-Teller (BET) method, using nitrogen adsorption isotherms. The refinement of $Ni_{2-x}Cu_xMo_3N$ and $Ni_2W_xMo_{3-x}N$ powder X-ray diffraction data confirms a linear dependence of lattice parameters versus Cu or W content where x = 0.0, 0.1, 0.2, 0.3, and then the lattice parameters no longer change as the doping level is increased, indicating that copper or tungsten can be substituted at the nickel or molybdenum sites in Ni_2Mo_3N structure up to a solubility limit of x = 0.3. $Ni_{2-x}Fe_xMo_3N$ was observed to have a linear increase in the lattice parameters up to x = 1. These metal nitrides show good ammonia synthesis activity at 500 °C under ambient pressure. The activity fell with copper content and increased with iron and tungsten content, although these changes appear to be related to changing surface areas of the catalysts. The η-6 Co_3No_3M structure is a promising material for ammonia synthesis. The substitution of molybdenum with tungsten into this structure in the formula $Co_3W_xMo_3N$ resulted in some single phases where x = 0.1, 0.2, 0.4, 0.7 and 0.8. However, the compositions with x = 0.3, 0.5 and 0.6 were found to have a trace impurity of Co_3Mo. These materials showed good activity for ammonia synthesis, but less than that of the parent compound Co_3Mo_3N. The oxide intermediates from the citrate gel process cleanly converted to the metal nitride under the ammonia synthesis gas stream (75% H_2, 25% N_2) providing more active catalysts than those pre-nitrided by ammonolysis.

List of Contents

List of Tables

List of Figures

List of Equations

Acknowledgements

First of all, I am very grateful to the almighty Allah, who gave me the opportunity, strength, determination to achieve my goal.
It is a pleasant task to express my thanks and gratitude to everyone who have supported me in any way to complete this study.
I would like to express my deep appreciation to my supervisor Professor Andrew Hector for his guidance and endless support throughout this PhD journey.
I warmly thank all members of the research and the technical staff in the school of chemistry at the University of Southampton. Many thanks to the members of the Hector group, with special thanks to Jon Allen who was always willing to help when needed.

Furthermore, I am very much thankful to Professor Justin Hargreaves and Dr. Ihfaf Alshibane from University of Glasgow for their valuable discussions and shared knowledge.

Many special thanks to my beloved parents, my dad Ibrahim and my mum Salma. Words are short to express how grateful I am to my parents, for their sincere encouragement and inspiration throughout my whole life.

I owe my most loving thanks to my husband, Nawaf and my two sons, Ibrahim and Elyas for their endless love, patience, support and understanding.
I also would like to send a special thank you to my sisters and brothers. All of them indeed supported me in many different ways.

I appreciatively acknowledge the financial support from Saudi Arabia government to pursue my research goals.

Declaration of Authorship

Samia Al Sobhi

'Synthesis of Complex Transition Metal Nitrides and their Ammonia Synthesis Activity'

I declare that this thesis and the work presented in it are my own and has been generated by me as the result of my own original research.

I confirm that:

1. This work was done wholly or mainly while in candidature for a research degree at this University;
2. Where any part of this thesis has previously been submitted for a degree or any other qualification at this University or any other institution, this has been clearly stated;
3. Where I have consulted the published work of others, this is always clearly attributed;
4. Where I have quoted from the work of others, the source is always given. With the exception of such quotations, this thesis is entirely my own work;
5. I have acknowledged all main sources of help;
6. Where the thesis is based on work done by myself jointly with others, I have made clear exactly what was done by others and what I have contributed myself.

Publications:

- S. Al Sobhi, N. Bion, J. S. J. Hargreaves, A. L. Hector, S. Laassiri, W. Levason, A. W. Lodge, A. R. Mcfarlane and C. Ritter, The reactivity of lattice nitrogen within the Ni_2Mo_3N and $NiCoMo_3N$ phases, *Mater. Res. Bull.*, 2019, **118**, 110519.
- S. Al Sobhi, J. S. J. Hargreaves, A. L. Hector and S. Laassiri,Citrate-gel preparation and ammonia synthesis activity of compounds in the quaternary $(Ni,M)_2Mo_3N$ (M = Cu or Fe) systems, *Dalton Trans.*, 2019, **48**, 16786–16792.

Signed: Samia Al Sobhi
Date: November 2019

List of Abbreviations

HBP	Haber-Bosch process
TMNs	Transition metal nitride materials
NPs	Nanoparticles
BCC	Body centred cubic
FCC	Face centred cubic
DOF	Density of states
PXRD	Powder X-ray diffraction
a.u	Arbitrary units
$\boldsymbol{d_{(hkl)}}$	Lattice d-spacing
$\boldsymbol{\lambda}$	X-ray beam wave-length
SEM	Scanning electron microscopy
EDX	Energy dispersive X-ray
TEM	Transmission electron microscopy
TGA	Thermogravimetric analysis
BET	Brunauer-Emmett-Teller (surface area)
SSA	Specific surface area
SEI	Secondary electron imaging
DSE	Backscattered electron imaging
ICSD	Inorganic crystal structure database
GSAS	General Structure Analysis System
EXPGUI	Graphical User Interface for GSAS (EXP) Experiment
$\mathbf{L_X}$	The Lorentzian components
$\boldsymbol{R_{wp}}$	Weight profile index
$\boldsymbol{R_{exp}}$	Expected index
I.D	Internal diameter
C.A	Citric acid
$\mathbf{TOF_S}$	Turnover frequency
CHN	Carbon, hydrogen and nitrogen

Chapter 1 Introduction

1.1 Ammonia: The molecule that changed the world

Nitrogen (N) is an element that is a fundamental nutrient and one of the key components of life. It is part of the chemical structure of DNA, enzymes, and proteins, but the most abundant form of this element (atmospheric N_2) is not readily available to be involved in the metabolism of most organisms due to the high stability of the N-N triple bond.[1] In the majority of ecosystems, natural nitrogen fixation is not able to satisfy the demand for reactive nitrogen.[2] That makes nitrogen a limiting factor for the growth of biomass.[3] Reactive forms of nitrogen include nitrogen dioxide (NO_2), nitrates (NO_3^-), nitric oxide (NO), nitrous oxide (N_2O), and ammonia (NH_3).[4] The importance of ammonia cannot be overstated. It is a reactive form of nitrogen that can be used for multiple applications.[5] Nowadays, there are three main sources of ammonia: Nitrogen fixation (either by direct deposition, or bacterial binding), ammonification of organic nitrogen from domestic animals by fungi or bacteria, and the Haber-Bosch process (HBP), which produces ammonia for refrigeration systems and fertilisers.

The majority of ammonia that is found in the Earth's atmosphere comes from human activity. It is the second most produced chemical in the world.[6] The current projections for the worldwide production of ammonia for 2020 is 170,761 thousand tones, with a demand of 118,763 thousand tonnes for fertiliser use, and an overall potential balance of 14,477 thousand tonnes.[7]

Ammonia is one of the main raw materials for the manufacture of fertilisers, and it's needed ultimately necessary to make possible the production of stable and affordable food supply for an increasing worldwide population. Chemicals used in the fertiliser industry such as ammonium phosphate ($(NH_4)_3PO_4$), urea ($(NH_2)_2CO$), and ammonium nitrate (NH_4NO_3), are prepared from ammonia.[8]

At the end of the twentieth century, fertilisers synthesised from ammonia were responsible for the agricultural production that fed 44% of all the population in the world,[9] and estimations for 2008 were that half of the world's population depended on ammonia for feeding.[5] The demand for reactive nitrogen in the form of ammonia will continue to grow, as the world population is expected to increase by 30% and the demand for meat and agricultural goods will grow by 200% and 70%, respectively.[10] Ammonia can also be the

basis for alternative energy sources. Fertilisers that use ammonia as a raw material are required to produce biofuels and bioenergy, contributing to a combined 11.5% of the global requirement of energy.[11]

1.2 Industrial production of ammonia

The industrial production of ammonia can be summarised with two names: Fritz Haber and Carl Bosch. Haber patented the synthesis of ammonia from its elements, and Bosch patented its application at an industrial scale. The world changed since the Haber-Bosch process was developed in 1913.[5, 12] Before the invention of this process, the nitrogen supply for fertilisers was far lower than the demand for it. The largest reservoir of nitrogen at the start of the twentieth century was a guano deposit located on Chile's coast. Scientists desired to find a way to synthesise ammonia from atmospheric nitrogen, but all previous attempts failed to develop a cost-effective way of doing so. The synthesis of ammonia from hydrogen and nitrogen is described by the reaction:[8,13]

$$N_{2\,(g)} + 3H_{2\,(g)} \rightleftarrows 2NH_{3\,(g)}, \quad \Delta H = -45.7\ kJ/mol \qquad \text{Equation 1-1}$$

According to Le Chatelier's principle, the formation of ammonia is favoured by high pressure and low temperature. The problem found by researchers was that the temperature needed for the activation of nitrogen (around 3000 °C) was favouring the reverse reaction. That is why the use of an iron catalyst was needed to bind the nitrogen and hydrogen molecules to its surface and decrease the activation energy and the temperature that are needed for the reaction to proceed (250-400 °C).[8]

Although iron catalysts were used, the reaction yield was still low. Haber contributed to this process by using much higher pressures and developing a recycling process. When the gas mixture passed over the catalyst a single time, the amount of ammonia formed was small for industrial purposes, so Haber separated the ammonia by condensation and recycled the gas mixture to react again, compensating the lost pressure with fresh gas input.[14]

In the new concept introduced by Haber, the static view that used reaction yield to determine the production of ammonia was abandoned, and a dynamic view that used space-time yield was introduced. He focused on the amount of ammonia that could be obtained per unit volume of the catalyst per unit time, and the real issue arose. The suitable catalyst needed to maximise the space-time yield, meaning that a maximum amount of product had to be obtained in the shortest time by using the minimum volume of catalyst possible.[14]

With the focus of maximizing space-time yield in mind, the Baden Aniline and Soda Company (BASF) assigned the task of developing the process for industrial purposes to Carl

Bosch, after signing an agreement with Haber. Some promising catalysts based on osmium and uranium were discovered, but it was Bosch's assistant, Mittasch, and other co-workers who found the first suitable catalyst for the synthesis of ammonia. The catalyst was made of iron with alumina, calcium oxide, and potassium, and it is the base for catalysts used today.[15] It has been reported that 500 million tons of NH_3 is produced annually *via* the Haber-Bosch process to generate N_2 for fertilisers.[16]

That ground-breaking discovery changed the nitrogen industry and the technology is still in development. Thanks to the continuous gradual increases in performance and efficiency, modern day ammonia plants are reaching a minimum in theoretical energy consumption. However, fossil fuels are still used to obtain the hydrogen needed for this process,[17] and 1% of the worldwide energy is utilised for the synthesis of ammonia,[18] motivating researchers to find ways to make ammonia synthesis an environmentally friendly process.[19]

Current research in the field of ammonia synthesis includes the development of alternative catalysts such as ruthenium-based catalysts, Co-Mo-N catalysts, electrocatalysts and fused Fe catalysts. Another challenge is to reduce the emission of CO_2 by increasing the efficiency of Haber-Bosch synthesis plants and using alternative energies such as electric, light, solar, or radiation to assist the process by activating nitrogen or changing the pathway for the NH_3 production.[20]

Another focus for research is understanding the nature of the N_2 molecule, which is one of the hardest molecules in nature to activate and reaching ammonia synthesis under normal conditions of pressure and temperature (1 atm and 20 °C), which is theoretically feasible based on thermodynamic data and simulations. At these conditions, even the use of selective enzymes or bacteria is possible to fix nitrogen and produce ammonia.

To overcome the high costs associated with the relatively high pressures and temperatures needed for the Haber-Bosch process (HBP), metal-nitride catalysts are being developed. These catalysts react by creating nitrogen vacancies when the N atoms in their surface are reduced to NH_3. The vacancies are then filled with gaseous N_2 in a Mars-van Krevelen mechanism,[21] rather than adsorbing N_2 first like in conventional catalysts. These types of catalysts can be the key to advance in the path that Haber started: achieving ammonia production with high yields at ambient conditions.[22]

1.3 Properties of transition metal nitrides (TMNS)

Nitride-based materials possess chemical and physical properties that render them as suitable catalytic materials in technological applications and science.[23] Group 6 (W, Mo and Cr), 5 (V, Nb and Ta) and 4 (Ti, Zr and Hf) transition metal nitrides possess high melting points

in the range 2000-800 °C. Their high melting points, hardness[24] and tensile strength put them in the range of refractory compounds. This combination of features enables them to be broadly applied as cutting tools.[25] Additionally, the nitride materials generally exhibit conductivity (electrical[26] or thermal[27]), magnetic susceptibility[28] and resistance against corrosion.[29] Further applications include being utilised as diffusion barriers,[30] superconductors, high temperature structural materials and magnetic devices. Concerning the catalytic properties, it is well documented that early transition metal nitrides and some noble group metals share similar electronic properties, which was mainly inspired by the pioneering work of Levy and Boudart,[31] who reported the "platinum-like" catalytic performance of tungsten carbide in hydrogenolysis and isomerization of 2,2-dimethylpropane.

The electronic modification that occurs in metal d-bands during the formation of transition nitrides is mainly responsible for the catalytic activities. The inclusion of nitrogen molecules results in an expansion of the metal host lattice, increasing the metal-metal distances and contracting the metal d-band of the parent metal. This results in a greater density of states (DOS) near the Fermi level of metal nitrides compared to the parent metal,[32] which causes the metal surface to exhibit an electron donating character. The redistribution in transition metal nitrides gives rise to their catalytic behaviours; resembling that of the noble metals.[33,34,35,36,31] Thus, they are desirable heterogeneous catalysts in a wide variety of industrial processes, including ammonia synthesis[37,38,39,40,41,42]and decomposition,[43]electrochemical reactions,[44] hydrogenolysis,[45] hydroprocessing[46] and isomerisation.[47]

It is argued that the incorporation of the nitrogen into the interstitial sites within the structure of metal nitrides plays no direct role for the behaviour of the catalyst but may be to provide a correct order on the active surface plane.[40]

Transition metal nitrides (TMN_S) can be divided broadly into three categories, ionic, covalent and interstitial type.[48,49] In the first category, there is significant ionic and covalent character, similar to that found in oxides, in that (*e.g.* Ca_3N_2). Bonding is more similar to that found in carbides in the second category with predominates metallic bonding; nitrogen atoms present in interstitial positions within the metal array (*e.g.* TiN, CrN).[48,49] The formation of the bonding in transition metal nitrides is due to the interaction of the 2s and 2p orbitals of nitrogen with metal d orbitals.[50,51]

1.4 Crystal structure

The structure of metal nitride materials is the most pivotal parameter that determines various properties. It has been reported that the structures of these materials are based on two fundamental factors; geometric and electronic.[33] Group 4-6 early transition metal nitrides have been classified as interstitial alloy compounds with complex and various crystal structures. The smaller nitrogen atoms (0.71 Å) are integrated randomly into the interstitial sites of their parent metals in cubic close-packed metallic structures (ccp),[33] which is the main contributing factor to their attractive electrical conductivity.[52] In this type, the metal atoms are arranged differently from those of their corresponding parent metals in either face centred cubic (fcc), or hexagonal closed packed (hcp), or simple hexagonal (hex) structures Figure 1-1. The largest interstitial site is an octahedral site in (fcc) and hcp which is occupied by nitrogen atoms. With regards to simple hexagonal structure, nitrogen atoms accommodate into trigonal prismatic sites.

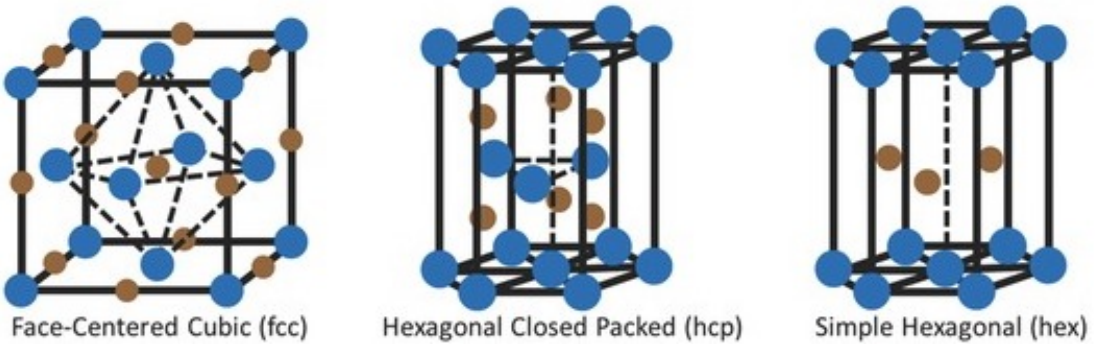

Figure 1-1 The typical crystal structures of TMNs, including face-centred cubic (fcc), hexagon-closed packed (hcp), and simple hexagonal (hex) structures. Reproduced from reference.[53] Copyright 2016, Wiley-VCH.

The body centred cubic (bcc) structure of metallic molybdenum Mo for instance could be modified by intercalation of nitrogen atoms to fcc-like structure of its analogue's stable nitride Mo_2N Figure 1-2.

The electronic factor is commonly cited as the reason behind the structural changes between the parent metals and nitrogen containing transitions metals. The structure of these compounds relies on two factors; geometric and electronic, as reported by Oyama.[49] For binary compounds, the structure changes from a simple to a more complex one as we move from the left to right side in the periodic table due to the strong effect of geometry on interstitial sites. The structure can be predicted based on the empirical rule which was developed by Hägg. According to this rule, the crystal structure can be determined depending on the radius ratio r = $\frac{r_x}{r_m}$, where r_x and r_m are the radii of the interstitial nonmetal and transition metal atom, respectively. When radius ratio is less than 0.59,[54] the transition metal

and interstitial non-metal atoms form interstitial compounds such as (ccp), (bcc), or (hcp), whereas greater than 0.59 complex structures form.

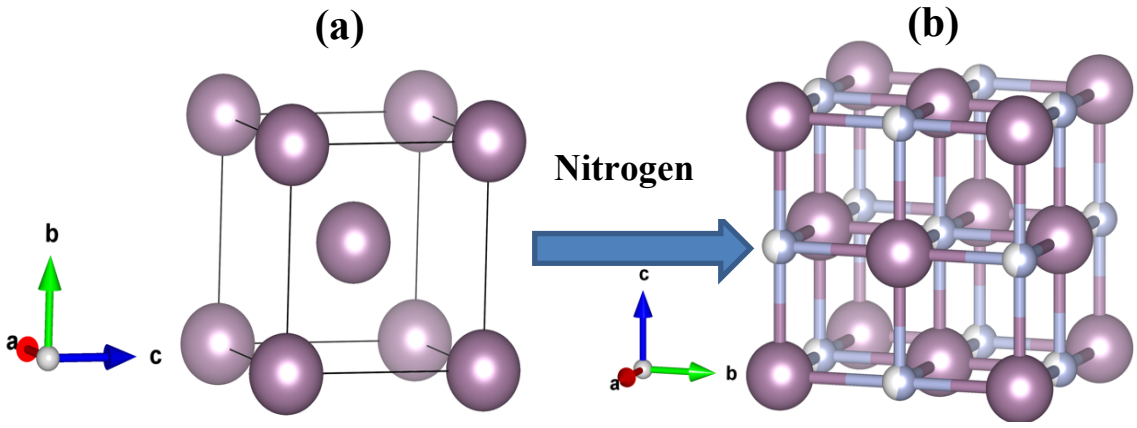

Figure 1-2 The typical crystalline structures of body centred cubic (bcc) for metallic Mo (a) and face centred cubic (fcc) of Mo_2N (b) unit cell's. Pink and grey spheres represent Mo and N atoms, respectively. Diagram prepared using Vesta and structure data from Jette *et al*[55] and Cao *et al*[56] for pure Mo and Mo_2N, respectively.

Binary molybdenum nitrides exist over a broad structure range with various stoichiometry. The most investigated of these materials are the rocksalt type Mo_2N molybdenum nitride and the hexagonal structures phases δ_1-MoN, δ_2-MoN and δ_3-MoN. Careful control of conditions during synthesis can also lead to β-Mo_2N, a tetragonally distorted rocksalt type phase with ordered stacking faults.

The structure-types of the bimetallic metal nitrides containing transition metals typically can be described as cubic, metallic perovskite or cubic, η-carbide type structures. Later on, however, another structural form of ternary molybdenum nitride which has a filled β-manganese structure has been identified.

In previous studies, it has been argued whether the XRD patterns generated from the ternary nickel molybdenum nitride material assigning to a phase containing Ni_2Mo_3N or the known ternary nitride Ni_3Mo_3N. However, Herle *et al*. suggested that as a separate metallic Ni phase was conducted in the post ammonolysis XRD, the nitride phase with Ni:Mo ratio of 1:1 is unlikely. They also demonstrated the excellent correlation between the observed intensity of the peaks corresponding to the Ni_2Mo_3N composition with that of Al_2Mo_3C which has been used as structural model. Furthermore, they extensively investigated the structure of Ni_2Mo_3N using different characterisation techniques, including powder X-ray diffraction (PXRD), transition electron microscopy (TEM) and temperature programmed reduction

(TPR). Ni_2Mo_3N crystallises with space group $P4_132$ and contains corner sharing [NMo_6] octahedra. The Ni atoms are placed in a 12-fold pseudo-icosahedral coordination, surrounded by nine Mo and three Ni atoms, giving Ni[Mo_9Ni_3] polyhedra. The pseudo-tetradecahedral site is comprised of six Ni, six Mo and two N atoms to form Mo[$Ni_6Mo_6N_2$] entities.

The filled β-manganese and η-carbide type structures have recently received considerable attention in various applications especially for ammonia synthesis. Typically, with a stoichiometry of M_2T_3X (M is a post transition metal, T is a transition metal and X is nitrogen). The nitride materials containing Mo with either Ni or Co have a filled β- manganese structure and η-carbide structure and are isostructural with the compositions developed in this study. In the following subsections, a brief description of each of these crystal structures is shown.

1.3.1 The crystal structure of the filled β -manganese structure

The filled β-manganese structure has been discussed elsewhere.[57,58] The filled β-manganese structure M_2T_3X (M and T= transition metals, X = small electronegative atom), as illustrated in Figure 1-3 is cubic and adopts the space group symmetry $P4_132$.[58,59] The structure is generated by the filling of an interstitial site with an electronegative non-metal atom such as carbon, nitrogen or oxygen, which is located at the centre of the T_6 octahedra. It is a complex structure, with a unit cell containing 20 Mn atoms.[60,61] Ni_2Mo_3N is an example of an interstitial nitride which crystallises in this structure, with corner-linked NMo_6 octahedra interpenetrated with a (10,3)-a network of nickel atoms.[58] The Ni_2Mo_3N structure has two inequivalent crystallographic sites: the Wyckoff 8*c* and 12d positions. Ni atoms on the 8*c* positions, result in a (10, 3)-a network of Mn atoms. Mo atoms occupy the 12d sites, which fill the space within the network, result in corner-sharing Mo_6N octahedra.[62]

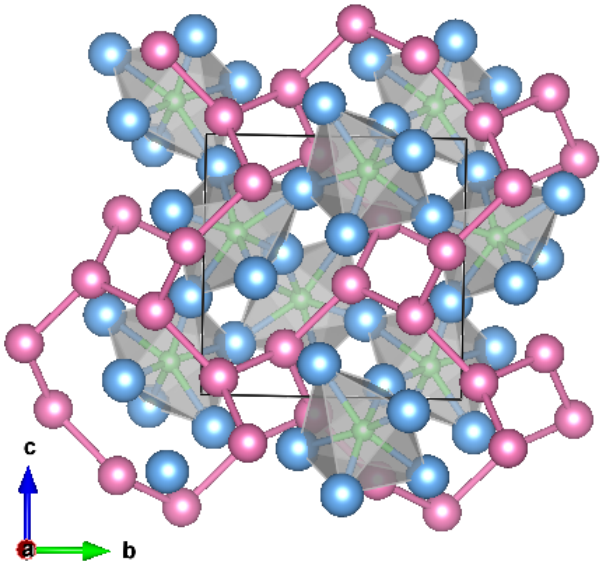

Figure 1-3 Unit cell of Ni_2Mo_3N viewed along [100] showing the corner linked NMo_6 octahedra and the interpenetrating (10,3)-a network of Ni atoms. Ni atoms are shaded pink, Mo blue and N_2 green. Diagram prepared using Vesta and structure data from Prior and Battle.[58]

1.3.2 The crystal structure of the η-carbide structure

Figure 1-4 illustrates the cubic unit cell image of η-6 Co_3Mo_3N structure. The structure of the η-phase Co_3Mo_3N phase has been well established and it was found to be isostructural with η-Fe_3W_3C,[63] which crystallises with space group $Fd\bar{3}m$. This compound reveals a face centred cubic (fcc) structure which composes of corner shared NMo_6 octahedra with the Co atoms that occupy the sites between the octahedrons. The Co (Co_1, Co_2) and Mo atoms are disordered over the Wyckoff sites (32e, 16d) and 48f, respectively. The octahedral 16c site is preferentially occupied by N atoms. In the η-6 Co_3Mo_3N structure, unlike Mo, Co is located at two crystallographically non-equivalent sites which resulting in the formation of site vacancies and interstitial defects within the crystal structure. Each Co is surrounded by six Mo and six Co atoms that led to the formation of Co [Mo_6Co_6], while Mo is bound to four Mo, six Co and two N species.

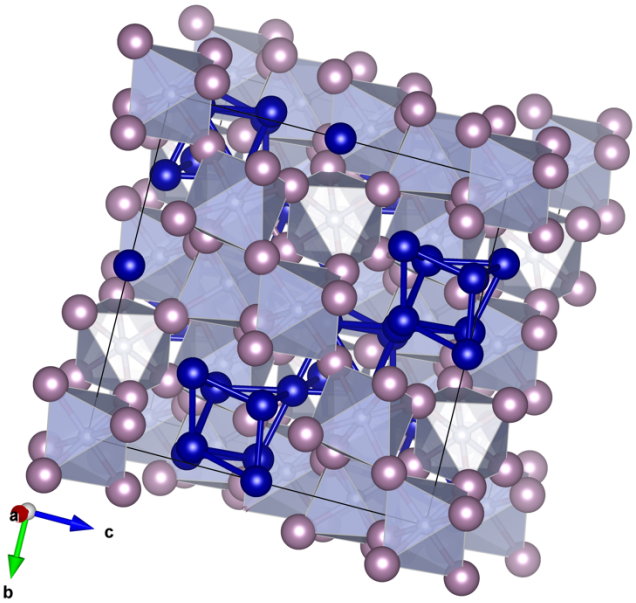

Figure 1-4 Unit cell of cubic Co_3Mo_3N showing the distorted corner- sharing NMo_6 octahedra. Mo atoms are shaded pink; Co dark blue; N_2 grey. Diagram drawn using Vesta and structure data from Jackson *et al.*[64]

1.4 Improving of the catalytic properties

Improving the performance of metal nitride catalysts can be achieved using various strategies. One common strategy involves the introduction of suitable transition metals into the crystal structure, one of the component metals of the catalyst acts as an activity promoter of the main active component of the compound. Some catalyst promoters such as Ni and Co, which are commonly used with Mo or W have been reported by Speight.[65] A series of nickel molybdenum nitride catalysts were reported by Chu *et al.*[66] using a sol-gel method and ammonolysis of oxide precursor with NH_3, and characterised by BET, X-ray diffraction and H_2 temperature programmed reduction. The primary function of supported catalysts is the maintenance of high surface area of active components. The different types of these catalytic metals were reported by several investigators. The dispersed metal component of the catalyst can be a single metal[67] or coupled with another metal.[66] Although the high temperature of metathesis method for example, may make this difficult, previous studies have proved that the control of these parameters can be achieved. Bem *et al.*[63] used a mixture of aqueous solution of Mo salt with aqueous solution of Ni salt or Fe salt to produce $NiMoO_4$ and $FeMoO_4$ precursors respectively. The mixture was dried under N_2 gas at 700 °C for 6 h. The salt precursors obtained were placed under flowing ammonia gas and heated at 5 °C min^{-1} to 700 °C to synthesise the corresponding ternary nitrides (Ni_3Mo_3N and Fe_3Mo_3N). The review on potentialities of metal nitrides for ammonia production is discussed below. The size, shape and crystalline structure of metal nitrides are critical for catalytic behaviour.

Furthermore, high surface area of the materials is very useful to alter their catalytic activities, which can be achieved *via* the ammonolysis of their oxide precursors using temperature programmed reaction.[68,69]

The researchers observed that the high surface area of nitride materials in correlation with their lower cost might improve their performance as a catalyst.[70] Catalytic interest has mainly centred upon the interstitial materials of molybdenum and tungsten based systems as they exhibit high performance in ammonia production comparable to that of ruthenium metal, which is the most active current commercial material.[70,40]

1.5 Catalytic activities of transition metal nitrides as catalysts for ammonia synthesis

As mentioned earlier**,** the Haber-Bosch process based on iron-based metal catalysts is the most common process for ammonia synthesis and has been widely studied. The large scale production of ammonia through this process involves the direct reaction of pure H_2 and N_2 over an iron-based catalyst promoted with K_2O and Al_2O_3 at high pressure and temperature.[71] New processes and catalysts to reduce temperature and pressure in Haber-Bosch are required. TMN_S with Pt-like catalytic properties have been suggested as the most promising alternative catalyst for ammonia synthesis.[72] In recent years, catalytic activity of binary and ternary nitride systems for ammonia production has gained growing interest and has been widely investigated, due to its unusual composite properties.

Earlier studies by Mittasch investigated the catalytic behaviour of some metals towards ammonia synthesis including, Fe, Co, Ni, Ru, Os, Mn, Mo, U and Ce. It was concluded that these metals share similar ammonia synthesis activity, and Ni had the lowest activity followed by cobalt metal.[73] Boudart developed molybdenum nitride catalysts with high surface areas, and also later the work of Aika and Kojima reporting the high surface area of the cobalt molybdenum bimetallic nitride catalyst synthesised- by nitridation of cobalt molybdate hydrate with ammonia at 973 K-under the same conditions. It has been demonstrated in recent extensive studies that, Co_3Mo_3N related catalysts have high catalytic activity that have drawn the researcher's attention. In particular, it has been stated that the Co–Mo bimetallic nitride Co_3Mo_3N doped with Cs^+ is one of the most active catalysts for ammonia synthesis and the activity of this phase can be exceeded that of conventional iron based Haber-Bosch catalysts.[74,75] Further investigations carried out by Jacobsen and co-workers demonstrated that bimetallic nitrides Fe_3Mo_3N and Co_3Mo_3N display high catalytic properties in ammonia synthesis, although the reaction was operated at high pressure. The theoretical studies of Jacobsen *et al.* have led to establishment of a volcano shaped

relationship between computed TOFs of different metals and their nitrogen adsorption energies. In general, the idea is that the nitrogen binding energies are an important factor for the performance of catalysts Figure 1-5. For example, Fe and Ru catalysts display much higher activity than pure Co and Mo catalysts because nitrogen binds too weakly to the Co and too strongly to the Mo compared to Fe and Ru. On the other hand, Co–Mo bimetallic catalyst is expected to exhibit high ammonia synthesis activity, as compared with Ru catalysts, owing to the intermediate nitrogen binding energy of the Co–Mo bimetallic catalyst.[76] It was recently reported that molybdenum nitride has the ability to store and transfer agents of active nitrogen species.[77] Hargreaves group has found that 50 % of lattice N species of Co_3Mo_3N can be eliminated to yield Co_6Mo_6N. Furthermore, they found that the treatment of Co_3Mo_3N under H_2/Ar can reduce Co_6Mo_6N to generate ammonia, adsorbed N species can be provided by N lattice in the presence of H_2.[81,83] Thompson *et al.* have reported that the activity of δ-Mo_2N films was more active than β-$Mo_{16}N_7$ and γ-Mo_2N films.[75] Bion *et al.* reported that the nickel molybdenum nitride materials prepared by ammonolysis and N_2/H_2 pre-treatment of the $NiMoO_4$ precursor have much greater activities for ammonia synthesis.[37,40] Fe_3Mo_3N has been shown to be isostructural with Co_3Mo_3N, cubic η-carbide structures, using Rietveld refinement.[80] Recently, Laassiri *et al.* demonstrated that the nitrogen transfer properties of tantalum nitride materials does not depend on the accessible surface area. It was also observed that doping tantalum nitrides with small content of cobalt resulted in high reactivity at low temperature to produce ammonia.[81]

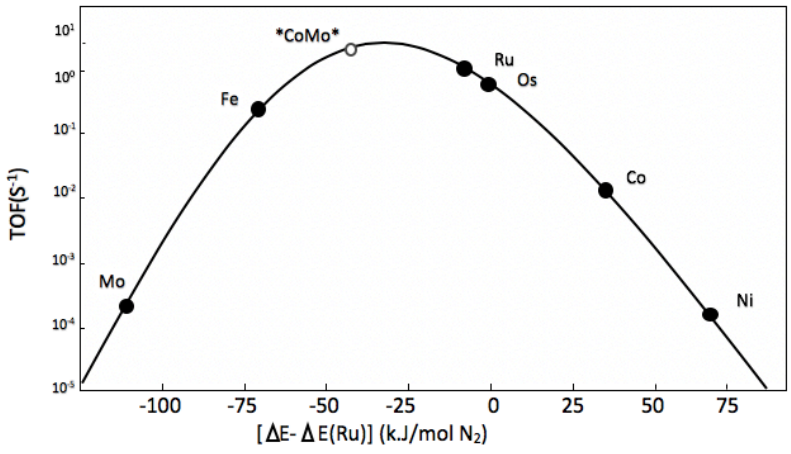

Figure 1-5 Relationship between the turnover frequencies (TOF) of different metals for the ammonia synthesis reaction at 400 °C with respect to their nitrogen adsorption energy.[76]

Table 1-1 The reported catalytic activities of molybdenum nitride materials

Ref	catalyst	Method	Starting materials	Reaction conditions	Sintering conditions (°C, time, gas)	Ammonia rate	Ammonia reaction
[42]	Ni_2Mo_3N	Citrate Sol-gel Ammonolysis	$(NH_4)_6Mo_7O_{24}\cdot 4H_2O$ + $Ni(NO_3)_2\cdot 6H_2O$ + Citric acid+ HNO_3	Evaporation at 70 °C, calcined at 500 °C, 2 h	900 °C, 12 h, NH_3	116 μmol g^{-1} h^{-1}	0.3 g, 400 °C, 0.1MPa, 60 ml min^{-1} N_2 + $3H_2$
[42]	$NiCoMo_3N$	Citrate Sol-gel Ammonolysis	$(NH_4)_6Mo_7O_{24}\cdot 4H_2O$ +$Ni(NO_3)_2\cdot 6H_2O$ + $Co(NO_3)_2\cdot 6H_2O$+ Citric acid+ HNO_3	Evaporation at 70 °C, calcined at 500 °C, 2 h	900 °C, 12 h, NH_3	166 μmol g^{-1} h^{-1}	
[41]	Co_3Mo_3N	Coprecipitation	$Co(NO_3)_2\cdot 6H_2O$ + $NH_4)_6Mo_7O_{24}\cdot 4H_2O$	85 °C, 5 h. Calcined 500 °C, 5 h.	357 °C, 5.6 °C min^{-1}, 447 °C min^{-1}, 0.2 °C min^{-1}, 785 °C, 2.1 °C min^{-1} for 5 h, NH_3	489 ± 17 μmol g^{-1} h^{-1} 18 m^2 g^{-1}	0.3 g, 500 °C 0.1MPa, 60 ml min^{-1} of N_2 + $3H_2$
[82]	Mo_2N	Nitridation	MoO_3	Dry overnight at 423 K	10.K min^{-1} to 623 K, 0.6 K min^{-1} to 723 K, and 3.0 K min^{-1} to 973 K for 1 h	35 μmol g^{-1} h^{-1} 186 m^2 g^{-1}	0.4 g, 673 K, 0.1MPa, 60 ml min^{-1} N_2 + $3H_2$
[82]	Ni_2Mo_3N	Nitridation	$Ni(NO_3)_2\cdot 6H_2O$+ $NH_4Mo_7O_{24}\cdot 4H_2O$	Dry overnight at 423 K	973 K, 5 K/ min^{-1} , 6 h, NH_3	270 μmol g^{-1} h^{-1} 20 m^2 g^{-1}	
[82]	Fe_3Mo_3N	Nitridation	$Fe(NO_3)_3\cdot 9H_2O$+ $NH_4Mo_7O_{24}\cdot 4H_2O$	Dry overnight at 423 K	973 K, 5 K/ min^{-1}, 6 h, NH_3	143 μmol g^{-1} h^{-1} 7 m^2 g^{-1}	
[82]	Co_3Mo_3N	Nitridation	$Co(NO_3)_2\cdot 6H_2O$ + $NH_4Mo_7O_{24}\cdot 4H_2O$	Dry overnight at 423 K	973 K, 5 K/ min^{-1} , 6 h, NH_3	652 μmol g^{-1} h^{-1} 21 m^2 g^{-1}	

[82]	Co_3Mo_3N-Cs2	Impregnation	$CoMoO_4 \cdot nH_2O$+ $CsNO_3$	-	-	986 μmol g^{-1} h^{-1} 16 m^2 g^{-1}	
[82]	Co_3Mo_3N-Cs10	Impregnation	$CoMoO_4 \cdot nH_2O$+ $CsNO_3$	-	-	586 μmol g^{-1} h^{-1} 10 m^2 g^{-1}	0.4 g, 673 K, 0.1MPa, 60 ml min^{-1} N_2 + $3H_2$
[82]	Co_3Mo_3N-K5	Impregnation	$CoMoO_4 \cdot nH_2O$+ KNO_3	-	-	869 μmol g^{-1} h^{-1} 17 m^2 g^{-1}	0.4 g, 673 K 0.1MPa, 60 ml min^{-1} of N_2 $3H_2$
[82]	Co_3Mo_3N-K30	Impregnation	$CoMoO_4 \cdot nH_2O$+ KNO_3	-	-	364 μmol g^{-1} h^{-1} 8 m^2 g^{-1}	
[37]	Co_3Mo_3N	*In situ*	$Co(NO_3)_2 \cdot 6H_2O$ + $(NH_4)_6Mo_7O_{24} \cdot 4H_2O$ γ-Mo_2N + Co	400 °C, 2 h	600 °C, 0.1 °C min^{-1}, 4.5% NH_3 in 3:1 H_2–N_2	120 ml h^{-1} g^{-1} 11 m^2 g^{-1}	1 to 100 bar, 320-500 °C, 3:1 and 1:1 H_2–N_2
[37]	Cs /Co_3Mo_3N	Impregnation	$CsNO_3$+ Co_3Mo_3N	400 °C, 2 h	600 °C, 0.1 °C min^{-1} , 4.5% NH_3 in 3:1 H_2–N_2	1040 ml h^{-1} g^{-1}	
[37]	Ni_2Mo_3N	*In situ*	$Ni(NO_3)_2 \cdot 6H_2O$ + $NH_4)_6Mo_7O_{24} \cdot 4H_2O$	400 °C, 2 h	600 °C, 0.1 °C min^{-1} , 4.5% NH_3 in 3:1 H_2–N_2	80 ml h^{-1} g^{-1} 7 m^2 g^{-1}	
[37]	Cs/Ni_2Mo_3N	Impregnation	$CsNO_3$+Ni_2Mo_3N	400 °C, 2 h	600 °C, 0.1 °C min^{-1} , 4.5% NH_3 in 3:1 H_2–N_2	530 ml h^{-1} g^{-1}	
[37]	Fe_3Mo_3N	*In situ*	$Fe(NO_3)_3 \cdot 9H_2O$+ $NH_4Mo_7O_{24} \cdot 4H_2O$	400 °C, 2 h	600 °C, 0.1 °C min^{-1}, 4.5% NH_3 in 3:1 H_2–N_2	90 ml h^{-1} g^{-1} 8 m^2 g^{-1}	1 to 100 bar, 320-500 °C, 3:1 and 1:1 H_2–N_2
[37]	Cs/Fe_3Mo_3N	Impregnation	$CsNO_3$+ Fe_3Mo_3N	400 °C, 2 h	600 °C, 0.1 °C min^{-1} , 4.5% NH_3 in 3:1 H_2–N_2	440 ml h^{-1} g^{-1}	

[37]	γ-Mo_2N	*In situ*	$NH_5(CoOHMoO_4)_2$	470 °C	600 °C, 0.1 °C min^{-1} , 4.5% NH_3 in 3:1 H_2–N_2	30 ml h^{-1} g^{-1} 203 m^2 g^{-1}	
[83]	Co_3Mo_3N	Precipitation	$Co(NO_3)_2{\cdot}6H_2O$ + $(NH_4)_6Mo_7O_{24}{\cdot}4H_2O$ ($CoMoO4{\cdot}nH_2O$)	80 °C. Dry overnight at 150 °C, 500 °C in air.	357 °C at 5.6 °C min^{-1} to 447 °C at 0.5 Cmin^{-1} to 785 °C at 2.1 °C min^{-1} for 5 h, NH_3	165 μmol g^{-1} h^{-1} 18 m^2g^{-1}	0.4 g, 673K, 0.1MPa, 60 ml min^{-1} N_2 + $3H_2$
[83]	Ni_2Mo_3N	Precipitation	$Ni(NO_3)_2{\cdot}6H_2O$ + $(NH_4)_6Mo_7O_{24}{\cdot}4H_2O$	Dry overnight at 150 °C, 700 °C for 6 h, N_2	357 °C at 5.6 °C min^{-1} to 447 °C at 0.5 °C min^{-1} to 785 °C at 2.1 °C min^{-1} for 5 h, NH_3	27 μmol g^{-1} h^{-1} 1 m^2 g^{-1}	
[83]	$NiMoO_4$	Precipitation	$Ni(NO_3)_2{\cdot}6H_2O$ + $(NH_4)_6Mo_7O_{24}{\cdot}4H_2O$	Dry overnight at 150 °C, 700 °C for 6 h, N_2	357 °C at 5.6 °C min^{-1} to 447 °C at 0.5 °C min^{-1} to 785 °C at 2.1 °C min^{-1} for 5 h, NH_3	46 μmol g^{-1} h^{-1} 3 m^2 g^{-1}	
[83]	$CoMoO_4{\cdot}nH_2O$	Precipitation	$Co(NO_3)_2{\cdot}6H_2O$ + $(NH_4)_6Mo_7O_{24}{\cdot}4H_2O$	Dry overnight at 150 °C, 700 °C for 6 h, N_2	*In situ* by N_2/H_2 700 °C, 2 h, 60 ml min^{-1}	135 μmol g^{-1} h^{-1} 13 m^2 g^{-1}	
[78]	Fe_3Mo_3N	Precipitation	$Fe(NO_3)_3{\cdot}9H_2O$ + $NH_4Mo_7O_{24}{\cdot}4H_2O$	Dry overnight at 150 °C, 700 °C for 6 h, N_2	357 °C , 5.6 °C min^{-1} , 357 to 447 °C at 0.5 °C min^{-1} , 785 °C at 2.1 °C min^{-1} 5 h.	95 µmol g^{-1} h^{-1}	

1.6 Conversion of oxide precursors into nitride materials

1.6.1 Ammonolysis of binary oxides

Molybdenum nitride based materials have captured great attention since they display good catalytic properties for ammonia synthesis reaction.[38] Preparation of molybdenum nitrides has been reported using a variety of methods, but the majority of them are based on the temperature programmed reaction of Mo-containing precursors.[38,84] Since ammonia provides nitrogen more easily than other sources, it is the most preferred nitridation agent. Volpe and Boudart[72] reported that high surface areas of nitride materials based on molybdenum can be obtained by the nitridation of the metal oxide precursors with ammonia *via* a temperature programmed reaction. Furthermore, it was found that the properties of the prepared materials were highly dependent on the synthesis condition. In the application of temperature programmed reaction, slow temperature ramping rates and space velocities of ammonia gas were recommended to maximise the surface area.

Wise and Markel [85] pointed out the problem associated with the endothermic decomposition of ammonia. They concluded that using mixtures of H_2/N_2 for nitridation has several benefits over the use of NH_3, the main ones being that γ-Mo_2N could be obtained with high surface area. Choi *et al*.[86] used temperature programmed reaction of MoO_3 to synthesise a series of molybdenum nitride catalysts by employing two segment temperature program. They concluded that the selectivity with respect to the surface area and phase constituents of the molybdenum nitrides depended on the heating rates combined and space velocity individually. High temperature rates in the interval 450 °C to 650 °C produce high surface areas of molybdenum nitride. Slow heating rates in the interval temperature from 250 °C to 450 °C led to a route going through H_xMoO_3. Colling *et al*.[86] investigated the surface chemistry of bulk molybdenum nitrides with surface area of up to 193 $m^2\ g^{-1}$, which were prepared using temperature programmed reaction of MoO_3 with NH_3, from ambient temperature to 500 °C. The catalysts were investigated by temperature programmed desorption (TPD) measurements. They concluded that the passivated layer of oxygen was removed by reaction with decomposed NH_3 and H_2 gas left on the surface of the catalyst at temperatures 277 °C or with H_2 gas at higher temperatures. Research on the synthesis of transition metal nitrides is ongoing.

Nitrides including transition metals such as Mo, W were reported by Ramanthan and Oyama.[46] The catalysts were synthesised by temperature programmed reaction of oxide

precursor under a flow of ammonia gas, and analysed using X-ray diffraction and BET surface area.[87,88]

Synthesis of metal nitrides is well explored. Processing complexity of tungsten nitride synthesis is related to necessity of nitrogen atom incorporation into the tungsten lattice which is problematic to realise at atmospheric pressure.[89] Normally use ammonia reduction is used to produce tungsten nitride from tungsten oxides at a high temperature 700-900 °C.[90]

DiSalvo reported a simple method to form mesoporous transition metal nitrides (NbN, VN, Ta_3N_5 and TiN) by the ammonolysis of ternary zinc metal oxide precursors.[91] Transition metal nitrides with pore sizes from 10 to 40 nm, particle sizes of 5–40 nm, and surface areas 15–60 $m^2\ g^{-1}$, depending on both the starting composition and the ammonolysis variables such as synthesis temperature, heating rates and space velocity have been studied. Neylon *et al*.[47] prepared phase-pure early transition metal nitrides, γ-Mo_2N, VN and β-W_2N by the method of temperature programmed reaction of metal oxide precursors with NH_3 flow. Furthermore, they investigated the catalytic properties of these materials. They found that the nitrides were mesoporous, the pore size was in two ranges of about 2 and 50 nm and the surface area was 81 $m^2\ g^{-1}$.

1.6.2 Ammonolysis of ternary oxides

Mixed metal nitrides can be produced *via* the ammonolysis of metal oxide precursors. This approach was used by Weil and Kumta to prepare Co_3W_3N and Fe_3Mo_3N.[92,93,94] The preparation of the precursors was first done by adding a complexing agent (ethanolamine and triethylamine to form Fe_3Mo_3N and Co_3W_3N, respectively.) to stoichiometric mixtures of the interrelated transition metal chlorides that are dissolved in acetonitrile. Evaporating the solvent and successive ammonolysis at around 950°C for 4 hours generated ternary transition metal nitrides. Fe_3W_3N was subsequently prepared using the same method to rapidly precipitate a homogenous mixture of the ions from solution. Another method provides technology of ternary V-Mo-N synthesis from the amine. It includes further steps: mixing of ternary oxide hexadecylamine in acetone, addition of hydrogen peroxide, foaming process with spreading of the product onto a clean glass, transferring in a furnace and treating by high temperature (up to 800 °C) under ammonia flow. This scheme allows forming a high surface area material, which is important for V-Mo-N systems.[29,95]

A variety of known ternary metal nitrides have been prepared from binary nitrides, metals or by the ammonolysis of ternary oxide. Synthesis of ternary metal nitrides has been accomplished by using various preparative procedures.

Conventional high temperature routes lead to low surface area, so for catalysts different approaches are needed. Focussing on the past several years, extensive research on metal nitrides has been carried out, numerous ternary and quaternary metal nitride catalysts have been synthesised using different routes *via* controlled temperature programmed ammonolysis of metal oxide precursor. The major synthetic approaches to transition metal nitride catalysts have been employed and reported in detail by several investigators. Sapina *et al*.[96] prepared pure phase Ni_2Mo_3N by freeze drying a solution of metal salts followed by heating and subsequently ammonolysis. This method has been applied in the formation of vanadium molybdenum oxynitrides. Hada *et al*. reported the nitrides of Co and Mo mixtures at Co/ (Co+Mo) ratios of 0.25 and 0.5 and documented that the species formed at 750 °C were γ-Mo_2N, β-$Mo_2N_{0.78}$ and Co_3Mo_3N phases. Gomathi developed a new process to prepare interstitial molybdenum nitrides with η-carbide structure such as Co_3Mo_3N and Fe_3Mo_3N *via* urea route.[97] In this method pellets of the corresponding oxide precursors were heated with urea in a 1:12 molar ratio under nitrogen stream for 3 h in the temperature range 900 - 1000 °C.

A similar route that was applied to the synthesis of η-carbide nitrides was used to prepare Ni_2Mo_3N.[97] Unfortunately, due to the stoichiometry of the starting material (Ni_2MoO_4), the results showed unwanted Ni impurities in the Ni_2Mo_3N.

Other routes based on the transformation of organometallic oxide precursors into metal nitrides by the direct reaction between metal oxide with ammonia were applied for the production of metal nitride materials.[98] A very similar technique to that used to prepare η-carbide nitrides was used by Herle *et al.* to prepare the filled *β*-manganese nitride Ni_2Mo_3N.[57] The obtained precursor which was made by dissolving the corresponding metal chlorides in acetonitrile was reacted under flowing ammonia gas at 950 °C for 4 h. Attempts were made to prepare Ni_2Mo_3N *via* the reduction of $NiMoO_4$. This, however, resulted in a mixed phase containing Ni_2Mo_3N and Ni metal, due to the difference in stoichiometry of the precursor and desired product. This mixture of Ni_2Mo_3N and Ni metal has been erroneously reported in the literature as Ni_3Mo_3N.[99,100,101,102] Ni_2W_3N was also synthesised *via* the ammonolysis of chemically complexed precursors.[103] Pt_2Mo_3N and $PtPdMo_3N$ have been prepared by the ammonolysis of amorphous precursors obtained by the freeze-drying of aqueous solutions of the appropriate metal salts: $(NH_4)_6Mo_7O_{24}.4H_2O$, $(NH_4)_2[PdCl_6]$ and $(NH_4)_2[PtCl_6]$.[104] The individual salts were dissolved in water and added to each other in stoichiometric amounts. Then, droplets of this solution were flash-frozen in liquid nitrogen and successively freeze-dried.

The resulting amorphous powders were calcined in air at 600 °C for 12 h, in order to induce crystallinity. The crystalline precursors were then heated with NH_3 flow for 12 h at 900 °C. This route was also used to prepare Pd_2Mo_3N.[104]

1.6.3 Reduction-nitridation of oxide precursors

The reduction–nitridation of oxides under dilute hydrogen in nitrogen have also been used to synthesise ternary nitrides that contain two transition metals. The water produced as a by-product in the reaction is blown away by the flow of dilute hydrogen in nitrogen gas through the furnace. This process can be applied to binary and ternary oxides, as in the synthesis of the filled β-manganese compounds of Ni_2Mo_3N, Co_2Mo_3N (impure), and the solid solutions $Ni_{2-x}M_xMo_3N$ (M = Co, $0 \leq x \leq 1$; M = Pd, $0 \leq x \leq 1.5$),[58] $Fe_{2-x}M_xMo_3N$ (M = Ni, Pd, Pt) [105] and $Fe_{2-x}Rh_xMo_3N$.[59] The η-carbide compounds prepared in this way include the common η-carbides Fe_3Mo_3N and Co_3Mo_3N,[58] the solid solution of Fe in Co_3Mo_3N ($Co_{3-x}Fe_xMo_3N$),[106] and the ordered quaternary η-carbide Ni_2GaMo_3N.[106] The benefit of this route is a quick preparation of highly pure phases from oxide precursors.

Herel *et al.*[103] prepared Ni_2Mo_3N by the reduction of Ni_2MoO_4. They observed that the sample contains some amount of bimetallic nitride impurity, due to stoichiometry of the starting materials. Wang *et al.*[107] reported that the reduction temperature of the passivation layers of nitride, which prepared using temperature programmed reaction, has been decreased as a consequence of increase amount of Ni added. A new synthetic route to interstitial ternary nitrides which based on the reduction of mixed metal oxides under 10 % hydrogen in nitrogen has been developed.[58] The route was employed in the synthesis of ternary and quaternary metal nitrides adopting the filled β-manganese structure and the η-carbide structure. An example of a typical reaction equation is given below:[108]

$$2NiO + 3MoO_3 \xrightarrow{10\ \%\ H_2/N_2} Ni_2Mo_3N + 11H_2O \qquad \text{Equation 1-2}$$

1.7 Citrate gel method

Since the preparation of oxide materials can be achieved in an oxygen containing atmosphere, these compounds are widely studied compared to nitride materials. Similar chemical methods are not successful for producing nitrides owing to the thermodynamic factors. Synthetic routes of transition metal nitride materials generally require high temperature and long synthesis times. The obvious process to manufacture transition metal nitrides is the direct reaction of metals with nitrogen gas.[44] This route requires a large amount

of energy in order to cleave the strong triple bond in molecular nitrogen (945 kJ mol^{-1} for N≡N compared to only 498 kJ mol^{-1}, the bond dissociation energy for O=O).[109] Accordingly, increasing the activation energies for the formation of nitrides over oxides results in a low standard free energy of formation. As a result of long-term research efforts in nanoscience field, different approaches were developed. The preparation of metal nitride materials using different techniques is dependent upon the required materials properties for a particular application. As for many advanced materials, particle size reduction, high surface area and well-defined morphologies in transition metal nitrides are of key importance to produce active and efficient catalysts. At high synthetic temperatures, the resultant materials have various drawbacks including particle aggregation, high-energy consumption, poor crystallinity and incomplete conversions which result in oxygen and carbon contaminations that reduce their use in catalytic applications.[110] In addition, some transition metal nitrides are sensitive to air and moisture. Therefore, it is still necessary to develop a facile and highly efficient route to most nitrides in order to meet the increasing demand for high performance materials into many fields including catalysis. In the case of catalytic applications, the catalysts used, especially in ammonia synthesis reaction, are typically in the form of high surface area nanoparticles (NPs) with a narrow size distribution, which are deposited and dispersed uniformly on a high surface area support. Despite the synthetic challenges of nitrides, there has been substantial progress in the synthesis and processing of nitrides with development of various synthetic approaches leading to new well-crystallised metal nitride catalysts.

Wet chemical methods to metal nitride materials *via* suitable precursors are widely used, and lead to a rapid reaction rate at lower temperature processing. Among them, alkoxide sol gel process and co-precipitation are the most promising techniques that have been successfully employed for the development of a homogeneous mixed metal nitride. However, both are rather limited owing to the difficulties in the solubility of the different reactant metal salts components in the solution.[111] Accordingly, the Pechini method is required to overcome previously mentioned limitations. In 1967, Pechini produced an alternative method for the preparation of inorganic materials. Later, this route was modified to form multi component metal oxides, and coined as the "Pechini method" or the "Liquid Mix Process".[112] In order to prepare the optimum oxide precursors for metal nitride, this method was initially regarded as a suitable candidate for its key properties, which will be briefly described here. The modified Pechini-like process is based on two stages: first, the reaction between initial components, such as nitrates, carbonates and alkoxide with α-carboxylic acids, in the aqueous solution which leads to the formation of the gel. The second step consists of the

formation of metal oxide through the thermal decompositions of the obtained metal-polymer compositions.[113] Due to the polymeric matrix, the nucleation of intermediate precursors is constrained to the nanoscale and stays well dispersed in the reaction medium.[114] The sol–gel based Pechini method stands out as an efficient and versatile process, due to its distinctive advantages such as the use of different temperatures and proportions of citric acid and desired metal ions, to produce nanocrystalline powders, e.g. precursors to metal nitride catalysts. This approach involves the production of solid state material from a solution, where metallic ions are immobilized in a rigid organic polymeric network at the molecular level without precipitation and phase segregation.[114,115] In Pechini method citric acid is added to the solution to chelate the metal ions, and then polybasic acid chelates can be obtained. Chelation is a complexation process in which a ring structure forms to reduce the mobility of a metal atom, thus producing homogenous precursors. It has become one of the most common chelating agents used because the citrate ion metal complexes tend to be stable. This is owing to strong coordination of the two carboxyl and one hydroxyl group of the citrate ion to a metal ion in solution. In addition, this chelating agent could effectively help to control metal agglomeration during high temperature in the calcination stage.[116]

There are several factors that need to be considered in the Pechini method. These include solvent; rate and final temperature of calcination, precursors, pH and temperature of gelation.[117] The presence of solvents affects the conformation of the precursors.[118] The controlling values of pH in the citrate sol–gel method play an important role in the binding of citrate to metal ions, and also it can strongly affect homogeneity of metal citrate solutions and particle size in the final product.[115] It has been reported that lower pH values resulting in an increase protonation of the citrate, high pH resulting in the formation of metal hydroxides precipitation.[119,120]

Other conventional ceramic processing methods involves extensive milling and grinding. This has often resulted in the contaminants and inhomogeneity in particle distribution. Moreover, these techniques require prolonged temperatures while the Pechini route is characterised by typical higher reaction velocity and lower synthesis temperatures which turns to be improvement in many ways and allows production of homogeneous materials.

Bion *et al.*[40] synthesised Ni_2Mo_3N by utilising the Pechini method in the form of a citrate gel. They reported that Ni impurity phase is formed in the materials prepared from a $NiMoO_4$ precursors and was shown to be inactive to ammonia synthesis. On the other hand, they observed that the synthetic route based on the nitridation of the crystalline intermediate prepared by the Pechini method with the desired Ni: Mo 2:3 metal ratio produced single-phase Ni_2Mo_3N.

This method has some advantages over other studied routes (e.g. alkoxide based sol gel) of being low cost, easy preparation, nontoxic, it is also easy to disperse obtained nanoparticles in the proper media.[121] Like many techniques, the disadvantages of the Pechini method, it requires a large scale of the precursor, it also loses weight during the calcination stage.

1.8 Objectives

The aim of this research project is to develop a series of quaternary nitride based nanostructured compounds containing molybdenum using the sol-gel Pechini method and evaluate their activities as ammonia synthesis catalyst. The high surface area and small particle size are potentially important for the improvement of catalytic properties; therefore, they have been considered as the initial goal of this study. The ternary nitride Ni_2Mo_3N with a β-manganese structure is the first target compound, where doping of the nickel and molybdenum sites with copper or iron and tungsten, has been attempted, respectively. This will be extended over the course of this study. The high activity of Co_3Mo_3N stimulates our interest to develop new catalytic materials by doping this system with tungsten. Therefore, their catalytic performance as new materials for ammonia production against Co_3Mo_3N and Ni-W-Mo-N systems has been studied. In order to clearly understand the structural features of the samples, further investigation is required throughout this work. Powder X-ray diffraction technique provides a greater understanding of crystal structure and properties of the phases. Furthermore, complementary analytical tools have been applied, such as thermogravimetric analysis (TGA) to study the thermal stability and scanning electron microscopy (SEM) and transition electron microscopy (TEM) to determine nanoparticle shape and size distribution. Nitrogen porosimetry is used to measure surface area. The next chapter describes the experimental techniques utilised in this study.

Chapter 2 Instrumental Techniques

This chapter describes the main techniques that have been used to characterise the morphology, structures and compositions of the materials prepared during this project.

2.1 Scanning electron microscopy (SEM)

A scanning electron microscope (SEM), images a sample by using a high –energy electron beam that is scanned across its surface to produce various signals. These signals produce images revealing the surface topography or other features.[122] The low energy secondary electrons produced in the scanning electron microscope are most frequently used to characterise crystal shape, surface morphology**,** dispersed and agglomerated nanoparticles.

A schematic of a typical SEM is shown in Figure 2-1. The electron gun is the main component in the instrument that contains the tungsten filament and electrodes. By heating the tungsten filament, which acts as cathode, electrons are generated and emitted. These generated electrons can be accelerated by a positive charge through two electrodes, one of which is the positive electrode (anode), producing a beam of electrons. However, all the electrons are repelled toward the optic axis due to the negative charge of Wehnelt Cap. They are then collected in space between the filament and Wehnelt Cap, called a space charge.[123] The beams of the electrons are pass sequentially through the sample and two electromagnetic condenser lenses. The condenser collects and focuses the electrons to small, thin, coherent beam. The resulting signals are then collected, magnified and transmitted to a detector by the use of the magnetic lens system.

In this work, scanning electron microscopy was conducted using a Philips XL-30 ESEM (15 kV) with an attached Thermofisher Ultradry EDS detector and Noran System 7 processing electronics. Characterised samples were prepared using conductive carbon pads. A very small amount of finely crushed powder was dispersed on a carbon pad glued onto the surface of a standard SEM sample stub.

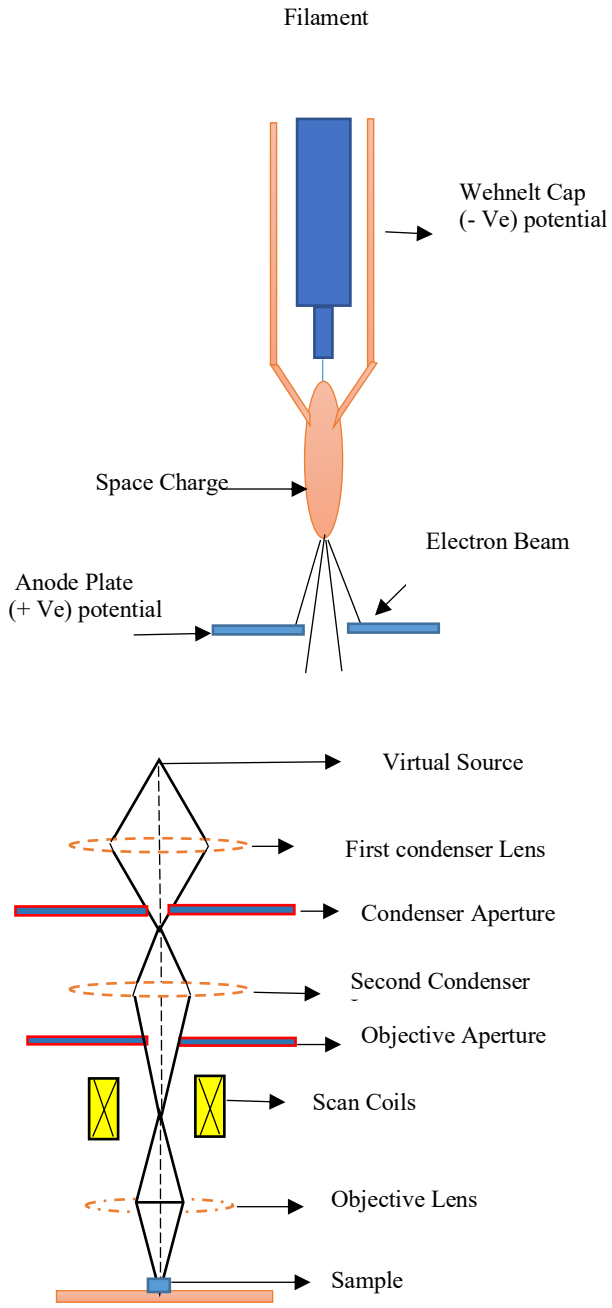

Figure 2-1 The electron gun and schematic of SEM (top)[123] and (bottom),[124] respectively.

2.2 Energy dispersive X-ray analysis (EDX)

Energy dispersive X-ray analysis is an analytical technique that offers information about the elemental composition of a specimen. This technique is commonly used in combination with SEM which typically are based on the interaction of a source of excitation electrons and a sample. The X-ray spectrum produced by a solid sample provides a localized chemical analysis. The principle of EDX is illustrated in Figure 2-2.

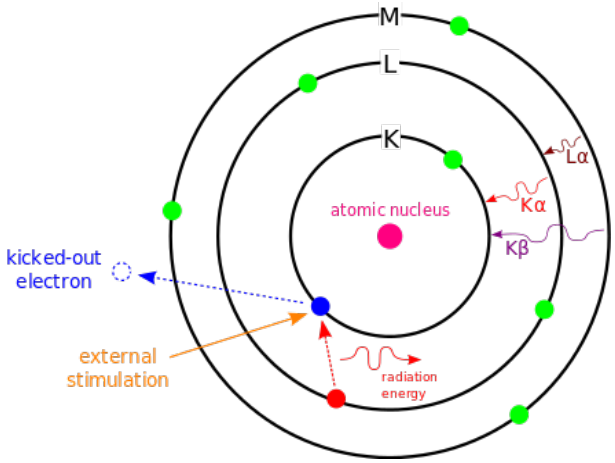

Figure 2-2 Principle of EDX

The operating principle relies on the fundamental concept that every element has a unique atomic structure and hence a distinctive line spectrum. A high-energy beam of electrons is focused onto the material being investigated to stimulate its emission of characteristic X- rays. An electron in an inner shell can be excited by the incident beam and get ejected from its shell while creating a vacancy and this can be occupied by an electron from an outer (higher-energy shell). The difference in energy between the higher and the lower energy orbitals will then be transmitted in the form of X-ray photon. The energy of these photons can be detected by EDX spectrometer which are characteristic of the atomic structure of the emitting element to enable an accurate elemental composition. The elemental composition of the specimen can be examined since these emission spectra are as characteristic to each element as fingerprints.

In this work, the EDX spectra were collected using a Thermofisher Ultradry detector with Noran System 7 (NS7) analysis platform on a Philips XL30- ESEM. The spot size was increased from the SEM monitor until for high magnifications of around 1000x and detector counts on the EDX monitor revealed a value of above 10,000. In the EDX experiments the live time was fixed at 100 seconds.

2.3 Transmission electron microscopy (TEM)

In transmission electron microscopy TEM Figure 2-3 an incident electron beam is transmitted through an ultra-thin specimen at high-accelerating voltage, 80–300 kV, which results in signals caused by the interaction between the specimen and incident electrons.[125] Electrons are emitted from the electron gun and illuminate the specimen through a two or three stage condenser lens system. Structures, compositions and chemical bonding of the specimen can be determined from these signals. The spatial resolution of TEM can be as low as 0.1 nm with electron probe size less than 0.5 nm, so that structural and compositional

analysis at atomic scale can be carried out easily.[126] TEM can be divided into two optical systems; the illumination and the imaging system. The illumination system contains the condenser lenses, which control the beam intensity and brightness. The imaging system hosts the objective lens and aperture, the selected area aperture, an intermediate lens and projector lens. The objective lens collects the transmitted electrons and disperses them into the back-focal plane (BFP) for imaging purpose.[127] The spatial distribution behind the specimen is imaged with a three or four stage lens system and viewed on a fluorescent screen.[128] In general, there are two basic modes of TEM imaging, namely, the bright field imaging and dark- field imaging. The bright mode imaging is the most common technique for the imaging using TEM. It means the formation of images only with the transmitted electron beam. On the other hand, dark-field images mode is formed if one or more diffracted electron beams are chosen by the objective aperture. In this case, the transmitted electron beam should be blocked. The advantage of the dark-field imaging method is its high-diffraction contrast and its ability for observing grain size distribution.[129]

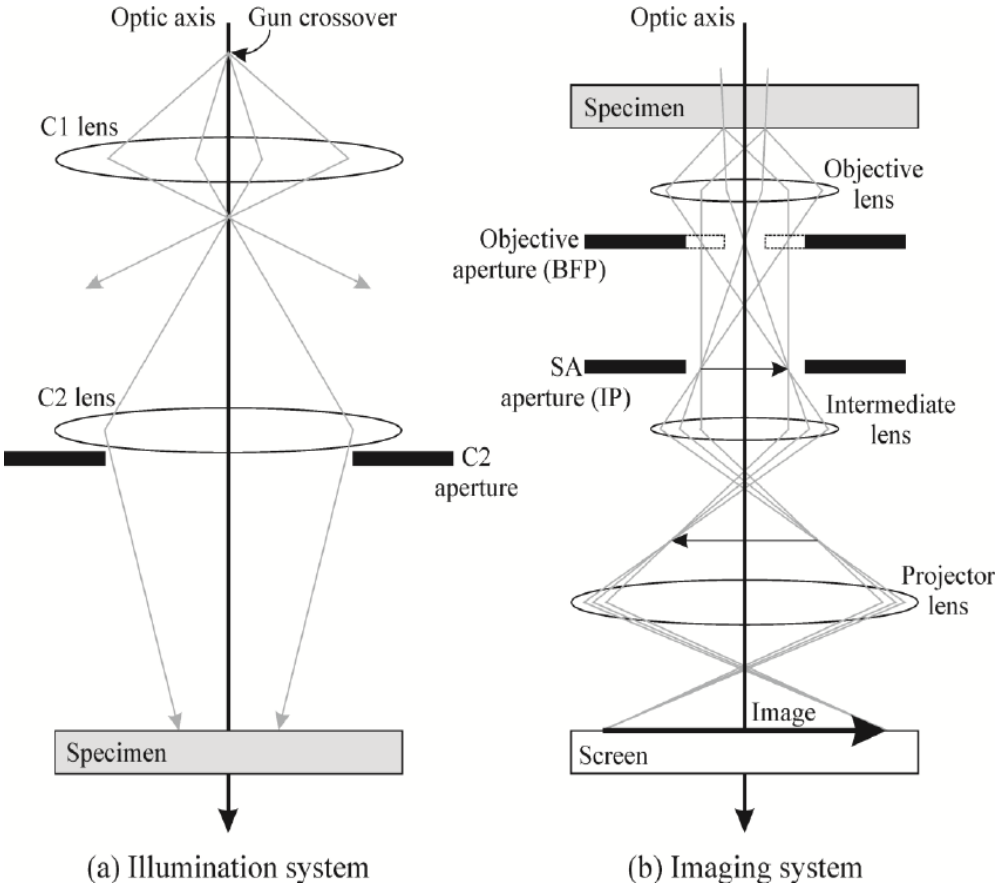

Figure 2-3 Schematic diagram of TEM, illumination system (a), imaging system (b).[128]

TEM was performed on Hitachi H7000 with accelerating voltage of 75 kV at the Biomedical Imaging Unit, Southampton General Hospital. Analysed samples were prepared by

ultrasound dispersal using propan-2-ol as the solvent and were deposited on carbon coated copper grids. The technique was applied to obtain images of the morphology of the nanopowder particles, and particle sizes.

2.4 Nitrogen porosimetry

During this study surface area measurements were performed on the samples. Surface area of catalysts is often found to be a critical factor in enhancing the catalytic activity. The method of evaluating the surface area was described by Brunauer, Emmett and Teller (BET) in 1938.[130] This adopted a multi-layered adsorption system which was originally extended from the Langmuir theory using the following hypotheses:[131]

(i) gas molecules adsorb infinitely on a solid in layers

(ii) the first and second layers of a solid are seen as different to each other and subsequent layers are the same as the second layer. Accordingly, the Langmuir theory can be applied to each layer and is given by:

$$\frac{P}{V_0(P - P_0)} = \frac{1}{V_m C} + \frac{C - 1}{V_m C}\left(\frac{P}{P_0}\right) \qquad \text{Equation 2-1}$$

Where

(i) P and P_0 are the equilibrium and the saturation vapor pressure of adsorbates, respectively.

(ii) V_0 is the adsorbed gas volume

(iii) V_m is the volume of gas required to complete a unimolecular adsorbed layer

(iv) C the BET constant, which is expressed by:

$$C = \exp\left(\frac{E_1 - E_L}{RT}\right) \qquad \text{Equation 2-2}$$

The BET method is widely used for the calculation of surface areas of solids by physical adsorption of gas molecules. The total surface area S_{total} and specific surface area S_{BET} are found through the equations:

$$S_{total} = \frac{(V_m \text{ N S})}{V} \qquad \text{Equation 2-3}$$

$$s_{BET} = \frac{s_{total}}{a}$$

Equation 2-4

Where

(i) N is Avogadro's number

(ii) S is the adsorption cross sectional area (16.2 Å) of N_2 gas.

(iii) V is the molar volume of adsorbent gas (22.414 ml)

(iv) a is the weight of the sample

2.4.1 Sample preparation for BET surface area determination

The surface areas of the samples were calculated by applying the Brunauer, Emmett and Teller19 (BET) method to nitrogen physisorption isotherms measured at 77 K using a Micromeritics Tristar II and samples previously degassed overnight at 120 °C.

2.5 Thermogravimetric analysis (TGA)

Thermogravimetric analysis (TGA) is used to measure the change in the weight of a sample over a range of temperatures in a given atmosphere (air, O_2, N_2, He, Ar). It is a useful tool to determine the changes in physical and chemical properties of materials either at a constant heating rate (as a function of increasing temperature), or at constant temperature and/or constant mass loss (as a function of time).[132,133] The basic principle of TGA is to follow mass changes of a material as it is heated, and it can be used to define the composition, thermal stability or phase transitions of the material. In general, during heating a material loses weight owing to decomposition, reduction, or vaporisation. If it undergoes oxidation, adsorption or absorption it can gain weight. During the analysis, the change in weight of the sample is monitored *via* a microgram balance. Temperature is tracked using a thermocouple. The TGA can also track change in weight as a function of time. Data can be plotted as weight percent or time vs temperature (°C).[134] For instance, if a tyre tread is being investigated, the rubber in the sample will have a lower decomposition temperature than carbon black and inert filler and hence will be the first to decompose. TGA instrumentation includes a sample holder (metallic/ceramic pans), microbalance, programmable heater (furnace), gas flow control, temperature control (thermostat) and temperature sensor (thermocouple).

Thermogravimetric (TGA) was performed using a Netzch TG 209 F1 Libra instrument. Pre-programmed heating regimes were adopted for the TGA samples heated under a flow of oxygen. The tested sample of approximately 16 mg was loaded in an alumina crucible (vol: 150 μL) under dry conditions, and then placed onto the balance within the analyser. It was

held at 25 °C for 10 minutes before gradually heating to 750 °C with a heating rate of 10 °C min^{-1} under 40 mL min^{-1} of 50 % oxygen and 50 % argon as reactant and protecting gas, respectively. At 750 °C the sample was then held for roughly one hour and 15 minutes before allowing it to cool down to room temperature.

2.6 Microanalysis

Combustion microanalysis is an analytical technique can be used for the quantitative determination of carbon, hydrogen and nitrogen contents of samples. During this project combustion analysis was performed on catalyst powders. The sample of approximately 3 mg was sealed and sent to MEDAC Ltd in order to determine elemental composition (carbon, hydrogen and nitrogen). This technique involves burning the specimen at high temperature under pure oxygen gas with tungstic oxide as a combustion aid, and then measuring the concentration of CO_2, H_2O and N_2 using a gas chromatograph to evaluate the original contents of C, H, N elements.

2.7 Powder X-ray diffraction (PXRD)

2.7.1 Principles of PXRD and Bragg's law

Powder X-ray powder diffraction (PXRD) is a versatile analytical technique mainly used for phase identification of a crystalline material and can provide detailed information on chemical composition and crystallographic structure. X-rays are produced in a cathode X- ray tube that contains a copper target and a tungsten filament. The high-speed electron beam from the filament is collided with the target by applying a high voltage. Copper metal is the most commonly target used due to its thermal conductivity, giving a K_α wavelength of 1.5418 Å. The K_α X-ray wavelength is selected by using a monochromator or curved mirror. The material under investigation must possess a crystalline structure. Since chemical substances usually differ in their crystal structures, the diffraction pattern can be used as a fingerprint for unknown crystalline materials.[135] Hence, unknown material can be identified by comparing their diffraction pattern against the diffraction patterns of known solid materials to find a match. Various crystallographic databases, such as the Cambridge Structural Database,[136] the Powder Diffraction File[137] and the Inorganic Crystal Structure Database,[138] have been established for this purpose.

The atoms in a crystal are in a periodic array and can scatter X-rays or other photons particles. Diffraction occurs when each object in a periodic array diffracts radiation coherently, generating constructive interference that gives high intensity and will be

observed at certain angles. In other directions, as the atoms are arranged differently, the scattered X-rays interfere destructively and this leads to loss of intensity.[135] The geometrical conditions for diffraction in crystals were first described by Bragg, as shown in Figure 2-4. He found that X-ray diffraction can be represented by sets of lattice planes (in which the atoms are located) which act as a semi-transparent mirror, allowing X-rays to interfere constructively as the beam incidence.[139]

For constructive interference of the scattered X-rays (the appearance of a diffraction peak) it is necessary that the beams, scattered on successive planes, be "in phase" (have a common wave front) after they leave the surface of the crystal. The beam paths labelled as 1 and 2 in Figure 2-4 vary by the length AB+BC, and this must be equal to an integral number of wavelengths (λ) of the incident radiation, accordingly:

$$AB + BC = n\lambda \qquad \text{Equation 2-5}$$

since $AB = BC \; and \; sin\theta \; AB/d_{(hkl)}$, we get the below the expression:

$$n\lambda = 2d_{(hkl)}sin\theta \qquad \text{Equation 2-6}$$

This relationship (Equation 2-7) is known as Bragg's equation[140] and it enables measurement of the wavelength and for determining angular position of the scattered beam in terms of λ and $/d_{(hkl)}$.

The term n =1, 2, 3, is designated as the order of reflection and $d_{(hkl)}$ is the inter-planar spacing of the lattice planes.[141]

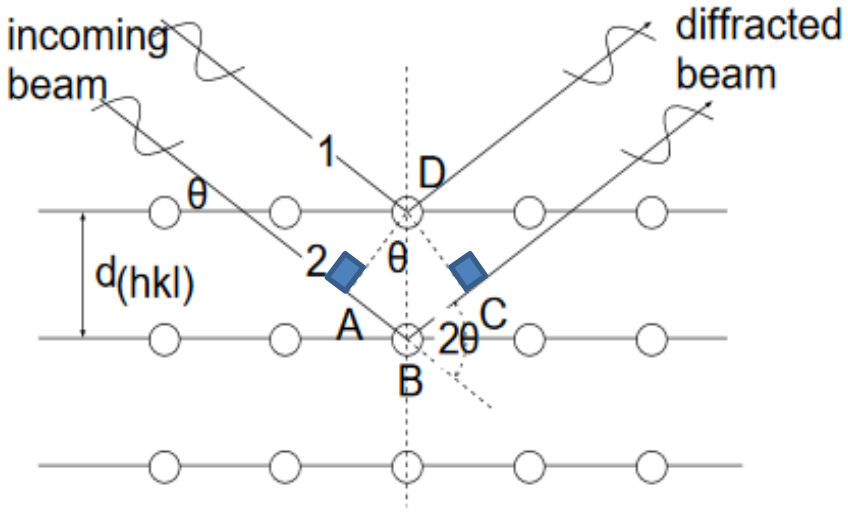

Figure 2-4 Bragg's law treating the planes of atoms as reflecting planes.

If we consider the figure 2-4, as representative for a "diffractometer" set-up, we have a collimated beam of X-rays impinging on a set of planes and at 2θ to the incident beam a detector which registers the intensity of radiation. For a glancing incident beam (small θ) the detector will register only background radiation. As θ increases to a value for which 2d sin θ = λ, the detector will register high intensity radiation producing a diffraction peak.[142] Hence, the XRD method is suitable to determine the crystal structures by analysing the positions and intensities of diffraction peaks typically observed for the well-crystallised material in the range of diffraction angle from 10° to 150°.[143] The method is also used for evaluating the microstructures by analysing the width and the shape of the peak profiles. Since the crystal structures of pure materials are precisely periodic in their atomic arrangements, the pattern of the intensities and the position of XRD peaks can be uniquely used for the material assignment. Therefore, PXRD measurement is critical to characterise the main crystalline phases of materials. Crystals offer a much stronger signal due to their periodicity.[135,143]

In this work, the PXRD patterns of the samples were collected using a Bruker D2 Phaser X- ray diffractometer with CuK_α radiation (λ = 1.5418 Å). The collection data was selected in the range of 2θ = 10–80º at room temperature with a counting time of 0.10 s per step. The PDXL software package and PDF database was used for pattern matching.

2.7.2 Rietveld method

The Rietveld method was developed by H. M. Rietveld to refine the crystal structure from the powder diffraction as well as for the estimation of crystallite size.[144] Rietveld realised that total intensity and peak shape of clusters of reflections can be determined by using

simple peak shape parameters. This circumvented the issue of the Bragg reflections being unable to be modelled as single entities due to them overlapping.[144,130]

It involves a set of programs for the processing and analysis of both single crystal and powder diffraction data obtained with X-rays or neutrons. The unit cell and structural parameters (atomic coordinates, site occupancy, zero point, and atomic displacement parameters) are determined by a least square process so that the intensity data calculated reproduce the measured intensity data. [145]

For many compounds it is impracticable to grow single crystals of adequate quality for a good structure determination even though good powder diffraction patterns can be attained with little difficulty. It would be desirable to refine a structure model to "fit" the powder pattern parallel to the way structure factors are refined against isolated hkl data. Moreover, in a powder pattern of a many-atom, low-symmetry, unit cell there will be enormous overlap of the reflection peaks in the "1D" powder pattern (i.e. a map of 2θ vs. intensity). This lack of spatial resolution makes it much more challenging to index the reflection peaks in the first place. It also increases the challenge for measuring accurate intensities for the peaks, due to the high degree of over lapping.[146] The Rietveld method is an elegant solution to this problem because the refinement is made against the entire peak profile. The contribution of all peaks to each data point is considered in turn. It is important to collect the entire powder profile carefully,[130,144] the method relies on the simple relationship,

$$W_P = S_p\,(ZMV)_P \,/\, \sum_{i-I}^{n} S_i (ZMV)_i \qquad \text{Equation 2-7}$$

Where W = relative weight fraction of phase p, n = number of phases, S = Rietveld scale factor, Z = number of formula units per cell, M= mass of the formula unit (in atomic mass units), V = unit cell volume (in Å³).

The refined model is a least squares best fit process which aims to minimise the residual S_y:

$$\mathrm{S_y} = \sum_{\mathrm{i}} w_{\mathrm{i}} \left(\mathrm{y_{i(obs)}} - \mathrm{y_{i(calc)}}\right)^2 \qquad \text{Equation 2-8}$$

Where the sum i is the step number, w_i is the statistical weight equal to $1/\mathrm{y_{i(obs)}}$, $\mathrm{y_{i(obs)}}$ and $\mathrm{y_{i(calc)}}$ are the actual observed and the calculated intensity from the model, respectively.[147] The calculated intensity, $\mathrm{y_{i(calc)}}$, is obtained from the equation:

$$y_{i(calc)} = s \sum_{hkl} \mathrm{L_{hkl}} |F_{hkl}|^2 \emptyset(2\theta_i - 2\theta_{hkl}) P_{hkl} A + y_{bi} \qquad \text{Equation 2-9}$$

Where s = scale factor, hkl = Miller indices L_{hkl} contains the Lorentz, polarisation and multiplicity factors, $\emptyset$ = reflection profile function, P_{hkl} = preferred orientation function, A = absorption factor, $F_{(hkl)}$= structure factor for the Bragg reflection corresponding to hkl and y_{bi} = background intensity at each step.[148]

The scattering factor, f_j, quantifies the efficiency of scattering from a group of electrons in an atom. Integrated peak intensities include the information on site occupancy N_j of jth atom, atomic displacement parameters and atomic positional x_j, y_j and z_j. The integrated intensity is proportional to the square of the absolute value of the structure factor F_{hkl} corresponding to a set of (hkl) planes. The structure factor is expressed as:

$$F_{hkl} = \sum_j N_j f_j \, exp\left[2\pi i\left(hx_j + ky_j + Iz_j\right)\right] exp\left[-M_j\right] \qquad \text{Equation 2-10}$$

The quantitative assessment of the agreement between the observed and calculated profile requires several indicators, including:

$$R_p = \frac{\sum |y_i(\mathrm{obs}) - y_i(\mathrm{calc})|}{\sum y_i\,(\mathrm{obs})} \qquad \text{Equation 2-11}$$

Where R_p= *R*-profile

$$R_{wp} = \left\{\frac{\sum_i^n w_i \;\left[y_i\,(\mathrm{obs}) - y_i(\mathrm{calc})\right]^2}{\sum_i w_i\,[y_i(\mathrm{obs})^2]}\right\}^{1/2} \qquad \text{Equation 2-12}$$

Where R_{wp}= *R-weighted profile*;

$$R_{exp} = \left[\frac{(N-P)}{\sum_i^n W_i \;\; y_i\;(\mathrm{obs})^2}\right]^{1/2} \qquad \text{Equation 2-13}$$

Where

i. R_{exp}= *R*-expected,
ii. *N* = number of observations,
iii. *P* = number of refined parameters

Chi-squared $\chi 2$ is another parameter which is a goodness of fit indicators in the refinement, defined by:

$$\chi 2 = \frac{Rwp}{R\text{exp}} \qquad \text{Equation 2-14}$$

In the present work the Rietveld refinement was carried out using the General Structure Analysis System (GSAS).[144] It is a comprehensive system for the refinement of structural models to both X-ray and neutron diffraction data. It is been used for crystallographic analysis, quantitative phase determination, texture mapping and stress-strain measurements.

The best fit can be obtained using the method of least squares by minimising the difference between experimental diffraction pattern against the calculated one acquired from the ICSD database.[149] In the present work, Rietveld refinement was carried out using the General Structure Analysis System (GSAS).[144,150]

Crystallite size can be evaluated by a Rietveld refinement method related to the peak shape in a diffraction pattern based upon the Scherrer equation. This equation can be obtained by rearrangement of the complex expressions that applied to model the peak shape (mostly instrumental broadening), in which the Lorentzian component mainly consists of mostly sample broadening.[151, 130]

$$P = \frac{18000K\lambda}{\pi X} \qquad \text{Equation 2-15}$$

Where

i. P is crystallite size
ii. K is the Scherrer constant (0.9)
iii. λ is the X-ray wavelength (0.1542 nm)
iv. X is the L_x Lorentzian profile coefficient extracted from the GSAS software

2.8 Catalyst preparations

A number of catalysts were prepared, characterised and tested in this study. They are predominantly molybdenum and tungsten containing nanostructured catalysts. The catalysts of interest in these studies were quaternary nitride materials derived from Pechini sol-gel synthesis, followed by ammonolysis reaction.

The ammonolysis reactor was used to prepare nitride materials by the reaction of the oxide precursors with dry ammonia NH_3. This process was undertaken by subjecting 1.6 g of precursor within an alumina boat placed inside the horizontal quartz tube reactor to treatment with ammonia NH_3 (BOC, 99.98 %). Due to the safety issues the reactor was situated in a ventilated fume cupboard as shown in Figure 2-5. The ammonia gas was allowed to pass through a column of molecular sieves to dry the ammonia before encountering the sample. The Elite furnace used was first flushed with dry NH_3 for at least 20 min before heating to remove any oxygen and moisture. Under a dry NH_3 the sample was heated to the target temperature at a heating rate of 5 °C min^{-1}, held for 12 h. The material was then cooled in flowing NH_3 to room temperature. To prevent runaway oxidation on exposure to air, the resulting material was flushed with nitrogen for 30 minutes then air was allowed to diffuse in. A schematic representation of the heat treatment is illustrated in Figure 2-6.

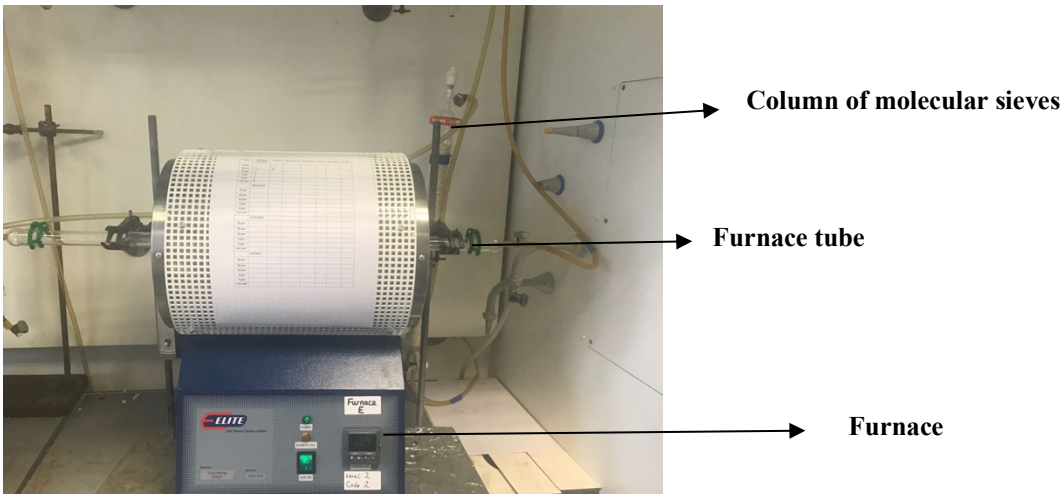

Figure 2-5 Apparatus used to synthesise nitrides by ammonolysis of metal oxide precursors.

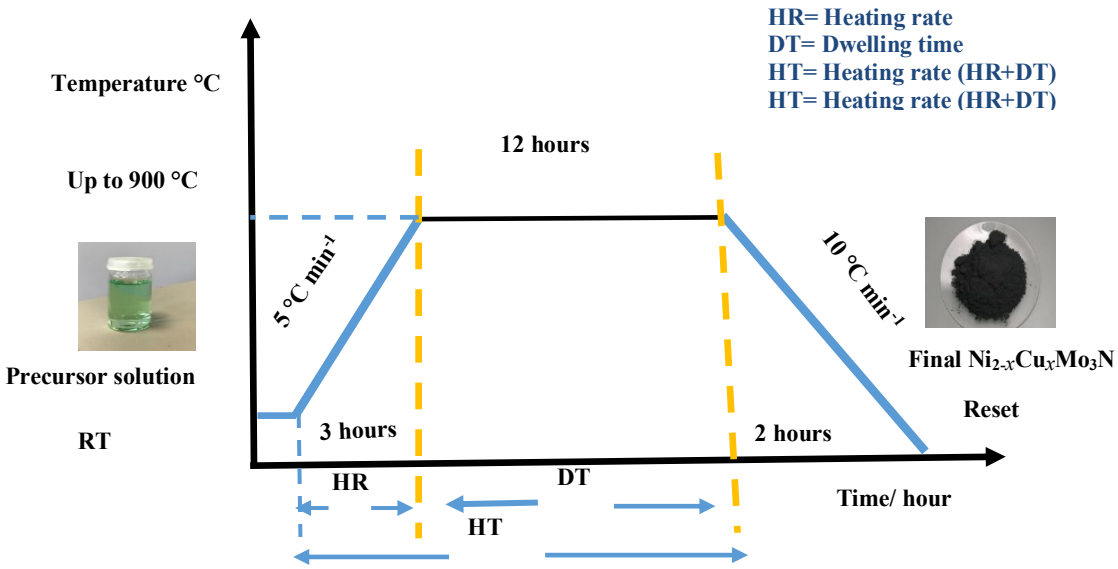

Figure 2-6 Schematic representation of the heat treatment using the preparation of $Ni_{2-x}Cu_xMo_3N$ as an example.

2.9 Catalyst testing

The catalytic performance measurements were carried out at the University of Southampton; Chemistry Department, on a tubular fixed bed reactor.

The catalytic performance of the obtained catalysts in ammonia synthesis was evaluated by a method similar to that described previously.[152] The catalyst (0.15 g) was loaded in the centre of a 4.2 mm internal diameter silica tube and held in a plug against a sinter using silica wool, then placed in a tube furnace. 13 mL min^{-1} 75% hydrogen, 25% nitrogen gas mixture (BOC, H_2 99.998 %, N_2 99.995 %) was passed through the tube and it was heated to 700 °C for 2 h to activate the catalyst followed by lower temperature steps to test ammonia production. On reaching the reaction temperature, the vent gas from the reactor was bubbled through a dilute solution of sulfuric acid (0.001 mol dm^{-3}, 100 ml) at ambient temperature and the rate of ammonia production was calculated from the conductivity decrease of the sulfuric acid solution with time (Orion Star A212 Portable Conductivity Meter).[152] A linear decrease in conductivity versus time was observed during the measurement using H_2/N_2 as the reactant gas. Figure 2-7 shows the apparatus used to conduct the ammonia synthesis experiments

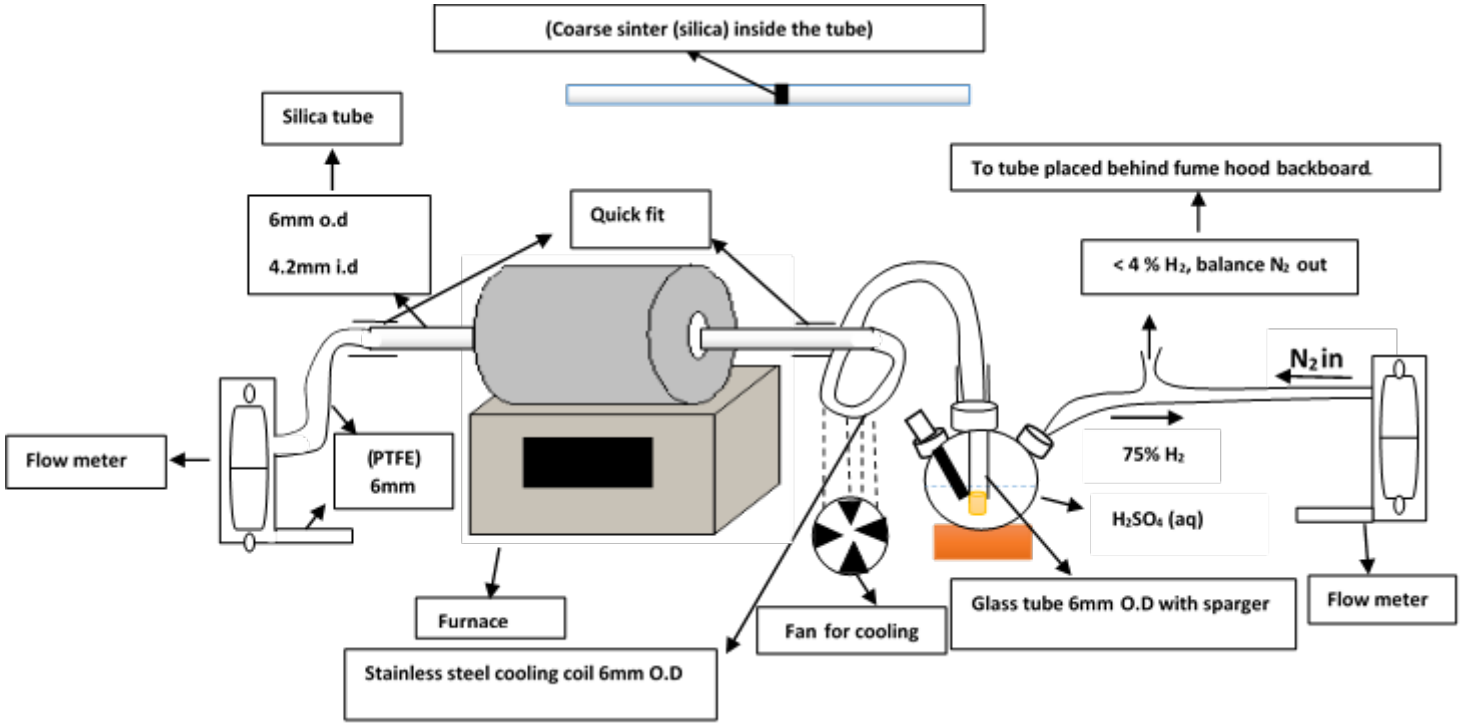

Figure 2-7 Catalytic testing reactor set-up.

2.10 Ammonia calculation

The ammonia produced during catalysis was bubbled through a dilute H_2SO_4 solution, whose conductivity is known to vary linearly with the acid concentration.

Moles of H_2SO_4 = Concentration (H_2SO_4) x Volume (H_2SO_4) = 0.001 mol L^{-1} × 0.1 L = 1 x 10^{-4} moles

0.0002 moles of ammonia are required to entirely react with H_2SO_4.

Change in conductivity for the reaction:

$H_2SO_4 + 2NH_3 \rightarrow (NH_4)_2SO_4$

= 802.2 μScm^{-1} – 332 μScm^{-1} = 470 μScm^{-1}

The calibration value = Number of moles of ammonia required/ Total change in conductivity

= 2 x 10^{-4} moles/ 470 μScm^{-1}

2.11 Calculation of the Scherrer crystallite size

The crystallite size was estimated using equation 2-15 in section 2.7.2. The example below shows how to calculate crystallite size

Associated L x error was calculated from the Rietveld refinement performed on this sample:

Lx = 6 (±0.2)

The Lx value was then used to estimate the crystallite size:

$$C = (18000 \times 0.9 \times 0.15405)/(3.14 \times 6) = 133\ nm$$

The standard error value was then calculated using the following points:

1: The upper C value was calculated as below:

$$C\ (upper) = (18000 \times 0.9 \times 0.15405)/(3.14 \times (6 - 0.2)\ ) = 137\ nm$$

2: The lower C value was then evaluated:

$$C\ (\ Lower) = \ (18000 \times 0.9 \times 0.15405)/(3.14 \times (6 + 0.2)) = 109\ nm$$

3: The difference between the upper C value and C was then calculated to give error max:

$$Error\ max = 137\ nm - 133\ nm = 4\ nm$$

4: The difference between C and the lower C value gave error min:

$$Error\ min = 133\ nm - 109\ nm = 24\ nm$$

therefore, the crystallite size will be 133 (24) nm

Chapter 3 Citrate-gel Preparation and Ammonia Synthesis Activity of Compounds in the Quaternary $(Ni,Cu)_2Mo_3N$ System

3.1 Overview

The synthesis of the nanostructured $(Ni,Cu)_2Mo_3N$ using a modified Pechini method is described in this chapter. These materials were evaluated for applications as catalysts for ammonia synthesis; their activities were linked to the surface area which in turn could be related to the temperature applied during the synthesis step.

3.2 Introduction

Copper has been studied as replacement for noble metals due to its attractive properties and relatively low cost. The ionic nitride Cu_3N, which can be formed by the combination of Cu ion with N^{3-} was reported to have a similar electronic structure with ionic metals. It has the anti-ReO_3 cubic structure type.[153,154] The Cu atoms occupy the middle of the cube edges instead of occupying the face centred cubic close packing sites (Figure 3-1). As a result, this arrangement leaves a large number of vacant interstitial sites that can be occupied by other metals.[154] The occupation of these sites could result in the tailoring of the optical and electrical properties of Cu_3N.

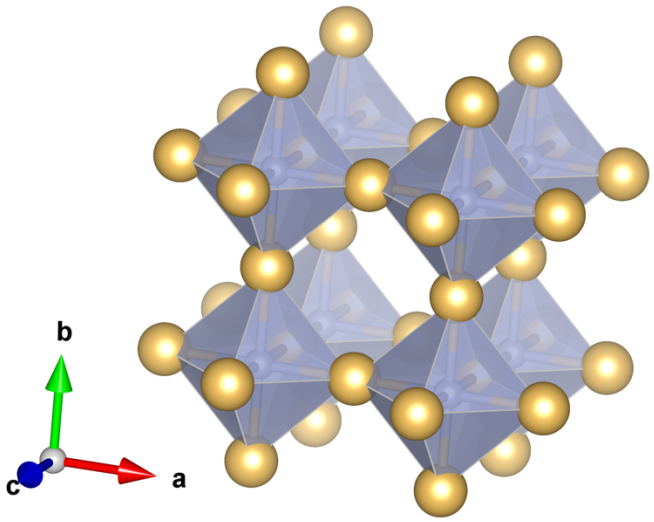

Figure 3-1 Unit cell of the cubic crystal structure of Cu_3N (anti-ReO_3 type) showing the regular corner-sharing NCu_6 octahedra. Cu atoms are shaded yellow and N_2 silver. Diagram drawn using Vesta and structure data from Paniconi *et al.*[155]

Historically, Cu_3N polycrystalline powder was successfully prepared by Hahn and Juza *via* the ammonloysis of CuF_2 at 280 °C.[156] Since this material has attractive properties, various synthesis methods have been employed to produce it such as ammonolysis,[155] thermal decomposition[157]and solvothermal method.[158] Attempts have been also made to produce Cu_3N by using CuO as a precursor. It has been demonstrated that with increasing temperature to 350 °C this material can be easily decomposed to Cu metal.[159] Furthermore, this material has been evaluated for ammonia synthesis at relatively low temperature as low as 300 °C under 3:1 H_2/N_2 atmosphere. It was observed that the material had high activity, but this dropped quickly after 30 minutes on stream.[160] Although binary copper based nitrides have been studied for ammonia synthesis, more complex ternary and quaternary copper nitride materials have not been reported.

Despite the substantial efforts that have been made on binary and ternary nitride catalysts, the catalytic behaviour of quaternary nitrides materials still in its first stages.[40]

The quaternary nickel cobalt molybdenum nitride ($NiCoMo_3N$) has been successfully prepared. Cobalt substitutes readily onto the Ni sites and the $(Ni,Co)_2Mo_3N$ system exhibited Vegard law behaviour (a linear variation in lattice parameter with composition) up to 50% cobalt and its activity was investigated for ammonia synthesis.[40, 42] It has been found that the substitution of 50 % of the Ni in the phase by Co has little effect upon lattice N reactivity. Lattice nitrogen reactivity does not seem to be able to be switched on by composition change, which is also in line with a recent study comparing Co_3Mo_3N with Co_2Mo_3N.[161] They concluded that the structure type is more important than electronic aspects. This may be linked to the stability of Co_6Mo_6N, which is formed on denitridation of Co_3Mo_3N with transfer of nitrogen to an alternative crystallographic site.

Further optimisation of these molybdenum nitrides may improve their activity. Cobalt substitution did not improve the catalytic performance of Ni_2Mo_3N so the hypothesis was that copper might have the opposite effect. Herein, copper substitution has been introduced into Ni_2Mo_3N lattice structure with the aim of improving its catalytic activity for ammonia synthesis.

3.3 Experimental

3.3.1 Synthesis

All chemicals were used as received without further purification or modification. Nanocrystalline samples of $Ni_{2-x}Cu_xMo_3N$ were prepared by a citrate gel route followed by ammonolysis. Stoichiometric amounts of $(NH_4)_6Mo_7O_{24}\cdot 4H_2O$ (2 g, Sigma Aldrich,

99.9 %), $Ni(NO_3)_2 \cdot 6H_2O$ (Sigma Aldrich, 99.9 %) and $Cu(NO_3)_2 \cdot 4H_2O$ (Sigma Aldrich, 99%) were dissolved in 60 cm^3 aqueous HNO_3 (2.6 mol dm^{-3}, prepared from Fisher Scientific 70% HNO_3, used for ammonium molybdate solubility). Citric acid monohydrate (7.935 g, Sigma Aldrich, ACS reagent, ≥99%) was then added to the green solution. Actual quantities are given in Table 3-1. The green solution was evaporated in a sand bath at 70 °C to ~10 cm^3 of viscous green gel Figure 3-2, then heated in an ashing furnace (60 °C min^{-1} heating rate) at 500 °C for 2 h. The resulting grey foam was ground to a powder then heated in flowing ammonia (BOC anhydrous grade, further dried with molecular sieves) at 5 °C min^{-1} at 900 °C and maintained for 12 h. Once cool, the furnace tube was flushed with N_2 for 30 mins then air was allowed to diffuse in slowly to passivate sample surfaces before the black crystalline product was recovered. Samples were then handled under aerobic conditions during characterisation. *Caution: a sand bath was used because citrate gels can occasionally ignite; the unpassivated metal nitrides are highly pyrophoric.*

Table 3-1 Quantities of reagents used in the synthesis of nickel copper molybdenum nitride $(Ni,Cu)_2Mo_3N$

***x* in $Ni_{2-x}Cu_xMo_3N$**	**$Ni(NO_3)_2 \cdot 6H_2O$**	**$Cu(NO_3)_2 \cdot 3H_2O$**	**$(NH_4)_6Mo_7O_{24} \cdot 4H_2O$**	**Citric acid monohydrate**
0.1	2.09 g / 7.19 mmol	0.09 g / 0.37 mmol	2 g / 1.62 mmol	7.94 g / 37.8 mmol
0.2	1.97 g / 6.77 mmol	0.18 g / 0.75 mmol		
0.3	1.86 g / 6.40 mmol	0.27 g / 1.12 mmol		
0.4	1.76 g / 6.05 mmol	0.36 g / 1.49 mmol		
0.5	1.65 g / 5.67 mmol	0.46 g / 1.90 mmol		
0.6	1.54 g / 5.30 mmol	0.55 g / 2.28 mmol		
0.7	1.43 g / 4.92 mmol	0.64 g / 2.65 mmol		
0.75	1.37 g / 4.71 mmol	0.68 g / 2.81 mmol		
0.9	1.21 g / 4.16 mmol	0.82 g / 3.39 mmol		
1.0	1.10 g / 3.78 mmol	0.91 g / 3.77 mmol		

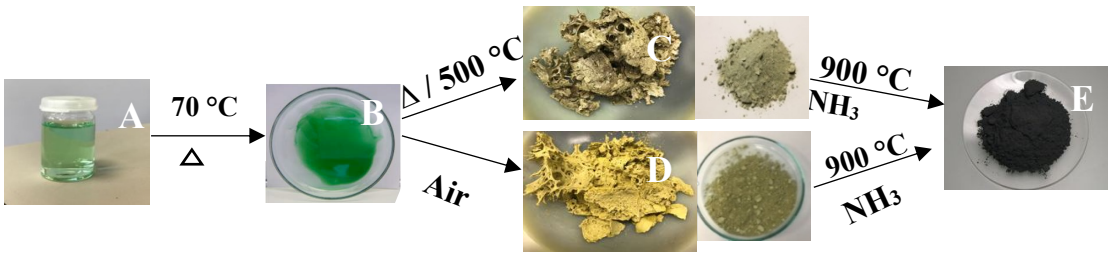

Figure 3-2 Schematic description of the citrate- gel process to produce the filled β- manganese type phases, with Ni_2Mo_3N and the $(Ni,Cu)_2Mo_3N$ compounds. From left to right: starting solution (green) (A), gel (green) (B) after evaporating, greyish (C) and yellowish (D) foams after heat treatment at 500 °C for 2 h in air and final fine powder (E) after heating at 900 °C in flowing NH_3.

3.3.2 Characterisation

The phase, purity and the degree of crystallinity of the synthesised materials were evaluated *via* the powder XRD technique. The powder X-ray diffraction (PXRD) patterns of the samples were collected in the range 10-80° 2θ using a Bruker D2 Phaser X-ray diffractometer with Cu-K_α radiation. The Rigaku PDXL2 package and the PDF database[162] were used for pattern matching. Rietveld refinement was carried out using GSAS[150,163] and structure models from ICSD.[164] Scanning electron microscopy (SEM) was conducted using a Philips XL-30 ESEM (20 kV accelerating voltage) with a ThermoFisher Ultradry energy dispersive spectroscopy (EDS) detector and Noran System 7 data processing. Transmission electron microscopy (TEM) was performed on a Hitachi H7000 with accelerating voltage of 75 kV with samples prepared by ultrasound dispersal in propan-2-ol and deposition on carbon-coated copper grids. Thermogravimetric analysis (TGA) used a NETSCH TG 209 F1 Libra instrument with a heating rate of 10 °C min^{-1} under 40 mL min^{-1} of 50% oxygen and 50% argon. The surface areas of the samples were calculated by applying the Brunauer, Emmett and Teller[165] (BET) method to nitrogen physisorption isotherms measured at 77 K using a Micromeritics Tristar II and samples previously degassed overnight at 120 °C. Combustion (CHN) analysis was outsourced to MEDAC Ltd.

3.3.3 Catalytic evaluation

The catalytic performance of the obtained catalysts in ammonia synthesis was evaluated by a method similar to that described previously.[40] The catalyst (0.15 g) was loaded in the centre of a 4.2 mm internal diameter silica tube and held against the sinter, which was placed in a tube furnace. 13 mL min^{-1} 75% hydrogen/ 25% nitrogen gas mixture (BOC, H_2 99.998 %, N_2 99.995 %) was passed through the tube and it was heated to 700 °C for 2 h to activate the catalyst followed by lower temperature steps to test ammonia production. On reaching the reaction temperature, the vent gas from the reactor was bubbled through a dilute solution of sulfuric acid (0.001 mol dm^{-3}, 100 ml) at ambient temperature and the rate of ammonia production was calculated from the conductivity decrease of the sulfuric acid solution with time (Orion Star A212 Portable Conductivity Meter).[40] A linear decrease in conductivity *versus* time was observed during the measurement using H_2/N_2 as the reactant gas.

3.4 Results and discussion

According to the literature, there are no known copper doped Ni_2Mo_3N systems. However, the parent compound Ni_2Mo_3N is a known phase, which only exists in the Ni: Mo = 2:3

composition.[63, 57, 166, 58, 97, 83, 40, 42, 167] Within the literature, the bimetallic Ni-Mo-N initially was reported to be pure Ni_3Mo_3N.[63, 168] Later, studies showed that impure phases were observed in which Ni_2Mo_3N was the predominant phase,[166] using precursors under high temperature ammonolysis reaction. The interstitial quaternary molybdenum nitride with nominal composition $Ni_{2-x}Cu_xMo_3N$ (x = 0; 0.1; 0.2; 0.3; 0.4; 0.5; 0.6; 0.7; and 0.75) was prepared using the modified Pechini route by the thermal ammonolysis of the metal oxide precursors. The advantage of citrate gel synthesis to produce solid solutions in the $(Ni,Cu)_2Mo_3N$ system is that the nickel and copper are mixed in solution, so could be well distributed in the products. A range of compositions was made starting with Ni_2Mo_3N and replacing nickel with copper. Previously in the $(Ni,Co)_2Mo_3N$ system we fired samples at 700 °C and found that, in addition to the filled β-manganese type phases, they contained a trace of a rocksalt-type impurity that resembled γ-Mo_2N.[40] The filled β-manganese structure has been discussed in more detail in section 1.4.1. In order to find the best temperature for obtaining single phase materials, the metal oxide precursors were subjected to different ammonolysis reaction temperatures. Firing Ni_2Mo_3N samples at temperatures between 600 and 1000 °C, the samples produced below 800 °C were found to contain the rocksalt-type phase γ-Mo_2N (Figure 3-3), but at 900 or 1000 °C the phase pure filled β-manganese material was produced. Hence, the $(Ni, Cu)_2Mo_3N$ used herein were produced at 900 °C.

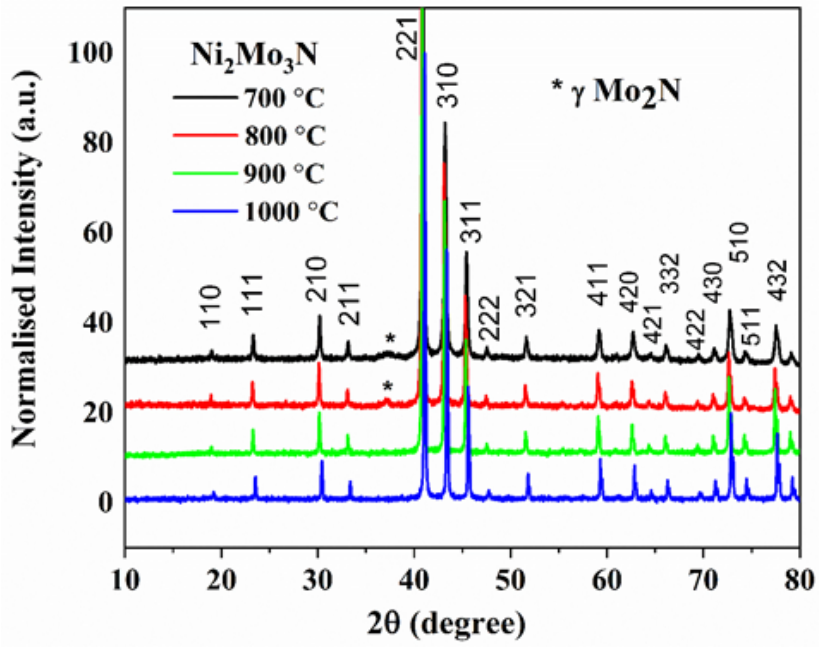

Figure 3-3 Powder XRD patterns for Ni_2Mo_3N powder prepared by firing the oxide precursors at 700 °C, 800 °C, 900 °C and 1000 °C under NH_3 gas. The peaks marked with asterisks (*) denote the γ-Mo_2N rock- salt as a secondary phase.

In order to further confirm the structural models, Rietveld refinements were performed against the experimental powder X-ray diffraction data using the General Structure Analysis System (GSAS) based on the filled β-manganese type structure and in cubic space group $P4_132$ as published by Prior and Battle.[58] The structural parameters, including the atom coordinates, lattice parameters, zero-point, background, thermal displacement parameters and the coefficient components L_x = Lorentzian isotropic crystallite size and L_y = Lorentzian isotropic strain broadening.

The refinement was carried out by first fitting the atomic positions, followed by the peak shapes (lattice parameters and zero point). Once those parameters were fitted, the background with function type 2 and 3 terms within GSAS was refined. Subsequently, the coefficient components L_x and L_y were refined successively until convergence. The isotropic thermal parameters, U_{iso}, were constrained to be equal for the nickel and copper. The 8c site was occupied with the nickel. The molybdenum atoms were placed on the 12d site with the interstitial nitrogen atoms on 4a site forming Mo_6N octahedra. The refined lattice parameters were 6.630(1), 6.632(2), 6.6364(1) and 6.639(2)Å at 700, 800, 900, and 1000 °C, respectively. (Figure 3-4).

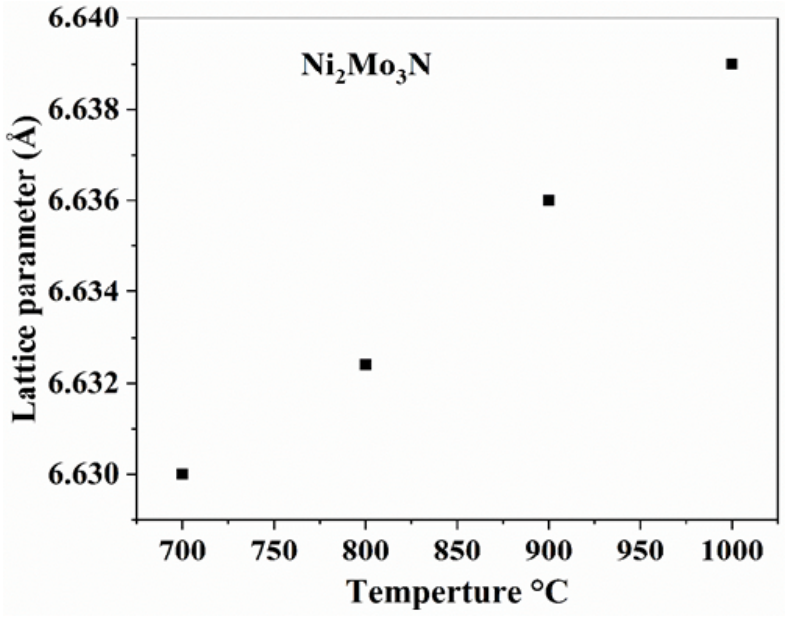

Figure 3-4 Firing temperature dependence of the lattice parameter for Ni_2Mo_3N

Figure 3-5 shows PXRD patterns for a series of $(Ni,Cu)_2Mo_3N$ compositions produced at 900 °C. Compositions from Ni_2Mo_3N to $Ni_{1.7}Cu_{0.3}Mo_3N$ were identified as the single phase filled β-manganese structure (space group $P4_132$). However, as the copper content was increased further, small reflections appeared in the patterns and grew in intensity. The

impurity of γ-Mo_2N (JCPDS Card No. 25-1366) at approximately 37.4° 2θ was clearly indicated along with copper metal (JCPDS Card No.01-0714608) with peaks at 2θ = 43.4 and 50.6°.

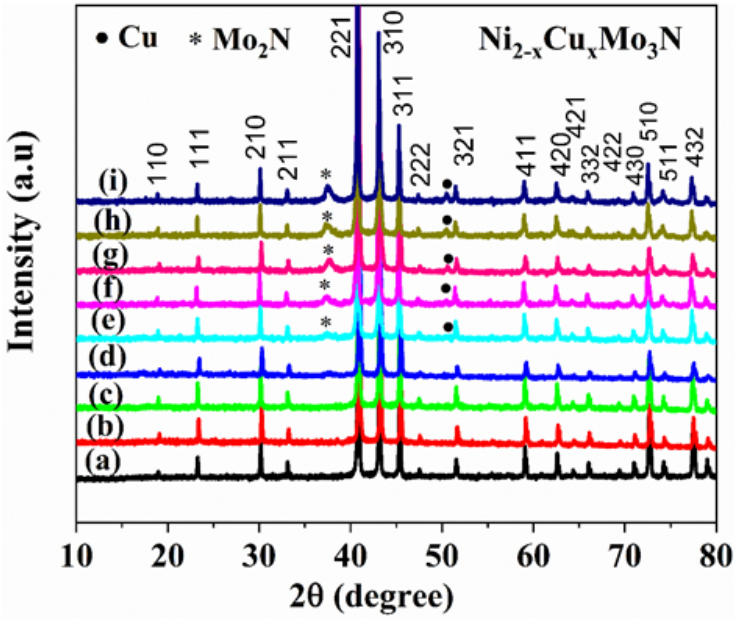

Figure 3-5 Powder XRD patterns for $Ni_{2-x}Cu_xMo_3N$ (overall composition x = 0 to 0.75) synthesized by firing the dry powder at 900 °C for 12 h under NH_3 gas, where x = 0.0 (a), 0.1 (b), 0.2 (c), 0.3 (d), 0.4 (e), 0.5 (f), 0.6 (g), 0.7 (h) or 0.75 (i). Asterisks indicate the Mo_2N reflections and black circles show reflections of Cu metals.

Powder X-ray diffraction patterns of the Cu-doped Ni_2Mo_3N samples were successfully refined using the data obtained from the inorganic crystal structure database (ICSD).[169] The Rietveld fit for $(Ni,Cu)_2Mo_3N$ compositions are shown in Figure 3-5, and the key refinement parameters data are summarised in Table 3-2. The isotropic thermal parameters, U_{iso}, were constrained to be equal for the nickel and copper at 8c site. The molybdenum atom position was refined (12d) with coordinates (1/8, y, z). The nitrogen atom on 4a is a special site and was not refined. It can be seen that the refinement results of all compositions Figure 3-6 are isostructural with the parent cubic Ni_2Mo_3N phase.

Table 3-2 Refinement details and structure information for $Ni_{2-x}Cu_xMo_3N$ series

Composition	a/Å	Ni/ Cu x (8c x, x, x)	Ni/ Cu U_{iso} / Å^2	Mo 12 d (1/8, y, z)			N 4a 3/8, 3/8, 3/8
				y	Z	U_{iso}/ Å^2	U_{iso} / Å^2
Ni_2Mo_3N	6.6364(1)	0.0663(2)	0.0262(8)	0.20176(1)	0.45176(1)	0.02668(5)	0.2500
$Ni_{1.9}Cu_{0.1}Mo_3N$	6.6399(6)	0.06644(1)	0.03452(1)	0.2018(1)	0.4518(1)	0.03345(4)	
$Ni_{1.8}Cu_{0.2}Mo_3N$	6.643(1)	0.06692(4)	0.04099(2)	0.20195(2)	0.45195(2)	0.0425(3)	
$Ni_{1.7}Cu_{0.3}Mo_3N$	6.645(3)	0.0672(4)	0.04385 (2)	0.20222(2)	0.45222(2)	0.04376 (1)	

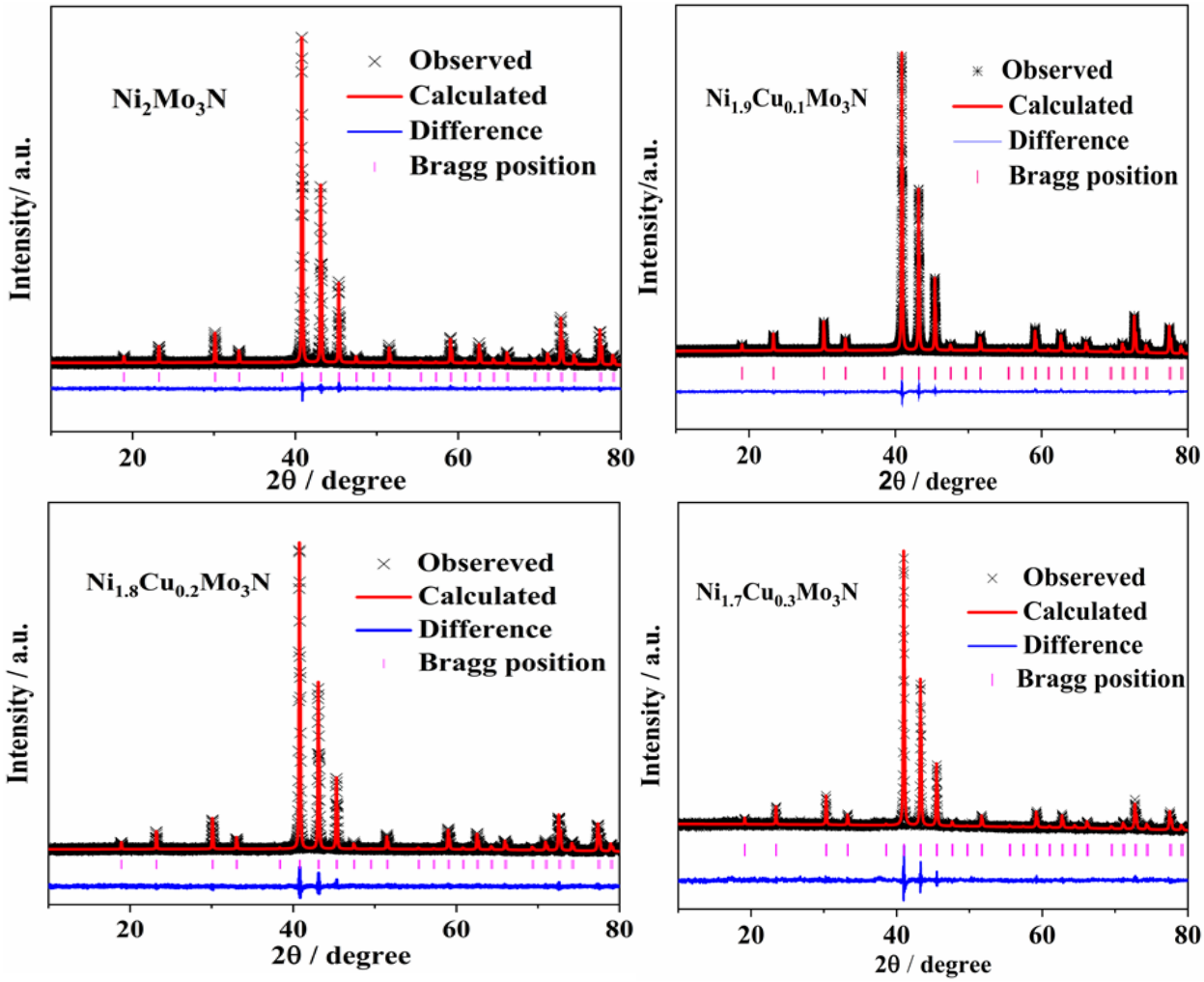

Figure 3-6 Rietveld fits to the PXRD patterns of Ni_2Mo_3N (R_{wp}% = 8.23 and R_p% = 6.45, a = 6.634(1) Å, crystallite size = 113(2) nm, $Ni_{1.9}Cu_{0.1}Mo_3N$ (R_{wp}% = 7.6 and R_p% = 6.2, a= 6.6399(6) Å, crystallite size= 119(3) nm, $Ni_{1.8}Cu_{0.2}Mo_3N$ (R% = 4.9 and R_p% = 3.9, a = 6.643(1) Å, crystallite size = 126(5) nm and $Ni_{1.7}Cu_{0.3}Mo_3N$ (R_{wp}% = 9.5 and R_p% = 7.6, a = 6.645(3) Å, crystallite size = 142(11) nm. Black crosses mark the data points, the red continuous line the fit and the blue continuous line the difference. Pink tick marks show the position of the allowed reflections for the filled β-manganese structure in $P4_132$.

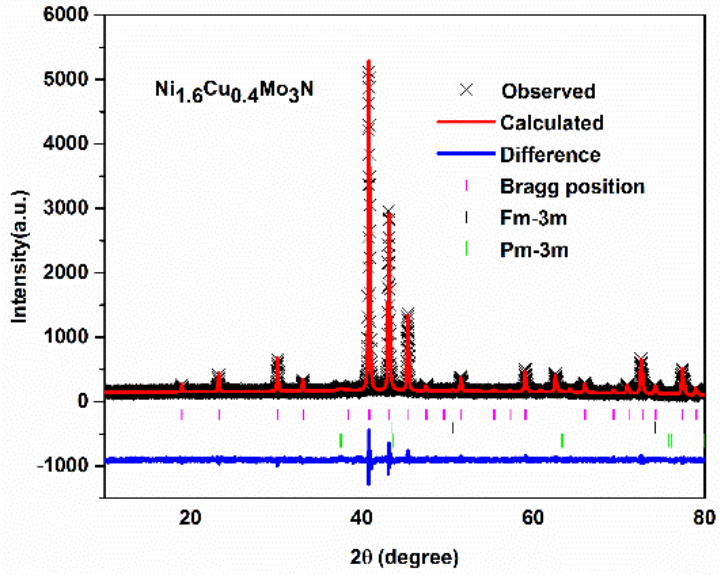

Figure 3-7 Rietveld fit to the PXRD data of $Ni_{1.6}Cu_{0.4}Mo_3N$. Black crosses mark the data points, the red continuous line the fit and the blue continuous line the difference. Pink tick marks show the positions of the allowed reflections for the filled β-manganese structure in $P4_132$. (R_p = 6.12 %, R_{wp} = 7.77 %, weight fraction = 96(2) %, a = 6.6447(2) Å, crystallite size = 147(5) nm. Black crosses mark the data positions for Cu metal ($Fm\bar{3}m$, weight fraction = 1.3 %, a = 3.6(1)Å, (green) tick marks represent allowed reflection positions for γ-Mo_2N (space group: $Pm\bar{3}m$, weight fraction = 2.6 %, a = 4.17(3) Å).

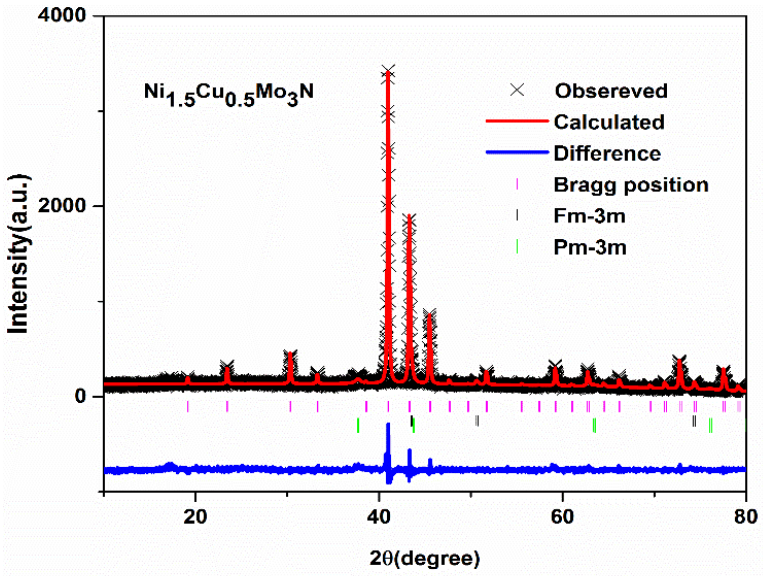

Figure 3-8 Rietveld fit to the PXRD data of $Ni_{1.5}Cu_{0.5}Mo_3N$. Black crosses mark the data points, the red continuous line the fit and the blue continuous line the difference. Pink tick marks show the positions of the allowed reflections for the filled β-manganese structure in $P4_132$. (R_p = 7.95 %, R_{wp} = 10.28 %, weight fraction = 94.3(3) %, a = 6.6445(8) Å, crystallite size = 139(5) nm. Black tick marks represent allowed reflection positions for Cu metal ($Fm\bar{3}m$, weight fraction= 2.5 %, a = 3.62(1)

Å). Green tick marks represent allowed reflection positions for γ-Mo_2N ($Pm\bar{3}m$, weight fraction = 3.2%, a = 4.17(2) Å).

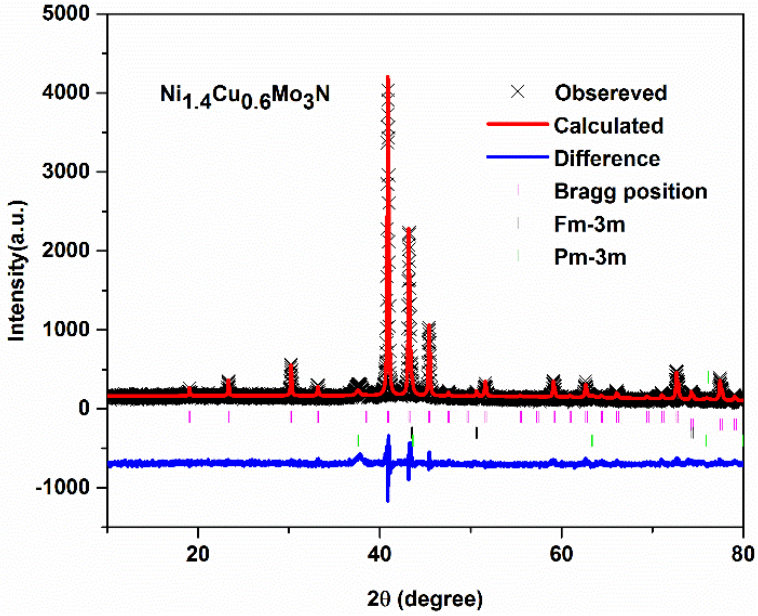

Figure 3-9 Rietveld fit to the XRD data of $Ni_{1.4}Cu_{0.6}Mo_3N$. Black crosses mark the data points, the red continuous line the fit and the blue continuous line the difference. Pink tick marks show the positions of the allowed reflections for the filled β-manganese structure in $P4_132$. (R_p = 13.25 %, R_{wp} = 10.2 %, weight fraction = 96(6) %, a = 6.6442(4), crystallite size = 116(2) nm. Black tick marks represent allowed reflection positions for Cu metal ($Fm\bar{3}m$, weight fraction = 1.8 %, a = 3.62(5) Å. Green tick marks represent allowed reflection positions for γ-Mo_2N ($Pm\bar{3}m$, weight fraction = 2.3%, a = 4.167(2) Å.

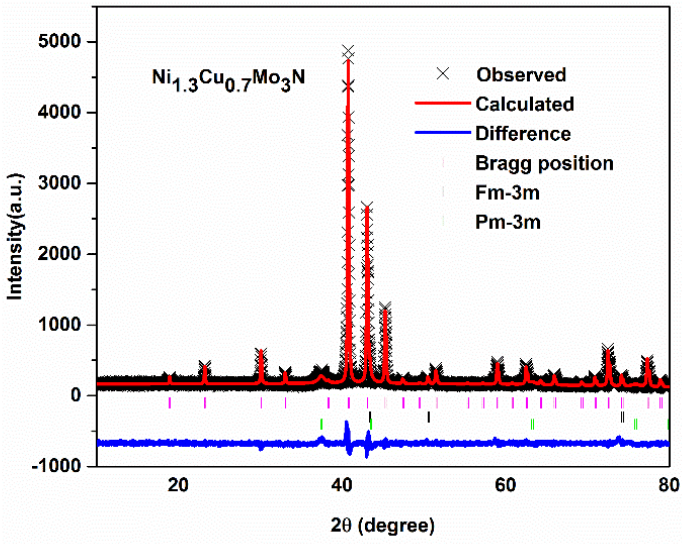

Figure 3-10 Rietveld fit to the PXRD data of $Ni_{1.3}Cu_{0.7}Mo_3N$. Black crosses mark the data points, the red continuous line the fit and the blue continuous line the difference. Pink tick marks show the positions of the allowed reflections for the filled β-manganese structure in $P4_132$ (R_p = 6.73 %, R_{wp} = 8.90 %, weight fraction = 89.2(8) %, a = 6.6441(2) Å, crystallite size = 120(13) nm. Black tick

marks represent allowed reflection positions for Cu metal ($Fm\bar{3}m$, weight fraction = 3.5 %, a = 3.62(3) Å. Green tick marks represent allowed reflection positions for γ-Mo_2N ($Pm\bar{3}m$, weight fraction = 7.3 %, a = 4.16(1) Å.

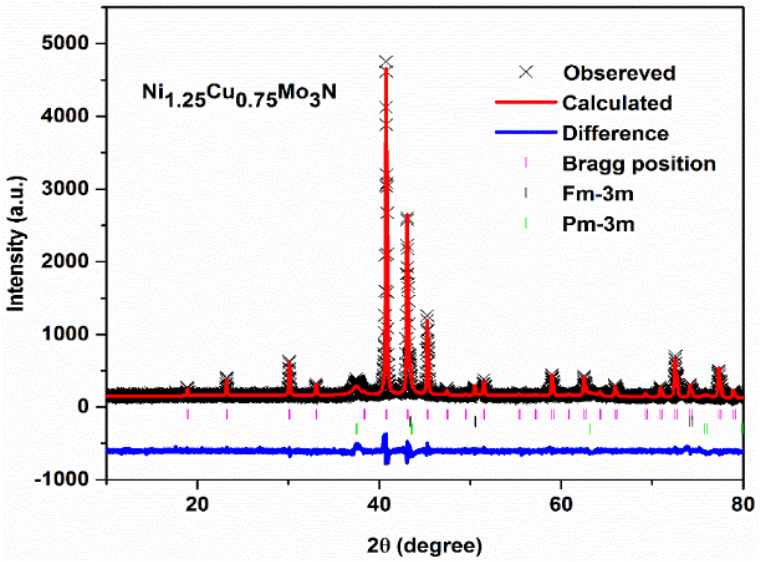

Figure 3-11 Rietveld fit to the XRD data of $Ni_{1.25}Cu_{0.75}Mo_3N$. Black crosses mark the data points, the red continuous line the fit and the blue continuous line the difference. Pink tick marks show the positions of the allowed reflections for the filled β-manganese structure in $P4_132$ (R_p = 6.88 %, R_{wp} = 9.03 %, weight fraction = 86(1) %, a = 6.644(2) Å, crystallite size = 120(15) nm. Black tick marks represent allowed reflection positions for Cu metal ($Fm\bar{3}m$), weight fraction= 4.4(2) %, a = 3.616(3) Å. Green tick marks represent allowed reflection positions for γ-Mo_2N ($Pm\bar{3}m$), weight fraction = 9.6(3) %, a = 4.16(1) Å.

Three phase Rietveld refinements were also performed for the impure phases $Ni_{1.6}Cu_{0.4}Mo_3N$, $Ni_{1.5}Cu_{0.5}Mo_3N$ $Ni_{1.4}Cu_{0.6}Mo_3N$, $Ni_{1.3}Cu_{0.7}Mo_3N$ and $Ni_{1.25}Cu_{0.75}Mo_3N$. The Rietveld fit and the refined data are shown in Figures (3-7) to (3-11). The models published by Prior and Battle,[58] Kawashima *et al.*[170] and Otte *et al.*[171] were used for the refinements of the single phase, the second phase γ-Mo_2N and the third phase Cu metal, respectively. The added second phase, corresponding to the impurity γ-Mo_2N crystallise in space group $Pm\bar{3}m$ with a = 4.16 (1) Å, whereas, the third phase is Cu metal which adopts the space group $Fm\bar{3}m$ with a = 3.6 Å. The all aforementioned parameters for the single phase along with two scale factors were refined in turn until the refinement become stable. The refined weight fractions of gamma molybdenum nitride (γ-Mo_2N) in each composition were 2.6, 3.2, 3.2, 7.3 and 6.9 wt% for $Ni_{1.6}Cu_{0.4}Mo_3N$, $Ni_{1.5}Cu_{0.5}Mo_3N$ $Ni_{1.4}Cu_{0.6}Mo_3N$, $Ni_{1.3}Cu_{0.7}Mo_3N$ and $Ni_{1.25}Cu_{0.75}Mo_3N$. Their respective weight percentages of copper metal (Cu) were determined to be 1.3, 2.5,1.8, 3.5 and 4.4 wt%. In addition, it is clear that the same

weight percentages of γ-Mo_2N were seen for $Ni_{1.5}Cu_{0.5}Mo_3N$ and $Ni_{1.4}Cu_{0.6}Mo_3N$. In addition, the weight fraction of Cu metal increased in an almost linear trend.

The lattice parameter variation obtained from Rietveld refinement of the diffraction data is shown in Figure 3-12. The lattice parameters show a Vegard trend in the single-phase compositions, suggesting a good distribution of copper in the solid solutions. The values increase with copper content as expected from the larger metallic radius of Cu (1.28 Å) compared with Ni (1.24 Å).[172] The lattice parameter of the filled β-manganese phase is then constant for overall compositions from $Ni_{1.7}Cu_{0.3}Mo_3N$ to $Ni_{1.25}Cu_{0.75}Mo_3N$. Hence no further copper had been introduced into the Ni_2Mo_3N structure and the limit of solubility of Cu in Ni_2Mo_3N is around the $Ni_{1.7}Cu_{0.3}Mo_3N$ composition. The refined lattice parameters of 6.6399(6) Å, 6.643(1) Å and 6.645(3) Å were obtained for the single phases $Ni_{1.9}Cu_{0.1}Mo_3N$, $Ni_{1.8}Cu_{0.2}Mo_3N$ and $Ni_{1.7}Cu_{0.3}Mo_3N$, respectively.

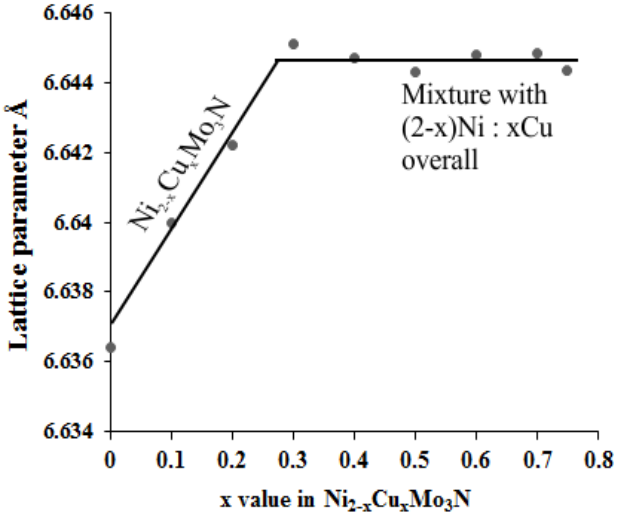

Figure 3-12 The lattice parameter of the filled β-manganese phase versus the concentration of Cu in $Ni_{2-x}Cu_xMo_3N$, with lines added as a guide to the eye.

3.5 Thermogravimetric analysis

The composition was also tested by TGA Figure 3-13, with the samples heated in an oxygen-rich gas mixture to convert them to oxides containing Ni (II), Cu (II) and Mo (VI) (mass gain) as shown in Equation 3-1. The mass was unchanged up to ~330 °C, above which the oxidation of the material was observed with a resulting mass increase. This occurred in three distinct steps, with an overall mass increase of 38.3 % observed by 550 °C for Ni_2Mo_3N compared to the calculated value of 38.6 %. No further mass increases were observed above 650 °C, but mass was lost sharply above 750 °C. This can be attributed to the sublimation of MoO_3.[96] The mass gains for the Cu-doped compositions Table 3-3 were consistent with

expected values. The observed overall mass increase values of $Ni_{1.9}Cu_{0.1}Mo_3N$, $Ni_{1.8}Cu_{0.2}Mo_3N$ and $Ni_{1.7}Cu_{0.3}Mo_3N$ were 38, 38.3, 38.4 % compared to the calculated values of 37.6, 37.55, 37.45 %.

$$Ni_{1.8}Cu_{0.2}Mo_3N + \frac{11}{2}O_2 \rightarrow 2Ni_{0.9}Cu_{0.1}MoO_4 + MoO_3 + \frac{1}{2}N_2 \qquad \text{Equation 3-1}$$

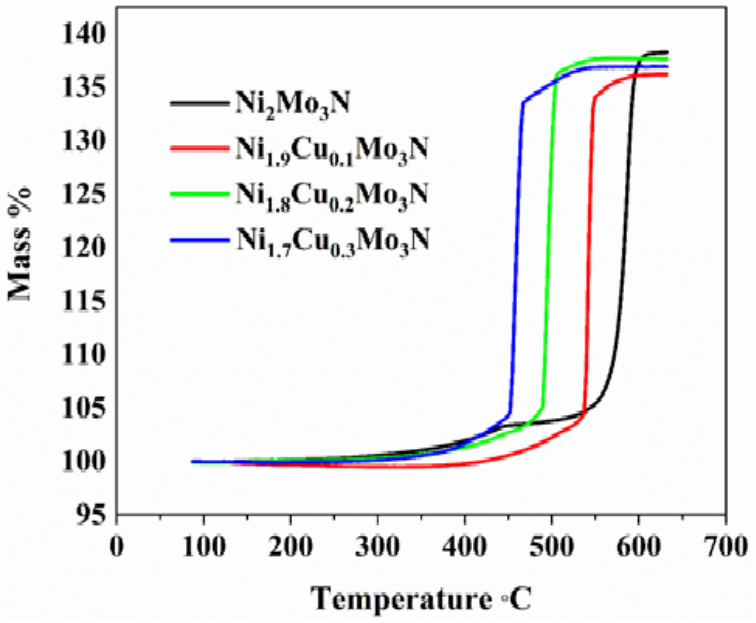

Figure 3-13 TGA curves (50 % O_2/50 % Ar environment) showing mass gain % of the Ni_2Mo_3N, $Ni_{1.7}Cu_{0.3}Mo_3N$, $Ni_{1.8}Cu_{0.2}Mo_3N$ and $Ni_{1.9}Cu_{0.1}Mo_3N$ samples prepared at 900 °C with heating rate of 5 °C min^{-1} under ammonia.

Table 3-3 Mass % of various oxides formed from TGA of the resulting composites

Composition	Overall Mass Gain Observed/ %	Expected Mass Gain/ %
Ni_2Mo_3N	38.30	37.95
$Ni_{1.9}Cu_{0.1}Mo_3N$	37.60	38.10
$Ni_{1.8}Cu_{0.2}Mo_3N$	37.55	38.26
$Ni_{1.7}Cu_{0.3}Mo_3N$	37.45	38.41

Figure 3-14 post-TGA PXRD patterns of Ni_2Mo_3N (left) and $Ni_{1.7}Cu_{0.3}Mo_3N$ (right). Analysis of the X-ray diffraction of the post-TGA Ni_2Mo_3N pattern revealed that a mixture of α-Ni(MoO_4) and MoO_3 were observed, with standard patterns used published by Ehrenberg *et al.*[173] and Sitepu *et al.*[174], respectively. Similar mixtures of α-Ni(MoO_4)[173] and MoO_3 [175] were presented in the post- TGA $Ni_{1.7}Cu_{0.3}Mo_3N$ pattern.

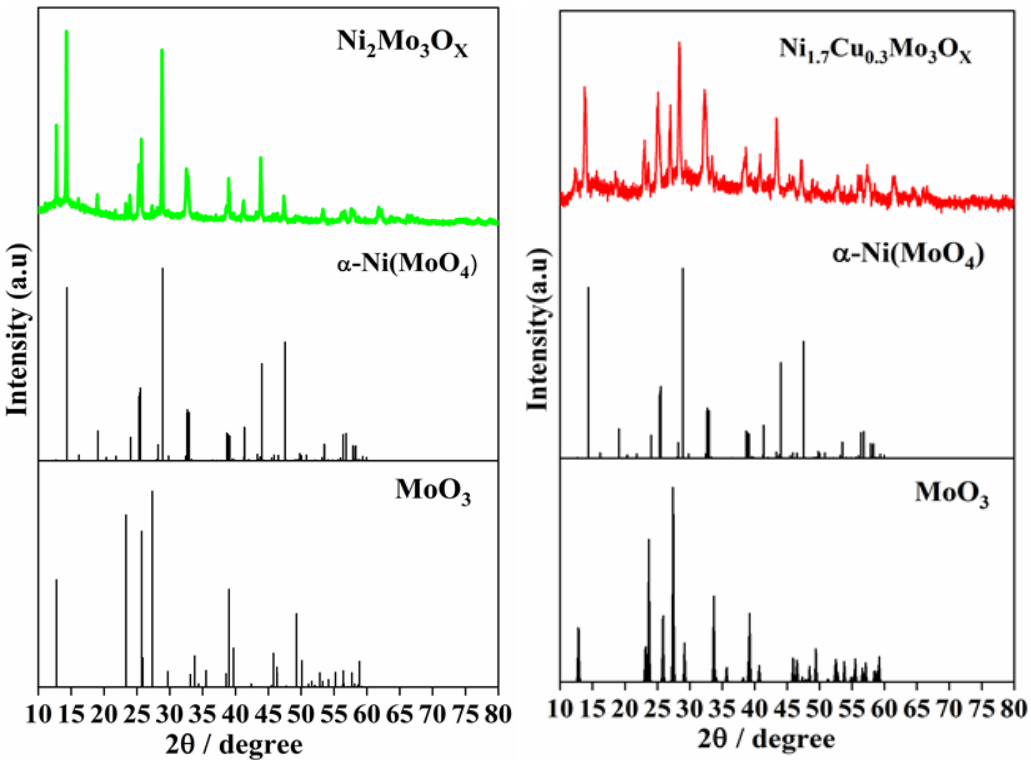

Figure 3-14 Powder XRD patterns of the products of heating Ni_2Mo_3N (left) and $Ni_{1.7}Cu_{0.3}Mo_3N$ (right) in the TGA to 700 °C in 50% O_2 / 50 % Ar.

3.6 Electron microscopy

EDX showed the Ni: Mo ratio of the Ni_2Mo_3N sample to be 36.4: 63.6 (expected 40: 60 for Ni_2Mo_3N). As copper was substituted in, the copper contents were measured a little below the nominal compositions, but with an increasing trend Table 3-4. Note there is some overlap between the nickel and copper EDX peaks so there is a significant uncertainty in the analysis of these small amounts of copper.

Table 3-4 The atom % of the Cu-doped samples from (0-0.3) evaluated by EDX analysis

Element	Ni_2Mo_3N		$Ni_{1.9}Cu_{0.1}Mo_3N$		$Ni_{1.8}Cu_{0.2}Mo_3N$		$Ni_{1.7}Cu_{0.3}Mo_3N$	
	Calculated	Actual	Calculated	Actual	Calculated	Actual	Calculated	Actual
Ni	40	36.4	38	36.5	36	32	34	27.9
Cu	0	0	2	1.7	4	2.8	6	4
Mo	60	63.6	60	61.2	60	65	60	67

Not only the crystalline structure and the chemical composition are important to understand the catalytic properties, also the morphological structure can be significant. Figure 3-15 shows typical images of a $Ni_{1.7}Cu_{0.3}Mo_3N$ sample obtained from the citrate-gel derived oxide metal precursors thermally treated at 900 °C with ammonia gas for 12 h. An open structure of interconnected, rounded particles with diameters around 200 nm were found, which is in

a good correlation with the average crystallite dimeter of 142 nm calculated by using an adaptation of the Scherrer equation incorporated into the Rietveld fitting package.[176]

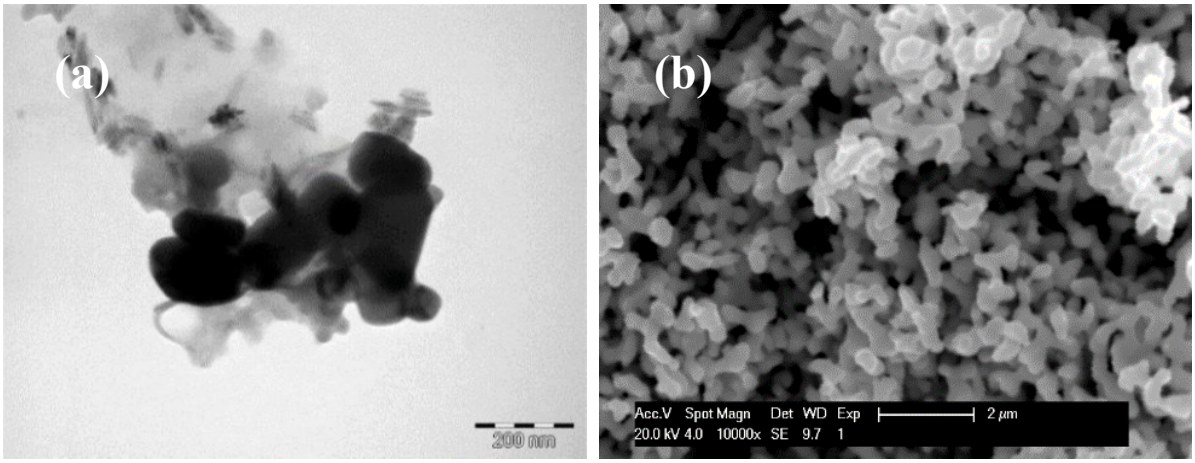

Figure 3-15 TEM (a) and SEM (b) images of $Ni_{1.7}Cu_{0.3}Mo_3N$ sample obtained from the citrate-gel derived metal oxide precursors heated in ammonia at 900 °C for 12 h.

3.7 The BET surface area

The nitrogen adsorption–desorption isotherm measurements were carried out to evaluate the BET surface area of the prepared samples Figure 3-16.

The need to produce these samples at a relatively high temperature of 900 °C has resulted in quite low surface areas below 5 $m^2\ g^{-1}$. It was observed that the surface area is reduced with increasing copper content from 2.2 $m^2\ g^{-1}$ for undoped sample to 1.6 $m^2\ g^{-1}$ for $Ni_{1.7}Cu_{0.3}Mo_3N$. This can be attributed partly to crystallite growth and partly to agglomeration, both occurring through sintering at this high reaction temperature, but the surface areas are fairly typical for this type of material.[177,177] However, the surface area of Mo based nitride materials can be strongly influenced by synthesis factors such as flow rates of NH_3 and temperature ramp rates, and achieving higher surface areas should be a future priority.

Volpe and Boudart reported that the large surface area of Mo nitrides were achieved using high space velocities of NH_3 and low temperature ramp rates.[72] The surface area of Mo based nitride materials can be strongly influenced by the synthesis factors as suggested by Choi *et al*.[178] The lower ammonia flow rates have been reported to produce higher concentrations of water formed during the oxide precursor reduction. The accumulated water in the bed reactor may decrease the conversion of oxide to nitride by decreasing the contact between ammonia and the oxide precursors, as described elsewhere.[179] The presence of water may cause the hydrothermal sintering and aggregation of the nanoparticles.[86]

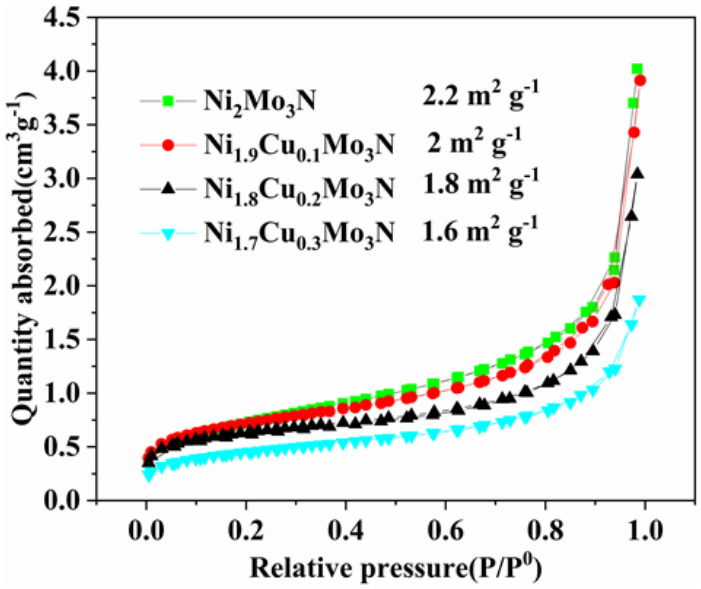

Figure 3-16 Nitrogen adsorption/desorption isotherms curves of mesoporous (Ni, Cu)$_2$Mo$_3$N series, fired at 900 ºC for h under NH_3, adsorption is given in units of cm^3 of adsorbate per gram adsorbent.

The recorded BET surface area for Ni_2Mo_3N catalyst (2.2 $m^2\ g^{-1}$) is similar to that given in the literature for molybdenum nitride material.[177] The reported nitride material has been prepared at lower temperature without using any chelating agent. However, in this study the sample was prepared at elevated temperature by using the citric acid (CA) as chelating agent.

3.8 Catalytic activity

Efficacy of the series of catalysts of the formula (Ni, Cu)$_2$Mo$_3$N were evaluated for the formation of ammonia according to the method described in (section 2.9). The materials were simply heated under 75% H_2 / 25% N_2 (BOC, 99.98 %) first at 700 °C to activate the catalyst by removing surface oxide, then at 400 °C where ammonia synthesis is more favored due to a lower decomposition rate. Initially, the materials have been measured at 400 °C at atmospheric pressure and lower activities were recorded. Increasing the reaction temperature from 400 to 500 °C significantly enhanced the performance. The ammonia synthesis increased from 147 to 272 μmol $g^{-1}\ h^{-1}$ for Ni_2Mo_3N and from around 95 to 179 μmol $g^{-1}\ h^{-1}$ for $Ni_{1.7}Cu_{0.3}Mo_3N$ as the process temperature was raised from 400 to 500 °C, (Figure 3-17). Hence, 500 °C was chosen for the evaluation of the ammonia production in this study. The conductivity versus time plots for the reaction of (Ni,Cu)$_2$Mo$_3$N under 3:1 H_2 in N_2 at atmospheric pressure and 500 °C is shown in Figure 3-18.

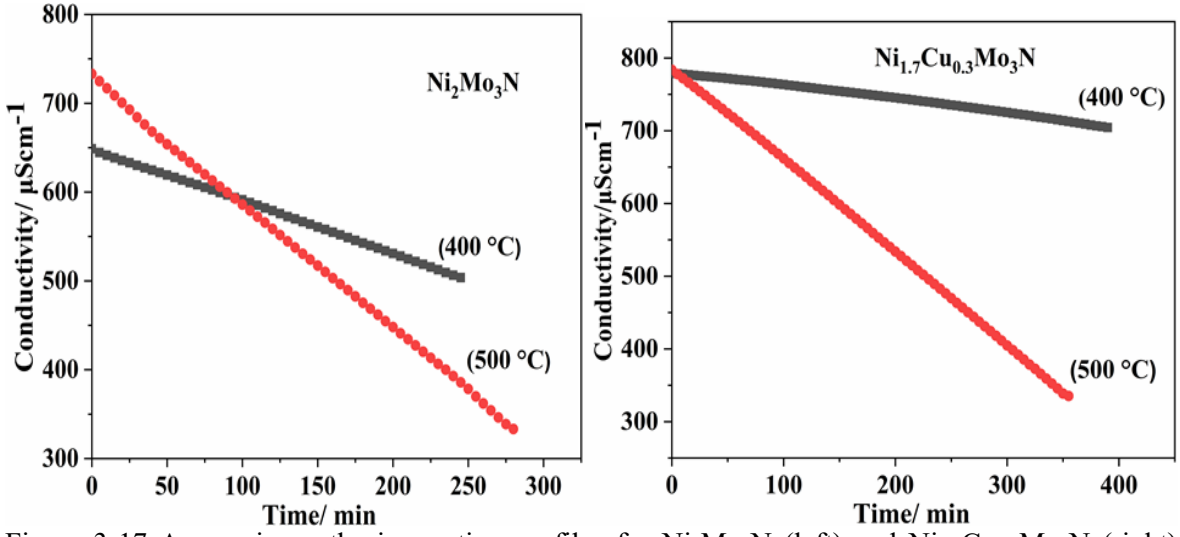

Figure 3-17 Ammonia synthesis reaction profiles for Ni_2Mo_3N (left) and $Ni_{1.7}Cu_{0.3}Mo_3N$ (right) under 75 vol % H_2 in N_2 (BOC,99.98 %) at 400 and 500 °C.

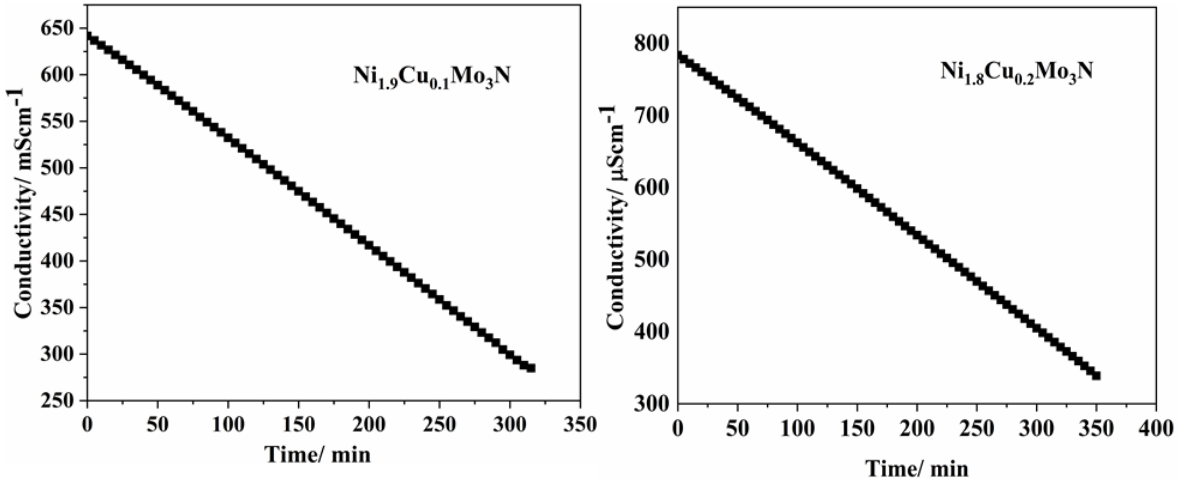

Figure 3-18 Conductivity profiles of the $Ni_{1.9}Cu_{0.1}Mo_3N$ (left) $Ni_{1.8}Cu_{0.2}Mo_3N$ (right) acid scrubber placed after heated at 500 °C under 75 vol % H_2 in N_2 (BOC, 99.98 %).

The results of the performance over each sample showed that the reaction conditions were important. For instance, BET surface areas of the catalysts along with transition metal dopant contents were also shown to be another important contributing factor to the catalytic properties. It was observed that the copper additions could reduce the surface area, and this might be related to formation of agglomerated particles on the surface. This in turn could contribute to a gradual decrease in activity in the following order: Ni_2Mo_3N > $Ni_{1.9}Cu_{0.1}Mo_3N$ > $Ni_{1.8}Cu_{0.2}Mo_3N$ > $Ni_{1.7}Cu_{0.3}Mo_3N$, 272 > 252 > 231 > and 179 µmol-NH_3 g^{-1} h^{-1}, respectively Table 3-5. These findings clearly indicate that the decrease in the surface area of the investigated catalysts was proportionate to the decrease in the catalytic performance. It can be clearly seen that all the synthesized catalysts exhibited high catalytic performance for this reaction.

Table 3-5 BET surface areas, elemental analysis, ammonia synthesis rate and specific activity of $(Ni, Cu)_2Mo_3N$

Catalyst	Surface area ($m^2 g^{-1}$)	Crystallite diameter (nm)	Ammonia synthesis rate at 500 °C ($\mu mol\ h^{-1} g^{-1}$)	Specific activity at 500 °C ($\mu mol\ h^{-1} m^{-2}$)
Ni_2Mo_3N	2.2	113(2)	272(5)	124(2)
$Ni_{1.9}Cu_{0.1}Mo_3N$	2.1	119(3)	252(2)	120(1)
$Ni_{1.8}Cu_{0.2}Mo_3N$	1.8	126(5)	231(2)	128(1)
$Ni_{1.7}Cu_{0.3}Mo_3N$	1.6	142(11)	179(6)	112(4)

Table 3-6 shows a summary of the elemental analysis for nitrogen content for pre-and post-catalysis samples of copper doped Ni_2Mo_3N. The chemical analysis (CHN) was carried out for each composition in order to determine the nitrogen content.

Table 3-6 Pre-and-post catalysis nitrogen content and expected nitrogen content of Ni_2Mo_3N and $(Ni, Cu)_2Mo_3N$ samples.

Catalyst	Nitrogen content (wt.%)		
	Pre-catalysis	Post-catalysis	Expected N content
Ni_2Mo_3N	3.4	3.3	3.3
$Ni_{1.9}Cu_{0.1}Mo_3N$	3.6	3.4	3.3
$Ni_{1.8}Cu_{0.2}Mo_3N$	3.6	3.4	3.3
$Ni_{1.7}Cu_{0.3}Mo_3N$	3.6	3.4	3.4

Data presented in Table 3-6 confirmed the presence of nitrogen in the synthesised materials. The actual nitrogen content in Ni_2Mo_3N measured from combustion analysis was 3.4 wt. %; (expected wt.%N is 3.3%). The actual nitrogen contents in $Ni_{1.9}Cu_{0.1}Mo_3N$, $Ni_{1.8}Cu_{0.2}Mo_3N$ and $Ni_{1.7}Cu_{0.3}Mo_3N$ were almost the same of 3.6 wt. % which correspond to the calculated percentage of nitrogen contents of 3.3 wt. % for $Ni_{1.9}Cu_{0.1}Mo_3N$ and $Ni_{1.8}Cu_{0.2}Mo_3N$, and 3.4 for $Ni_{1.7}Cu_{0.3}Mo_3N$. Therefore, the calculated stoichiometries are $Ni_{1.9}Cu_{0.1}Mo_3N_{1.07}$, $Ni_{1.8}Cu_{0.2}Mo_3N_{1.07}$ and $Ni_{1.7}Cu_{0.3}Mo_3N_{1.05}$. Results show that the nitrogen content of each composition are in good agreement with the expected values. The post-reaction nitrogen contents of Ni_2Mo_3N and Cu-doped samples are similar to that of pre-reaction materials. Results from PXRD, EDX, CHN analysis alongside the TGA observation confirmed the formation of single-phase materials.

The ammonia synthesis rates of the studied catalysts here are rather different from the previous and recent reported catalysts. For example molybdenum nitrides were found to be

active catalysts for ammonia synthesis at 400 °C,[180, 33] and their catalytic performance was significantly improved by the addition of a second transition metal such as Ni, Co or Fe. Comparisons between various ternary metal nitride phases for the ammonia synthesis reaction were made by Kojima and Aika. It was found that among the investigated samples bimetallic cobalt molybdenum nitride synthesise ammonia at an efficiency two times greater than that of the commercial based catalyst, particularly when a material is promoted with Cs^+, their reported activities 652 μmol g^{-1} h^{-1} and 986 μmol g^{-1} h^{-1}, respectively.[38, 37, 181, 78, 182, 82] Since their discovery, Co_3Mo_3N catalyst has been widely investigated.[41] The high activity of the Co_3Mo_3N has been linked to the fact that CoMo alloy has an average N_2 adsorption energy close to the optimal nitrogen binding energy for catalytic performance.[76,183] Kojima el al. investigated the doping effect of some transition metals Ni, Co, Cr, Fe and Cu on rhenium catalyst. Results from this investigation revealed that the copper rhenium had less activity (60 μmol g^{-1} h^{-1}) when compared to other investigated materials.

Although doping metal nitrides such as binary nitrides with transition metals has been previously reported as an effective way to improve the efficiency of ammonia synthesis, this is not consistent with the current study.[82] That is, the activity was found to be reduced by copper addition.

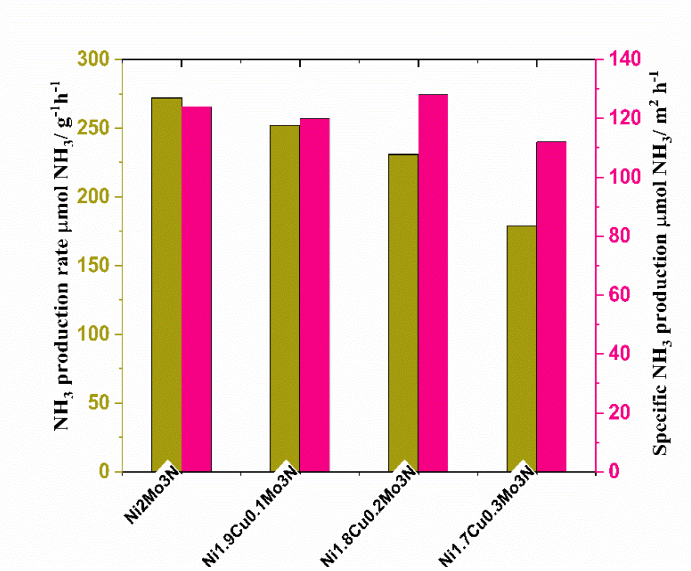

Figure 3-19 Catalytic activity of Cu-doped Ni_2Mo_3N catalysts, for NH_3 synthesis at atmospheric pressure. Reaction conditions: catalyst, 0.15 g; reactant gas, H_2/N_2= 3:1; flow rate = 13 mL/min; reaction temperature, 500 °C. (Green the catalytic activity per mass; Pink the catalytic activity per surface area).

The catalytic activity of the copper doped Ni_2Mo_3N catalysts was normalised per surface area. Combining the result in Figure 3-19 and the catalytic activity data tabulated in Table 3- 5, it is apparent that the specific activities of Ni_2Mo_3N, $Ni_{1.9}Cu_{0.1}Mo_3N$, $Ni_{1.8}Cu_{0.2}Mo_3N$ and $Ni_{1.7}Cu_{0.3}Mo_3N$ samples in the same conditions were 124 μmol h^{-1} m^{-2}, 120 μmol h^{-1} m^{-2}, 128 μmol h^{-1} m^{-2} and 112 μmol h^{-1} m^{-2}, respectively. The observed trends suggested that the specific activities in the current work may have been influenced by the surface area of all materials.

On comparing the specific activities of the catalysts in this study to those of metal nitrides reported in the literature, it was found that the data obtained from current study show better specific activities compared to that previously reported. It was demonstrated by Kojima *et al*. that the specific activity of Mo_2N was 1.1 μmol h^{-1} m^{-2}, and the addition of transition metals such as Ni, Fe and Co resulted in a substantial increase of the specific activities in the order $Co_3Mo_3N > Fe_3Mo_3N > Ni_2Mo_3N$ with 14 μmol h^{-1} m^{-2}, 20 μmol h^{-1} m^{-2} and 20 μmol h^{-1} m^{-2}, respectively. These results were reported to be comparable with the results observed by Mittasch.[38] In previous work from the literature, ammonia synthesis reactions were performed using 0.4 g of catalyst at 350°C under N_2/H_2 (1:3) using a flow rate of 60 cm^3 min^{-1} at ambient pressure. The literature available on quaternary metal nitrides for ammonia synthesis is extremely scarce with only a few studies having been reported on nanocrystalline nickel cobalt molybdenum nitride with a production rate of 160 μmol g^{-1} h^{-1}.

From studying the as-prepared and post-reaction X-ray diffraction patterns, shown in Figure 3-20, it is clear that the formation of ammonia shows no appreciable change on the structure throughout the series of samples. Hence, all the tested samples are stable under the reaction conditions used.

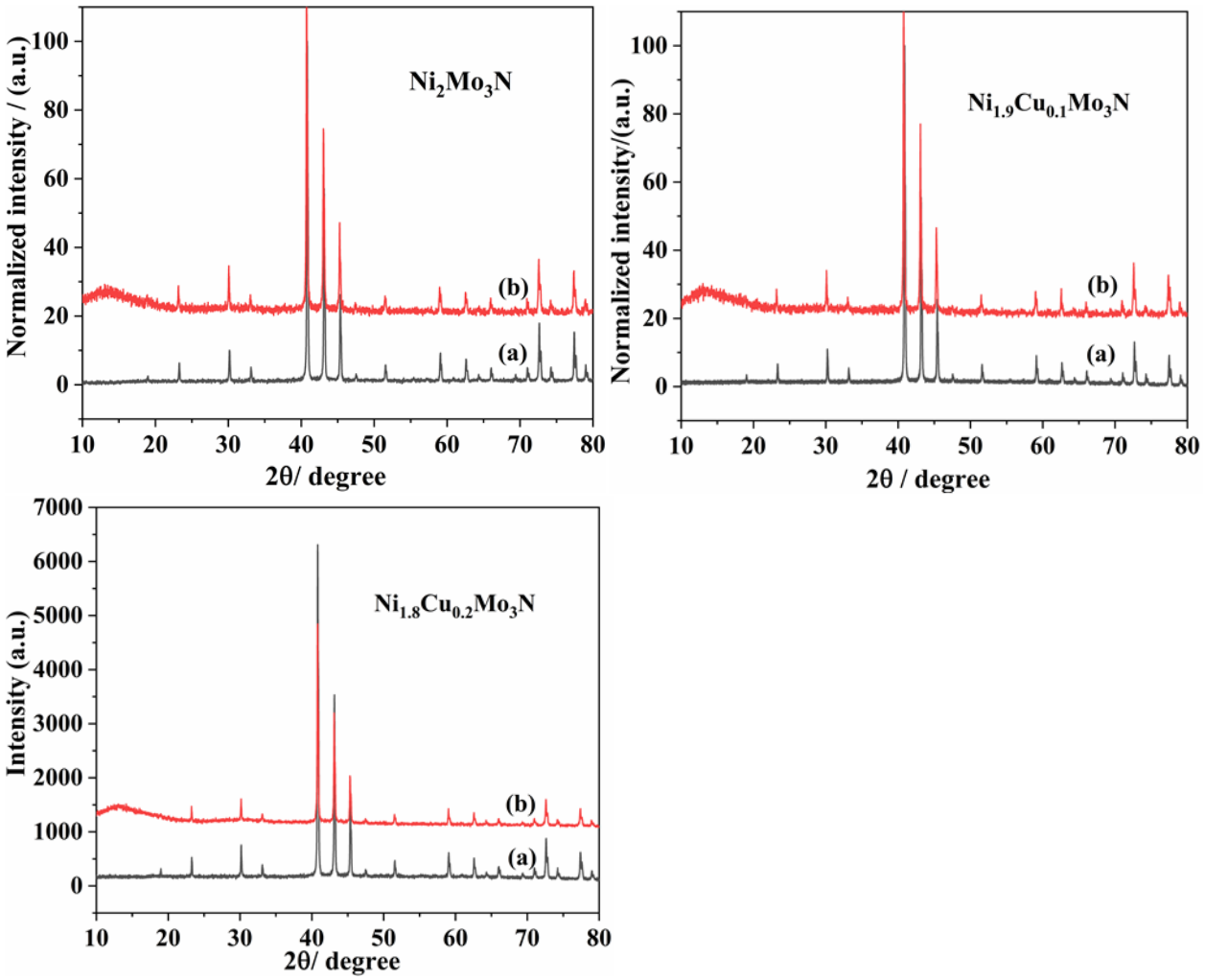

Figure 3-20 XRD patterns collected for (a) pre-reaction and (b) post-reaction of Ni_2Mo_3N, $Ni_{1.9}Cu_{0.1}Mo_3N$ and $Ni_{1.8}Cu_{0.2}Mo_3N$.

3.9 Conclusion

Filled β-Mn type materials with composition Ni_2Mo_3N and $Ni_{2-x}Cu_xMo_3N$ up to $x = 0.3$ were synthesised *via* a modified Pechini route, followed by ammonolysis of the metal oxide precursors. There was a limit to the amount of the Cu that could be substituted under these conditions. That seemed to be due to a solubility limit of copper in the host phase. Furthermore, the BET surface area of the catalysts decreases with increasing copper concentration. For ammonia synthesis reaction, the ammonia synthesis rate improves with increasing of the reaction temperature. Moreover, the parent compound Ni_2Mo_3N demonstrated the best ammonia production rate among other investigated compositions, which indicates that the addition of copper into Ni_2Mo_3N structure lower the catalytic performance.

Chapter 4 Synthesis and Ammonia Synthesis Activity of Nickel Iron Molybdenum Nitride

4.1 Overview

A series of nickel iron molybdenum nitrides were produced and evaluated for ammonia synthesis; their activities were correlated with the surface area of the catalysts.

4.2 Introduction

Iron-based materials are the most successful and prominent catalysts for ammonia production by the Haber-Bosch process due to their ability to interact with dinitrogen and enhance N–N bond weakening.[184] Nitride catalysts can produce ammonia at lower reaction pressure and therefore are regarded as potential alternative catalysts for ammonia production. Due to the desirable features of nanostructured metal nitride materials in diverse applications, there have been expanded efforts to find ways to improve the catalytic ammonia performance. In this chapter, attempts to develop nanostructured quaternary nitride materials with iron substitution were made.

Iron based nitride compounds have been widely studied due to the natural abundance of iron. It is known that moderate temperature synthetic routes are preferable for the successful design and optimization of ternary nitrides with desirable properties. The nitridation or ammonolysis of oxide precursors is the most commonly used method. The nitrides obtained through these methods were found to be catalytically active for ammonia synthesis. For example, Fe-Mo-N showed good catalytic performance. The synthesis of Fe_3Mo_3N with the η-carbide structure was first reported in 1993 *via* nitridation of oxide precursors in ammonia atmosphere. Fe_3Mo_3N was found to be isostructural with η-Fe_3W_3C.[64] Since then, different approaches have been developed to synthesize this material. Weil and Kumta demonstrated the synthesis of Fe_3Mo_3N *via* hydrolysed alkanolamine complexed precursors. In this method the precursors were prepared by the addition of ethanolamine, as a complexing agent, to stoichiometric mixture of iron chloride tetrahydrate dissolved in acetonitrile. Evaporation of the solvent and subsequent thermal treatment in NH_3 at 950 °C for 4 h yielded the final product Fe_3Mo_3N. The nano-sized Fe_3Mo_3N particles were prepared by thermal annealing of Fe-Mo particles under either flowing N_2 or NH_3 at various temperatures between 400 - 980 °C.[92, 185, 93] An alternative synthesis method has been reported by heating ternary oxide precursors with urea. For example, Fe_3Mo_3N was synthesized by reacting

$FeMoO_4$ with urea.[97] Ternary nitrides containing iron such as Ca_6FeN_5[186] and Li_3FeN_2[187] have been prepared by reacting a transition metal with an alkali or alkaline earth nitride/amide. $FeWN_2$ has been synthesized by ammonolysis of $FeWO_4$ under NH_3 at 700 °C for 15 h.[188] $FeWN_2$ was produced by treating the solid-state precursor $FeWO_4$ with ammonia at 625 and 800 °C.[100] The quaternary nitrides, $Fe_{2-x}M_xMo_3N$ (M = Ni, Pd, Pt),[189] $Fe_{2-x}Rh_xMo_3N$[190] and $Fe_{3-x}Co_xMo_3N$[106] have been synthesised by the reduction of the corresponding oxides under dilute hydrogen nitrogen.

The reported synthetic methods to ternary and quaternary iron nitride materials are tabulated in Table 4-1.

Although iron based binary and ternary nitride materials have been well studied towards ammonia synthesis, quaternary nitride systems are rather young and still at the beginning.[40]

Table 4-1 The reported synthesis methods for iron-based nitride materials

Product and Synthesis method	**Starting materials**	**Sintering conditions (°C, time, gas)**	**Ref**
Fe_3Mo_3N	$FeCl_2$+ $Na_2MoO_4{\cdot}2H_2O$ +	Dry overnight 150 °C in air 900 °C, 0.5 h.	64
Fe_3Mo_3N	$Fe(NO_3)_3{\cdot}9H_2O$+ $NH_4Mo_7O_{24}{\cdot}4H_2O$	975 °C for 36 h, (10 %) H_2 /N_2	167
Fe_3Mo_3N	$FeCl_2{\cdot}2H_2O$ + $MoCl_5$+ HPLC grade ace-tonitrile + C_2H_7NO+	Dry overnight under vacuum at 80 °C, 120°C at 10 °C min^{-1}, 120 °C for 1 h, 120 °C to 950 °C at 3 °C min^{-1}, 950 °C for 4 h, NH_3.	92
Solid-state reduction Fe_3Mo_3N	$FeCl_2$ + $Na_2MoO_4{\cdot}2H_2O$	Dry at 150 °C, 24 h in air. 700 °C, 6 h, N_2. 800 °C, 5 °C/min. NH_3	63
Co-precipitation Fe_3Mo_3N	$FeCl_2$ +$NH_4Mo_7O_{24}{\cdot}4H_2O$+ Urea	Dry at 150 °C, 24 h, 900 °C, 3 h, 750 °C	97
Nitridation of the oxide precursor Fe_3Mo_3N	$Fe(NO_3)_3{\cdot}9H_2O$+ $NH_4Mo_7O_{24}{\cdot}4H_2O$	Dry overnight at 423 K. 973 K, 5 °K/min^{-1}, 6 h, NH_3	82
Fe_3Mo_3N	$Fe(NO_3)_3{\cdot}9H_2O$+ $NH_4Mo_7O_{24}{\cdot}4H_2O$	400 °C, 2 h. 600 °C 0.1 °C min^{-1}, 4.5% NH_3 in 3:1 H_2–N_2	37
Fe_3Mo_3N	$Fe(NO_3)_3{\cdot}9H_2O$+ $NH_4Mo_7O_{24}{\cdot}4H_2O$	357 ºC, 5.6 ºC min^{-1} , 357 to 447 ºC at 0.5 ºC min^{-1} , 785 ºC at 2.1 ºC min^{-1} 5 h.	78

One-step solid-state Fe_3Mo_3N	Fe_2O_3+ Mo + NaN_3	750 °C,10 h, 10 °C min^{-1}. Dry in vacuum at 60 °C for 10 h.	191
Fe_3Mo_3N 31 nm 8.8 m^2 g^{-1}	$Fe(NO_3)_3 \cdot 9H_2O$+ $NH_4Mo_7O_{24} \cdot 4H_2O$	80 °C, 24 h. 350 °C ,15 h, calcined at 600 °C, 5 h in air. 30 to 350 °C (5 °C min^{-1}), 700 °C (1 °C min^{-1}), 3 h.	177
Nitridation of the oxide precursor. Fe_3Mo_3N	$(NH_4)_2MoO_4$+ $(NH_4)_2Fe(SO_4)_2$	Dry overnight at 150 °C, air. 923-973 K, 4 - 15 h. Pellets 973 K for 12 h	192
$FeMoN_2$	Fe_3Mo_3N	300°C, 6 h, NH_3	193
Single-step reaction by the ammonolysis $(Fe_{0.8}Mo_{0.2})MoN_2$	$FeCl_3 \cdot 6H_2O$+ $Na_2MoO_4 \cdot 2H_2O$	700 °C, 69 h, NH_3	194
Co precipitation Fe-Mn-N	Fe-Mn-O	800 °C for 8 h	195
Ammonolysis Fe_3Mo_3N Cs/Fe_3Mo_3N	$FeMoO_4 \cdot nH_2O$	600 °C, 0.1 °C min^{-1} in 4.5% NH_3 in 3:1 H_2/N_2	37
Standard ceramic $Fe_{2-x}M_xMo_3N$ (M = Ni, Pd, Pt)	Fe_2O_3+NiO+ MoO_3 Fe_2O_3+ PdO + MoO_3 Fe_2O_3+ PtO_2+ MoO_3	10% H_2/N_2 ,48 h at 700 °C, 24 h at 750 and 875 °C, twice at 975 °C	189
Standard ceramic $Fe_{2-x}Rh_xMo_3N$	Fe_2O_3+ MoO_3 Rh_2O_3	10 % H_2/N_2 for 48 h at 700 °C, 24 h at 750 °C, 875 °C, twice at 975 °C	190
Nitridation $Co_{3-x}Fe_xMo_3N$	Fe_2O_3+ Co_3O_4 + MoO_3	10 % H_2/N_2 ,700 °C (48 h), 750 °C (24 h), 875 °C (24 h), 975 °C (2 × 24 h)	106

4.3 Experimental

Substituting iron into Ni_2Mo_3N, the synthesis proceeded in the same way as for the copper (chapter 3) except that a brown colour developed as the sol was concentrated.

A range of compositions following the formula $Ni_{2-x}Fe_xMo_3N$ (x = 0, 0.1, 0.2, 0.3, 0.4, 0.5, 0.6, 0.7, 0.8, 0.9, 1, 1.1, 1.2, 1.3, 1.4 and 1.6) were prepared by the modified Pechini method. Stoichiometric mixtures of $(NH_4)_6Mo_7O_{24} \cdot 4H_2O$ (Sigma Aldrich, > 99.0 %), Ni $(NO_3)_2 \cdot 6H_2O$ (Sigma Aldrich, 99.9 %) and Fe $(NO_3)_3 \cdot 9H_2O$ (Sigma Aldrich, 98.0 %) were dissolved in aqueous solutions of HNO_3 (60 ml, 10 %) (Fisher Scientific, 70 %) at room temperature to yield green solutions. 7.94 g citric acid monohydrate (Sigma Aldrich,

> 99.0) was added to the solution. The quantities and the ratios of reagents for the different compositions are listed in Table 4-2. The materials were subsequently calcined and ammonolysed following the same experiment conditions described in chapter 3. After 12 hr of the reaction, the colour of the sol changed from light green to dark brown, which could be ascribed to the oxidation of Fe^{2+} to Fe^{3+} see Figure 4-1.

Table 4-2 Quantities of reagent used in the synthesis of $Ni_{2-x}Fe_xMo_3N$.

***x* in $Ni_{2-x}Fe_xMo_3N$**	**$Ni(NO_3)_2{\cdot}6H_2O$**	**$Fe(NO_3)_2{\cdot}6H_2O$**	**$(NH_4)_6Mo_7O_{24}{\cdot}4H_2O$**	**Citric acid monohydrate**
0.1	2.09 g / 7.19 mmol	0.15 g / 0.37 mmol	2 g / 1.62 mmol	7.94 g / 37.8 mmol
0.2	1.97 g / 6.77 mmol	0.31 g / 0.77 mmol		
0.3	1.86 g / 6.40 mmol	0.46 g / 1.14 mmol		
0.4	1.76 g / 6.05 mmol	0.61 g / 1.51 mmol		
0.5	1.65 g / 5.67 mmol	0.76 g / 1.89 mmol		
0.6	1.54 g / 5.30 mmol	0.92 g / 2.28 mmol		
0.7	1.43 g / 4.92 mmol	1.07 g / 2.65 mmol		
0.8	1.37 g / 4.71 mmol	1.22 g / 3.02 mmol		
0.9	1.21 g / 4.16 mmol	1.37 g / 3.39 mmol		
1.0	1.10 g / 3.78 mmol	1.53 g / 3.79 mmol		
1.1	0.99 g / 3.40 mmol	1.68 g / 4.16 mmol		

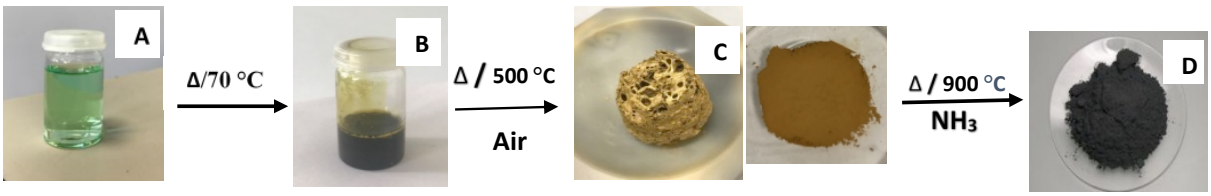

Figure 4-1 Schematic description of the citrate- gel process to produce the filled β- manganese type phases, with Ni_2Mo_3N and the $(Ni,Fe)_2Mo_3N$ compounds. From left to right: starting solution (green) (A), gel (brown) after evaporating (B), goldish foams(C) and product (D).

4.4 Results and discussion

4.4.1 Structural characterisation of $Ni_{2-x}Fe_xMo_3N$

Figure 4-2 shows that all the X-ray diffraction peaks of the samples with iron contents up to $NiFeMo_3N$ could be indexed to the characteristic pattern of the filled β- manganese structure of Ni_2Mo_3N (PDF card no. 01-089-4564) having space group $P4_132$. These observations

imply that the resulting materials were phase pure, which was also confirmed further by Rietveld refinement. Upon further increase of Fe loading beyond $NiFeMo_3N$, some impurity reflection peaks were observed, which can be assigned to both molybdenum metal (JCPDS X-ray index card No 42-1120) and binary iron nitride (JCPDS X-ray index card No 12-1206). Although some impurities have been presented beyond $x = 1$, we did not observe any indication of the solubility limit upon the substitution of iron onto nickel sites. Magnified diffraction peaks show a slight shift of the peaks positions to lower 2θ values, as d-spacing increased with doped iron content. This might be attributed to the expansion of the lattice parameters as shown in Figure 4-3.

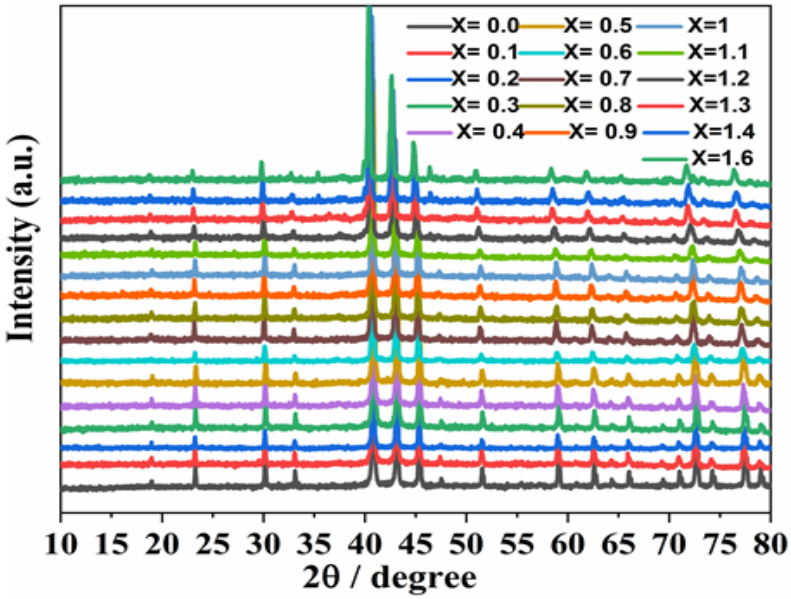

Figure 4-2 PXRD patterns of $Ni_{2-x}Fe_xMo_3N$ samples heated under NH_3 at 900 °C for 12 h.

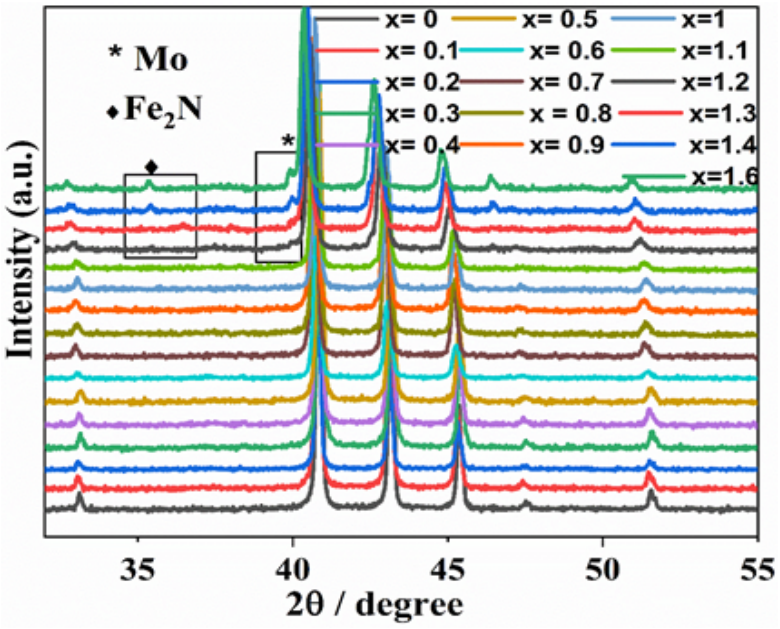

Figure 4-3 The magnified PXRD patterns of $Ni_{2-x}Fe_xMo_3N$ samples heated under NH_3 at 900 °C for 12 h in the vicinity of 2θ = 31°. (*) symbol indicates the Mo metal reflections and (•) shows reflections of the Fe_2N phase.

Structural analysis of the single phase patterns was undertaken using Rietveld refinement, using standard patterns published by Prior and Battle[58] as the initial model obtained from inorganic crystal structure database (ICSD).[169] The refined parameters were: atomic positions, the space group, the lattice parameter (*a*), zero point, the background, phase fraction and profile parameters L_x and L_y. The best fits to the data were obtained using models with disordered Ni and Fe occupying the equivalent 8c position which is constrained to give a total occupancy of one. The isotropic thermal parameters, U_{iso}, were constrained to be equal for the nickel and iron. Mo was placed at the 12d site forming Mo_6N octahedra with the interstitial nitrogen atom on 4a site. The background was modelled using by a type 2 function and 3 terms. The refinement parameters are summarised in Table 4-3 and the representative fit of refinement profile is shown in Figure 4-4 and 4-5. An increasing linear trend in lattice parameter with iron content (Figure 4-6) indicates the formation of well distributed solid solutions and is consistent with the larger metallic radius of Fe (1.26 Å) compared with Ni (1.24 Å).[172]

Increasing the iron content further, molybdenum metal and Fe_2N impurities were observed, although in contrast with the $(Ni,Cu)_2Mo_3N$ solid solutions (chapter 3) the lattice parameter of the $(Ni, Fe)_2Mo_3N$ continued to increase, suggesting that there is no strong barrier to forming solid solutions in this more iron-rich region of the phase space. Crystallite diameters were calculated using an adaptation of the Scherrer equation (Equation 2-8) incorporated into the Rietveld fitting package.[176] Based on the PXRD data the crystallite diameter of

$(Ni,Fe)_2Mo_3N$ materials decreases with Fe content. Compositions were initially annealed at 700 °C under flowing ammonia (data not shown). An additional peak associated with impurity phases that was detected at approximately *ca.*37.5° suggests the presence of traces of the γ-Mo_2N cubic phase (JCPDS X-ray index card 25-1366).

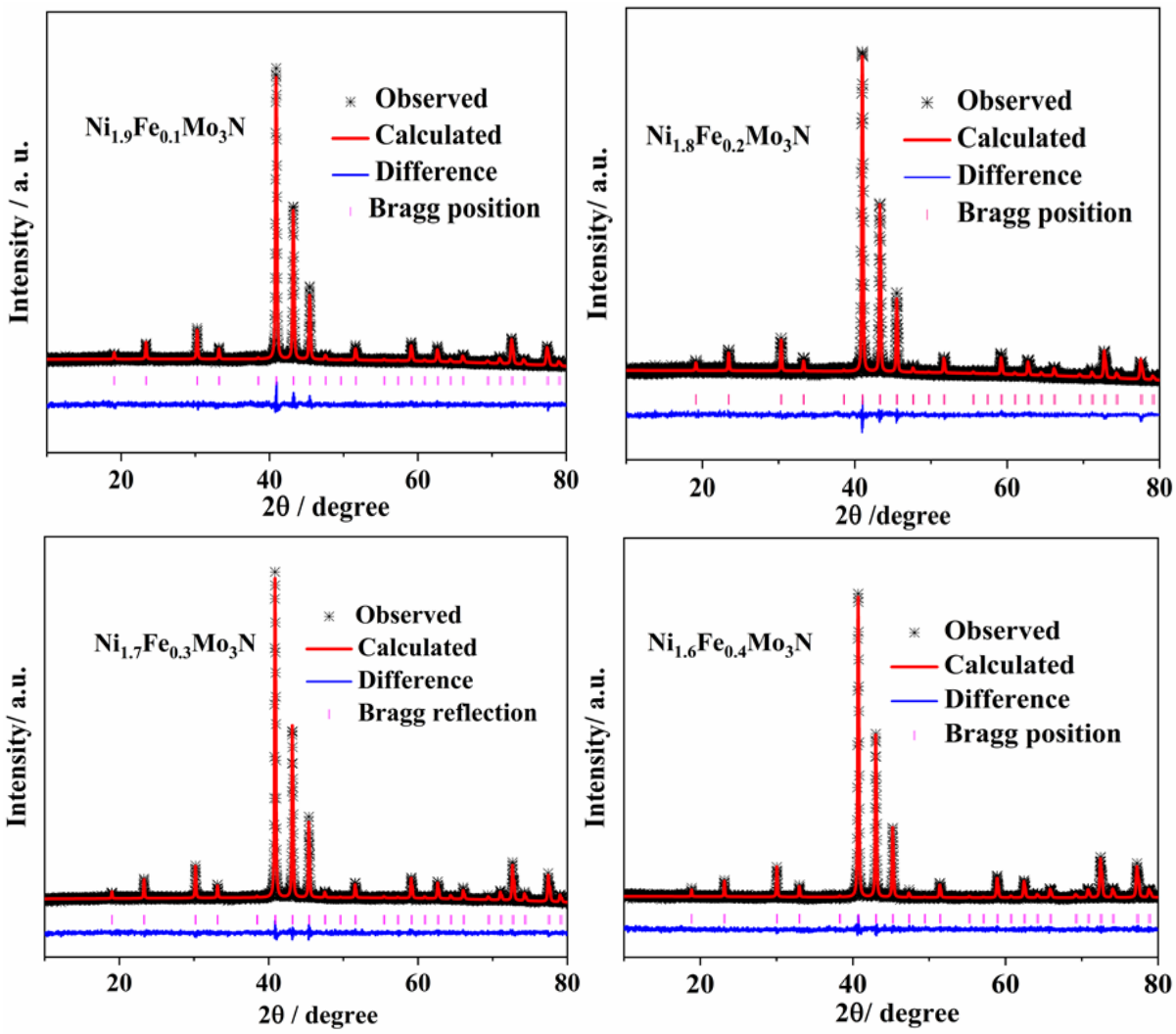

Figure 4-4 Rietveld fit to the PXRD data of $Ni_{1.9}Fe_{0.1}Mo_3N$, $Ni_{1.8}Fe_{0.2}Mo_3N$, $Ni_{1.7}Fe_{0.3}Mo_3N$ and $Ni_{1.6}Fe_{0.4}Mo_3N$. Black crosses mark the data points, the red continuous line the fit and the blue continuous line the difference. Pink tick marks show the positions of the allowed reflections for the filled β-manganese structure in space group $P4_132$.

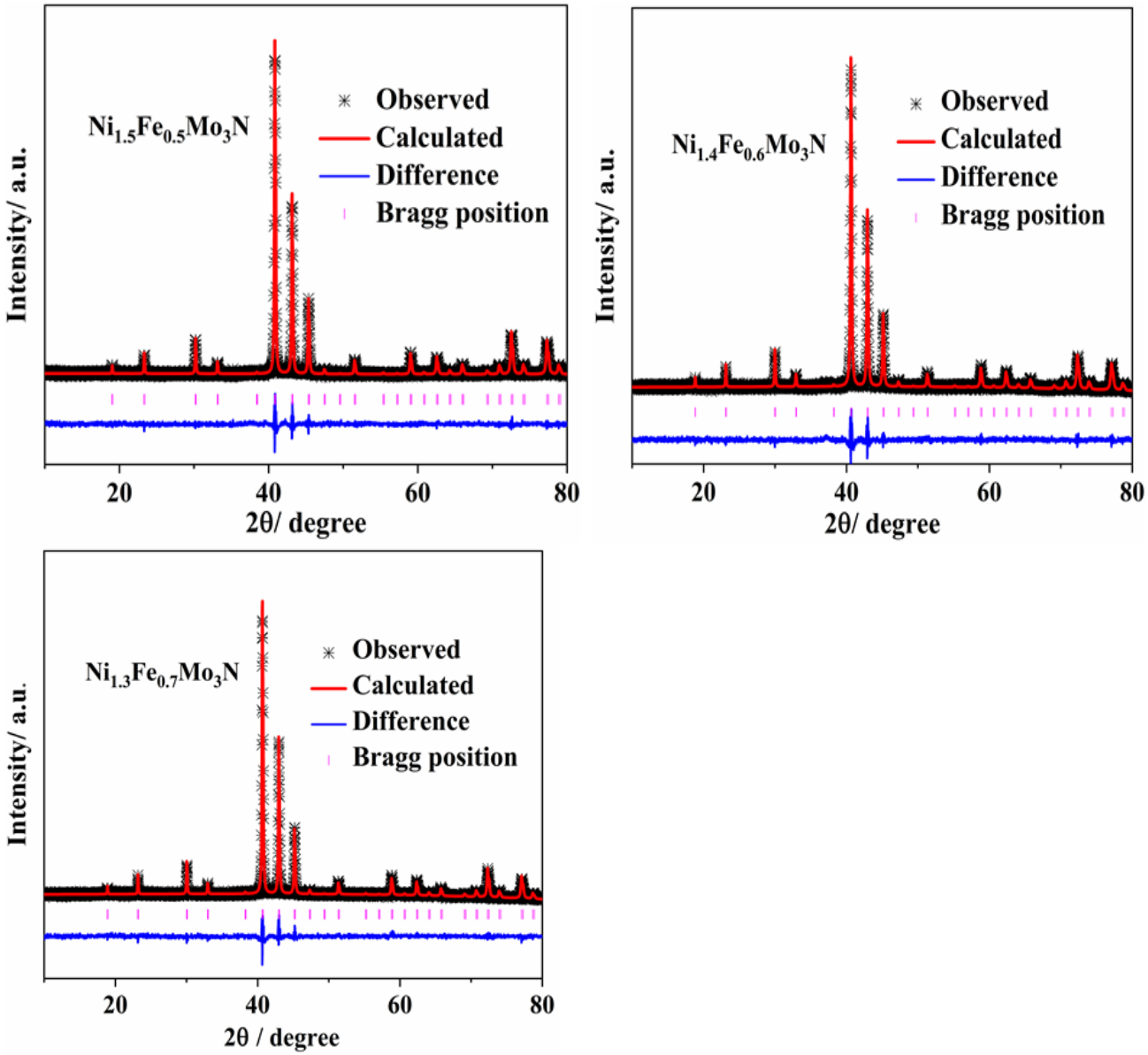

Figure 4-5 Rietveld fit to the PXRD data of $Ni_{1.5}Fe_{0.5}Mo_3N$, $Ni_{1.4}Fe_{0.6}Mo_3N$, $Ni_{1.3}Fe_{0.7}Mo_3N$. Black crosses mark the data points, the red continuous line the fit and the blue continuous line the difference. Pink tick marks show the positions of the allowed reflections for the filled β-manganese structure in $P4_132$.

Table 4-3 Refinement details and structure information for the $Ni_{2-x}Fe_xMo_3N$ series.

Composition	a/Å	Ni/ Fe x (8c x, x, x)	Ni/ Fe U_{iso} / Å^2	Mo 12 d (1/8, y, z)			N 4a 3/8, 3/8, 3/8
				y	Z	U_{iso}/ Å^2	Uiso / Å^2
Ni_2Mo_3N	6.6364(1)	0.0663(2)	0.0262(8)	0.20176(1)	0.45176(1)	0.02668(5)	
$Ni_{1.9}Fe_{0.1}Mo_3N$	6.63698(2)	0.06692(3)	0.026(1)	0.2019(1)	0.4519	0.024	
$Ni_{1.8}Fe_{0.2}Mo_3N$	6.64193(1)	0.06695(4)	0.0154(2)	0.20165(2)	0.45165	0.0127(1)	
$Ni_{1.7}Fe_{0.3}Mo_3N$	6.64765(3)	0.0672(4)	0.04385 (2)	0.20222(2)	0.45222	0.04376 (1)	
$Ni_{1.6}Fe_{0.4}Mo_3N$	6.650198(3)	0.067704(3)	0.0322(2)	0.20246(2)	0.45246	0.0271(1)	
$Ni_{1.5}Fe_{0.5}Mo_3N$	6.65532(2)	0.06778(4)	0.02688(1)	0.2025(2)	0.4525	0.010274(1)	0.2500
$Ni_{1.4}Fe_{0.6}Mo_3N$	6.65905(4)	0.068364(5)	0.01862(2)	0.202472(3)	0.45472	0.01887(1)	
$Ni_{1.3}Fe_{0.7}Mo_3N$	6.664 (3)	0.068439(6)	0.0304(2)	0.20307(2)	0.45307(1)	0.03188(1)	
$Ni_{1.2}Fe_{0.8}Mo_3N$	6.66784 (5)	0.067652(5)	0.048330(2)	0.203614(3)	0.45614	0.04304(2)	
$Ni_{1.1}Fe_{0.9}Mo_3N$	6.67298 (5)	0.067666(5)	0.042884(2)	0.20284 (2)	0.4584	0.042553(2)	
$NiFeMo_3N$	6.6812 (5)	0.054013(4)	0.0154(2)	0.20355(2)	0.4555	0.026(1)	

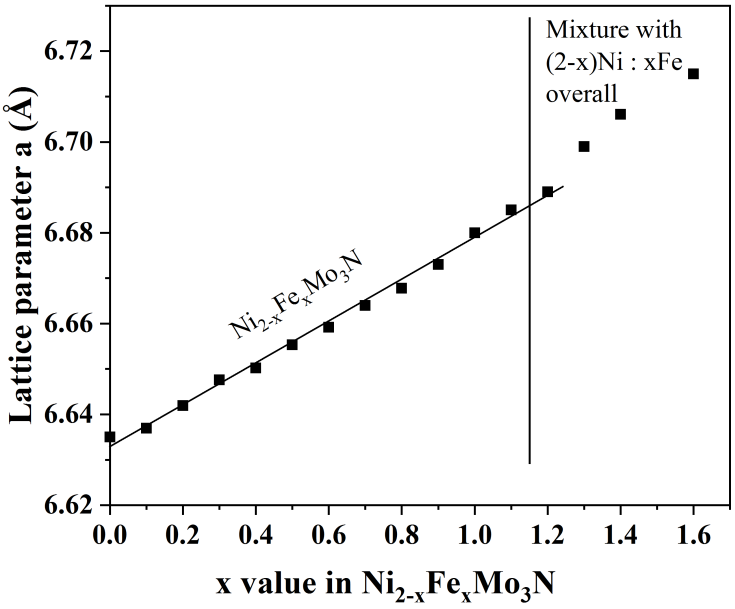

Figure 4-6 Lattice parameters obtained by Rietveld refinement versus the concentration of Fe in the $Ni_{2-x}Fe_xMo_3N$ system.

4.5 Thermogravimetric analysis

The thermal behaviour of the Fe doped Ni_2Mo_3N (x = 0, 0.1, 0.2 and 0.3) was measured using thermogravimetric analysis (TGA) during the oxidation process. Figure 4-7 illustrates two step mass gains upon heating the materials under 50 cm^3 min^{-1} of flowing oxygen/argon at ramp rate of 10 ºC/ min from room temperature to 700 °C. TGA curves showed that all the doped samples were thermally stable up to around *ca*. 400 °C. Further increasing temperature leads to gradual mass increase up to *ca.* 500 °C followed by a sharp increase. On heating further, there is a sharp mass loss up to around 750 °C not shown in Figure 4-7, which could correspond to the MoO_3 evaporation. The mass gains for the iron-doped compositions were consistent with expected values. The TGA data during oxidation showed the expected mass gains Table 4-4, with thermal stability decreasing with concentration of the second metal, similarly to the $(Ni, Cu)_2Mo_3N$ system. PXRD diffraction was carried out on the $Ni_{1.6}Fe_{0.4}Mo_3N$ sample after TGA Figure 4-8.

$$Ni_{1.6}Fe_{0.4}Mo_3N + \frac{11}{2}O_2 \rightarrow 2Ni_{0.8}Fe_{0.2}MoO_4 + MoO_3 + \frac{1}{2}\,N_2 \qquad \text{Equation 4-1}$$

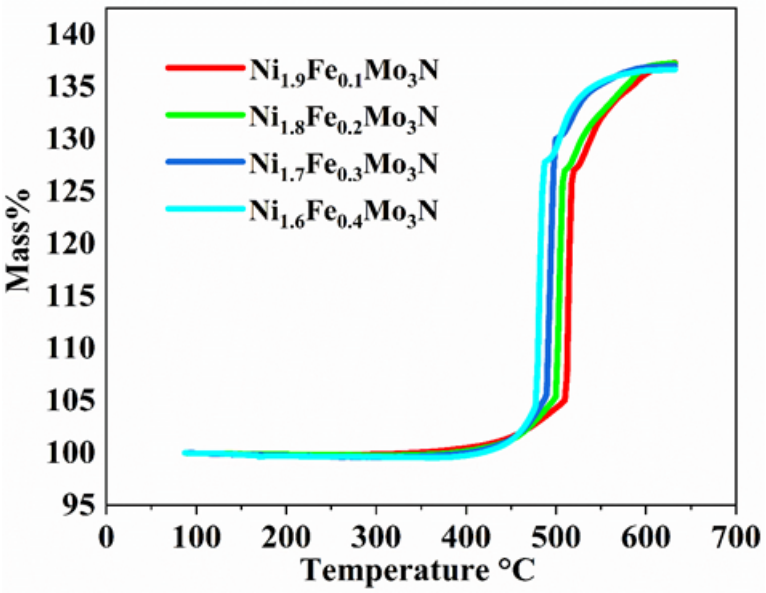

Figure 4-7 Thermogravimetric analysis curves under oxygen atmosphere for the different Fe contents $Ni_{2-x}Fe_xMo_3N$ (x = 0, 0.1, 0.2 and 0.5) samples with the heating rate of 10 °C /min from room temperature to 700 °C. The initial weight of every sample before measurement is 0.015 g.

Table 4-4 Mass % of various oxides formed from TGA of the resulting composites.

Composition	Overall Mass Gain Observed/%	Expected Mass Gain/ %
Ni_2Mo_3N	38.43	38.63
$Ni_{1.9}Fe_{0.1}Mo_3N$	37.45	38.61
$Ni_{1.8}Fe_{0.2}Mo_3N$	37.59	38.68
$Ni_{1.7}Fe_{0.3}Mo_3N$	37.13	38.71
$Ni_{1.6}Fe_{0.4}Mo_3N$	38.14	38.74

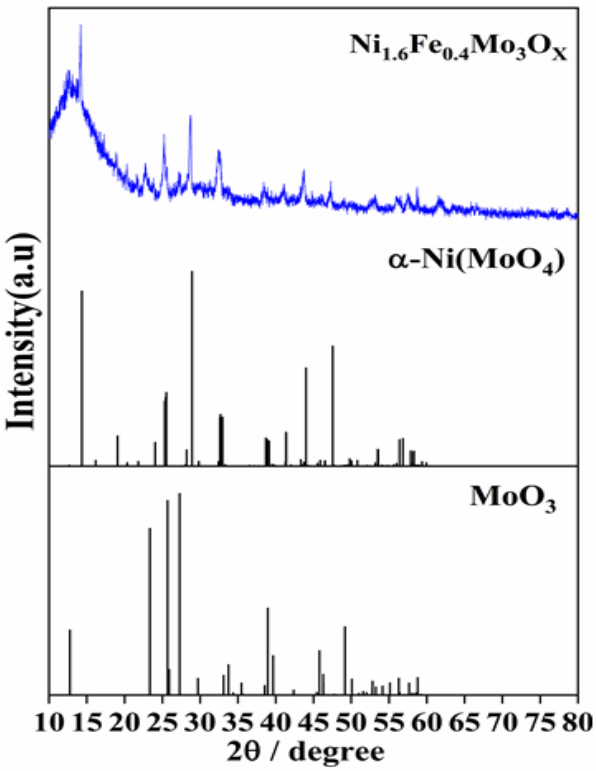

Figure 4-8 Powder XRD patterns of the products of heating $Ni_{1.6}Fe_{0.4}Mo_3N$ in the TGA to 700 °C in 50% O_2 / 50 % Ar.

4.6 SEM and EDX analysis

Scanning electron microscopy (SEM) combined with energy dispersive X-ray spectroscopy (EDX) was used to analyse morphology and chemical composition for the $Ni_{2-x}Fe_xMo_3N$. Figure 4-9 (a), (b) and (c) illustrates representative SEM micrographs for the $Ni_{1.9}Fe_{0.1}Mo_3N$, $Ni_{1.5}Fe_{0.5}Mo_3N$ and $Ni_{1.2}Fe_{0.8}Mo_3N$, respectively. It can be seen that the morphology of the selected materials is similar to that of Ni_2Mo_3N in section 3.6. Furthermore, the material comprises of agglomerated particles.

EDX analysis was performed on the $Ni_{1.9}Fe_{0.1}Mo_3N$, $Ni_{1.7}Fe_{0.3}Mo_3N$, $Ni_{1.5}Fe_{0.5}Mo_3N$ and $Ni_{1.2}Fe_{0.8}Mo_3N$ and the data are listed in Table 4-5. The atomic percentage data of Ni, Fe and Mo was found to be close to the theoretical values. By combining the results of EDX along with PXRD and microanalysis data, it can be concluded that all metals have been successfully incorporated into the filled β-Mn lattice structure in compositions in the range $NiFeMo_3N$.

Table 4-5 The atom % of the Fe-doped Ni_2Mo_3N 900 °C samples evaluated by EDX analysis.

Element	$Ni_{1.9}Fe_{0.1}Mo_3N$		$Ni_{1.7}Fe_{0.3}Mo_3N$		$Ni_{1.5}Fe_{0.5}Mo_3N$		$Ni_{1.2}Fe_{0.8}Mo_3N$	
	Calculated	Actual	Calculated	Actual	Calculated	Actual	Calculated	Actual
Ni	38	36	34	31.6	30	27.5	24	20
Fe	2	0.8	6	5	10	8.6	16	14
Mo	60	63	60	64	60	63	60	61

The TEM image of a prepared nanocrystal $Ni_{1.7}Fe_{0.3}Mo_3N$ sample is shown in Figure 4-9(d). From TEM results, it can be seen that the samples are in the diameters ranging from 178-288 nm. TEM measurements suggest the formation of much larger particles than calculated by the use of the Scherrer equation, this could be due to larger particles consisting of many smaller crystalline particles. Agglomerates of aggregated particles are observable in the TEM images.

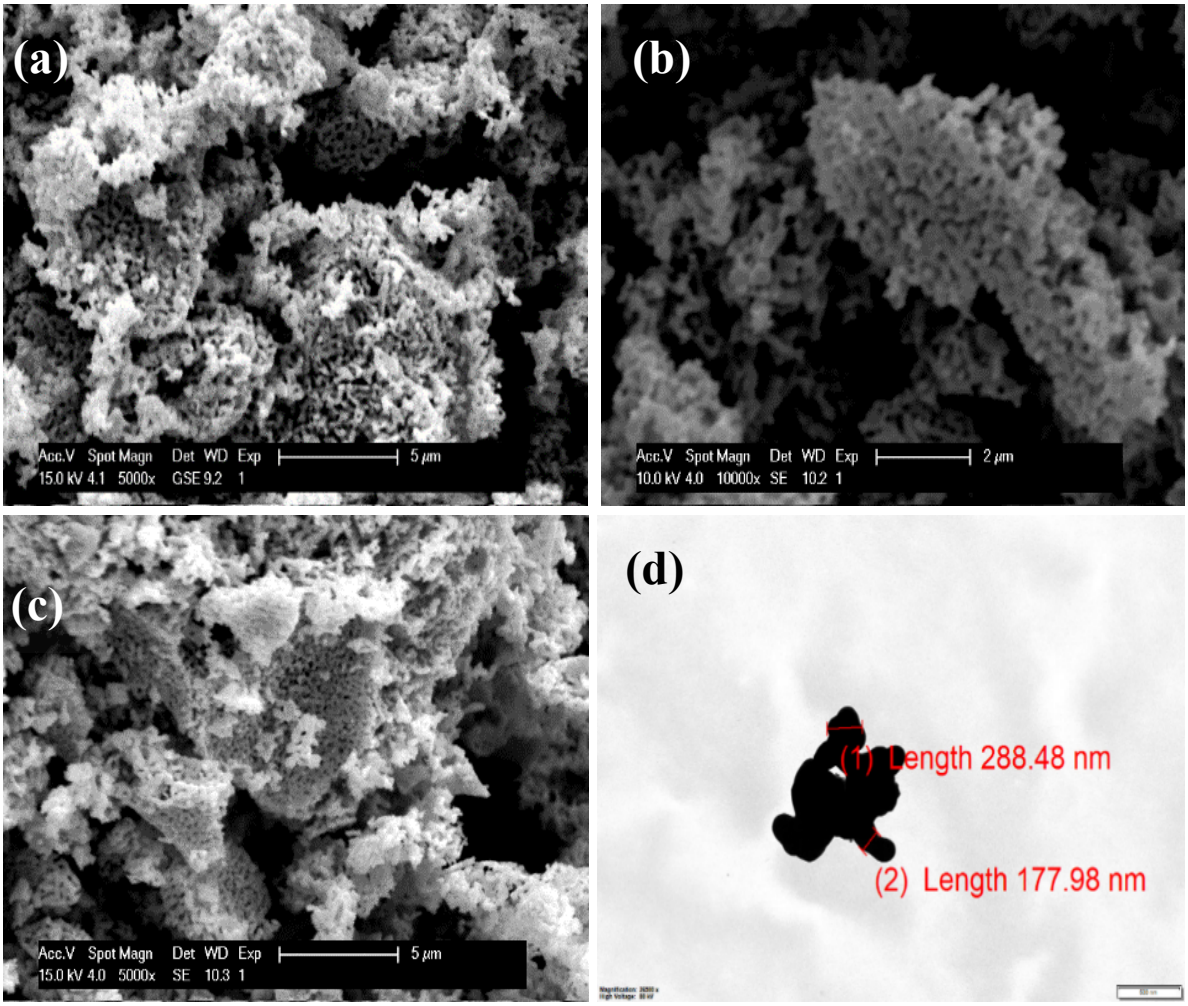

Figure 4-9 SEM images (a), (b) and (c) of $Ni_{1.9}Fe_{0.1}Mo_3N$, $Ni_{1.5}Fe_{0.5}Mo_3N$ and $Ni_{1.2}Fe_{0.8}Mo_3N$, respectively. TEM images of the fresh $Ni_{1.7}Fe_{0.3}Mo_3N$ catalyst is shown in (d).

4.7 Catalytic performance

The materials were investigated under the same reaction conditions used for copper doped samples (chapter 3). The ammonia synthesis production rates for the prepared samples versus time/min are shown in Figure 4-10.

The results of the performance over each sample in $(Ni,Fe)_2Mo_3N$ showed that the reaction conditions were important. Even after activation at 700 °C, the samples have low NH_3 synthesis activity at 400 °C, even upon several h on steam. However, further heating to 500 °C resulted in significant improvement of ammonia production rates. From the reaction profiles Figure 4-10, it is apparent that no deactivation was observed. Ammonia production rates for $Ni_{1.8}Fe_{0.2}Mo_3N$ were calculated from the reaction conductivity profiles as 116 and 311 μmol g^{-1} h^{-1} at 400 and 500 °C, respectively Figure 4-11.

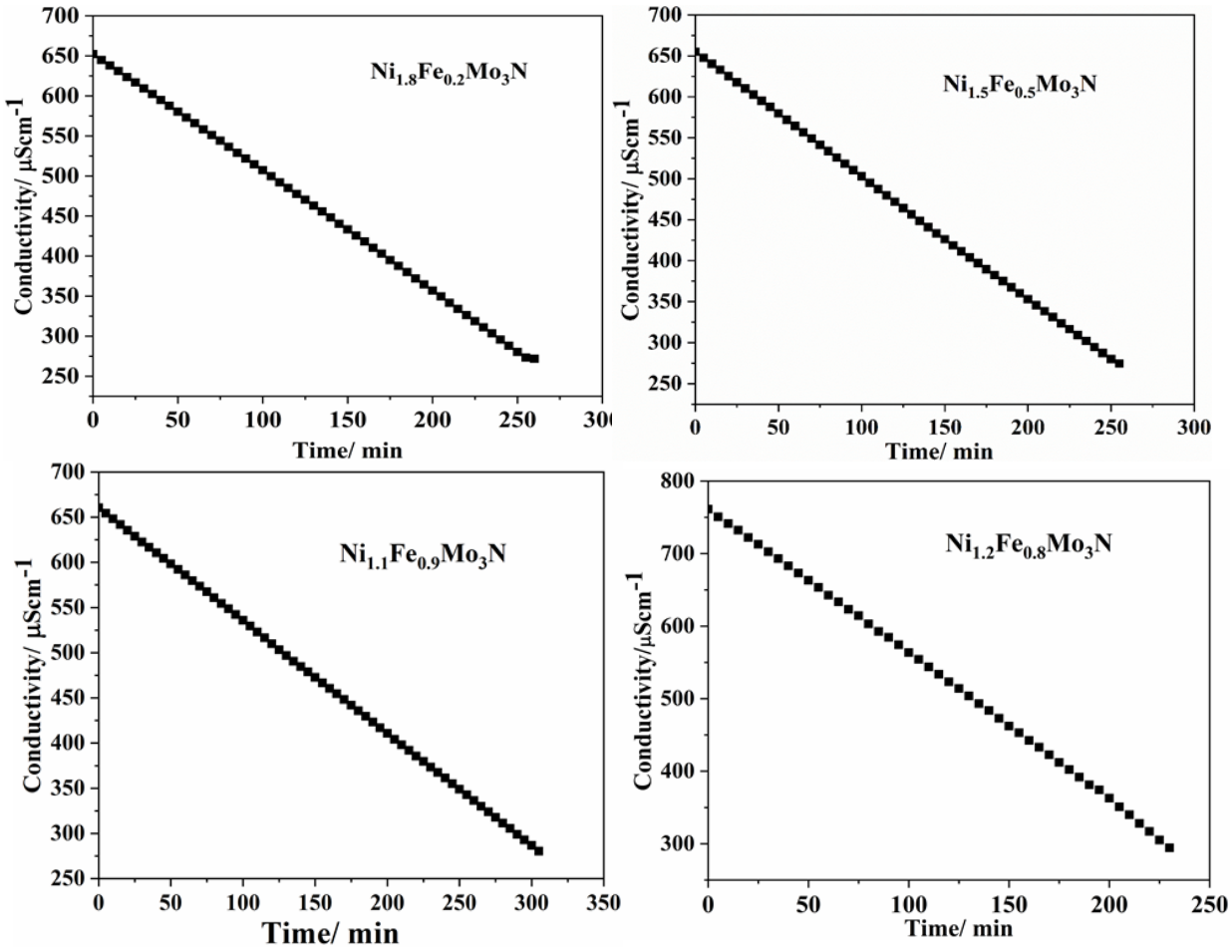

Figure 4-10 Conductivity of the $(Ni, Fe)_2Mo_3N$ acid scrubber placed after heated at 400 and 500 °C under 75 vol % H_2 in N_2 (BOC, 99.98 %).

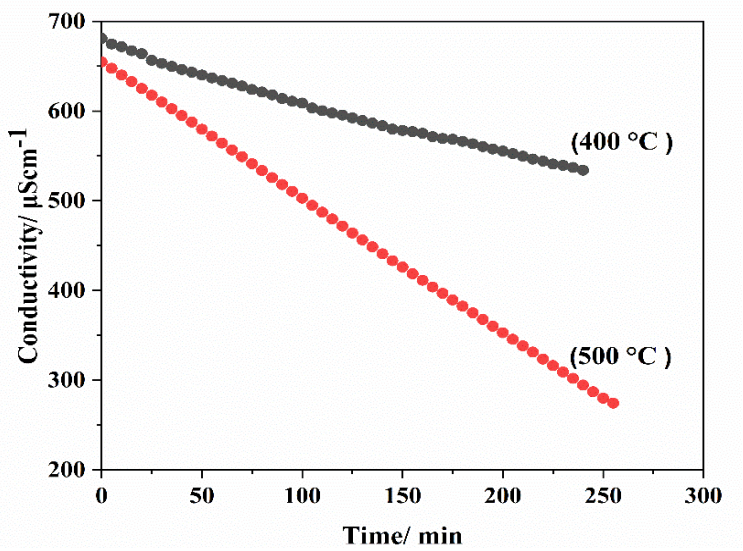

Figure 4-11 Conductivity of the $Ni_{1.8}Fe_{0.2}Mo_3N$ acid scrubber placed after heated at 400 and 500 °C under 75 vol % H_2 in N_2 (BOC, 99.98 %).

Table 4-6 BET surface areas and ammonia synthesis rate and specific activity of $Ni_{2-x}Fe_xMo_3N$.

composition	Surface area (m^2 g^{-1})	Ammonia synthesis rate at 500 °C (µmol h^{-1} g^{-1})	Specific activity at 500 °C (µmol h^{-1} m^{-2})
Ni_2Mo_3N	2.2	272(5)	124(2)
$Ni_{1.8}Fe_{0.2}Mo_3N$	2.4	311(2)	130(1)
$Ni_{1.5}Fe_{0.5}Mo_3N$	2.5	322(2)	129(1)
$Ni_{1.2}Fe_{0.8}Mo_3N$	2.7	337(4)	125(1)
$Ni_{1.1}Fe_{0.9}Mo_3N$	2.8	354(4)	126(2)

Table 4-6 shows a summary of the BET surface area and ammonia production rates. Efficacy of a series of catalysts of $Ni_{2-x}Fe_xMo_3N$ (x = 0, 0.2, 0.5, 0.8 and 0.9) was examined for the formation of ammonia. All of the synthesized catalysts exhibited high catalytic performance for this reaction. Therefore, 500 °C is considered as an optimal catalytic ammonia synthesis temperature in the present work. This is in contrast to 400 °C, which has been usually used previously.[83, 37, 182]

The BET surface areas of the Fe-doped samples were acquired by N_2 adsorption. The addition of iron as a dopant into Ni_2Mo_3N lattice increased surface areas of the samples gradually even with such low iron loadings as low as x = 0.1, while Ni_2Mo_3N as a single nitride has a low surface area. It could be related to the decreased crystallite and particle size due to distribution of iron dopant in Ni_2Mo_3N. Generally, the obtained iron doped samples had low surface areas values below 5 nm. This could be attributed to the thermal effect during ammonolysis process as the materials were heated at higher annealing temperatures.

BET surface areas of the catalysts along with transition metal dopant contents were also shown to be another important contributing factor to the catalytic properties. For iron doped samples as mentioned above the addition of iron leads to a linear increase of the surface area with increasing iron content. Table 4-6 shows the corresponding values of the investigated catalysts. It is noteworthy that the catalytic activity rates of these materials are substantially improved which is likely due to increasing both the surface area and iron content of the catalysts, suggesting a positive influence of the iron incorporation. Among the tested catalysts, the maximum surface area value was shown by $Ni_{1.1}Fe_{0.9}Mo_3N$ and the same catalyst gave the highest activity of around 354(4) μmol g^{-1} h^{-1}. These results clearly indicate that the surface area of the investigated catalysts is the key parameter for the catalytic activity behaviour. Activities for Ni_2Mo_3N and doped analogues are typically lower despite the structural and electronic similarities between these two systems, and that may be linked at least partly to the lack of lattice nitrogen mobility exhibited by this compound.[42] Activities observed here are significantly higher than those observed in many other studies of this material and were seen to increase with iron doping, although our activities were measured at 500 °C due to a relatively low activity observed at 400 °C (Figure 4-10).

In addition, it has been reported the lattice N in η-carbide Fe_3Mo_3N structure is less reactive than that of its cobalt counterpart.[78] $Co_{3-x}Fe_xMo_3N$ quaternary systems have been investigated for ammonia synthesis. The results showed that the catalytic activity of these materials were between that of Co_3Mo_3N and Fe_3Mo_3N.[196]

The pre and post catalysis nitrogen contents were measured from CHN combustion analysis, theoretical atomic percentages for the content of nitrogen in $Ni_{2-x}Fe_xMo_3N$ were calculated and compared with the experimental ones and the main results are summarized in Table 4- 7. As shown in Table 4-7 the nitrogen contents in the samples are approximately consistent with the calculated values. The nitrogen content in Ni_2Mo_3N sample is 3.4 wt % and this is consistent with the previously published literature.[40] For the $Ni_{1.5}Fe_{0.5}Mo_3N$ the nitrogen content is about 3.35 wt % which is consistent with the reported value.[189] The results in each case indicate the full occupancy of the 4a interstitial site by nitrogen. In addition, the overall agreement between theoretical and experimental data, together with PXRD data, confirm the generation of ($Ni_{2-x}Fe_xMo_3N$) series. The nitrogen contents of the post-catalysis samples also remain consistent with the stoichiometric compositions.

Table 4-7 Chemical analysis data for $Ni_{2-x}Fe_xMo_3N$

Catalyst	Nitrogen content (wt.%)		
	Calculated	**Pre-catalysis**	**Post-catalysis**
Ni_2Mo_3N	3.3	3.4	3.3
$Ni_{1.8}Fe_{0.2}Mo_3N$	3.4	3.5	3.4
$Ni_{1.5}Fe_{0.5}Mo_3N$	3.4	3.5	3.4
$Ni_{1.2}Fe_{0.8}Mo_3N$	3.4	3.6	3.4
$Ni_{1.1}Fe_{0.9}Mo_3N$	3.4	3.6	3.2

% C and % H < 0.10 throughout

Figure 4-12 presents the PXRD powder diffraction patterns on the as-prepared materials and post-reaction materials. As shown above, the as-prepared materials had a phase pure match to the filled β-manganese structure with space group $P4_132$. Post reaction XRD analysis showed that the filled β-manganese structure was maintained upon reaction in all the investigated materials. In addition to the linear conductivity changes observed in the catalysis, this suggests that the catalysts are stable under the reaction conditions used. The reaction rates, obtained in this study, is higher than other reported iron-based nitride materials. Substituting iron into the Ni_2Mo_3N lattice can improve the catalytic activity.

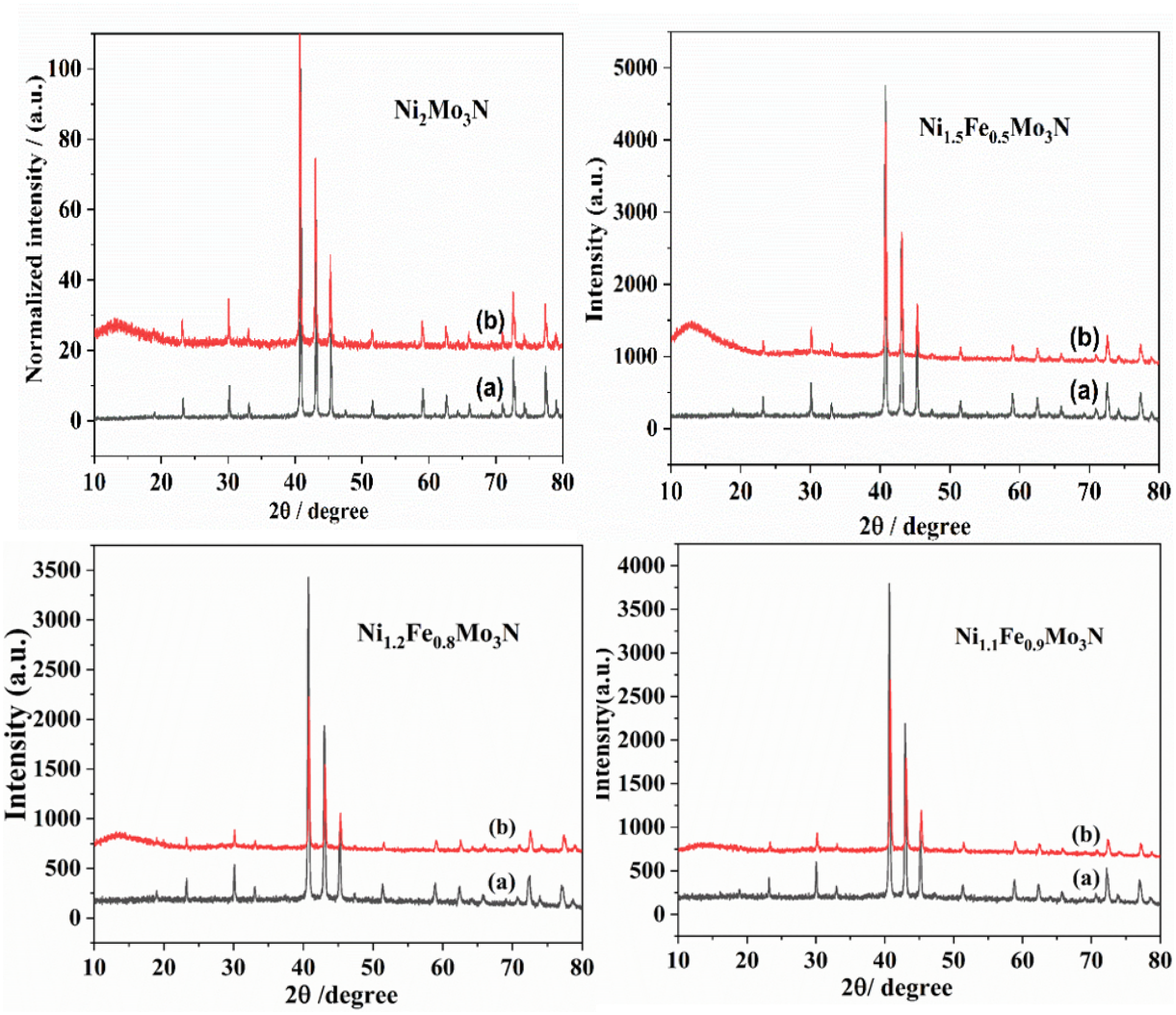

Figure 4-12 PXRD diffraction patterns of (a) pre-reaction and (b) post-reaction of Ni_2Mo_3N, $Ni_{1.5}Fe_{0.5}Mo_3N$, $Ni_{1.2}Fe_{0.8}Mo_3N$ and $Ni_{1.1}Fe_{0.9}Mo_3N$.

4.8 Conclusion

Pechini method along with high temperature ammonolysis reaction have shown to be promising routes for developing catalytically active materials. In this study results from PXRD patterns and CHN microanalysis confirmed that $Ni_{2-x}Fe_xMo_3N$ were successfully prepared. In addition, all samples matched the cubic structure with space group $P4_132$. The refined lattice parameters were found to increase linearly as further iron is doped into the structure. Further to this, the same trend was observed for the surface area of the catalysts. The $Ni_{2-x}Fe_xMo_3N$ with x = 0.2, 0.5, 0.8 and 0.9 showed good activity towards ammonia synthesis.

Chapter 5 Synthesis, Structural Characterisation and Ammonia Synthesis Activity of W-substituted Ni_2Mo_3N and Co_3Mo_3N

Overview

A series of nickel tungsten molybdenum nitride and cobalt tungsten molybdenum nitride materials were developed and investigated for ammonia synthesis; their structures and activity were compared.

5.1 Introduction

Tungsten mono carbide was first explored as a potential catalyst by Levy and Boudart, which subsequently led to the development of many binary nitride catalysts based on molybdenum and tungsten.[197] Tungsten nitride based materials have been attracting much attention as their properties show a close resemblance to those of platinum metal catalysts. Factors influencing the properties of tungsten materials include the nature of dopant and the synthesis routes used, as those factors have a strong impact on the material's microstructure and impurity levels. Binary tungsten nitrides have shown promising performance for CO hydrogenation and NO reduction with H_2.[198] However, it has been found that the synthesis of interstitial tungsten nitride materials was a challenge, as the inclusion of nitrogen into the tungsten lattice structure under ambient pressure is thermodynamically unfavourable.[199] A wide variety of techniques were adopted for producing tungsten nitride materials with the desired properties. One of the commonly used routes is ammonolysis, which has been widely employed for the preparation of tungsten nitride-based materials. A comparative chart of synthesis methods to tungsten nitrides carried out by various authors has been tabulated Table 5-1.

Panda *et al*. synthesised W_2N bulk nitride with high surface area through nitridation of oxide precursors WO_3 prepared *via* the precipitation method. In this study the oxide precursors were obtained by three different methods including commercial WO_3, acid route and the citrate sol gel method.[200] In the acid route, the solution of $Na_2WO_4{\cdot}2H_2O$ was mixed with dilute HNO_3 in H_2O, which was then heated while stirring. The precipitate was filtered and dried under air. This dried powder was used in the nitridation reaction. Similar results have

been reported by Kim *et al* who prepared β-W_2N from high surface area sol-gel derived WO_3 *via* temperature programmed reduction-nitridation.[201] In another study, β-W_2N was synthesised by the temperature programmed reduction-nitridation of the oxide precursor WO_3.[200] Choi *et al*. reported the synthesis of WN from tungsten hexachloride (WCl_6) as a precursor and $CHCl_3$ as a solvent via low temperature process.[202] The formation of ternary NiWN and CoWN *via* NH_3 treatment of nickel and cobalt tungsten molybdate precursors has been reported by Rico *et al*.[79] In this study the oxide precursors were prepared using thermal reaction. Commercial tungsten oxides containing Mn, Ni, and Co were applied as the precursors and then converted into their nitride counterparts by ammonolysis at low temperature.[79] The ternary nitride, $FeWN_2$, has been prepared by Bem *et al*. *via* ammonolysis of $FeWO_4$ which was prepared by co-precipitation and solid state reaction.[100] Weil and Kumta prepared Co_3W_3N *via* the ammonolysis of the oxide precursors.[93] The precursor was prepared by the addition of triethylamine to cobalt chloride. Fe_3W_3N was subsequently prepared by the same group using a similar method to rapidly precipitate a homogenous mixture of iron from solution.[203] Previous studies have focused on the preparation and investigations of binary and ternary tungsten nitrides. The $(Fe_{0.8}W_{0.2})WN_2$ material obtained from the oxide precursor $Fe_2(WO_4)_3$ was prepared *via* a facile aqueous precipitation technique.[204] High surface area Co–W–N has been prepared by nitriding the oxide precursor $CoWO_4$ derived from a precipitation method.[200] In this work quaternary cobalt and nickel tungsten molybdenum nitride catalysts were obtained by the ammonolysis of metal oxide precursors using a citrate sol-gel method.

Table 5-1 Reported synthesis routes to tungsten nitride materials including starting materials, solvents, reaction and sintering conditions, and structures.

Product description	Method	Starting materials	Reaction conditions	Sintering conditions (Time & gas)	Ref
$(Fe_{0.8}W_{0.2})WN_2$ Hexagonal	Co-precipitation	$FeCl_2$ + $Na_2WO_4 \cdot 2H_2O$/ Acetic acid	Stirring for 1 h, dry overnight.	700 °C, 69 h, NH_3	204
$FeWN_2$ layered hexagonal	Co-precipitation	$FeCl_2$ + $Na_2WO_4 \cdot 2H_2O$	Stirring for 1 h, dry at 150 °C for 24 h. 700 ºC / He	700 °C, 12 h, NH_3	100
$FeWN_2$ layered hexagonal	Solid state	Fe + Fe_2O_3+ WO_3	900 °C for 48 h, 5 °C/min,	700 °C, 12 °h, NH_3	100
β-W_2N Bulk, Cubic phase unheated gel 79.53 m^2/g Heated gel 68.92 m^2/g	Sol-gel / (TPR)	Tungstic acid (H_2WO_4) H_2O: methanol = 1: 1	80 °C / Aging for 24 h / dried at 110 ºC 500 °C / 5 h.	NH_3, 100 $cm^3\ min^{-1}$ 670-700 °C, 1.0 ºC/min	201
β-W_2N Bulk, 55 m^2/g	Acid route	$Na_2WO_4 \cdot 2H_2O$ H_2O: HNO_3 = 1: 5	Boiling while stirring for 30 min, RT stirring for 6 h. 90 °C air.	600 -700 °C, 3 ºC/min, NH_3	200

β-W_2N Bulk, 60 m^2/g	Sol-gel / (TPR)	$H_{26}N_6O_{41}W_{12}$ Citric acid, H_2O	80 °C for 1 h, 90 °C for 4 days, air, 200 -500 °C for 1 h.	600 -700 °C, 3 °C/min, NH_3	200
Co–W–N Bulk, 40 m^2/g	Co-precipitation	$Na_2WO_4 \cdot 2H_2O$, + $Co(NO_3)_2 \cdot 6H_2O$	Dry at 90 °C for 1 h in air.	700 °C, 5 C/min, NH_3	200
W_2N Nanostructured Hexagonal	Temperature-programmed nitridation (TPN)	WO_3	-	350 °C for 30 min, 350 °C to 450 °C at 0.5 /min, 450 °C to 700 °C at a rate of 1.25 °C /min for 2 h, NH_3	200
Fe_3W_3N Cubic	Ammonolysis	$FeCl_3$ + WCl_6 Triethylamine anhydrous acetonitrile	Dry under vacuum	(3 K min^{-1}), 1223 K, 4 h, NH_3	203
Co_3W_3N Cubic	ammonolysis	$CoCl_2$+ WCl_6 Triethylamine anhydrous acetonitrile	Dry under vacuum at 120 °C for 12 h.	950°C, 4h, NH_3	93
Ni_2W_3N+ Ni Cubic	Co-precipitation Ammonolysis	$NiCl_2$+ $Na_2WO_4 \cdot 2H_2O$	Dry in air at 100 °C for 12 h.	725 °C, 12 h, NH_3	103
CoWN 7.5 m^2/g	Hydrothermal	$Na_2WO_4 \cdot 2H_2O$ + $Co(NO_3)_2 \cdot 6H_2O$	110 °C for 15 h, Dry at 110 °C for 12 hr, calcined at 500 °C for 5 h in air.	358 °C at 5 °C/min, then at 0.5 °C/min to 448 °C, 785 °C, 2 °C/min for 2.5 h	79

NiWN 6.5 m^2/g	Hydrothermal	$Na_2WO_4 \cdot 2H_2O$+ $Ni(NO_3)_2 \cdot 2H_2O$	110 °C for 15 h, at 110 °C for 12 hr, calcined at 500 °C for 5 h in air.	358 °C at 5 °C/min, then at 0.5 °C /min to 448 °C and finally to 785 °C at 2 °C/min for 2.5 h, in NH_3	79
WN	Ammonolysis	Anhydrous WCL_6	NH_3 for 10 h, 10 h, NH_3	675 °C, 10 h, NH_3	202
Nanostructured Hexagonal	Ammonolysis	$CHCl_3$	NH_3 for 10 h, 10 h, NH_3	675 °C, 10 h, NH_3	202
$MnWN_2$ Hexagonal	Co-precipitation Ammonolysis	$MnCl_2$+ $Na_2WO_4 \cdot 2H_2O$	150 °C, 24 h	700 °C, 14 h, NH_3 (120 cm^3 min^{-1})	188
$CoWN_2$ Hexagonal	Co-precipitation Ammonolysis	$CoCl_2$+ $Na_2WO_4 \cdot 2H_2O$	150 °C, 24 h	600 °C, 20 h, NH_3	188
$FeWN_2$ Hexagonal	Co-precipitation Ammonolysis	$FeCl_2$+ $Na_2WO_4 \cdot 2H_2O$	150 °C, 24 h	700 °C, 15 h, NH_3	188
$NiWN_2$ / Hexagonal	Co-precipitation Ammonolysis	$NiCl_2$+ $Na_2WO_4 \cdot 2H_2O$	150 °C, 24 h	600 °C, 20 h, NH_3	188

5.2 Experimental section

5.2.1 Synthesis of $Ni_2W_xMo_{3-x}N$ and $Co_3W_xMo_{3-x}N$ compositions

The raw materials were commercial chemicals used without further purification. A series of molybdenum-based metal oxide precursors containing transition metals (W, Ni, Co) were prepared as starting materials for the formation of the quaternary nitrides Ni-W-Mo-N with the filled β-Mn structure and Co–W–Mo–N with the η carbide structure. A broad range of W/Mo ratios were prepared following the methodology described in the previous chapters expect that $(NH_4)_6H_2W_{12}O_{40}{\cdot}4H_2O$ (Sigma Aldrich, 99 %) and Co $(NO_3)_2{\cdot}6H_2O$ (Sigma Aldrich, ≥ 98 %) were used as dopant sources for tungsten and cobalt, respectively. Moreover, the nanostructured $Ni_2W_xMo_{3-x}N$ based precursors were subjected to ammonolysis at 800 °C under NH_3 for 12 h. In order to study the effect of the inclusion of tungsten into the η-carbide structured Co_3Mo_3N on ammonia synthesis performance a series of nanostructured $Co_3W_xMo_{3-x}N$ (x = 0, 0.1, 0.2, 0.3, 0.4, 0.5, 0.6, 0.7, 0.8 and 0.9) solid solutions were synthesised using a similar procedure to that described above. In this experiment the nickel source Ni $(NO_3)_2{\cdot}6H_2O$ (Sigma Aldrich, 99.9 %) was replaced by cobalt nitrate Co $(NO_3)_2{\cdot}6H_2O$ (Sigma Aldrich, ≥ 98 %) as a source for cobalt. Unlike the filled β-Mn structured $Ni_2W_xMo_{3-x}N$, the η-carbide structured $Co_3W_xMo_{3-x}N$ system was found to be highly impure at 800 °C. Therefore, the $Co_3W_xMo_{3-x}N$ derived oxide precursors were ammonolysed at 900 °C instead of 800 °C. The quantities and the ratios of reagents for the different compositions are given in Table 5-2. A Schematic representation of the optimised citrate sol-gel route pathway is given in Figure 5-1.

Table 5-2 Quantities of reagents used in the synthesis of $Ni_2W_xMo_{3-x}N$ and $Co_3W_xMo_{3-x}N$

x in $Ni_2W_xMo_{3-x}N$	$(NH_4)_6Mo_7O_{24}\cdot 4H_2O$	$(NH_4)_6H_2W_{12}O_{40}\cdot 4H_2O$	$Ni(NO_3)_2\cdot 6H_2O$	Citric acid monohydrate
0.1	2.9 g / 2.35 mmol	0.142 g / 0.047mmol	3.294 g/ 11.33 mmol	7.94 g / 37.8 mmol
0.2	2.8 g /2.23 mmol	0.29 g / 0.049 mmol		
0.3	2.7 g / 2.17 mmol	0.43 g / 0.14 mmol		
0.4	2.6 g / 0.93 mmol	0.57 g / 0.19 mmol		
0.5	2.5 g / 2.013 mmol	0.71 g / 0.23 mmol		
0.6	2.4 g /1.932 mmol	0.85 g / 0.28 mmol		
x in $Co_3W_xMo_{3-x}N$	$(NH_4)_6Mo_7O_{24}\cdot 4H_2O$	$(NH_4)_6H_2W_{12}O_{40}\cdot 4H_2O$	$Co(NO_3)_2\cdot 6H_2O$	Citric acid monohydrate
0.1	1.93 g / 1.56 mmol	0.095 g / 0.03 mmol	3.297 g / 11.27 mmol	7.94 g / 37.8 mmol
0.2	1.86 g / 1.51 mmol	0.19 g / 0.06 mmol		
0.3	1.79 g / 1.45 mmol	0.29 g / 0.09 mmol		
0.4	1.73 g / 1.39 mmol	0.38 g / 0.13 mmol		
0.5	1.66 g / 1.35 mmol	0.48 g / 0.16 mmol		
0.6	1.59 g / 1.29 mmol	0.57 g / 0.19 mmol		
0.7	1.53 g / 1.24 mmol	0.67 g / 0.22 mmol		
0.8	1.46 g / 1.18 mmol	0.76 g / 0.25 mmol		
0.9	1.4 g / 1.13 mmol	0.86 g / 0.28 mmol		
1.0	1.33 g / 0.97 mmol	0.95 g / 0.31 mmol		
1.1	1.2 g / 0.54 mmol	1.14 g / 0.38 mmol		

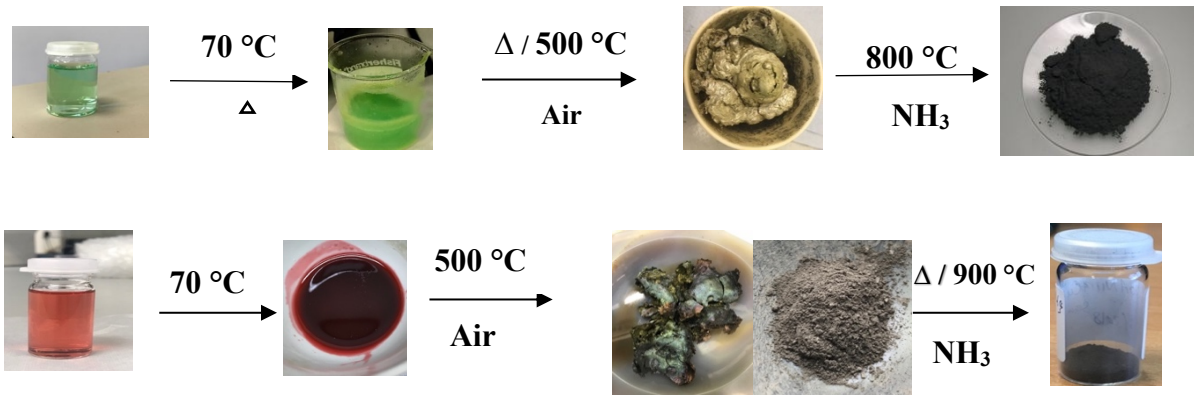

Figure 5-1 Schematic description of the citrate-gel process to produce the filled β-manganese ($Ni_2W_xMo_{3-x}N$) represented in the top scheme. From left to right: starting solution (green), gel (green) after evaporating, yellowish foams after heat treatment in air at 500 °C, and final fine powder after heating at 800 °C in flowing NH_3. The η carbide ($Co_3W_xMo_{3-x}N$) represented in the bottom scheme. From left to right: starting solution (pink), gel (red) after evaporating, grey foams upon heat treatment at 500 ºC for 2 h in air, and final fine black powder ($Co_3W_xMo_{3-x}N$) after heating at 900 ºC for 12 h.

5.3 Results and discussion

5.3.1 Solubility

Sodium tungstate dihydrate $Na_2WO_4{\cdot}2H_2O$ is a common starting material in the synthesis of tungsten compounds; however, this precursor was not used it in this study because by using the sol-gel modified Pechini route the sodium metal would be retained in the products. In addition, these materials are sensitive to air and moisture making their handling and storage difficult. Ammonium paratungstate $(NH_4)_{10}H_2W_{12}O_{42}{\cdot}4H_2O$, (Sigma Aldrich, 99 %) which has been reported as the main compound used in the formation of tungsten metal powders,[205] and tungstic acid, H_2WO_4,were both initially used as the dopant sources for tungsten *via* the sol-gel modified Pechini method. However, this formed a yellow precipitate of tungstic acid. Further attempts were made to obtain a homogenous aqueous solution by using ammonium metatungstate salt $(NH_4)_6H_2W_{12}O_{40}{\cdot}4H_2O$ which is highly soluble, and no precipitation occurred. Therefore, this compound was selected to be used as a raw material in the present study.

5.4 Crystal structure and composition

5.4.1 Quaternary nitrides – nickel tungsten molybdenum nitride

The X-ray diffraction patterns of the nanostructured doped $Ni_2W_xMo_{3-x}N$ (x = 0, 0.1, 0.2, 0.3, 0.4, 0.5 and 0.7) samples which underwent ammonolysis at 800 °C are presented in Figure 5-2. The PXRD patterns of the obtained samples confirmed that the main material formed was a filled β-manganese phase having space group $P4_132$. However, an additional weak peak appeared at $2\theta = 37.5°$, indicating traces of rock salt type Mo_2N analogues present in the parent compound,[168] and its analogue $Ni_2W_xMo_{3-x}N$. As the W content increased beyond $x = 0.3$ into the systems some further small peaks were additionally presented and could not be reliably identified. When the temperature was increased up to 900 °C, pure phase structures were obtained up to $x = 0.5$ and metallic Mo peaks were observed beyond this point. Heating at the higher temperature of 900 °C produced single phase materials, but it was also reduced the surface area. The compositions with low W content are shown in Figure 5-3. The Rietveld refinement of structural models against the XRD data was applied for each sample in the $Ni_2W_xMo_{3-x}N$ series using GSAS,[150,163] Figure 5-4. The position of atoms (x, y, z) in unit cell, the space group, and peak positions (lattice parameters and zero point) were refined. The U_{iso} thermal displacement parameters were refined after the

molybdenum 12d Wyckoff lattice site occupancy was split between two cations, tungsten and molybdenum. Then, the background was modelled by a type 2 function and 3 terms within GSAS. In the final refinement cycle the profile broadening coefficients, L_x and L_Y were refined until the unit cell values become stable. Rietveld refinement fit and the key refined parameters data are given in Figure 5-4 and Table 5-3, respectively. The R-factors obtained from these refinements Table 5-3 confirm that the chosen models gave a good fit to the PXRD data, and hence the conclusion that the structure of the developed compositions can be fitted adequately with the parent $P4_132$ space group. Crystallite size, Table 5-3, was estimated from the Lorentzian broadening component using an adaptation of the Scherrer formula shown in section 2.7.2. It was observed that there was a slight decrease of crystallite size as the tungsten content increases from ($x = 0.0$) up to ($x = 0.3$) Figure 5-3. The reduction of the crystallite size is likely to be because of the addition of tungsten increases the melting point and hence makes sintering slower. The refined lattice parameters "a" of the samples are presented in Table 5-3, where it can be seen that the lattice parameter displayed a linear increase up to $x = 0.3$ at 800 °C (Figure 5-6). Above this tungsten concentration, however, the lattice parameter tended to level off and tungsten could reach its solubility limit. The evolution of the lattice parameters as would be expected due to the substitution of molybdenum ion by the relatively larger tungsten ions in the octahedral site.

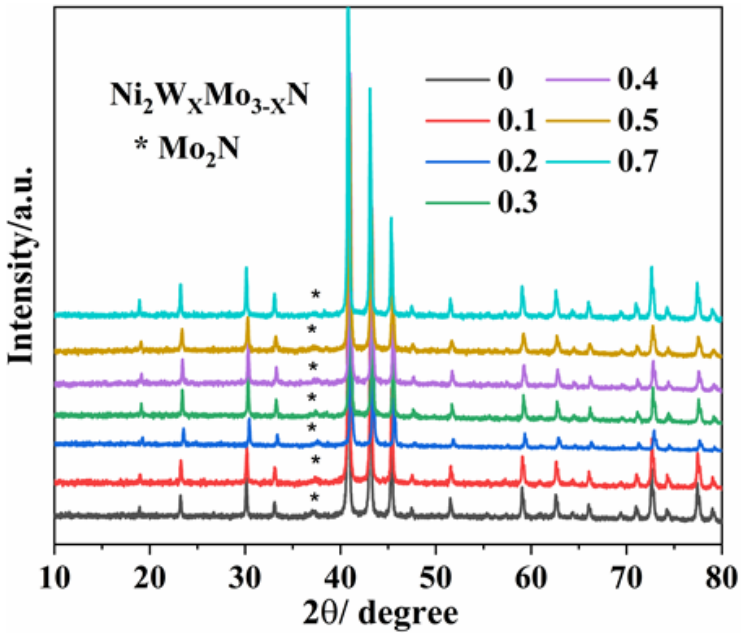

Figure 5-2 Powder XRD patterns for $Ni_2W_xMo_{3-x}N$ samples synthesised by firing the dry powder at 800 °C for 12 h under NH_3 gas. (*) symbol indicates the Mo_2N reflections.

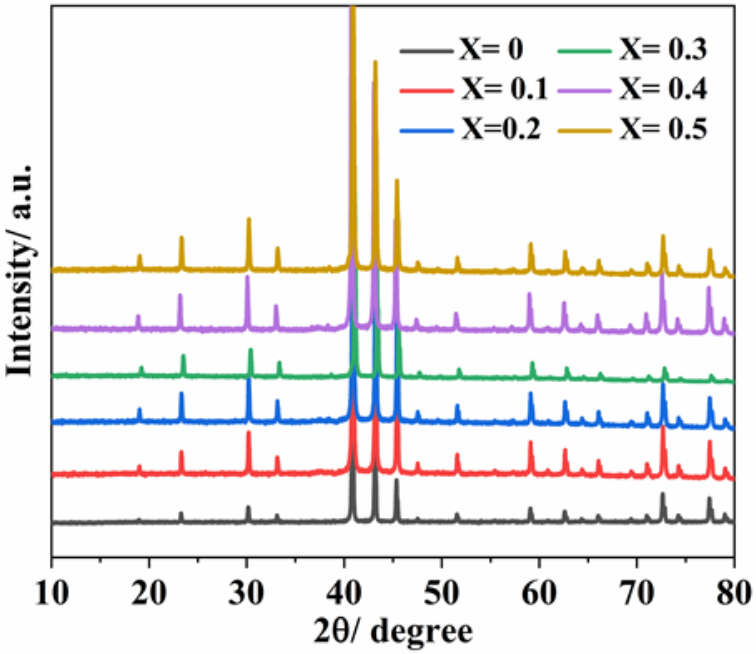

Figure 5-3 Powder XRD patterns for $Ni_2W_xMo_{3-x}N$ samples synthesized by firing the dry powder at 900 °C for 12 h under NH_3 gas.

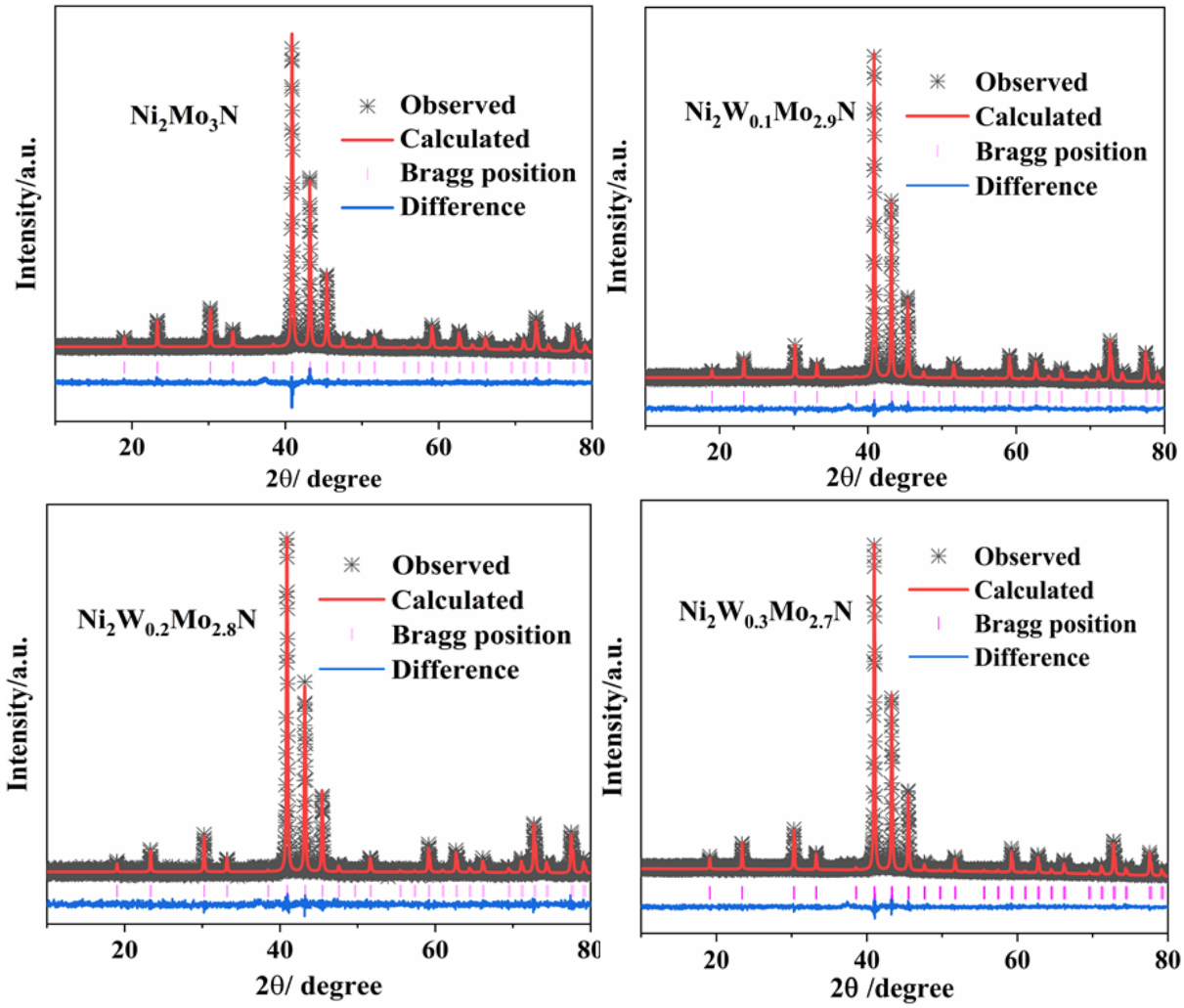

Figure 5-4 Rietveld fits to the XRD patterns of Ni_2Mo_3N (R_{wp} % = 4.9 and R_p % = 3.9), $Ni_2W_{0.1}Mo_{2.9}N$ (R_{wp} % = 4.9 and R_p % = 3.9), $Ni_2W_{0.2}Mo_{2.8}N$ (R_{wp} % = 4.9 and R_p % = 3 .9) and

$Ni_2W_{0.3}Mo_{2.7}N$ (R_{wp} % = 4.9 and R_p % = 3.9). Black crosses mark the data points, the red continuous line the fit and the blue continuous line the difference. Pink tick marks show the positions of the allowed reflections positions for $Ni_2W_xMo_{3-x}N$ series with space group $P4_132$.

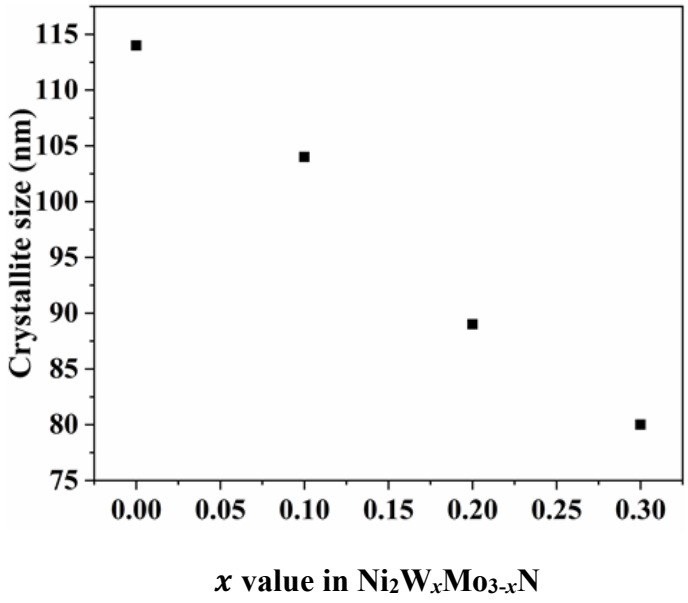

Figure 5-5 Crystallite size as a function of the composition of tungsten doped Ni_2Mo_3N samples, thermally treated at 800 °C for 12 h under NH_3 gas.

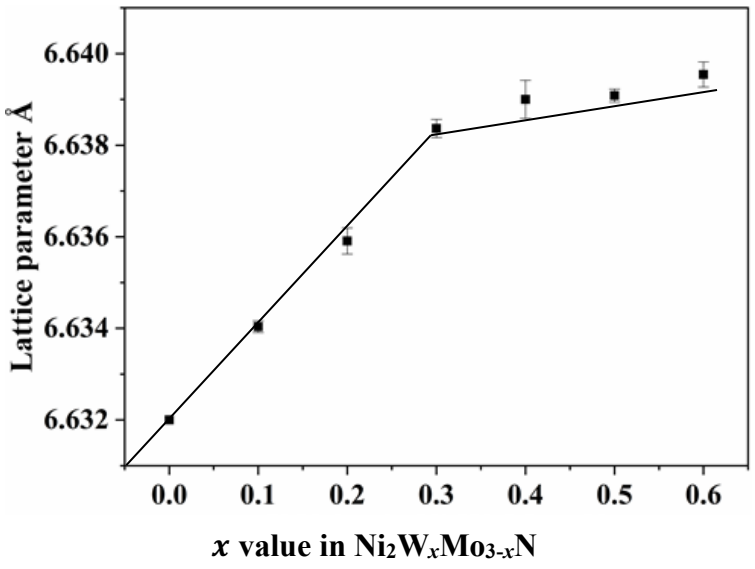

Figure 5-6 The lattice parameter (Å) versus the concentration of W in $Ni_2W_xMo_{3-x}N$ system, thermally treated at 800 °C for 12 h under NH_3 gas.

Table 5-3 Atomic parameter and crystallographic information obtained from Rietveld refinement of $Ni_2W_xMo_{3-x}N$ series.

Composition	**a/Å**	**R_{wp}, R_p/ %**	**Crystallite size/ nm**	**Ni 8c (*x*, *x*, *x*)**		**W/Mo 12 d (1/8, y, z)**			**N 4a 3/8, 3/8,3/8**
				x	**U_{iso}/ Å^2**	**y**	**z**	**U_{iso}/ Å^2**	**U_{iso} / Å^2**
Ni_2Mo_3N	6.632(2)	11.9, 9.24	114(5)	0.067284(3)	0.0674(2)	0.2017(2)	0.4517(2)	0.03105(9)	0.2500
$Ni_2W_{0.1}Mo_{2.9}N$	6.63404(2)	7.3, 5.64	104(9)	0.066204(3)	0.02926(1)	0.2018(2)	0.4518(2)	0.03012(1)	
$Ni_2W_{0.2}Mo_{2.8}N$	6.6359(2)	11.52, 8.83	89(7)	0.067084(5)	0.0144(2)	0.201793 (3)	0.451793(3)	0.01644(1)	
$Ni_2W_{0.3}Mo_{2.7}N$	6.63837(2)	8.22, 6.34	80(3)	0.067536(3)	0.05186(2)	0.201897(2)	0.4519(2)	0.04713(1)	

5.4.2 Ternary nitride- nickel tungsten nitride (Ni_2W_3N)

Ni_2W_3N has been reported previously.[188] It was found that the formation of this phase by precipitation method followed by ammonolysis of $NiWO_4$ at 600 °C have resulted in a material containing nickel metal as impurity. Only three years later, the same approach was applied by the same group using various temperatures ranging from 750 to 800 °C.[103] They found that Ni_2W_3N with a small amount of nickel was obtained at 750 °C. On heating the precursor further in ammonia gas at 800 °C for 12 h a mixture of nickel metal, Ni_2W_3N and NiW_3N was observed. In this study, attempts were made to achieve a single-phase of Ni_2W_3N using a Pechini-type sol−gel ammonolysis method.

Figure 5-7 demonstrates the X-ray diffraction patterns of the resulting materials fired in ammonia at various temperatures. On heating the precursor at 750 °C for 12 h a mixture of Ni_2W_3N and cubic phase W (PDF no. 04-0806) with a small amount of cubic phase Ni metal (PDF no. 65-0380) peaks was detected. Furthermore, small shoulder peaks were presented at about $2\theta = 69^{o}$ and 74^{o}. Heating at 800 °C for 12 h increased the amount of surface impurity phases. Heat treatment up to 900 °C for 12 h led to excluding of W impurity peaks, as well as additional peaks which can be ascribed/ can therefore be ascribed to NiW_3N were detectable, Ni metal was still seen as shown in Figure 5-7. This indicates that the sample is unstable and decomposes at elevated temperature. Similar observations were made for tungsten mononitride WN.[103]

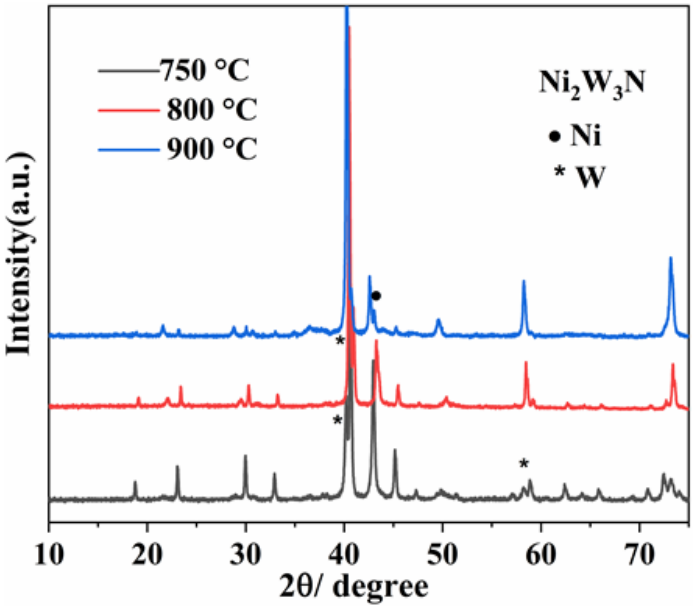

Figure 5-7 Powder X-ray diffraction of Ni_2W_3N obtained by heating $Ni_2W_3O_x$ in ammonia at different temperatures using the modified Pechini route, (*) symbol indicates the W metal reflections and (•) shows reflections of metallic Ni phase.

5.4.3 Quaternary nitrides – cobalt and tungsten molybdenum nitride

Figure 5-8 shows the PXRD patterns of $Co_3W_xMo_{3-x}N$ with different tungsten doping concentrations were mainly consistent with the standard cubic structure of Co_3Mo_3N (space group $Fd\bar{3}m$).[64] As shown in Figure 5-8, PXRD patterns of the materials with compositions x = 0.0, 0.1, 0.2, 0.4, 0.7 and 0.8 show pure phase cubic structure of Co_3Mo_3N, while small peaks corresponding to a minority Co_3Mo hexagonal phase with space group $P6_3/mmc$ were identified in the samples where x = 0.3, 0.5 and 0.6 Figure 5-9. The crystal structures of nine compositions of the $Co_3W_xMo_{3-x}N$ series (x = 0.0, 0.1, 0.2, 0.3, 0.4, 0.5, 0.6,7.0 and 0.8) were refined against PXRD data using a published structural model of Co_3Mo_3N.[64] Representative refined patterns are shown in Figures 5-10 and 5-11, and key parameters are summarised in Tables 5-4 and 5-5. The relatively low percentages values of R_{wp} and R_p indicate good fits with reliable structural parameters. The lattice parameters of the Co_3Mo_3N sample (11.024 Å) agree well with those previously reported for Co_3Mo_3N (11.0245 Å).[41] With increasing tungsten doping content, the particle diameter first increased going through a maximum value of 199 nm for $Co_3W_{0.3}Mo_{2.7}N$ and eventually decreased again to diameter of about 114 nm for $Co_3W_{0.6}Mo_{2.4}N$, $Co_3W_{0.7}Mo_{2.3}N$ and $Co_3W_{0.8}Mo_{2.2}N$.

Furthermore, the refined lattice constants are summarised in Table 5-4. Figure 5-13 shows the linear variation of lattice parameters with tungsten-concentration following Vegard's law. Contrary to the filled β-Mn $Ni_2W_xMo_{3-x}N$ series, the refined cell parameters in the η-

carbide structure $Co_3W_xMo_{3-x}N$ decrease linearly with increasing tungsten- ions doping content. The decreasing trend in the lattice parameters is unexpected since tungsten in octahedral coordination has a larger ionic radius than that of the host molybdenum in octahedral coordination. However, this result is reducible. If tungsten substitutes into a molybdenum site then the lattice should expand as the size of molybdenum is smaller than that of tungsten but in our case, there is shrinkage in unit cell. Therefore, the observed variation of the lattice constants cannot be explained on the basis of difference of ionic or metallic radii of the host and dopant. However, the formal oxidation state of Mo or W is 1^+, and no ionic radii for this ion were found. These results clearly indicate that tungsten-doping into the lattice of Co_3Mo_3N induced noticeable structural changes from the parent phase. It can be observed the refined lattice parameters of the η-carbide structure $Co_3W_xMo_{3-x}N$ behave differently from the filled β-Mn tungsten doped Ni_2Mo_3N system Figure 5-13.

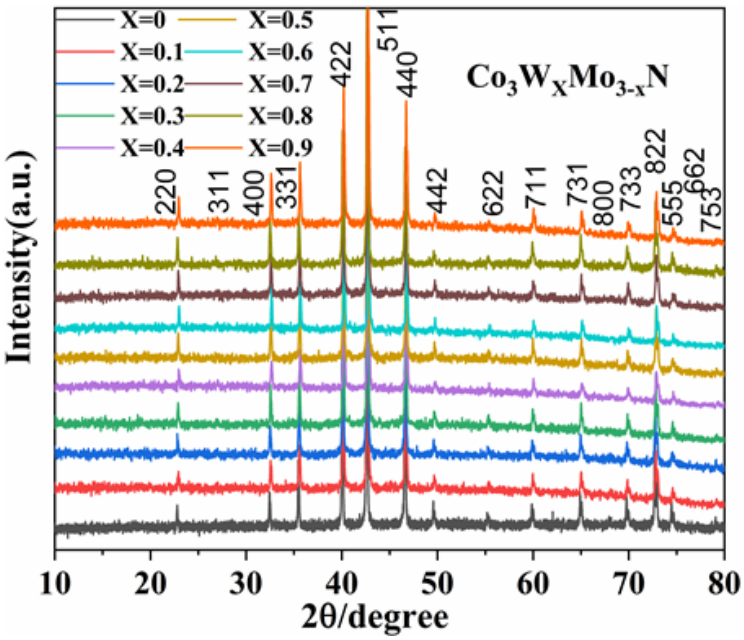

Figure 5-8 PXRD patterns of $Co_3W_xMo_{3-x}N$ (x = 0.0, 0.1, 0.2, 0.3, 0.4, 0.5, 0.6, 0.7, 0.8 and 0.9),thermally treated at 900 °C for 12 h under NH_3 gas.

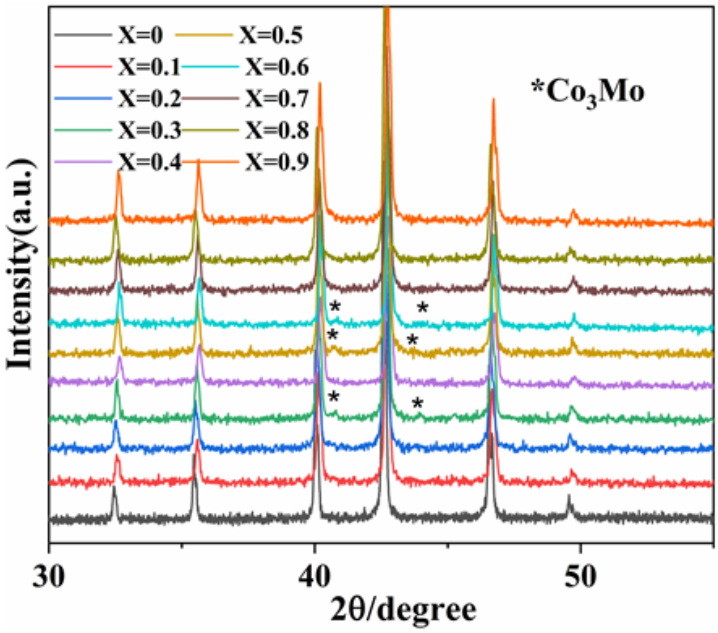

Figure 5-9 The magnified PXRD patterns in the vicinity of 2θ = 30° of $Co_3W_xMo_{3-x}N$ (x = 0.0, 0.1, 0.2, 0.3, 0.4, 0.5, 0.6, 0.7, 0.8 and 0.9) samples heated under NH_3 at 900 °C for 12 h (*) symbol indicates the Co_3Mo phase reflections.

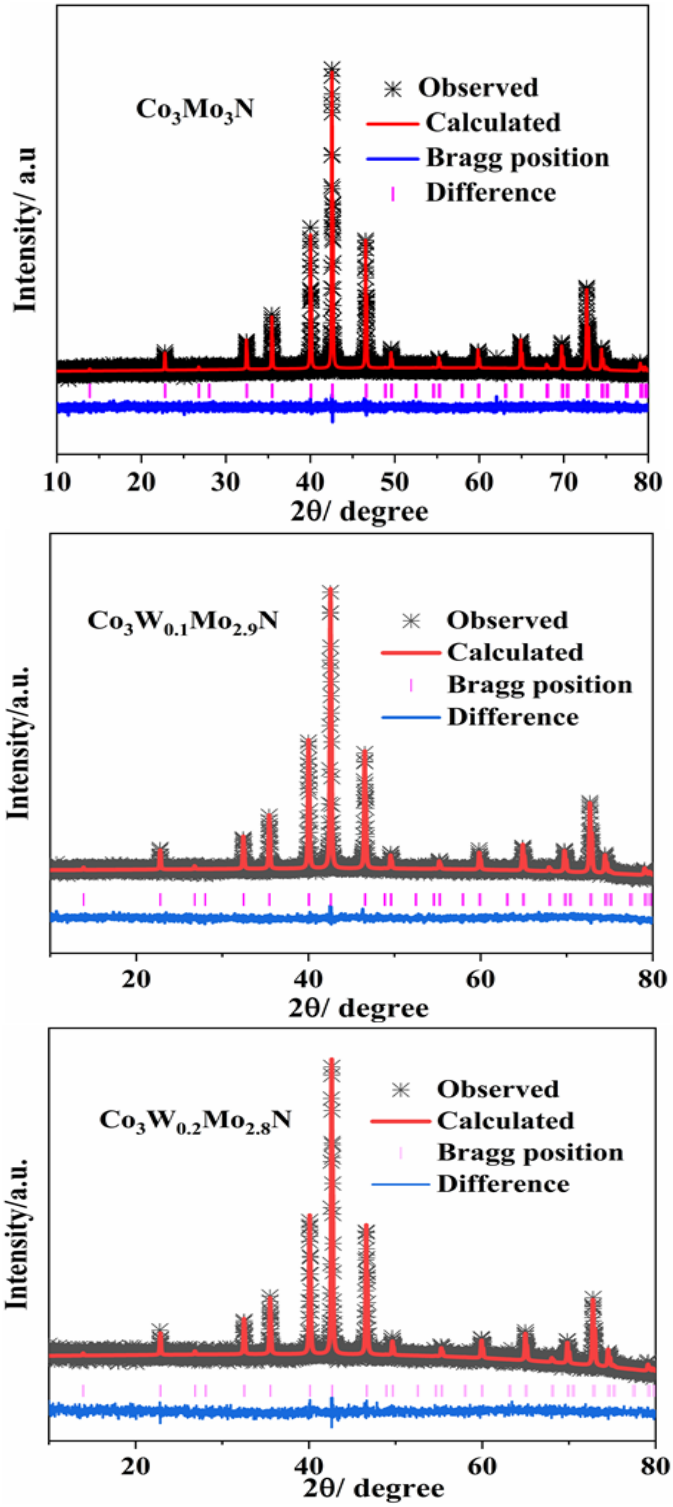

Figure 5-10 Rietveld fits to the PXRD patterns of $Co_3W_xMo_{3-x}N$ series, where x = 0; (R_{wp} % = 3.9 and R_p% = 3.13), 0.1; (R_{wp} % = 4.9 and R_p % = 3.9) and 0.2; (R_{wp} % = 4.9 and R_p % = 3.9). Black crosses mark the data points, the red continuous line the fit and the blue continuous line the difference. Pink tick marks show the positions of the allowed reflections for the η-carbide structure $Co_3W_xMo_{3-x}N$ series in space group $Fd\bar{3}m$.

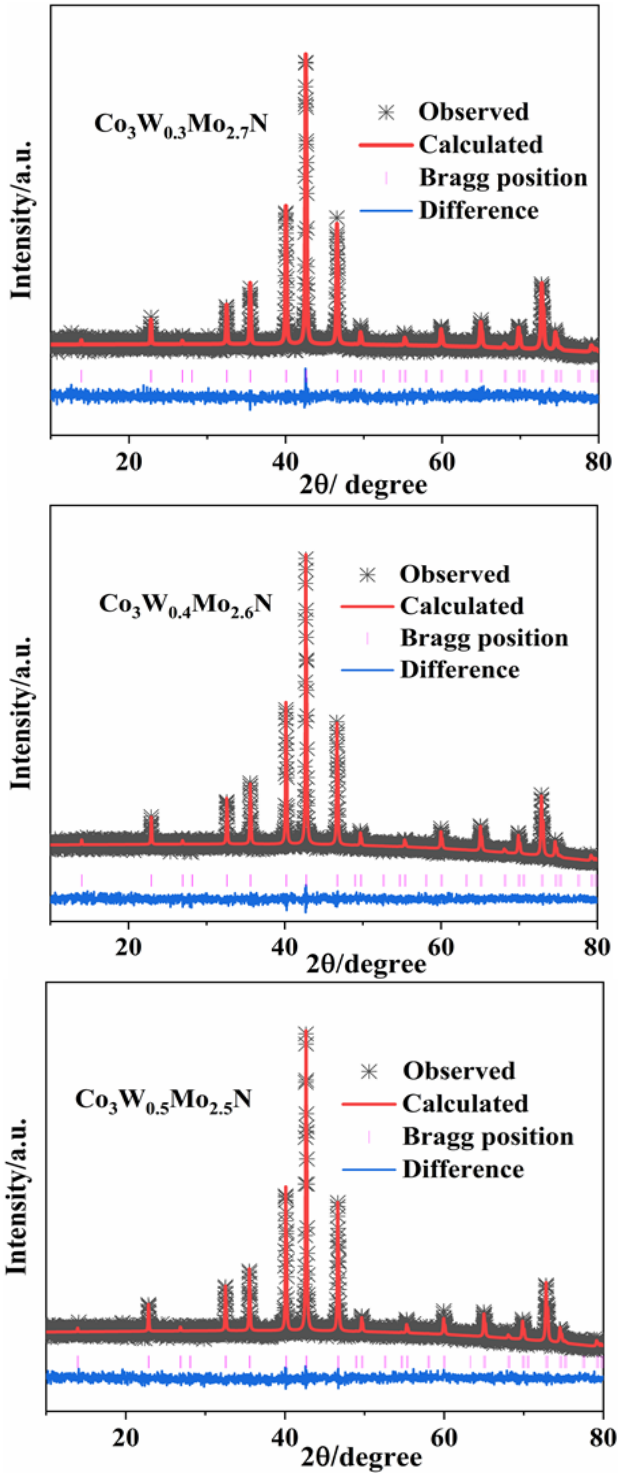

Figure 5-11 Rietveld fits to the PXRD patterns of $Co_3W_xMo_{3-x}N$ series, where $x = 0.3$; (R_{wp} % = 4.9 and R_p % = 3.9), and 0.4; (R_{wp} % = 4.73 and R_p % = 3.9) and 0.5; (R_{wp}% = 4.9 and R_p % = 3.9). Black crosses mark the data points, the red continuous line the fit and the blue continuous line the difference. Pink tick marks show the positions of the allowed reflections for the η-carbide structure $Co_3W_xMo_{3-x}N$ series in space group $Fd\bar{3}m$.

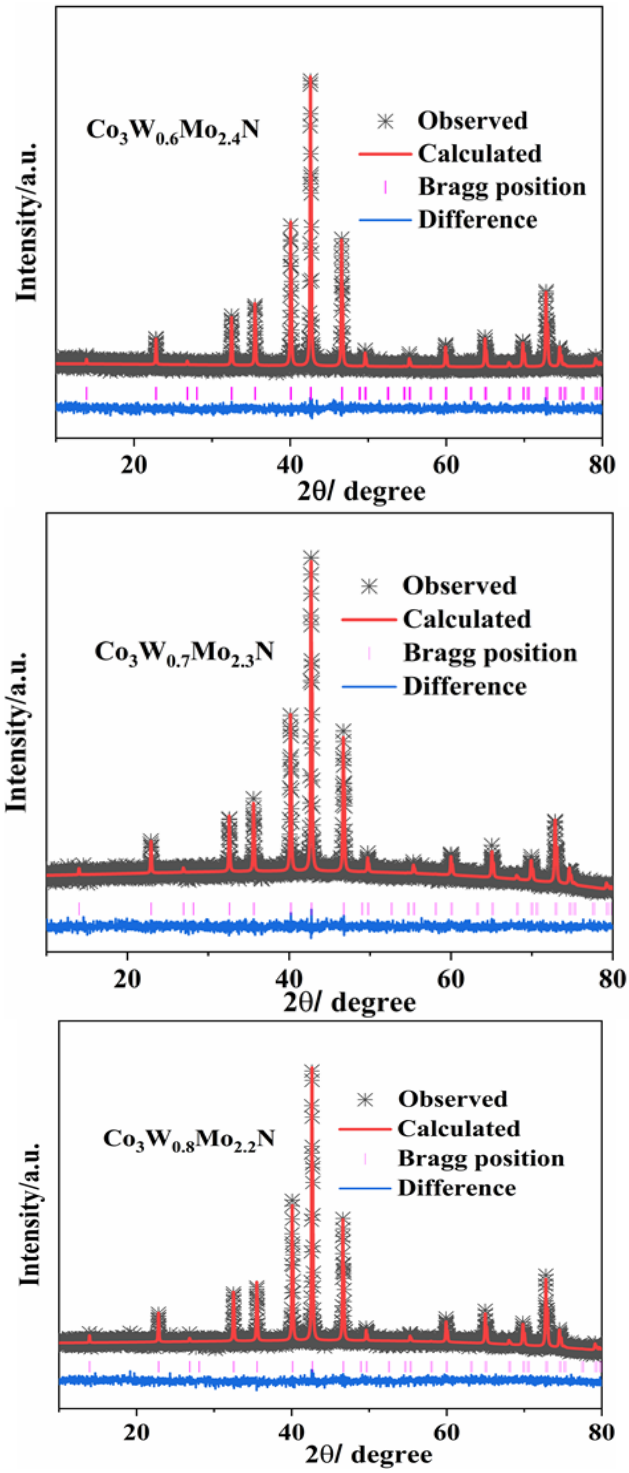

Figure 5-12 Rietveld fits to the PXRD patterns of $Co_3W_xMo_{3-x}N$ series, where x = 0.6; (R_{wp} % =5.03 and R_p % = 4), 0.7; (R_{wp} % = 5.3 and R_p % = 4.18) and 0.8; (R_{wp} % = 5.2 and R_p % = 4.08). Black crosses mark the data points, the red continuous line the fit and the blue continuous line the difference. Pink tick marks show the positions of the allowed reflections for the η-carbide structure $Co_3W_xMo_{3-x}N$ series in space group $Fd\bar{3}m$.

Table 5-4 Refined parameters of $Co_3W_xMo_{3-x}N$ obtained from PXRD refined data.

Atomic parameters	**Co_3Mo_3N**	**$Co_3W_{0.1}Mo_{2.9}N$**	**$Co_3W_{0.2}Mo_{2.8}N$**	**$Co_3W_{0.3}Mo_{2.7}N$**	**$Co_3W_{0.4}Mo_{2.6}N$**
			Co 32e *x* , *x* , *x*		
x	0.2917(3)	0.290373(5)	0.29111(4)	0.290993(4)	0.29127(3)
U_{iso}	0.3377(3)	0.029683(3)	0.03739(3)	0.01568(4)	0.0257 (3)
			Co 16d 1/2, 1/2, 1/2		
U_{iso}	0.03125	0.019074(5)	0.0267(5)	0.00176(4)	0.32489 (2)
			W/Mo 48f *x* , 1/8, 1/8, 1/8		
x	0.32513(3)	0.324154(3)	0.324854(3)	0.32418(3)	0.32489 (2)
U_{iso}	0.3697 (1)	0.02212(2)	0.0238 (1)	0.00886(1)	0.02499 (1)
N 16c 0,0,0 U_{iso}			0.025		

	$Co_3W_{0.5}Mo_{2.5}N$	**$Co_3W_{0.6}Mo_{2.4}N$**	**$Co_3W_{0.7}Mo_{2.3}N$**	**$Co_3W_{0.8}Mo_{2.2}N$**
Co 32e (*x*, *x*, *x*)				
x	0.291759(4)	0.290684(4)	0.291809(4)	0.29037(4)
U_{iso}	0.02448(3)	0.0325(3)	0.02546(3)	0.02287(3)
Co 16d (½, ½, ½)				
U_{iso}	0.01538(4)	0.03249(4)	0.01795(4)	0.02344(2)
W/Mo 48f (*x*, $^1/_8$, $^1/_8$, $^1/_8$)				
x	0.3256(3)	0.324849(2)	0.325296(2)	0.325325 (2)
U_{iso}	0.02769(1)	0.03196 (1)	0.03081(1)	0.01786 (1)
N 16c (0,0,0)				
U_{iso}			0.025	

Table 5-5 Crystallographic information obtained from Rietveld refinement of $Co_3W_xMo_{3-x}N$ series.

x in $Co_3W_xMo_{3-x}N$	a/Å	R_{wp}, R_p/ %	Crystallite size/ nm
0	11.024(4)	3.9, 3.13	94(5)
0.1	11.02337(5)	4.89, 3.86	97(7)
0.2	11.02322(5)	4.86, 3.88	133(12)
0.3	11.02218(5)	4.87, 3.88	199(33)
0.4	11.02104(5)	4.73, 3.78	159(14)
0.5	11.02006(5)	4.86, 3.85	133(11)
0.6	11.01935(5)	5.03, 4.01	114(8)
0.7	11.01872(4)	5.27, 4.18	114(8)
0.8	11.01741(4)	5.18, 4.08	114(8)

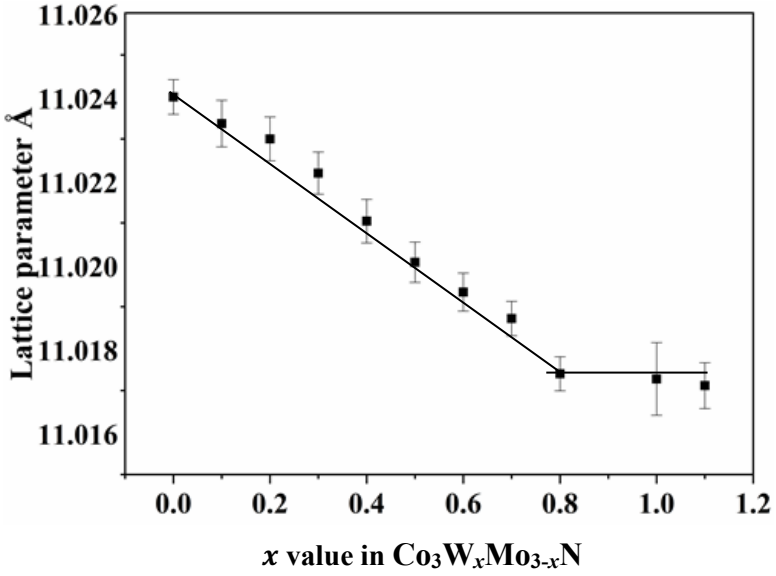

Figure 5-13 Lattice parameters variation with tungsten content for $Co_3W_xMo_{3-x}N$ samples.

5.5 5.5 Textural characterisation

The surface area was determined by nitrogen adsorption using the BET-model for data interpretation. Nitrogen (N_2) adsorption isotherms studies were conducted on the single-phase samples in order to determine the specific surface area (SSA). BET curves were used to evaluate this value. The obtained isotherms of the synthesised quaternary nitride samples in this study typifies that of materials with a predominantly mesoporous structure.

Figure 5-14 illustrates the nitrogen adsorption/desorption isotherm curves of the filled β-Mn structure samples in $Ni_2W_xMo_{3-x}N$ series. The incorporation of tungsten ions into the

Ni_2Mo_3N lattice leads to an increase of the surface area as seen in Figure 5-14. The BET specific surface area of Ni_2Mo_3N, $Ni_2W_{0.1}Mo_{2.9}N$, $Ni_2W_{0.2}Mo_{2.8}N$ and $Ni_2W_{0.3}Mo_{2.7}N$ samples were at a range of 2.8 - 4.8 $m^2\ g^{-1}$ (Figure 5-14). The obtained results revealed that the samples exhibited low surface area which is below 5 $m^2\ g^{-1}$, this could be probably related to the high ammonolysis temperature employed in their preparation. In addition, the BET surface area decreased and thus most likely caused by an increase of catalyst pores plugging with increasing tungsten content. The resultant isotherm curves display type II, which can be attributed to relatively weak adsorbent–adsorbate interactions.

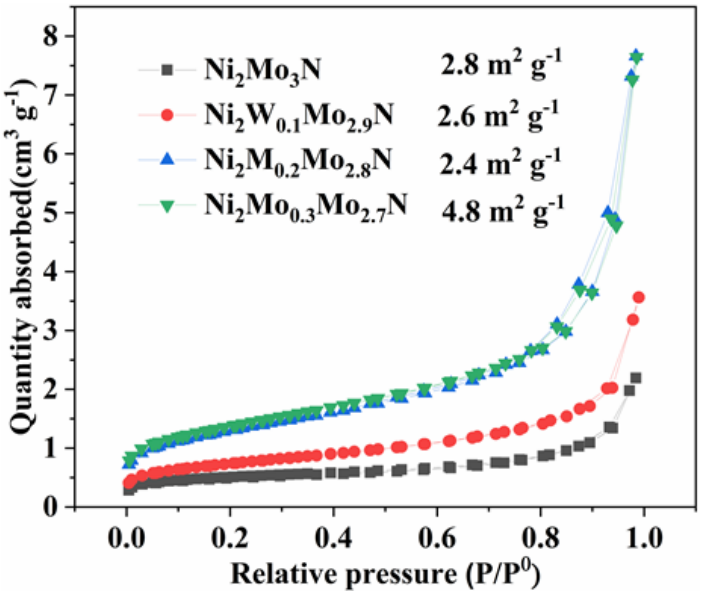

Figure 5-14 Nitrogen adsorption/desorption isotherms curves of mesoporous $Ni_2W_xMo_{3-x}N$ series, adsorption is given in units of cm^3 of adsorbate per gram adsorbent.

Figure 5-15 gives the adsorption/ desorption N_2 isotherm for the η carbide structure samples in $Co_3W_xMo_{3-x}N$ which also indicating a type III isotherm and shows no hysteresis. The BET surface area of Co_3Mo_3N, $Co_3W_{0.1}Mo_{2.9}N$, $Co_3W_{0.2}Mo_{2.8}N$ and $Co_3W_{0.4}Mo_{2.6}N$ were 3.4, 2.8, 2.6 and 2.4, respectively. The obtained surface areas were lower than that observed for $Ni_2W_xMo_{3-x}N$ samples.

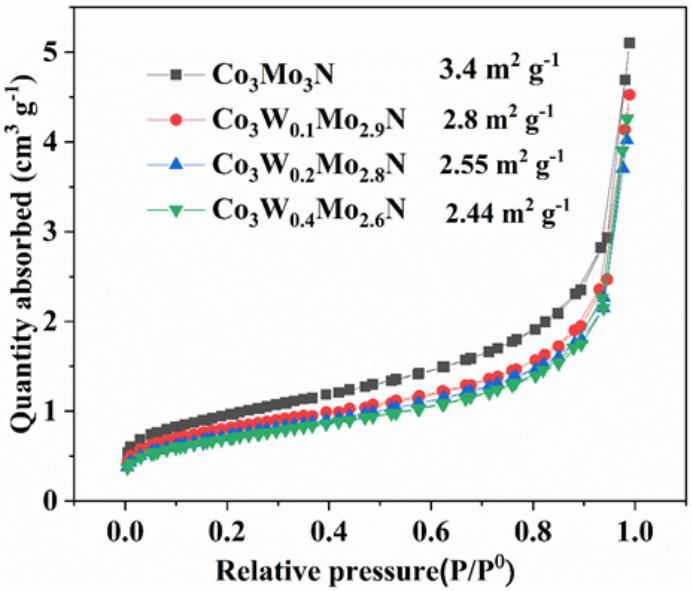

Figure 5-15 Nitrogen adsorption/desorption isotherms curves of mesoporous $Co_3W_xMo_{3-x}N$ series, adsorption is given in units of cm^3 of adsorbate per gram adsorbent.

5.6 TGA study of cobalt molybdenum nitride and cobalt tungsten molybdenum nitride

Thermogravimetric analysis TGA, described in section 2.5 was carried out in order to study the thermal stability of the materials. Figure 5-16 shows the TGA plot for Co_3Mo_3N and $Co_3W_{0.4}Mo_{2.6}N$ heated in oxygen- rich gas mixture at ramp rate of 10 °C/ min from room temperature to 800 °C. The TGA result showed that the observed total mass gain for Co_3Mo_3N and $Co_3W_{0.4}Mo_{2.6}N$ was (36.40 %) and (34 %). This is close to the expected values (37.19 %) and (34.6%), respectively. Figure 5-16 also shows that both samples underwent decomposition and the final products are given in the equations below.

$$Co_3Mo_3N + 6O_2 \rightarrow 3CoMoO_4 + \frac{1}{2}N_2 \qquad \text{Equation 5-1}$$

$$Co_3\,W_{0.4}Mo_{2.6}\,N + 6O_2 \rightarrow 3CoO + 0.4WO_3 + 2.6MoO_3 + \frac{1}{2}N_2 \qquad \text{Equation 5-2}$$

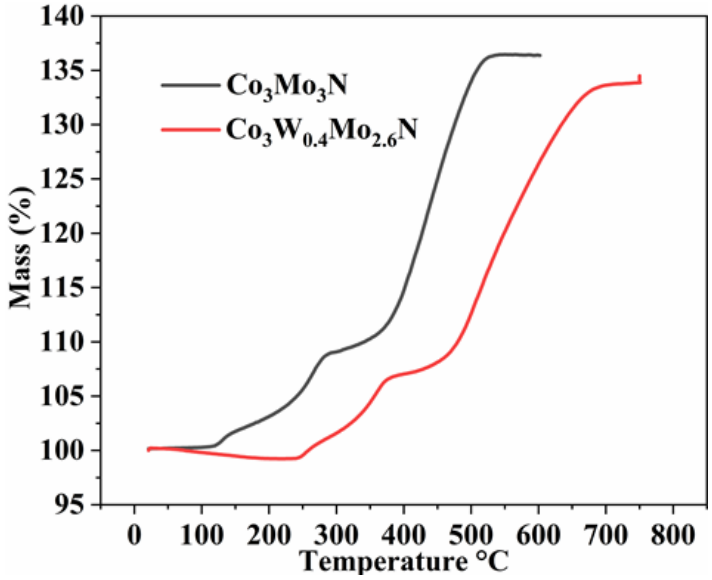

Figure 5-16 Thermogravimetric analysis curves under oxygen atmosphere for the nanostructured Co_3Mo_3N and $Co_3W_{0.4}Mo_{2.6}N$ samples with the heating rate of 10 °C /min from room temperature to 800 °C. The initial weight of every sample before measurement is 0.015 g.

Table 5-6 Mass % obtained from TGA for Co_3Mo_3N and $Co_3W_{0.4}Mo_{2.6}N$

Sample	Overall Mass Gain Observed/ %	Theoretical Mass Gain/ %	Difference/ %
Co_3Mo_3N	36.40	37.19	0.79
$Co_3W_{0.4}Mo_{2.6}N$	33.8	34.6	0.8

5.7 Catalytic activity

The effect of the addition of W into the η–carbide structure Co_3Mo_3N and the filled β-Mn structure Ni_2Mo_3N toward ammonia synthesis was compared. Initially, the reactions were conducted at 400 °C then followed by increased temperature up to 500 °C using 0.15 g of the catalyst under atmospheric pressure (0.1 MPa) of flowing 1: 3 N_2/H_2 gas. With regards to the catalytic activity of $Ni_2W_xMo_{3-x}N$ system, Figure 5-17 showed that at 400 °C the ammonia production rate of the $Ni_2W_{0.3}Mo_{2.7}N$ catalyst was very limited 292 μmol g^{-1} h^{-1}. However, when the temperature is increased to 500 °C, a high ammonia production rate of 395 μmol g^{-1} h^{-1} was observed. Hence all samples were tested at 500 °C (Figure 5-17). The reaction was a steady state process with the formation of ammonia being constant throughout the reaction. This is shown in the reaction profile (Figure 5-18).

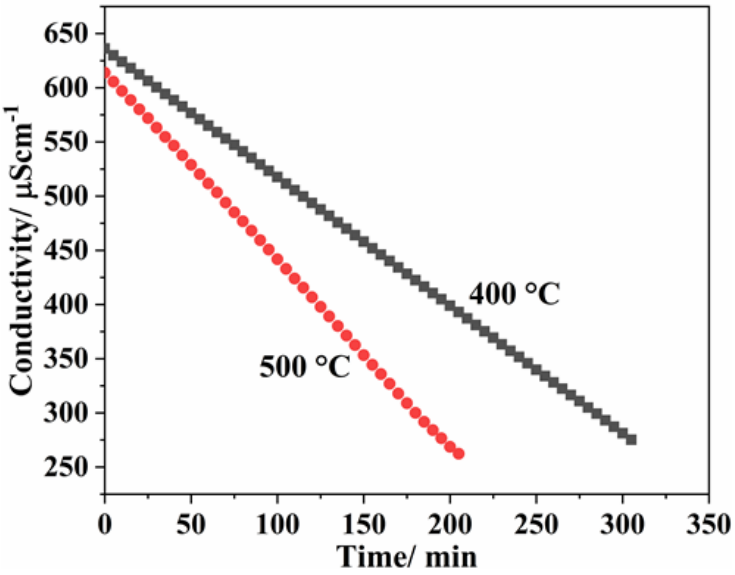

Figure 5-17 Comparison of the reaction profiles for the nanostructured $Ni_2W_{0.1}Mo_{2.9}N$ at 400 and 500 °C.

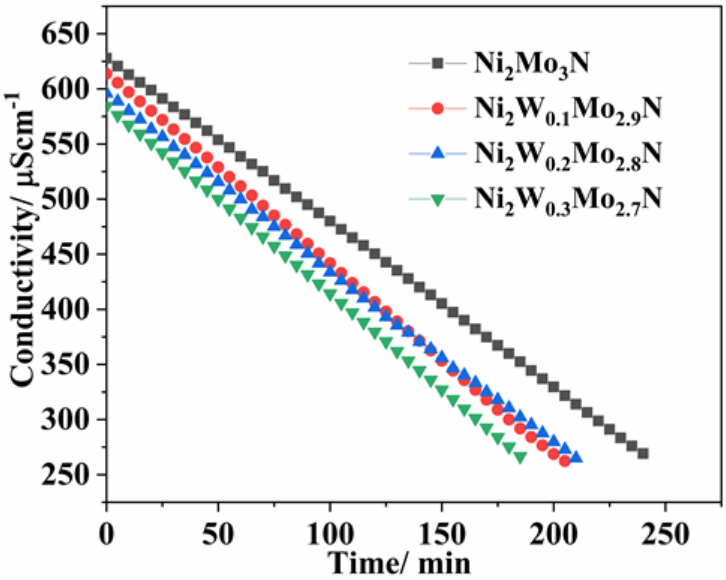

Figure 5-18 Conductivity profile for the $Ni_2W_xMo_{3-x}N$ (x = 0, 0.1, 0.2 and 0.3) sample under 3:1 H_2 in N_2 at 500 °C.

The ammonia synthesis activities of the materials developed upon the inclusion of W into the filled β-Mn structure Ni_2Mo_3N are shown in Figure 5-18 and listed in Table 5-7. The BET surface areas of the doped samples follow the order of $Ni_2W_{0.3}Mo_{2.7}N$> $Ni_2W_{0.2}Mo_{2.8}N$ > $Ni_2W_{0.1}Mo_{2.9}N$. The ammonia production rate was generally observed to increase from approximately 364(20), 395(8) to 439(15) µmol g^{-1} h^{-1} for $Ni_2W_{0.1}Mo_{2.9}N$, $Ni_2W_{0.2}Mo_{2.8}N$ and $Ni_2W_{0.3}Mo_{2.7}N$ with surface areas of 2.6, 2.4 and 4.8 m^2 g^{-1}, respectively. Such improved performance could be attributed to the increased surface area.

The performance of Ni_2Mo_3N (400 μmol g^{-1} h^{-1}) for ammonia synthesis was close to that for $Ni_2W_{0.2}Mo_{2.8}N$ (395 μmol g^{-1} h^{-1}) although the surface area of Ni_2Mo_3N higher than that of $Ni_2W_{0.2}Mo_{2.8}N$.

The corresponding specific activities were calculated as 140, 94 and 91 μmol m^{-2} h^{-1}. These specific activities dramatically decrease as the surface area increases or with increasing W content. The $Ni_2W_{0.1}Mo_{2.9}N$ catalyst ammonolysed at 800 and 900 °C showed that the activity dropped from 364 to 260 μmol g^{-1} h^{-1} with surface areas of 2.6 and 2 m^2 g^{-1}, respectively. This example could further support the positive correlation between the ammonia synthesis activity and the surface area.

Table 5-7 Surface area, ammonia synthesis and specific activities for $Ni_2W_xMo_{3-x}N$ (x = 0, 0.1, 0.2 and 0.3) catalysts fired in NH_3 at 800 °C for 12 h.

Catalyst	**BET surface area m^2 g^{-1}**	**Ammonia synthesis rate (μmol h^{-1} g^{-1})**	**Specific activity (μmol h^{-1} m^{-2})**
		500 °C	**500 °C**
Ni_2Mo_3N	2.8	400(41)	143
$Ni_2W_{0.1}Mo_{2.9}N$	2.6	364(20)	140
$Ni_2W_{0.2}Mo_{2.8}N$	4.2	395(8)	94
$Ni_2W_{0.3}Mo_{2.7}N$	4.8	439(15)	91

Having discussed the catalytic activity of $Ni_2W_xMo_{3-x}N$ system, we are now considering the catalytic performance of $Co_3W_xMo_{3-x}N$ Figure 5-19 and 5-20. In the case of tungsten doped Co_3Mo_3N samples, the catalytic performance was evaluated under the same conditions of that employed for tungsten doped Ni_2Mo_3N samples. Since the presence of impurities has been noted to lower catalytic activity,[182] the ammonia synthesis reactions were carried out on the purer phases.

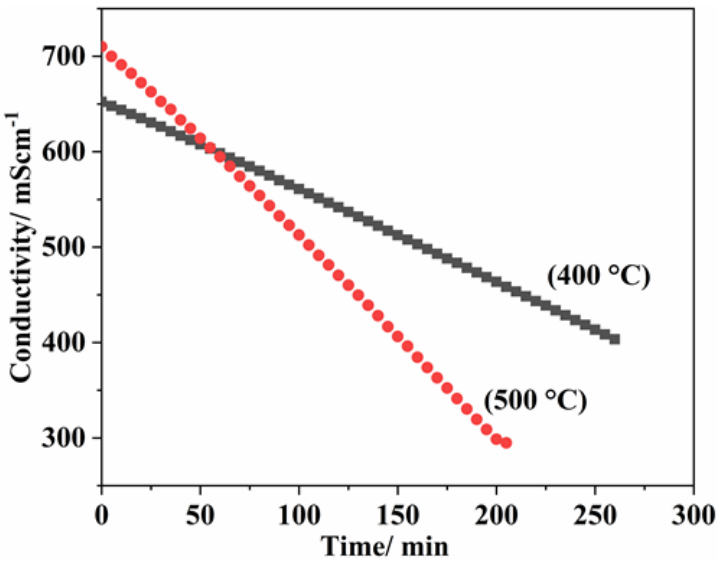

Figure 5-19 Comparison between the reaction profiles for the nanostructured Co_3Mo_3N at 400 and 500 °C.

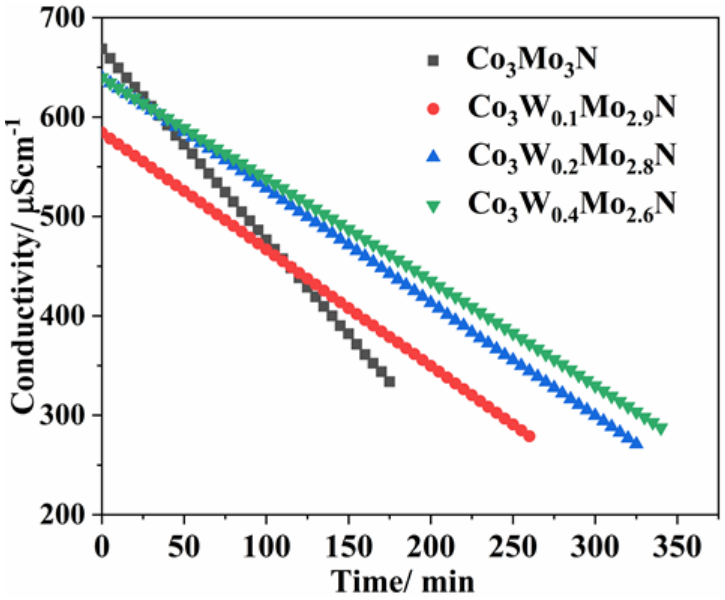

Figure 5-20 Conductivity profile for the $Co_3W_xMo_{3-x}N$ (x = 0, 0.1, 0.2, 0.6) samples under 3:1 H_2 in N_2 at 500 °C.

The catalytic performance of the developed materials is summarised in Table 5-8. The NH_3 production rates for Co_3Mo_3N, $Co_3W_{0.1}Mo_{2.9}N$, $Co_3W_{0.2}Mo_{2.8}N$ and $Co_3W_{0.4}Mo_{2.6}N$ samples were found to be ca. 383(15), 288(19), 267(25) and 239(12) µmol g^{-1} h^{-1}, respectively. The differences between the surface areas of these catalysts are not that significant and they follow the order of Co_3Mo_3N > $Co_3W_{0.1}Mo_{2.9}N$> $Co_3W_{0.2}Mo_{2.8}N$ >

$Co_3W_{0.4}Mo_{2.6}N$. It can be noted that the performance of these catalysts gradually dropped with decreasing surface area, the activity is consistent with their surface area order.

This means that the addition of W did not show any obvious improvement with respect to the undoped sample. Apparently, Co_3Mo_3N catalyst reveals the highest surface area and demonstrated the highest NH_3 formation rate compared with that of its analogue tungsten doped samples. These observations may indicate that the surface area could be the direct reason behind the decline in the ammonia production rate, it does seem to be the key variable. The literature also shows that the catalytic behaviour could be associated specifically with the surface area. Hence, further optimisation is required to improve the accessibility of the active site surface in order to achieve higher performance. One possible potential strategy is the addition of alkali promoter such as Cs^+. Bulk Co_3Mo_3N catalyst, to date, is one of the most active reported nitride-based catalysts for ammonia synthesis at ambient pressure.[82,37,41] This material showed an outstanding ammonia synthesis rate of 986 μmol g^{-1} h^{-1} particularly when promoted with small content of Cs^+ ion and ca._652 μmol g^{-1} h^{-1} for non-promoted ones.[82] The mass activity was normalised to the BET surface area.

From Table 5-8, it is noticeable that the Co_3Mo_3N exhibits the highest specific activity with/of around 113 μmol m^{-2} h^{-1} as well as the highest performance compared to the doped samples. In addition, $Co_3W_{0.1}Mo_{2.9}N$ and $Co_3W_{0.2}Mo_{2.8}N$ showed similar specific activity 103 μmol m^{-2} h^{-1}. The $Co_3W_{0.4}Mo_{2.6}N$ catalyst has the lowest surface area (2.44 m^2 g^{-1}) and the lowest specific activity (98 m^{-2} h^{-1}) among the five samples. These results are significantly higher than those reported in the literature. Kojima *et al*. compared the specific activity of bimetallic molybdenum nitride catalysts Co_3Mo_3N, Ni_2Mo_3N and Fe_3Mo_3N. They found that Co_3Mo_3N had the highest specific activity followed by Fe_3Mo_3N with rates of 31 and 20 μmol m^{-2} h^{-1}, respectively, whereas that of Ni_2Mo_3N was 14 μmol m^{-2} h^{-1} which exhibited the lowest specific activity.[82] No structural changes observed in the post reaction patterns PXRD (Figure 5-21).

Table 5-8 Surface area, ammonia synthesis and specific activities for $Co_3W_xMo_{3-x}N$ (x = 0, 0.1, 0.2 and 0.4) catalysts fired in NH_3 at 900 °C for 12 h.

Catalyst	BET surface area m^2 g^{-1}	Ammonia synthesis rate (μmol h^{-1} g^{-1})	Specific activity (μmol h^{-1} m^{-2})
		500 °C	500 °C
Co_3Mo_3N	3.4	383(15)	113
$Co_3W_{0.1}Mo_{2.9}N$	2.8	288(19)	103
$Co_3W_{0.2}Mo_{2.8}N$	2.6	267(25)	103
$Co_3W_{0.4}Mo_{2.6}N$	2.44	239(12)	98

Combining the activity data presented in Table 5-7 and 5-8, it is clearly seen that substituted molybdenum with tungsten into Ni_2Mo_3N catalyst show promising activity compared to tungsten doped Co_3Mo_3N catalysts. This is likely due to the former having larger surface area values resulting from the applied lower ammonolysis temperature of 800 °C compared to 900 °C for the latter. The performance of Co_3Mo_3N phase is close to that of 484 μmol g^{-1} h^{-1} which tested at 500 °C and higher than that evaluated at 400 °C.[41,83] The post-catalysis reaction PXRD powder diffraction patterns of the tungsten doped Ni_2Mo_3N samples after the ammonia synthesis are shown in Figure 5-21. The data revealed that no changes occurred within the crystalline structures of the post-reaction patterns.

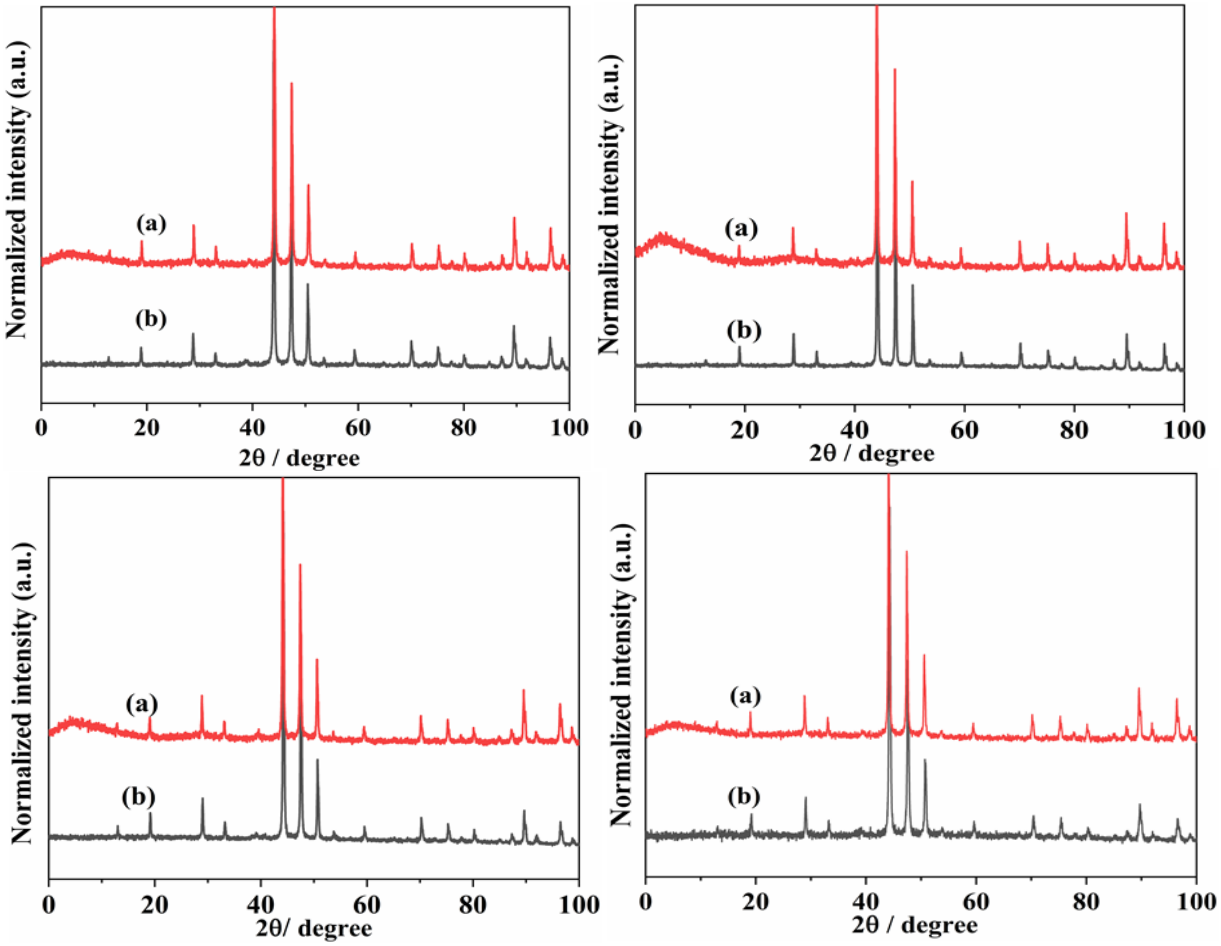

Figure 5-21 PXRD diffraction patterns of pre (b) and post-reaction (a). The compositions were Ni_2Mo_3N (top left), $Ni_2W_{0.1}Mo_{2.9}N$ (top right), $Ni_2W_{0.2}Mo_{2.8}N$ (bottom left), $Ni_2W_{0.3}Mo_{2.7}N$ (bottom right).

On comparing the PXRD patterns of pre-and post-catalysis reactions of W doped Co_3Mo_3N Figure 5- 22, it can be seen that no structural changes observed.

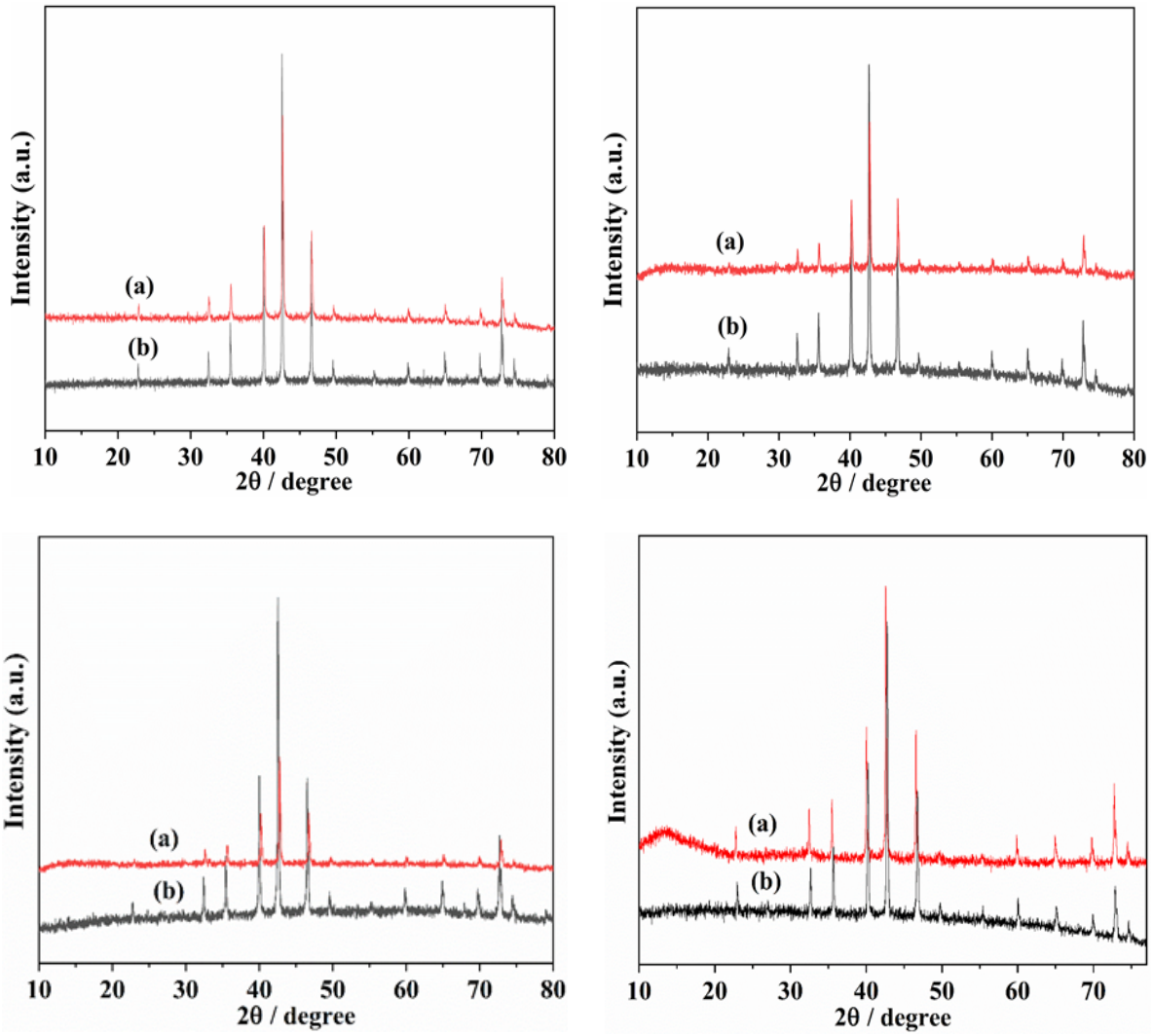

Figure 5-22 PXRD diffraction patterns of pre (b) and post-reaction (a). The compositions were Co_3Mo_3N (top left), $Co_3W_{0.1}Mo_{2.9}N$ (top right), $Ni_2W_{0.2}Mo_{2.8}N$ (bottom left), $Ni_2W_{0.6}Mo_{2.4}N$ (bottom right).

5.8 Combustion (CHN) analysis of pre-and post-catalysis samples

Combustion (C, H, N) analysis was performed on pre and post catalysis samples and data are listed in Table 5-9. The obtained nitrogen contents of the Ni_2Mo_3N, $Ni_2W_{0.1}Mo_{2.9}N$, $Ni_2W_{0.2}Mo_{2.8}N$ and $Ni_2W_{0.3}Mo_{2.7}N$; match with the theoretical stoichiometric values. From studying the pre- and post-catalysis reaction of nitrogen content, it can be seen that no change is observed in the nitrogen contents of all the investigated catalysts. The results obtained by PXRD, TGA, SEM and elemental analysis (CHN) indicate the phase purity of Ni_2Mo_3N, $Ni_2W_{0.1}Mo_{2.9}N$, $Ni_2W_{0.2}Mo_{2.8}N$ and $Ni_2W_{0.3}Mo_{2.7}N$.

Table 5-9 Pre and post catalysis nitrogen contents, and expected nitrogen content of Ni_2Mo_3N and $Ni_2(W, Mo)_3N$ samples produced at 800 °C in NH_3.

Catalyst	Nitrogen content (wt.%)		
	Pre-catalysis	Post-catalysis	Expected N content
Ni_2Mo_3N	3.4	3.3	3.3
$Ni_2W_{0.1}Mo_{2.9}N$	3.3	3.4	3.3
$Ni_2W_{0.2}Mo_{2.8}N$	3.4	3.0	3.3
$Ni_2W_{0.3}Mo_{2.7}N$	3.0	3.2	3.2

The nitrogen content was found to be 3.2 wt. % for Co_3Mo_3N, 3.3 wt. % $Co_3W_{0.1}Mo_{2.9}N$, 3.33 wt. % $Co_3W_{0.2}Mo_{2.8}N$ and 2.66 wt. % for $Co_3W_{0.4}Mo_{2.6}N$, which is close to the expected stoichiometric values of Co_3Mo_3N (2.9 wt. %), $Co_3W_{0.1}Mo_{2.9}N$ (2.9 wt. %), $Co_3W_{0.2}Mo_{2.8}N$ (2.8 wt. %) and $Co_3W_{0.4}Mo_{2.6}N$ (2.72 wt. %). As can be shown in Table 5-10, there is no change in the nitrogen contents between the pre-and-post catalysis reaction data. The obtained nitrogen content of Co_3Mo_3N is comparable to that reported by Alshibane *et al*. (3.1 wt. %).[41]

Table 5-10 Pre and post catalysis nitrogen contents, and expected nitrogen content of Co_3Mo_3N and $Co_3(W, Mo)_3N$ samples after heating at 900 °C in NH_3.

Catalyst	Nitrogen content (wt.%)		
	Pre-catalysis	Post-catalysis	Expected N content
Co_3Mo_3N	3.2	3.3	2.9
$Co_3W_{0.1}Mo_{2.9}N$	3.3	3.2	2.9
$Co_3W_{0.2}Mo_{2.8}N$	3.3	3.1	2.8
$Co_3W_{0.4}Mo_{2.6}N$	2.7	3.0	2.7

5.9 SEM images of $Ni_2W_{0.3}Mo_{2.7}N$ samples pre-and post-catalysis

In order to investigate the structural morphology of the pre-and post-catalysis reaction of the $Ni_2W_{0.3}Mo_{2.7}N$ material, SEM was used. Figure 5-23 presents typical SEM micrographs of (a; scale bar 20 μm) pre-reaction and (b; scale bar 5 μm) post-reaction of the $Ni_2W_{0.3}Mo_{2.7}N$. The SEM analysis was taken at a magnification of 5000x to 1000x. From SEM image Figure 5-23 (a) of as-synthesised $Ni_2W_{0.3}Mo_{2.7}N$, it can be clearly observed that nanosheets are, present, which could increase the surface area and subsequently enhance the catalytic

performance. The post catalysis reaction $Ni_2W_{0.3}Mo_{2.7}N$ sample still retained the same type of morphology as observed by SEM (Figure 5-23 (b)). This suggests that the production of ammonia does not affect the morphology. White areas in some parts of the samples could indicate the agglomerated nanoparticles. These agglomerated particles could be induced by the higher temperature (800 °C) ammonolysis reaction.

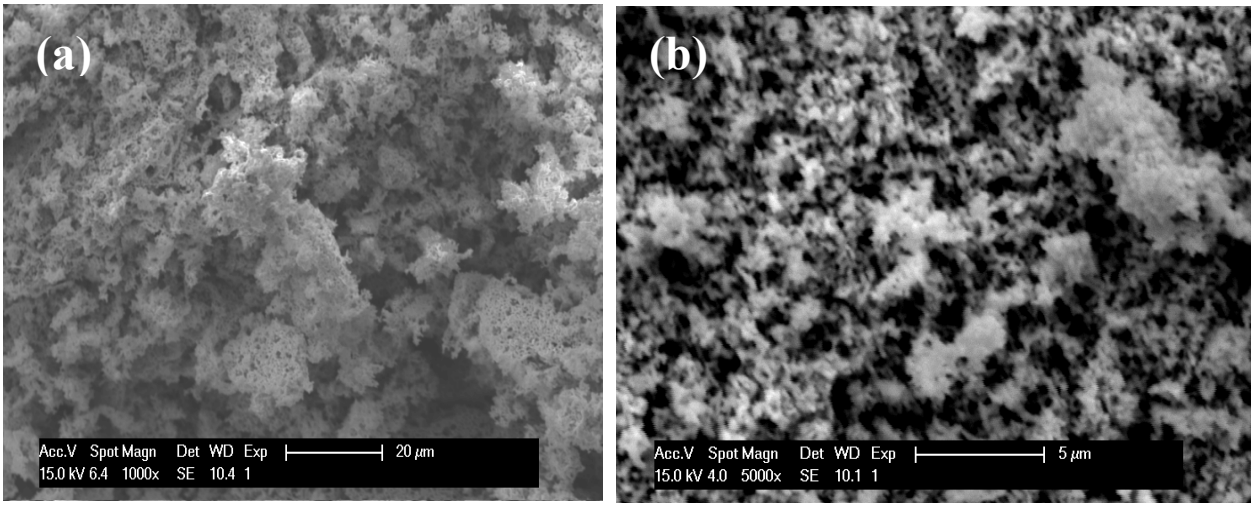

Figure 5-23 SEM micrographs images (a; scale bar 20 μm) Pre-reaction(a) and (b; scale bar 5 μm) Post-reaction $Ni_2W_{0.3}Mo_{2.7}N$ produced at 800 °C for 12 h under NH_3(b).

5.10 SEM and EDX analysis of Co_3Mo_3N and $Co_3W_{0.4}Mo_{2.6}N$

The morphologies of pre- and post- catalysis samples of Co_3Mo_3N and $Co_3W_{0.4}Mo_{2.6}N$ catalysts were investigated by applying high magnifications in scanning electron microscopy (SEM). Figure 5-24 a and b, has shown that the structure of Co_3Mo_3N and $Co_3W_{0.4}Mo_{2.6}N$ catalysts consist of irregular particles with different sizes, as reported in the literature.[177,191, 206, 207] In addition, there are needles and plate shapes alongside the quasi-spherical nanoparticles (highlighted region) with some degree of porosity observed in $Co_3W_{0.4}Mo_{2.6}N$ as shown in (Figure 5-24, c). The aggregated needles structure was reported for Co_3Mo_3N in earlier research.[208,41] It is obvious from SEM images of post-catalysis reaction samples (Figure 5-24 c, e and d) that the ammonia synthesis reaction had no remarkable influence on the morphologies.

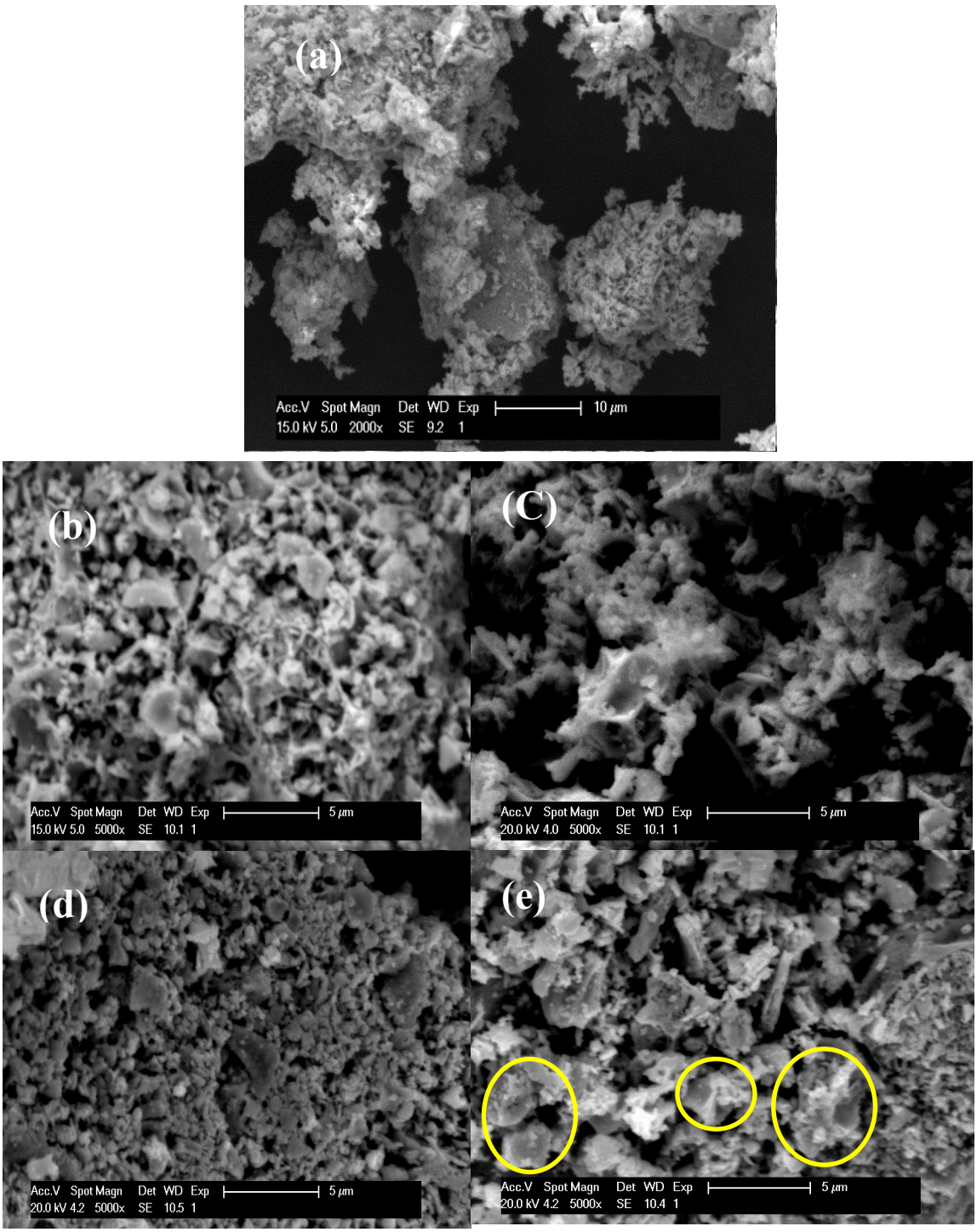

Figure 5-24 Representative SEM micrographs images at 2000x and 5000x magnification of (a; scale bar 10 µm) and (b; scale bar 5 µm) pre-catalysis reaction and (c; scale bar 5 µm) post-catalysis reaction of the Co_3Mo_3N nanoparticles, (d and e; scale bar 5 µm) pre- and post-reaction of $Co_3W_{0.4}Mo_{2.6}N$ nanoparticles, respectively.

EDX was used to verify the composition and phase purity of the obtained materials. EDX spectra of Co_3Mo_3N and $Co_3W_{0.4}Mo_{2.6}N$ are depicted in Figures 5-25 and 5-26. The EDX spectrum of Co_3Mo_3N showed that the sample was composed of elemental cobalt,

molybdenum and nitrogen with 40 atomic % of Co and 48 atomic % of Mo. The results can be found in Figure 5-25. These values are close to the expected stoichiometric value of 42.9 % of Co and Mo in Co_3Mo_3N which suggests that this material is almost pure Co_3Mo_3N. EDX analysis of $Co_3W_{0.4}Mo_{2.6}N$ Figure 5-26 indicates the presence of cobalt, tungsten and molybdenum within the structure.

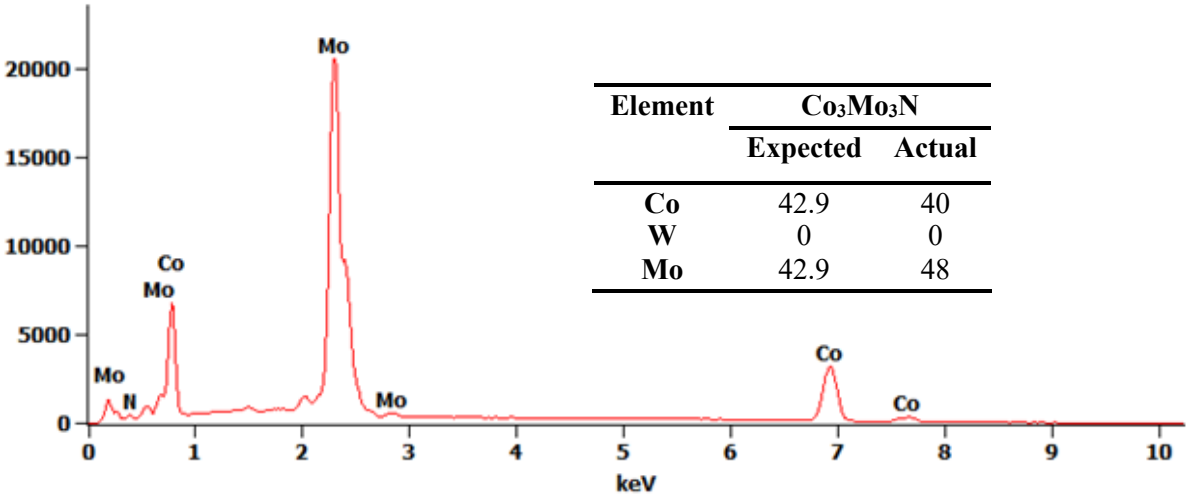

Element	Co_3Mo_3N	
	Expected	Actual
Co	42.9	40
W	0	0
Mo	42.9	48

Figure 5-25 EDX analysis for nanostructured Co_3Mo_3N (900 °C) using a 15 KeV accelerating voltage and the atom % of the Co_3Mo_3N sample evaluated by EDX analysis.

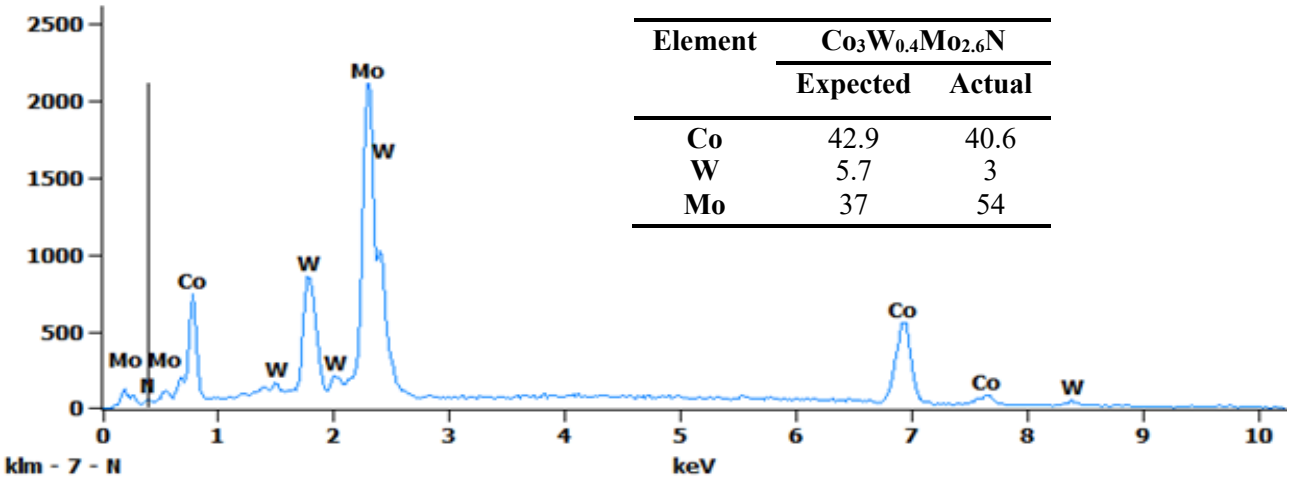

Element	$Co_3W_{0.4}Mo_{2.6}N$	
	Expected	Actual
Co	42.9	40.6
W	5.7	3
Mo	37	54

Figure 5-26 EDX analysis for nanostructured $Co_3W_{0.4}Mo_{2.6}N$ (900 °C) using a 15 KeV accelerating voltage and the atom % of the $Co_3W_{0.4}Mo_{2.6}N$ sample evaluated by EDX analysis.

5.11 Conclusions

In this chapter, the filled β-manganese $Ni_2W_xMo_{3-x}N$ and the η-carbide $Co_3W_xMo_{3-x}N$ structured materials were prepared by a gel citrate route and thermally treated at 800 °C and 900 °C, respectively. The compositions were structurally studied using X-ray powder

diffraction along with Rietveld refinements. The refined cubic lattice constants in both structures obey Vegard's law but exhibit a different structural behaviour. That is, substituting molybdenum with tungsten into Ni_2Mo_3N resulted in the expansion of the lattice parameters. However, in contrast to the $Ni_2W_xMo_{3-x}N$ data, the shrinkage of the lattice constants was observed with increasing tungsten substitution in the η-carbide $Co_3W_xMo_{3-x}N$, despite the larger metallic radius of tungsten. Also, the influence of tungsten substitution into the $Ni_2W_xMo_{3-x}N$ and $Co_3W_xMo_{3-x}N$ series was investigated for ambient pressure ammonia synthesis. The results have shown that the materials were highly active for ammonia synthesis under 500 °C compared with 400 °C. Among all the catalysts studied in this chapter, the tungsten doped Ni_2Mo_3N samples demonstrated the higher catalytic activity for ammonia synthesis. In particular, the best result of 439(15) μmol g^{-1} h^{-1} was obtained using the $Ni_2W_{0.3}Mo_{2.7}N$ catalyst. The difference in the activity between these structures may be connected to the surface area which could result from the applied different ammonolysis temperatures. As the reaction temperature increased, the surface area decreased due to particle aggregation.

Chapter 6 Activity of Transition Metal Nitride Quaternary Compounds Synthesised *in Situ*

6.1 Introduction

Various transition metal oxides (TMOs) are considered to be promising catalysts for a wide range of catalytic reactions due to their structural and electronic properties.[209] The variation in activity can be attributed to the combination of two or more metals in the oxygen lattice.[210] Among these oxides, the materials based on molybdate and tungstate have been intensively studied.[211] In ammonia synthesis, for example, the metal molybdates are complemented with transition molybdenum-based nitride materials. The nickel molybdate was found to exhibit a higher electrochemical performance which was ascribed to the Ni ion.[212] According to the previous literature, the preparation of these materials with higher surface area can be difficult due to the complex nature of molybdates.[213] It has been reported that the catalytic activities of the metal molybdates is determined by the structure of the material, which is mainly controlled by the method of preparation.[214]

Various approaches have been documented for producing transition metal oxides. Solid state reactions are one of the most commonly used methods. These require high temperatures above 900 ºC, which could result in a relatively large particle size, impure materials, and irregular morphology. This could cause a negative effect on their application. Efforts have been made and alternative synthesis routes such as co-precipitation [209] and hydrothermal[215, 216] methods are being employed to overcome these drawbacks. Although these routes show advantages including low synthesis temperature, good productpurity and particle size, it has been reported that after precipitation high calcination temperatures are required to complete the chemical reaction. The formation of transition metal oxides has been shown to be possible *via* molten salt synthesis, mechanochemical activation and microwave sintering techniques as described in Table 6-1.

The solid solutions of Ni and Co molybdate and $Ni_{1-x}Co_xMoO_4$ composite have shown high catalytic performance for the oxidative dehydrogenation reaction of propane. Yoon *et al*. prepared a series of metal molybdate catalysts $MMoO_4$ (M = Mg, Ca, Zn, Co, Ni, Mn, Cu) and $M_2Mo_3O_{12}$ (M = Fe, Bi, Ce, La, Sm, Al, Cr) *via* a co-precipitation method and investigated them for propane oxidation in the temperature range 430-500 ºC. It was found that the catalytic performance is transition metal type dependent. Among all the investigated

catalysts, $CoMoO_4$ was active and selective for this reaction. Other compositions such as $NiMoO_4$, $CuMoO_4$, $Cr_2Mo_3O_{12}$, $Al_2Mo_3O_{12}$, and $Fe_2Mo_3O_{12}$ catalysts showed high performance but were non-selective. In contrast, $MnMoO_4$ demonstrated a very poor activity.[217] Mani *et al*. synthesized $NiMoO_4$ nanocrystal *via* a hydrothermal process, and reported a high performance for non-enzymatic glucose sensors. [215] Baoyi *et al*. studied the impact of the synthesis method on catalytic activity of α-$NiMoO_4$ and β-$NiMoO_4$ for propane oxidation reaction. It was found that β-$NiMoO_4$ prepared by the sol gel method gave excellent low temperature catalytic activity compared to α-$NiMoO_4$ prepared by the hydrothermal route.[218] These phases were also tested for hydrodesulfurisation reactions by Brito *et al*. It has been found that β-$NiMoO_4$ showed a better catalytic activity than α-$NiMoO_4$.[219] Chen *et al*. prepared the $NiMoO_4$ and iron doped $Ni_{0.9}Fe_{0.1}MoO_4$ samples using a facile hydrothermal method. In comparison to the $NiMoO_4$ sample, the iron-doped sample exhibited significant catalytic activity for alkaline oxygen evolution reaction.[220] Liao *et al*. prepared $Co_{0.8}Cu_{0.2}MoO_4$ through the hydrothermal method and investigated its catalytic activity for the hydrolysis of Ammonia Borane.[221] Different compositions of $Cu_{1-x}Co_xWO_4$ (x = 0; 0.5; 1) were synthesized using the co-precipitation method and examined for their activity for hydrodeoxygenation reaction (HDO).[222] Alshehri *et al*. prepared a $CoWO_4$ using a molten salt method, and reported its efficiency towards the water redox reactions for oxygen evolution and oxygen reduction reactions.[223] He also employed the same method for preparing $NiMoO_4$ samples.[224] Bi *et al*. prepared nanostructured $NiMoO_4$ sample *via* a hydrothermal process and investigated its catalytic performance for the hydrodesulfurisation reactions. It was found that the $NiMoO_4$ sample showed a significant activity, higher than that of commercial NiW/Al_2O_3.[216] The simple co-precipitation method has been employed by Niu *et al*. to prepare amorphous $NiMoO_4$ nanostructured samples.[225] García-pérez *et al*. used the co-preciptation method to prepare a series of MWO_4 (M= Ni^{2+}, $Cu^{2+}$and Co^{2+}). The $CuWO_4$ sample exhibited the best photocatalytic activity.[209] Quintana-Melgoza *et al*. examined the effect of the reaction temperature on particle size and the surface area of $NiWO_4$ that was synthesised by reacting ammonium metatungstate and nickel nitrate as a function of temperature.[226] Mancheva *et al*. prepared nanostructured $NiWO_4$ through a mechanochemical activation route.[227] Tian *et al*. synthesized $NiWO_4$ nanoparticles by using an ethylene glycol-assisted solvothermal method.[228] A simple**,** eco-friendly, and cost-effective hydrothermal method has been reported by Rajagopal *et al*. to optimize the nanostructured $FeWO_4$ and $CoWO_4$ and investigate their chemical properties.[229] The hydrothermal route has been employed by Li *et al*. using urea as a starting material for the preparation of the nanostructured $CoWO_4$. This material was also prepared by Pan *et al*. *via*

the hydrothermal method.[230] Rico *et al*. synthesised $NiWO_4$ and $CoWO_4$ through co-precipitation method.[79] Li *et al*. prepared the $Co_{0.5}Ni_{0.5}MoO_4$ by a scale up spray-drying method.[231] A series of $Ni_xCo_{1-x}MoO_4$ ($0 \leq x \leq 1$) prepared *via* the hydrothermal technique.[232]Naik *et al*. prepared $Co_{1-x}Cu_xWO_4$ (x = 0; 0.3; 0.5; 0.7 and 1.0) through the co-precipitation method.[233] De Moura *et al*. synthesised α, β-$NiMoO_4$ *via* a microwave sintering technique.[234] Rodriguez *et al*. reported the transformation between a series of cobalt and nickel molybdate phases. For example β-$NiMoO_4$ was obtained upon heating the $NiMoO_4 \cdot nH_2O$ hydrate to 500 ºC, then quenching from 300 ºC, wherease slow cooling to room temperature led to α-$NiMoO_4$. α-$CoMoO_4$ was also obtained upon grinding the β-$CoMoO_4$. Table 6-1 presents a summary of the reported different routes to synthesising transition metal oxides.

Table 6-1 Synthetic procedures for transition metal oxide materials based on Mo or W.

Synthesis method	Precursors	Reaction conditions (°C, time)	Product	Ref
Precursor decomposition	$NiMoO_4 \cdot nH_2O$	550 ºC, cooling to 300 ºC	(β-$NiMoO_4$)	210
Precursor decomposition	$NiMoO_4 \cdot nH_2O$	550 ºC, cooling to room temperature	(α-$NiMoO_4$)	210
Precursor decomposition	$CoMoO_4 \cdot nH_2O$	550 ºC, 100 °C/min to room temperature	β-$CoMoO_4$	210
Phase change	β-$CoMoO_4$	Grinding	α-$CoMoO_4$	210
Co-precipitation	Corresponding metal nitrates + $(NH_4)_6Mo_7O_{24}$ + NH_4OH	Evaporation at 80°C. Calcined in air at 300°C for 3 h, calcined for 5-9 h at 450-600 °C.	$AMoO_4$ (A = Mg, Ca, Zn, Co, Ni, Mn, Cu) $A_2Mo_3O_{12}$ (A = Fe, Bi, Ce, La, Al, Cr)	217
Hydrothermal synthesis	$Na_2WO_4 \cdot 2H_2O$, $NiCl_2 \cdot 6H_2O$	Treated at 180 °C for 5 h, Dry overnight. Calcined in air at 300 °C for 2 h	$NiWO_4$	215
Sol- gel procedure	Ni $(NO_3)_2 \cdot 6H_2O$ + $(NH_4)_6Mo_7O_{24} \cdot 4H_2O$ + Citric acid	Evaporated at 75°C, solidified at 120 °C for 24 h, calcined at 500°C for 4h, 2°C/min	β-$NiMoO_4$	218
Hydrothermal route	Ni $(NO_3)_2 \cdot 6H_2O$ + $(NH_4)_6Mo_7O_{24} \cdot 4H_2O$	Ultrasound for 15 min, Teflon lined stainless steel autoclave 140 ºC for 12 h. Dry at 120°C for 24 h, 500 °C at 2°C/min, calcined at 500°C for 4 h.	α-$NiMoO_4$	218

Sol-gel method	Ni $(NO_3)_2 \cdot 6H_2O$ + $(NH_4)_6Mo_7O_{24} \cdot 6H_2O$+ Citric acid (aq)+	Evaporation at 75°C, solidified at 120°C for 24h. 500 ºC for 4 h at 2°C/min	β-$NiMoO_4$	219
Hydrothermal synthesis	Ni $(NO_3)_2 \cdot 6H_2O$ (aq) + $(NH_4)_6Mo_7O_{24} \cdot 6H_2O$ +	Teflon-lined stainless-steel autoclave 140 ºC for 12 h. Dry at 120 °C for 24 h. 500°C at 2°C/min. Calcined at 500 °C for 4h.	α-$NiMoO_4$	219
Hydrothermal process	Ni $(NO_3)_2 \cdot 6H_2O$ + $Na_2MoO_4 \cdot 2H_2O$+ $Fe(NO_3)_2 \cdot 9H_2O$+ Urea	Teflon lined stainless steel autoclave 160 ºC for 8 h. Dry at 65 ºC for 10 h. 500 °C for 2 h	$Ni_{0.9}Fe_{0.1}MoO_4$	220
Hydrothermal process	$CoCl_2$+ $CuCl_2$+ Molybdic acid +Urea	Teflon lined stainless steel autoclave 160 ºC for 8 h. Dry at 165 ºC for 7 h. Annealing in air at 500 °C for 2 h	$Co_{0.8}Cu_{0.2}MoO_4$	221
Co-precipitation method	(Na_2WO_4)(aq) + $CuCl_2$(aq) + $Cu(NO_3)_2$(aq)	Dry at 110 °C for 2 h, calcined at 750 °C,10 °C min^{-1} for 5 h.	$Cu_{1-x}Co_xWO_4$, $x = 0; 0.5; 1$	222
Molten salts method	$CoC1_2 \cdot 6H_2O$+ $Na_2WO_4 \cdot 2H_2O$+ ($NaNO_3$+ KNO_3)	Firing at 500 ºC in air for 6 h. Dry in oven at 60 ºC	$CoWO_4$	223
The modified molten salts	Ni $(NO_3)_2 \cdot 6H_2O$+ $Na_2WO_4 \cdot 2H_2O$+ ($NaNO_3$ + KNO_3)	500 ºC and 6 h. Dry at 50 ºC in air.	$NiWO_4$ 25 $m^2\ g^{-1}$	224

Hydrothermal synthesis	$Na_2WO_4 \cdot 2H_2O$ + Ni $(NO_3)_2 \cdot 6H_2O$	Teflon lined stainless steel autoclave 453 K for 4 h. Dry at 393 K for 4 h.	$NiWO_4$ 126 $m^2\ g^{-1}$ 7.8 nm	216
Co-precipitation	$Na_2WO_4 \cdot 2H_2O$, $NiCl_2 \cdot 6H_2O$	stirring at 70 °C for about 10 min, stirred at 70 °C for 3 h, centrifugation. Dry under vacuum at 60 °C, calcined 600 °C for 1 h.	$NiWO_4$ 26.3 $m^2\ g^{-1}$ 3.3 nm	225
Co-precipitation	$Na_2WO_4 \cdot 2H_2O$ + Ni $(NO_3)_2 \cdot 6H_2O$+ $CuCl_2 \cdot 2H_2O$+ $(Co(NO_3)_2 \cdot 6H_2O$	Dry at 90 ºC for 24h, 400 ºC for 24 h	$NiWO_4$ $CuWO_4$ $CoWO_4$	209
	$N_{26}H_6O_{41}W_{12} \cdot 18H_2O$ + Ni $(NO_3)_2 \cdot 6H_2O$	673 to 1073 K in O_2 for 1 h	$NiWO_4$ 16 to 3 $m^2\ g^{-1}$ 55 to 112 nm	226
Mechanochemical activation Planetary ball mill	NiO + WO_3	800 ºC	$NiWO_4$ 30 nm, 3 $m^2\ g^{-1}$	227
Solvothermal method	Ethylene glycol $((CH_2OH)_2)$ + $NiCl_2 \cdot 6H_2O$ +	Teflon-lined stainless-steel autoclave 180 ºC for 12 h. Dry under vacuum at 60 °C overnight.	$NiWO_4$	228
Hydrothermal process	$Na_2WO_4 \cdot 2H_2O$+ $CoC1_2 \cdot 6H_2O$+ $[(NH_4)_2Fe(SO_4)_2 \cdot 6H_2O]$+ NaOH	Teflon lined stainless steel autoclave 180 ºC for 24 h, 100 ºC for 2 h	$CoWO_4$ $FeWO_4$	229

Hydrothermal process	$CoC1_2 \cdot 6H_2O + Na_2WO_4 + C_6H_7KO_2$	Teflon lined stainless steel autoclave 150 ºC for 14 h. Dry in vacuum at 80 ºC for 6 h	$CoWO_4$	230
Co-precipitation	$Ni(NO_3)_2 \cdot 6H_2O$+ $Na_2WO_4 \cdot 2H_2O$+ $Co(NO_3)_2 \cdot 6H_2O$	Teflon lined stainless steel autoclave 150 ºC for 15 h, Dry overnight at 110 ºC, 500 ºC for 5 h	$CoWO_4$ 4.5 $m^2\ g^{-1}$ $NiWO_4$ 3.8 $m^2\ g^{-1}$	79
Spray-drying method	$Mo + Co(NO_3)_2 \cdot 6H_2O + Ni(NO_3)_2 \cdot 6H_2O$ + sucrose + H_2O_2	Stirring at 70 ºC for 12 h. Dry at 220 ºC, 600 ºC for 3 h in air.	$Co_{0.5}Ni_{0.5}MoO_4$	231
Hydrothermal process	$Ni(NO_3)_2 \cdot 6H_2O$ + $Co(NO_3)_2 \cdot 6H_2O$ + $Na_2MoO_4 \cdot 2H_2O$	Teflon lined stainless steel autoclave 180 ºC for 8 h. Dry under vacuum at 60 ºC for 6 h. 500 °C for 2 h.	$Ni_xCo_{1-x}MoO_4$ x = 0; 0.25; 0.5; 0.75 and 1. 8-39 $m^2\ g^{-1}$	232
Co-precipitation method	$Na_2MoO_4 \cdot 2H_2O$ $Cu(NO_3)_2 \cdot 2H_2O$ $Co(NO_3)_2 \cdot 6H_2O$	Dry at 100 °C for two days, 500 °C for 5 h.	$Co_{1-x}Cu_xWO_4$, x = 0; 0.3; 0.5; 0.7 and 1. 30-50 nm	233
Hydrothermal method	$(NH_4)_6Mo_7O_{24} \cdot 4H_2O$+ $CoC1_2 \cdot 6H_2O$+ urea	Teflon lined stainless steel autoclave 120 ºC for 12 h. Dry at 60 ºC for 12 h, 500 ºC for 3 h	$CoMoO_4$	235
Hydrothermal method	$Co(NO_3)_2 \cdot 6H_2O$, $(NH_4)_6Mo_7O_{24} \cdot 4H_2O$, urea	Stirring for 1h, Teflon-lined stainless-steel autoclave at 180 °C for 1 h. Dry at 60 °C in vacuum, 400 °C in air for 2 h.	$CoMoO_4$	236
Microwave Sintering	$Na_2WO_4 \cdot 2H_2O$ + $Ni(NO_3)_2 \cdot 6H_2O$	Dry at 60 ºC for 12 h in air. 600 ºC for 10 minutes	α, β-$NiMoO_4$	234

6.2 Metal oxide precursors to ternary nitrides

Metal tungstates (AWO_4; A is a bivalent ion with relatively small radius such as Ni, Co, Fe and Mg) have been found to adopt the monoclinic wolframite-type structure. These are common precursors to metal nitrides such as Co_3W_3N. The crystal structure of a wolframite was first reported by Broch in 1929 using diffraction methods, but was not completely determined by Keeling until 1957.[237] Examples of this type of structure are shown in Figure 6-1.

The wolframite structure can simply be described as slightly distorted hexagonal close packing of oxygen atoms. The distorted WO_6 octahedra are joined by edge sharing oxygen atoms forming zig-zag chains orientated along the c axis. The bivalent cations occupy octahedral sites and have corner sharing oxygen atoms, forming zig zag chains of WO_6 units.

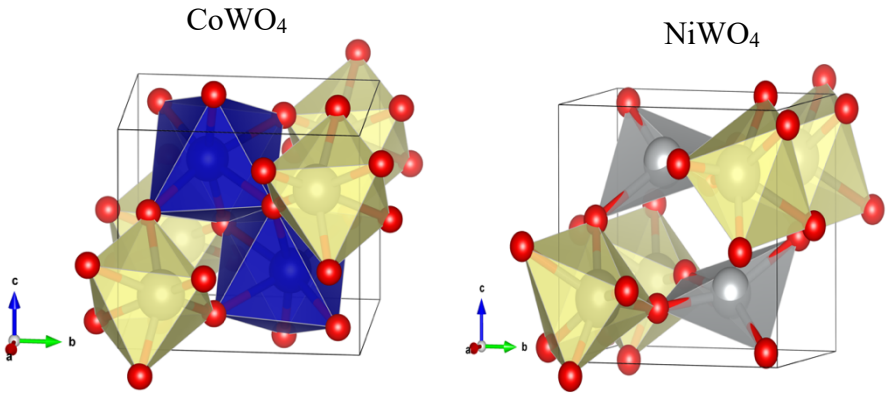

Figure 6-1 Schematic representation of the monoclinic wolframite-type structure, $CoWO_4$ and $NiWO_4$. Co atoms are shaded dark blue; Ni grey; W yellow; O_2 red. Diagrams drawn using Vesta and structure data from Weitzel.[238]

Three polymorphic forms of $CoMoO_4$ (Figure 6-2) have been reported; the low temperature α-phase with (space group *C2/m*, the high pressure (*hp*-) phase with (space group *P2/c*), and the hydrate a violet phase with (space group $P\bar{1}$).[239, 240, 241, 41]

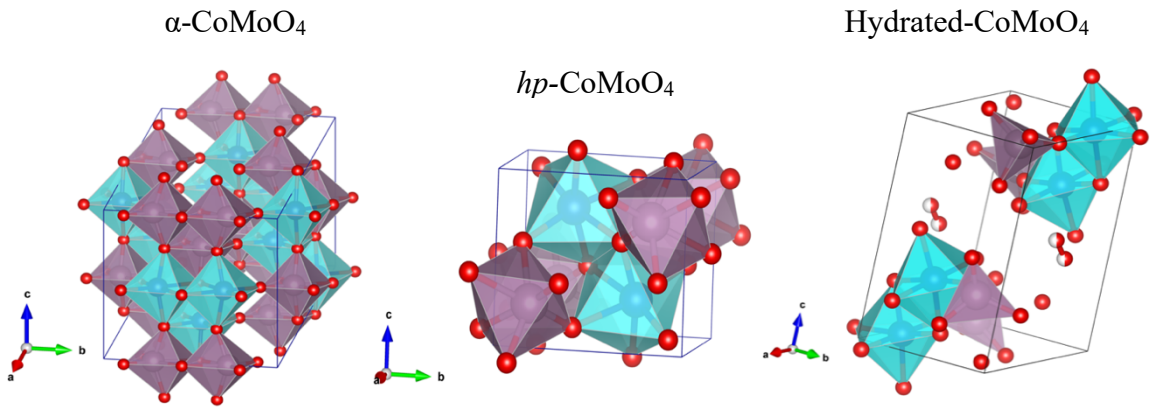

Figure 6-2 Schematic representation of the crystalline structure of different $CoMoO_4$ polymorphous α-, (*hp*-), and hydrated $CoMoO_4$ unit cell's. Diagram drawn using Vesta and structure data for α-, (*hp*-), and hydrated $CoMoO_4$ from Smith [242,] Livage *et al* [243] and Eda *et al* [244].

Nickel molybdates, $NiMoO_4$, are part of group of minerals that are subdivided into two isostructural categories: the wolframite or scheelite. $NiMoO_4$ typically adopts the scheelite structure, where A has a coordination number of eight, while the Mo cation is tetrahedrally coordinated to oxygen. The wolframite type structure consisting of close-packed oxygen ions with A and Mo cations occupying some of the octahedral sites. Under ambient pressure, three different phases of nickel molybdate (shown in Figure 6-3) can exist: the low temperature α-$NiMoO_4$ (space group *C2/m*), the high temperature β-$NiMoO_4$ (space group *P2/c*) and the hydrate $NiMoO_4 \cdot nH_2O$ (space group $P\bar{1}$).[245, 246]

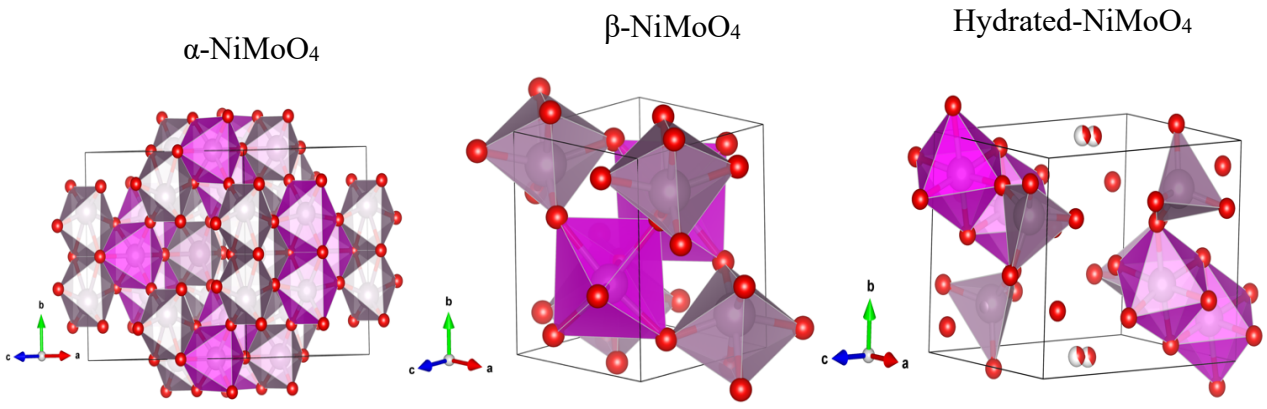

Figure 6-3 Scheme of the crystal structures of the polymorphous α-, β-, and hydrated $NiMoO_4$ unit cell's. Diagram drawn using Vesta and structure data for α-, β-, and hydrated-$NiMoO_4$ from Ehrenberg *et al* [173] , Wiesmann *et al* [247], Eda *et al* [248]

Several synthetic routes have been developed to synthesise nickel molybdate. Maione *et al* synthesised the nickel molybdate *via* sol the gel method.[249] Nanocrystalline $NiMoO_4$ was prepared *via* a citrate complex technique by Ryu *et al*.[250] Wang *et al*. successfully developed $NiMoO_4$ through a facile hydrothermal process.[251] Co-precipitation route is one of the most prevailing methods for producing nickel molybdate as catalyst.[252] Similar method from aqueous solutions of soluble salt was also employed by Kang *et al* for the production of $NiMoO_4 \cdot nH_2O$.[253] The nickel molybdate nanoparticles were developed by Alborzi *et al*. *via* a sonochemical route using ammonium molybdate and nickel nitrate hexahydrate in water without surfactant.[254] A novel approach was applied by Moreno *et al*. to prepare β-$NiMoO_4$ based on combustion synthesis.[255] In another study the same method was used to prepare α-$NiMoO_4$ by Baskar *et al*.[256] Among the different methods for the synthesis of nanoparticles, thermal decomposition has been reported as a novel technique to produce stable monodispersed particles which is a rapidly developing research area.[257] Compared to other processes, it is much faster, cleaner and economical. However, an improvement in the thermal decomposition process should be made to allow better control of shape and size of the particles. In this study, the nickel molybdate nanoparticles were prepared using citrate sol gel method. This process led to a mixture of α-$NiMoO_4$ and MoO_3, which is consistent with the previously published observations of Alconchel *et al*.[96]

Metal oxide materials have excellent catalytic properties. However, no literature was found on the application of these nanostructured molybdenum oxide-based materials as catalysts for ammonia synthesis. Therefore, in this chapter, a range of nanostructured metal oxide materials with different chemical compositions namely (Co-Mo-O) $Co_3Mo_3O_x$, (Co-W-Mo-O) $Co_3W_{0.8}Mo_{2.2}O_x$, (Ni-Mo-O) $Ni_2Mo_3O_x$,(Ni-Cu-Mo-O) $Ni_{1.8}Cu_{0.2}Mo_3O_x$, (Ni-Fe-Mo-O) $Ni_{1.2}Fe_{0.8}Mo_3O_x$ and (Ni-Fe-Mo-O) $Ni_2W_{0.3}Mo_{2.7}O_x$, have been developed and evaluated for the ammonia synthesis reaction. During these reactions they convert to the metal nitrides.

6.3 Results and discussion

The transition metal molybdates were the starting materials for the synthesis of the quaternary metal nitrides in previous chapters. The molybdates were formed *via* the citrate sol gel method as described in chapters 3, 4, and 5. The nitride materials were prepared *in- situ* in a fixed bed microreactor. 0.15 g of the metal oxides were activated at 700 °C for 2 h with 3:1 H_2/N_2 mixture (BOC, 99.998 % at a total gas feed of 12 ml min^{-1}, before reducing the temperature and testing catalytic activity.

6.3.1 Catalytic activity

The oxide materials were activated under the same conditions used for the metal nitrides described in chapters 3, 4 and 5). The performance of transition metal molybdate based materials for ammonia synthesis reaction was measured at ambient pressure using 75 vol. % H_2 in N_2 (BOC, 99.98 %) at 500 °C after activation of the catalysts at 700 °C for 2 h. The reaction run was repeated to confirm reproducibility. Low ammonia production rate was observed at lower temperatures 400 °C, whereas increasing the temperature to 500 °C resulted in increased ammonia formation. Figure 6-4 shows the ammonia production rate at 500 °C as a function of time. The reaction profile in Figure 6-4 shows that the materials exhibited a steady state rate of synthesis. The ammonia synthesis rate can be calculated from the gradient in this profile. From the data listed in Table 6-2, it is apparent that the pre-treated materials with 3/1 H_2/N_2 ammonia synthesis stream at 700 °C were found to be highly active for ammonia synthesis compared to their pre-nitrided counterparts (chapters 3, 4 and 5) which could possibly be related to the surface area.

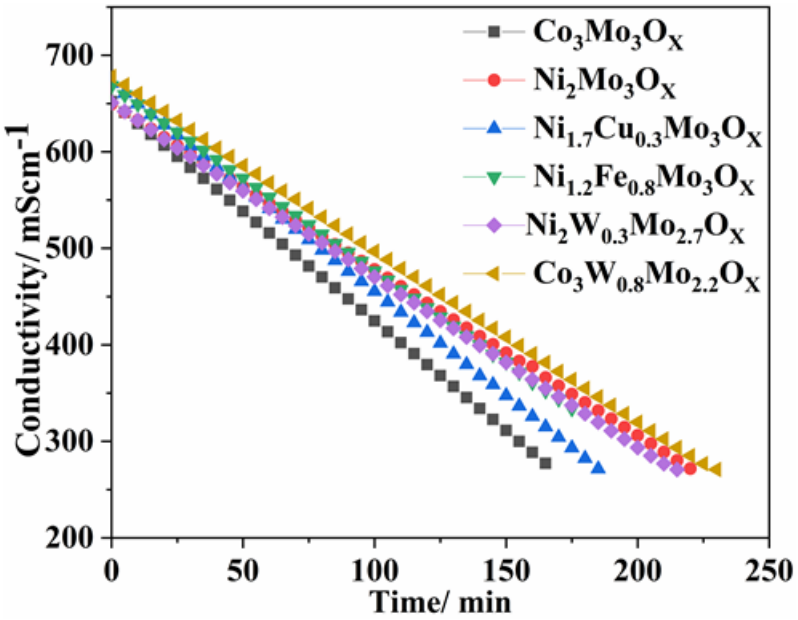

Figure 6-4 Conductivity profile for the transition metal molybdate reacted with 75 vol. % H_2 in N_2 at 700 °C materials reacted with 75 vol. % H_2 in N_2 then used to synthesis ammonia at 500 °C.

For comparison, the (Co-Mo-O) $Co_3Mo_3O_x$ sample exhibited the highest ammonia formation rate of 484(9) μmol-NH_3 g^{-1} h^{-1} which is similar to a previously reported Co_3Mo_3N catalyst with rate of 489(17) μmol-NH_3 g^{-1} h^{-1},[41] and almost three times greater than that evaluated at 400 °C (165 μmol-NH_3 g^{-1} h^{-1}).[258] Upon the inclusion of the tungsten

metal into the system the activity of the obtained $Co_3W_{0.8}Mo_{2.2}O_x$ catalyst was observed to decline from 484(9) μmol-NH_3 g^{-1} h^{-1} to 407(12) μmol-NH_3 g^{-1} h^{-1}. Similar observation was observed in the case of $Co_3W_{0.8}Mo_{2.2}N$ (chapter 5) under the same reaction conditions, the ammonia formed from $Ni_2Mo_3O_x$ displayed a rate of 466(16) μmol-NH_3 g^{-1} h^{-1}, which is very high when compared against the activity of the reported Ni_2Mo_3N system evaluated at 400 °C. This reaction rate is higher than previously reported Ni_2Mo_3N systems, with rates of 383(22) μmol-NH_3 g^{-1} h^{-1} and 395(6) μmol-NH_3 g^{-1} h^{-1} generated by ammonolysis and reduced under H_2/N_2 gas mixture, respectively.[40] Interestingly these materials exhibited significantly higher mass-normalised ammonia synthesis rates Table 6-2 than in the pre-formed nitrides which appears to be due to higher surface areas Table 6-2. The activity has not scaled linearly with surface area, as these catalysts have lower area-normalised activities than the pre-formed nitrides Tables 6-2, but nonetheless the increase supports the idea that increasing surface area could lead to higher overall activity levels in these materials.

The nitrogen contents of the post reaction oxide samples were identified using CHN microanalysis and the values are shown in Table 6-2. The nitrogen content of Ni_2Mo_3N was 3.08 which similar to the reported one 3.13 wt. %.[40] The Ni_2Mo_3N catalysts prepared by treating the metal oxide precursors with H_2/N_2 gas mixture was found to have higher performance than the reported one, their activities were around 448(13) and 395 μmol-NH_3 g^{-1} h^{-1}, respectively.[40]

Table 6-2 Nitrogen content, ammonia synthesis rates and specific activity of metal nitride catalysts formed *in situ* and used in ammonia synthesis.

Catalyst	Nitrogen content (wt.% post-catalysis)	Ammonia synthesis rate at 500 °C (μmol g^{-1} h^{-1})	Specific activity at 500 °C[a] (μmol h^{-1} m^{-2})
Ni_2Mo_3N	3.1	466(18)	78(3)
$Ni_{1.7}Cu_{0.3}Mo_3N$	3.3	368(9)	74(2)
$Ni_{1.2}Fe_{0.8}Mo_3N$	3.2	426(4)	82(1)
$Ni_2W_{0.3}Mo_{2.7}N$	3.0	454 (13)	99
Co_3Mo_3N	2.8	484(9)	69
$Co_3W_{0.8}Mo_{2.2}N$	2.2	407(12)	97

[a] Calculation based on the surface area of the nitride phase post-catalysis.

6.3.2 Pre- and post-catalysis reaction characterisation of the catalysts formed from *β*-$CoMoO_4$

Figure 6-5 (a) shows the powder X-ray diffraction pattern for the anhydrous β-$CoMoO_4$ produced from a citrate gel as described in section 5.2.1 and calcined at 500 °C. It can be

seen that the pure β-$CoMoO_4$ phase had identical peaks that corresponding with the monoclinic β-$CoMoO_4$ (JCPDS21-0868) [259] having space group C2/m (space group number 12) with unit cell a = 10.22 b = 9.28, c = 7.11 Å, β = 106.5, γ = α = 90°. The crystallites size determined using the Scherer equation was 14(12) nm. The evaluated surface area was 18 $m^2\ g^{-1}$, which is larger than the reported previously in literature of 7 $m^2\ g^{-1}$.[41] The post catalysis reaction sample Figure 6-5 (b) was almost not crystalline structure.

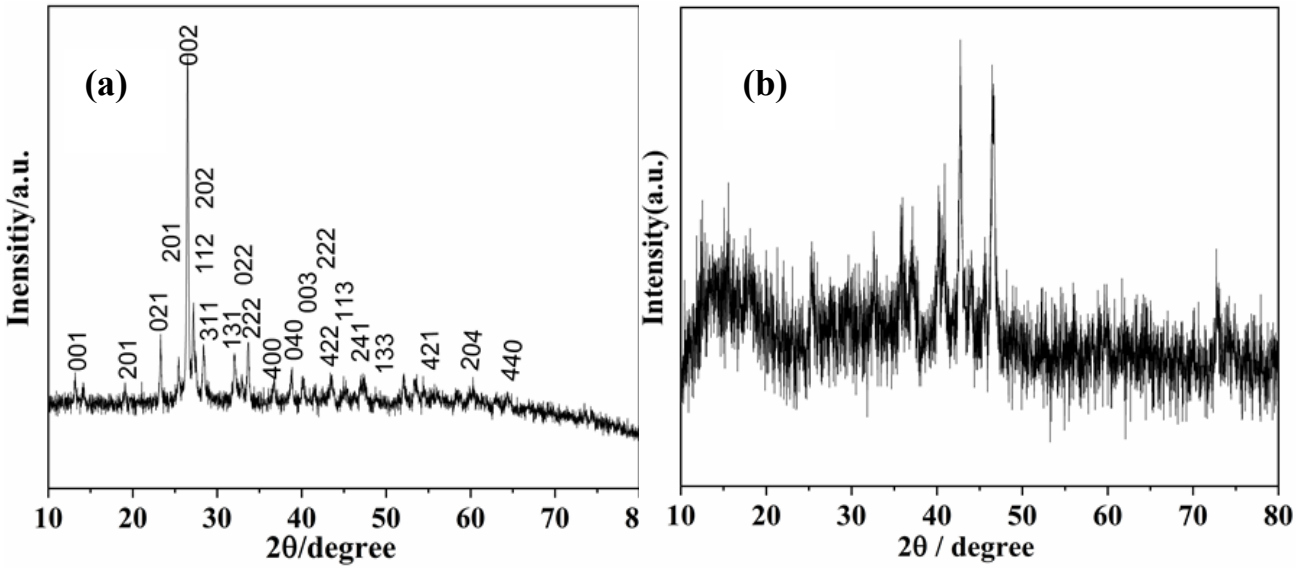

Figure 6-5 Powder X-ray diffraction pattern of the β-$CoMoO_4$ calcined at 500 °C for 2 h in air (a) and the Co_3Mo_3N product after catalysis (b).

The morphological changes of the pre-and post-catalysis β-$CoMoO_4$ sample were studied using scanning electron microscopy (SEM). The calcination process of the precursor gels in air atmosphere resulted in the formation of powder containing finer particles as shown in Figure 6-6 (a). From figure 6-6 (b), it is clear that the two types of the aggregated particles were observed in the post-reaction sample.

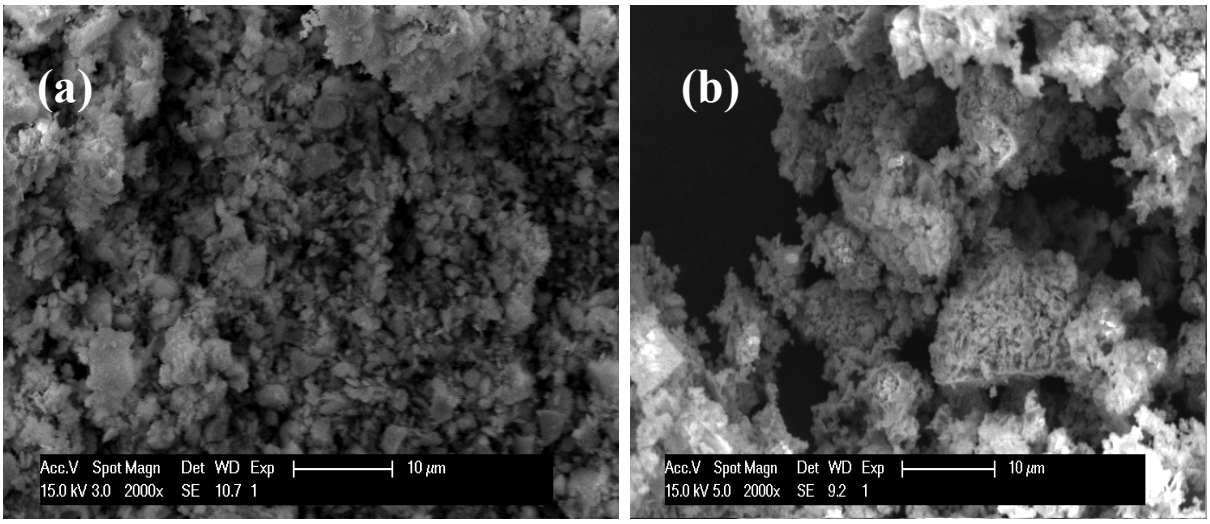

Figure 6-6 SEM images showing the microstructure of as-prepared β-$CoMoO_4$ (a; 10 μm) and post-reaction $CoMoO_4$ (b; 10 μm). Magnification: 2000x.

6.3.3 Pre-and post-catalysis reaction of the catalyst formed from α-$NiMoO_4$

The phase purity and structure of the as-prepared and post-catalysis materials was characterised by powder X-ray diffraction. The calcination of the amorphous precursor at 500 ºC for 2 h under air resulted in a yellowish green solid, the powder X-ray diffraction peaks shown in Figure 6.7(a) were mainly indexed to a crystalline monoclinic phase of α-$NiMoO_4$ with the space group of *I2/m* and the typical strongest peak at 2θ = 28.7° (JCPDS Card No. 33-0948).[96] The rest of the diffraction peaks can be assigned to MoO_3 (JCPDS Card No. 35-0609),[96] indicating that the $NiMoO_4$ nanostructure phase is a mixture of α-$NiMoO_4$ along with the simple oxide of MoO_3.[96] The lattice parameters were a = 9.55 (5) Å, b = 8.7(4) Å, c = 7.6 (3) Å, and β = 114°, γ = α = 90°. The crystallite size and surface area were 15 nm and 10 $m^2\ g^{-1}$, respectively. The PXRD pattern of the post-catalysis reaction (*in- situ*) (Figure 6-7 (b)) revealed pure phase material. The structure of the Ni_2Mo_3N was refined and the data obtained are summarised in Table 6-3.

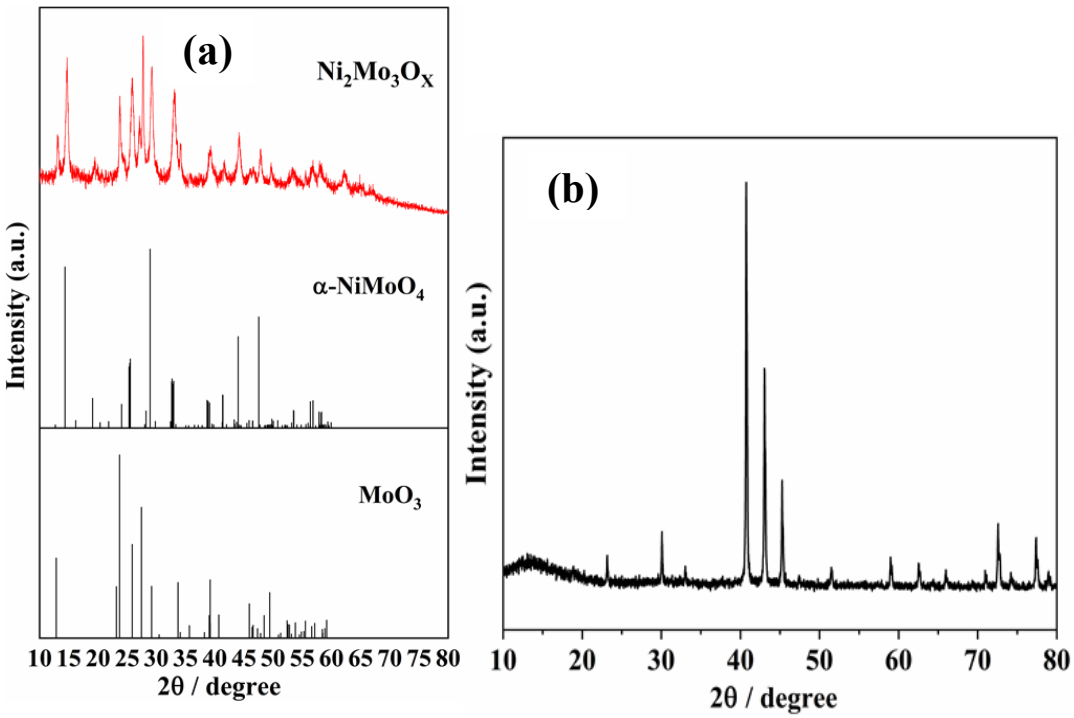

Figure 6-7 Powder X-ray diffraction pattern of the as-prepared (α-$NiMoO_4$ and MoO_3 (a)) and the Ni_2Mo_3N product after catalysis reaction(b).

In order to gain insight into the morphology transformation before and after ammonia synthesis reaction, the morphological structures of two crystalline forms of the $NiMoO_4$ catalysts were examined using scanning electron microscopy (SEM). (Figure 6-8(a)) reveals that the morphology of as-synthesised nickel molybdate has significantly changed. It can be seen that the precursor shows different sizes of polyhedral faceted particles of MoO_3, with the surface was covered with ball-like particles of α-$NiMoO_4$. The rounded particles are either agglomerated or isolated with porous structures were observed after ammonolysis (Figure 6-8(b)). The SEM image observation of the precursor is line with that made by Alconchel *et al*.[96]

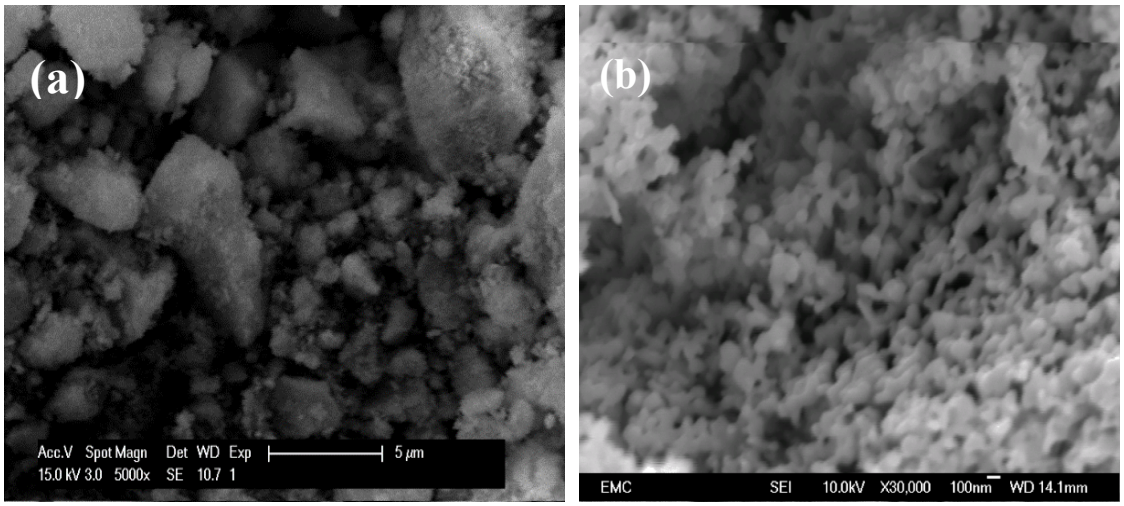

Figure 6-8 SEM images showing the microstructure of as synthesized (α-$NiMoO_4$, MoO_3) (a ;5 μm) obtained at 500°C under air and post-reaction Ni_2Mo_3N produced at 700 °C with H_2/N_2 gas mixture (b; 100 nm). Magnification: 5000x (a), 30000x (b).

6.3.4 Pre- and post-catalysis characterisation of the catalysis formed from $Ni_{1.7}Cu_{0.3}Mo_3O_x$

The crystal structure of the $Ni_{1.7}Cu_{0.3}Mo_3O_x$ precursor was studied using PXRD analysis, as shown in (Figure 6-9 (a)). The observed diffraction peaks are well matched with α-$NiMoO_4$ (JCPDS Card No. 33-0948) and MoO_3(JCPDS Card No. 35-0609). The lattice parameters a = 9.58 Å, b = 8.7 Å, c = 7.65 Å, and β = 114º are in good agreement with the α-$NiMoO_4$. The R_{wp} = 10.8 % and R_p = 8.6 %. The crystallite size of about 10(10) nm was calculated by Scherrer formula using the highest intensity diffraction peak. Post catalysis PXRD data (Figure 6-9(b)) shows extra phase which correspond to that of γ-Mo_2N.

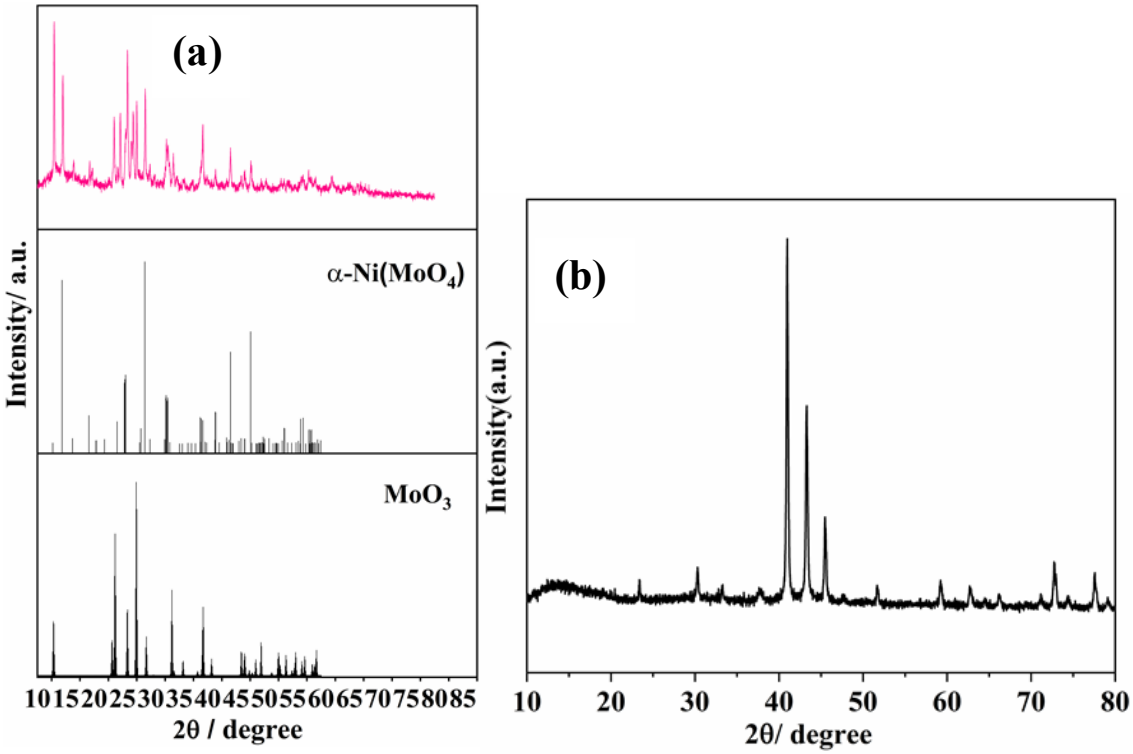

Figure 6-9 Powder X-ray diffraction pattern of the as-prepared $Ni_{1.7}Cu_{0.3}Mo_3O_x$ (a) and the $Ni_{1.7}Cu_{0.3}Mo_3N$ product after catalysis (b).

Figure 6-10 shows the SEM images of the $Ni_{1.7}Cu_{0.3}Mo_3O_x$ synthesised at calcining temperature of 500 ºC and heating rate of 60 ºC min^{-1} (a) and post reaction sample (b). Figure 6-10 (b) shows a set of agglomerated round nanoparticles identical to that of pre-nitride catalysts, presented in section 3-6.

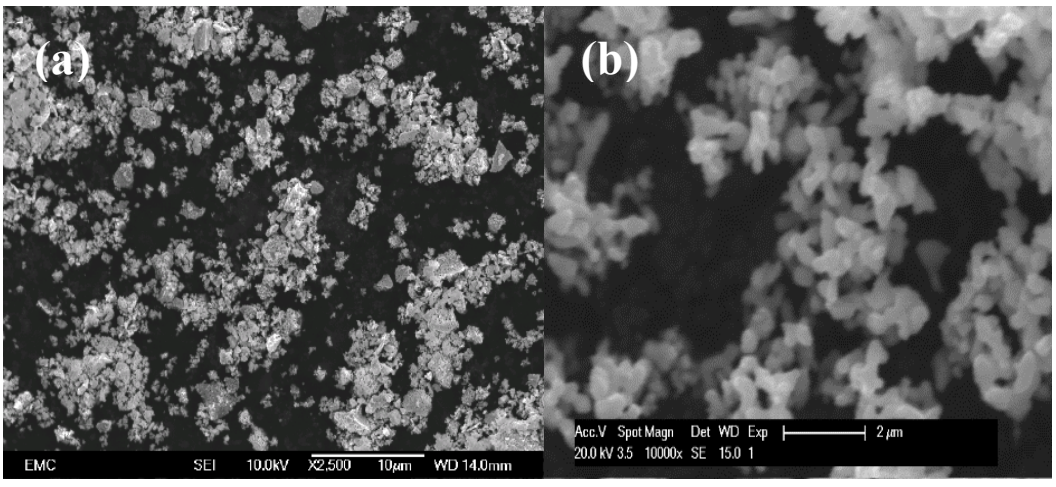

Figure 6-10 SEM images showing the microstructure of as synthesised $Ni_{1.7}Cu_{0.3}Mo_3O_x$ (a ;10 µm scale bar) obtained at 500°C under air and post-reaction $Ni_{1.7}Cu_{0.3}Mo_3N$ produced at 700 °C with H_2/N_2 gas mixture (b; 2 µm scale bar). Magnification: 2.500x (a), 10000x (b).

6.3.5 Pre- and post-catalysis reaction of the catalysis formed from $Ni_{1.2}Fe_{0.8}Mo_3O_x$

The powder X-ray diffraction peaks Figure 6-11 (a) of the resulting the $Ni_{1.2}Fe_{0.8}Mo_3O_x$were mainly consistent with the monoclinic α-$NiMoO_4$ structure (JCPDS Card No. 33-0948), space group (*C2/m*). In addition, some peaks were also detected in this precursor that corresponded to MoO_3 (JCPDS Card No. 35-0609). The refined unit cells: a =11.04(29) Å, b = 9.19(11) Å and c = 7 Å with β = 105°(10). Analysis of the adsorption data with the BET method gives surface of 6.2 $m^2 g^{-1}$. The calculated crystallite size was 7 nm. PXRD data of the post catalysis sample Figure 6-11(b) revealed that γ-Mo_2N phase was presented in the structure.

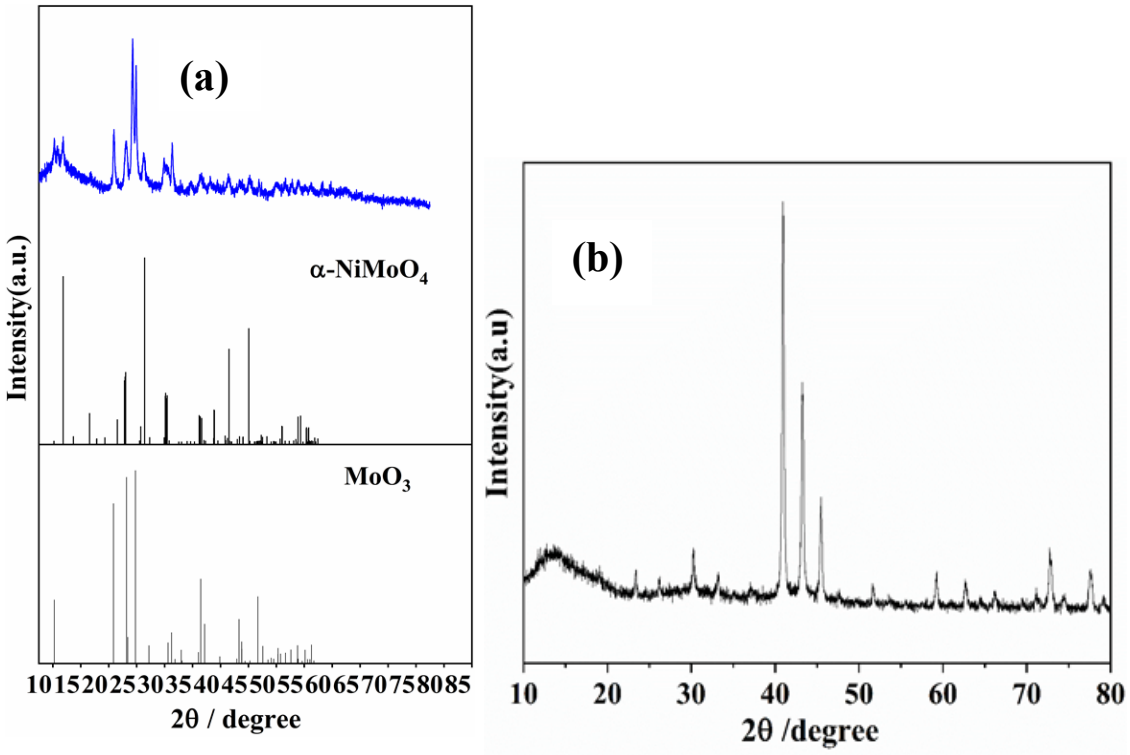

Figure 6-11 Powder X-ray diffraction pattern of the as-prepared and post $Ni_{1.2}Fe_{0.8}Mo_3O_x$ (a) and the $Ni_{1.2}Fe_{0.8}Mo_3N$ product after catalysis (b).

6.3.6 Pre-and post- catalysis reaction of the catalyst formed from $Ni_2W_{0.3}Mo_{2.7}O_x$

The powder X-ray diffraction peaks Figure 6-12(a) of the resulting the $Ni_2W_{0.3}Mo_{2.7}O_x$ were mainly consistent with the monoclinic α-$NiMoO_4$ structure (JCPDS Card No. 33-0948), space group *(*C2/m*)*. In addition, some peaks were also detected in this precursor that corresponded to MoO_3 (JCPDS Card No. 35-0609). The refined unit cells: a = 9.6(17) Å, b

= 8.8(11) Å and c = 7.6 Å with β = 113°(4). Analysis of the adsorption data with the BET method gives surface of 14 $m^2 g^{-1}$. The calculated crystallite size was 13 nm. Post-reaction PXRD pattern contains traces of γ-Mo_2N impurities.

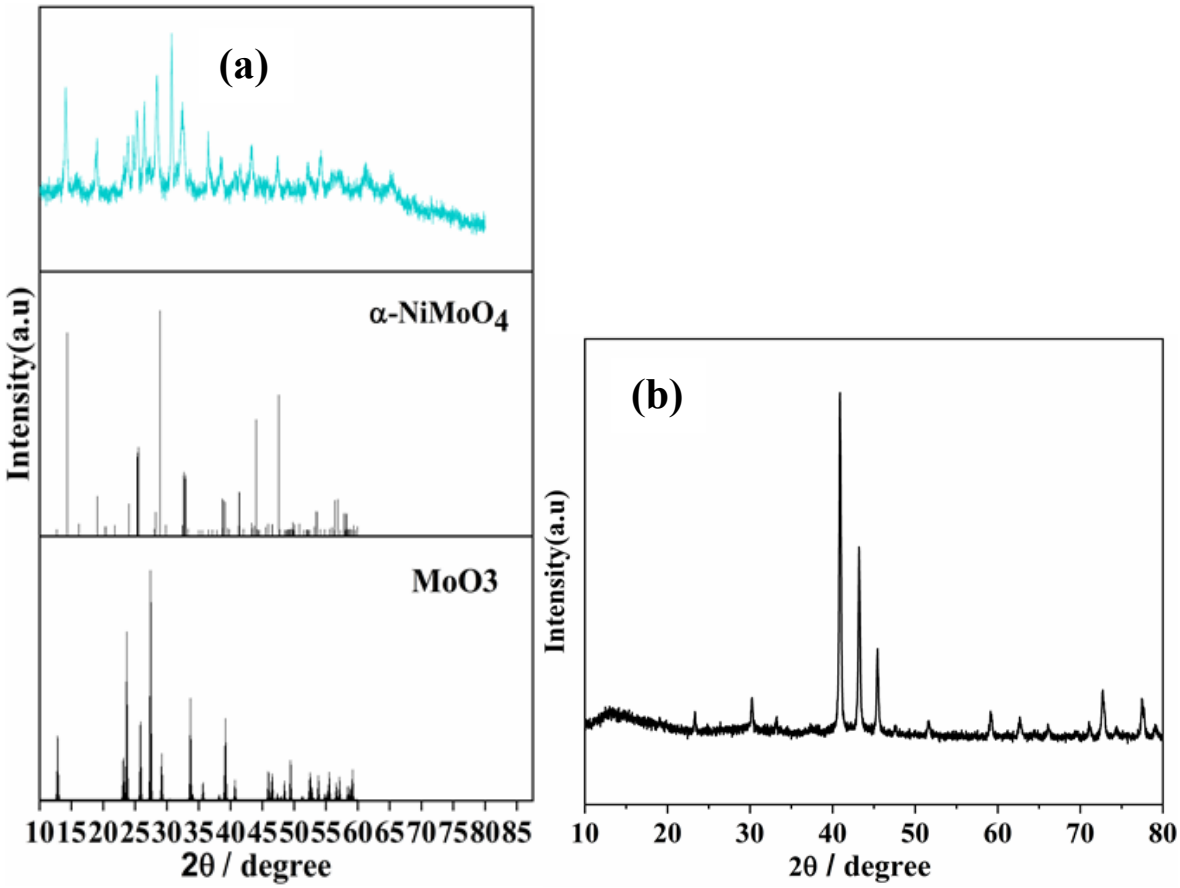

Figure 6-12 Powder X-ray diffraction pattern of the as-prepared and post $Ni_2W_{0.3}Mo_{2.7}O_x$ (a) and the $Ni_2W_{0.3}Mo_{2.7}N$ product after catalysis reaction (b).

The morphology of nickel tungsten molybdate $Ni_2W_{0.3}Mo_{2.7}O_x$ was studied using scanning electron microscopy (SEM). In this characterisation, the image was taken on uncoated pre- and post-catalysis samples at scale bar 1 (Figure 6-13, a) and 5 μm (Figure 6-13, b) with magnifications of 11000x (a), 5000x (b). From (Figure 6-13, a) the pre-catalyst $Ni_2W_{0.3}Mo_{2.7}O_x$ morphology appears to consist of irregular aggregate particles. After the precursor was treated at 700 °C under H_2/N_2 mixed gas, the morphology was completely changed. From Figure 6-13 (a) and (b), it appears that the aggregated particles generating fuzzy nanostructures in post-catalyst. This structure was observed on the pre-catalyst $Ni_2W_{0.3}Mo_{2.7}N$.

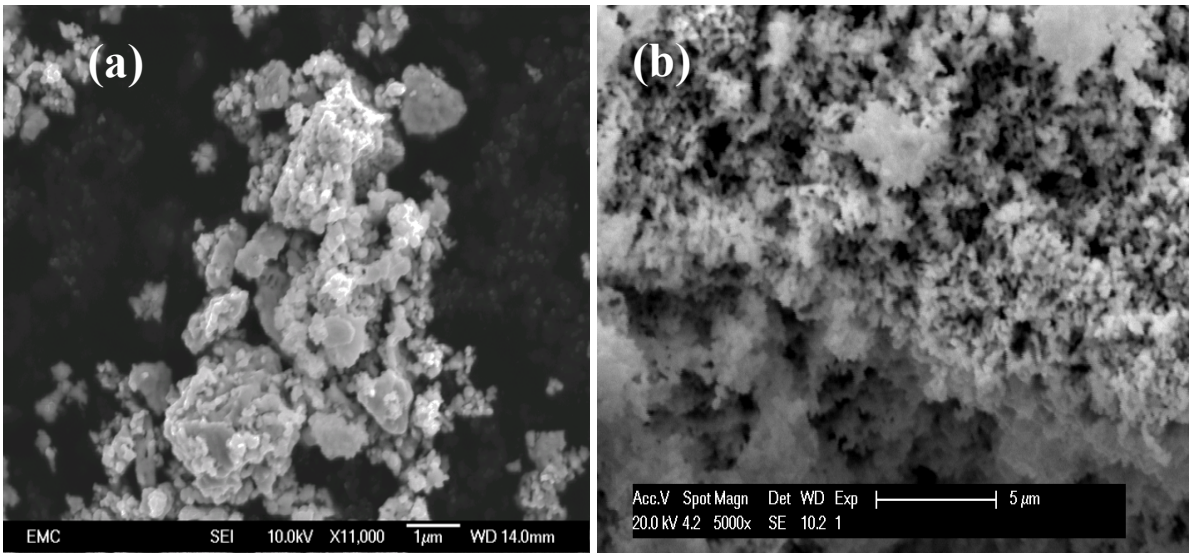

Figure 6-13 SEM images showing the microstructure of as synthesised $Ni_2W_{0.3}Mo_{2.7}O_x$ (a;1 μm scale bar) obtained at 500°C under air and post-reaction $Ni_2W_{0.3}Mo_{2.7}N$ produced at 700 °C with H_2/N_2 ammonia synthesis gas mixture (b; 5 μm scale bar). Magnification: 11000x (a), 5000x (b).

6.3.7 Pre- and post- catalysis characterisation of the catalyst formed from $Co_3W_{0.3}Mo_{2.7}O_x$

The powder X-ray diffraction peaks (Figure 6-14) of the resulting the $Co_3W_{0.3}Mo_{2.7}O_x$ were mainly consistent with the monoclinic $CoMoO_4$-II structure (space group (*P2/c*). In addition, some peaks were also detected in this precursor that corresponded to MoO_3. The refined unit cells: a = 9.7(6) Å, b = 8.9(6) Å and c = 7.7 Å with β = 113°(10). Analysis of the nitrogen adsorption data with the BET method gives surface of 17 $m^2\ g^{-1}$. The calculated crystallite size was 7 nm.

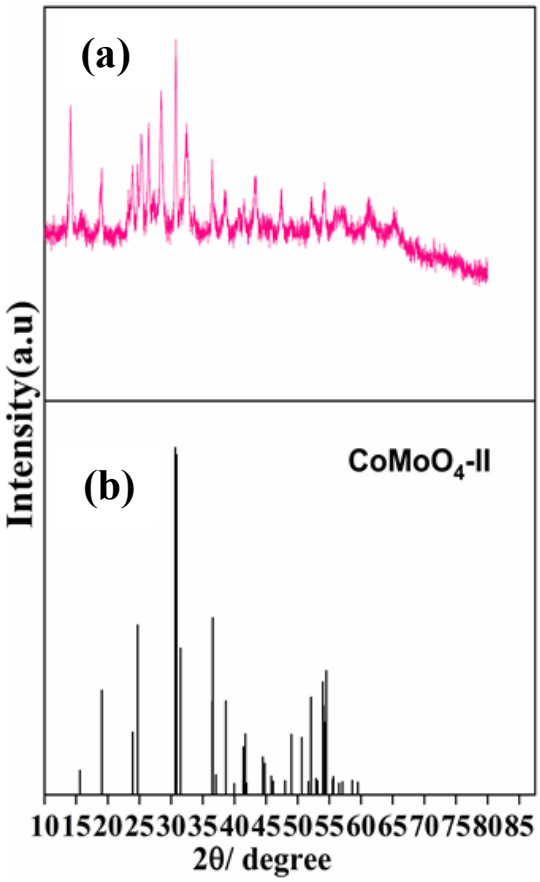

Figure 6-14 Powder X-ray diffraction pattern of the as-prepared $Co_3W_{0.8}Mo_{2.2}O_x$ and the standard file of $CoMoO_4$-II (b).

The morphological structures of the pre-and post-catalysts $Co_3W_{0.8}Mo_{2.2}O_x$ were examined using scanning electron microscopy (SEM). Figure 6-15 (a) and (b) show typical SEM images recorded at the same scale bar and magnifications of 5μm and 5000x, respectively. It can be seen that the precursor is composed of aggregated nanoparticles and the same morphology was retained in the post-catalyst sample. The brightness crystals in the post-catalyst sample Figure 6-15 (b) could be related to the charging. This indicates that the material is non-conductive.

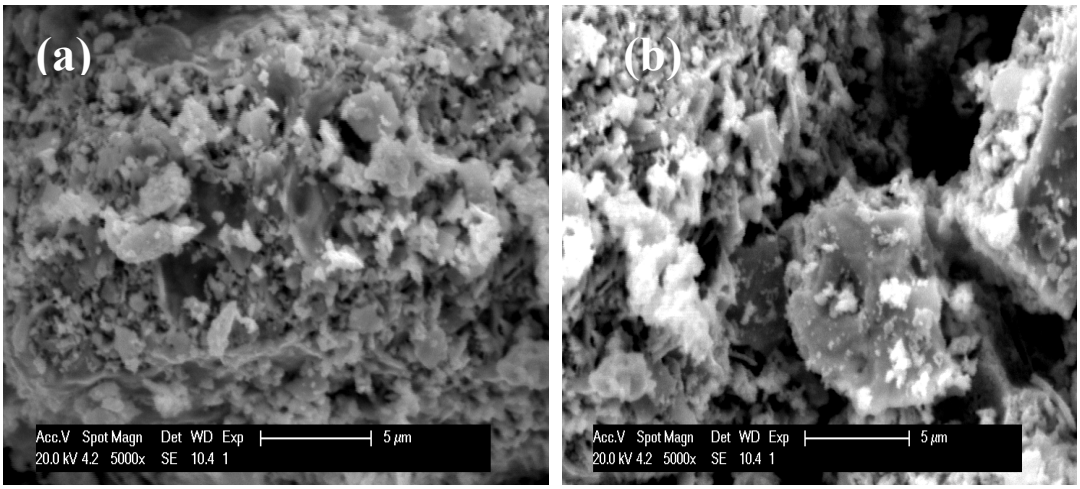

Figure 6-15 SEM images showing the microstructure of as-synthesised $Co_3W_{0.8}Mo_{2.2}O_x$ obtained at 500 °C under air (a; 5 µm scale bar) and post-reaction $Co_3W_{0.8}Mo_{2.2}N$ produced at 700 °C with H_2/N_2 ammonia synthesis gas mixture (b; 5 µm scale bar). Magnification: 5000x.

6.4 Surface area analysis

Figure 6-16 provides the nitrogen adsorption/desorption isotherms curves of different compositions of as prepared transition metal molybdate catalyst (Figure 6-16, left) as well as the used catalysts (Figure 6-16, right). The obtained values are listed in Table 6-3. The evaluated surface areas of as prepared samples $Ni_2Mo_3O_x$, $Ni_{1.7}Cu_{0.3}Mo_3O_x$, $Ni_{1.2}Fe_{0.8}Mo_3O_x$, $Ni_2W_{0.3}Mo_{2.7}O_x$, $Co_3Mo_3O_x$ and $Co_3W_{0.8}Mo_{2.2}O_x$, were 10, 6.6, 6.2, 6.8, 19 and 17 $m^2\ g^{-1}$, respectively. However, the surface areas of these materials decreased after ammonia reaction. The obtained surface areas of the used catalysts $Ni_2Mo_3O_x$, $Ni_{1.7}Cu_{0.3}Mo_3O_x$, $Ni_{1.2}Fe_{0.8}Mo_3O_x$, $Ni_2W_{0.3}Mo_{2.7}O_x$, $Co_3Mo_3O_x$and $Co_3W_{0.8}Mo_{2.2}O_x$, were 6, 5, 5.2, 4.6,7 and 4.2 $m^2\ g^{-1}$, respectively. Based on the IUPAC classification,[209] type III isotherms was displayed by the as prepared samples (Figure 6-16), which is characteristic of non-porous or macroporous materials.

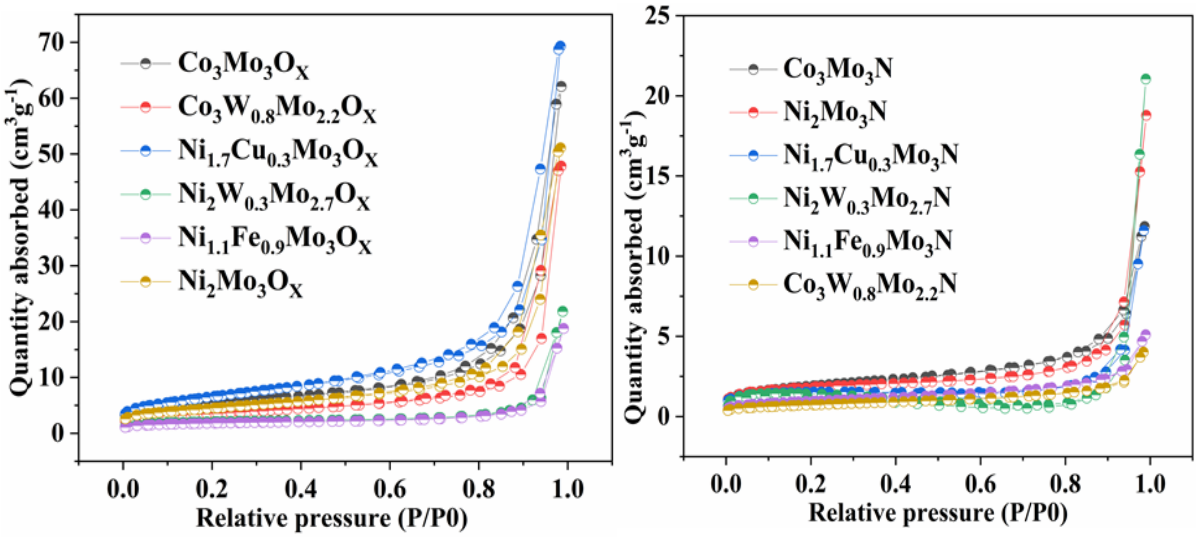

Figure 6-16 Nitrogen adsorption/desorption isotherms curves of as prepared transition metal molybdates obtained at 500 °C under air (left) and post-reaction materials generated at 700 °C with H_2/N_2 ammonia synthesis gas mixture (right).

Table 6-3 Surface areas of the pre -and post-catalysis transition of metal oxide materials

Pre-catalyst	Surface area pre-catalysis ($m^2\ g^{-1}$)	Post-catalyst	Surface area post-catalysis ($m^2\ g^{-1}$)
$Ni_2Mo_3O_x$	10	Ni_2Mo_3N	6
$Ni_{1.7}Cu_{0.3}Mo_3O_x$	24	$Ni_{1.7}Cu_{0.3}Mo_3N$	5
$Ni_{1.2}Fe_{0.8}Mo_3O_x$	6.2	$Ni_{1.2}Fe_{0.8}Mo_3N$	5.2
$Ni_2W_{0.3}Mo_{2.7}O_x$	6.8	$Ni_2W_{0.3}Mo_{2.7}N$	4.6
β-$CoMoO_4$	19	Co_3Mo_3N	7
$Co_3W_{0.8}Mo_{2.2}O_x$	17	$Co_3W_{0.8}Mo_{2.2}N$	4.2

6.4.1 Summary of post- reaction PXRD analysis for the *in-situ* transition metal nitrides

All the investigated materials collected after ammonia reaction underwent structural changes. The post-reaction PXRD patterns of Ni_2Mo_3N, $Ni_{1.7}Cu_{0.3}Mo_3N$, $Ni_{1.2}Fe_{0.8}Mo_3N$ and $Ni_2W_{0.3}Mo_{2.7}N$ were very similar to those of the pre-formed nitrides. In contrast, poorly crystalline structures were observed over the Co_3Mo_3N and $Co_3W_{0.8}Mo_{2.2}N$ materials. It has previously been noted that Ni_2Mo_3N can be synthesised from oxides using hydrogen-nitrogen mix, usually a key advantage compared with Co_3Mo_3N as it means the ammonia synthesis catalyst can be produced *in situ*, not requiring an ammonia firing step before use.[40]

We infer from this that the transformation to the filled β-manganese type nitride phases proceeds smoothly under the catalyst activation conditions (700 °C under 75 % H_2 /25 % N_2) yielding higher surface areas that are advantageous in the catalytic process. Use of ammonia in the synthesis at this temperature yields a rocksalt-type phase and some metal impurities.[40,42] The iron and tungsten nitride materials prepared by ammonia resulted in poor crystalline materials. However, heating these samples under 75% H_2/N_2 showed a minor amount of cubic, rock salt type. The crystal structures of the prepared filled β-manganese compounds could be accurately determined.

The crystal structure of each composition regenerated at 700 °C for 2 h with 3:1 H_2/N_2 were investigated using Rietveld refinements against PXRD data, the refined data are presented in Table 6-4. The refinement was done in a similar way to that employed for 900 °C ammonolysis reaction. The refinement fit resulted in the residuals values of R_{wp} =11.92 % R_p=9.2 % for Ni_2Mo_3N, R_{wp} =11.6 % R_p = 9.6 % for $Ni_{1.7}Cu_{0.3}Mo_3N$, R_{wp} =11.22 % R_p = 8.53 % for $Ni_{1.2}Fe_{0.8}Mo_3N$, R_{wp} =14.6 % R_p = 11.2 % for $Ni_2W_{0.3}Mo_{2.7}N$.

Table 6-3 Refinement details and structure information for the M doped Ni_2Mo_3N samples, M= Cu, Fe, or W

Composition	a/Å	R_{wp} / R_p %	Ni/ M=Cu or Fe (8c *x*, *x*, *x*)	Ni/ M U_{iso} / Å^2	Mo 12 d / W (1/8, y, z)			N 4a 3/8, 3/8, 3/8
					y	Z	U_{iso}/ Å^2	U_{iso} / Å^2
Ni_2Mo_3N	6.638(1)	11.92, 9.2	0.0662(8)	0.012(3)	0.2036 (4)	0.4536(4)	0.0156 (2)	
$Ni_{1.7}Cu_{0.3}Mo_3N$	6.6395(5)	11.06, 9.6	0.0663(3)	0.0264(3)	0.2032(3)	0.4532(3)	0.0284(3)	0.2500
$Ni_{1.2}Fe_{0.8}Mo_3N$	6.637(5)	11.22, 8.53	0.06412(7)	0.0152(3)	0.2032(4)	0.4532(4)	0.018(2)	
$Ni_2W_{0.3}Mo_{2.7}N$	6.6345(8)	14.6, 11.2	0.0645(1)	0.0172(4)	0.2042(2)	0.4542(5)	0.023(3)	

As reported in the literature, the bimetallic η-6 Co_3Mo_3N could be synthesised using various procedures with different treatment conditions.[260,83] In this study, Co_3Mo_3N was prepared by controlled ammonolysis of the oxide precursors at 700 and 900 °C or by the direct reaction of β-$CoMoO_4$ with 3:1 H_2/ N_2 for 2 h at 700 °C. In contrast to the method employed previously, the oxide precursor was prepared by the citrate gel method followed by higher temperature (900 °C) ammonolysis reaction. The PXD patterns of the resultant materials are presented in Figure 6-17. PXRD pattern of 700 °C ammonolysis reaction shows Co_3Mo_3N along with impurity peaks which could indexed to Co_3Mo were detected in the product. Heating at 900 °C, eliminates the surface impurities and single phase was observed as shown in Figure 6-17. The XRD pattern of the material treated at 700 °C under H_2/N_2 ammonia synthesis gas mixture showed noisy background and broad amorphous features. The latter form displayed the highest catalytic activity among the all materials investigated in this study, of 484(9) μmol-NH_3 g^{-1} h^{-1}.

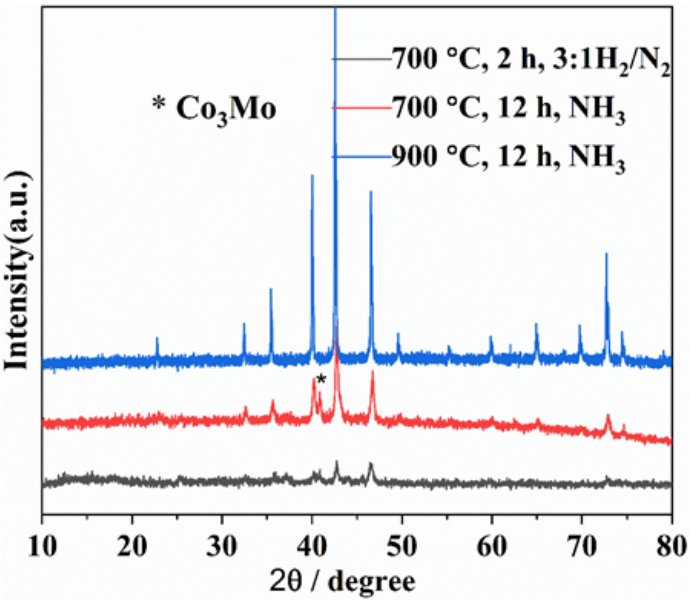

Figure 6-17 PXRD patterns of Co_3Mo_3N and post-reaction one, thermally treated at 700 and 900 ºC for 12 h under NH_3 and at 700°C under 3:1 H_2/N_2 for 2 h. The asterisk (*) indicates the second phase Co_3Mo being observed in the Co_3Mo_3N heated at 700 C for 12 h under NH_3.

6.5 Conclusions

A citrate sol-gel method has been used to synthesise various transition metal molybdates containing Ni, Cu, Co, W and Fe. All of these molybdates produced ammonia under a flow of a 3:1 H_2:N_2 at 500 °C after pre-treated at 700 °C for 2 h under the same gas mixture. This work has shown that, in contrast to their nitride counterparts, these materials were found to have higher ammonia synthesis activity. For example, the activity values 454 μmol-NH_3

g^{-1} h^{-1} for the pre-treated $Ni_2W_{0.3}Mo_{2.7}N$ was higher than 439 μmol NH_3 g^{-1} h^{-1} of that produced by ammonolysis. These results may be connected to the surface areas. In addition, ammonolysis reaction are not needed to prepare the nitride materials.

Chapter 7 Conclusions and Further Work

Transition metal nitrides and oxides are promising materials for catalytic applications. However, several fundamental properties of these materials must be understood before its commercial potential can be realised. In this thesis, the effect of some transition metal dopants such as copper, iron and tungsten into the Ni_2Mo_3N and Co_3Mo_3N compounds towards ammonia synthesis were screened. The key findings of this work and possible future research are presented in this chapter.

7.1 Conclusions

The underlying motivation of this study is to synthesise quaternary nitride-based materials and investigate their catalytic behaviour for ammonia synthesis. Although investigations of non-noble metal catalysts are growing, research interests are focused on developing binary and ternary transition metal nitrides and there are limited studies on quaternary nitrides. Often in catalysis metal contents are varied to the catalytic properties. The limited availability of multi-metal nitride materials could be related to the synthetic method, so this study developed new synthesis chemistry.

A series of different compositions adopting the filled β-manganese structure ($Ni_{2-x}M_xMo_3N$ where M = Cu or Fe) or ($Ni_2W_xMo_{3-x}N$) in addition to the η-6 carbide structured $Co_3W_xMo_{3-x}N$ were prepared *via* a citrate sol gel method followed by the ammonolysis reaction at various temperatures. The crystal structures and textural properties (morphology, surface area and crystallite size) of the pre-reaction samples have been studied. The obtained surface area was considerably affected by the sintering temperature. Low temperature ammonolysis led to higher surface area, whereas lower surface areas were observed with increasing ammonolysis temperatures. All the materials were screened for ammonia synthesis reaction under the same experimental conditions of temperature (500 °C), ambient pressure and reactant composition of 75 vol. % H_2/N_2 (BOC, 99.98%). The temperature was found to be of critical importance for the ammonia synthesis activity. At 500 °C the materials exhibited a steady state of reaction and were highly active towards ammonia synthesis in contrast to 400 °C. It was for this reason that a reaction temperature of 500 °C was employed in ammonia synthesis reaction in this study. The characterisation of post-reaction samples by PXRD, N_2-physisorption (BET) and CHN elemental analysis was undertaken.

Filled β-manganese type materials with composition Ni_2Mo_3N and with some Ni sites replaced by Cu or Fe were prepared by the ammonolysis reaction at 900 °C for 12 h. In both

cases there was a limit to the amount of the second metal that could be substituted under these conditions, in the copper case that seemed to be due to a solubility limit of copper in the host phase. Iron doping increased the activity of the phase as a catalyst for ammonia synthesis at 500 °C and copper decreased that activity, but in both cases surface area changes rather than any electronic differences appear to be the main contributor to the observed change.

Tungsten incorporation into Ni_2Mo_3N lattice also seems to be another potential catalyst for ammonia synthesis in this study. In chapter 5, the introduction of tungsten into nickel molybdenum nitride materials has proven to offer higher catalytic activity. These new materials were thermally treated at 800 °C under NH_3. With respect to the ammonia synthesis, it was found that undoped sample showed higher activity of 400(41) μmol-NH_3 g^{-1} h^{-1} compared to 364(20) and 395(8) μmol-NH_3 g^{-1} h^{-1} for x = 0.1 and 0.2, respectively. However, increasing the tungsten content beyond these points up to x = 0.3 the performance increases accordingly and yields notably higher activity value compared to undoped sample. The η-6 carbide structure Co_3Mo_3N is a promising catalyst for ammonia synthesis and other catalysis applications. This catalyst has been synthesised successfully in a similar manner to that of the filled β-Mn structure Ni_2Mo_3N. For ammonia synthesis study, Co_3Mo_3N catalyst exhibits steady state ammonia synthesis activity. The obtained value of 383 μmol-NH_3 g^{-1} h^{-1} was the highest among the tested nitride-based materials prepared at 900 °C under NH_3. Doping this material with tungsten produced some pure novel compositions in the series.

Besides transition metal nitrides, transition metal molybdates have also studied. In chapter 6, molybdate materials could be converted to the nitride phases during the catalyst activation step at 700 °C for 2 h under (3:1) H_2/N_2, avoiding the need to fire in ammonia as well simplifying preparation process and saving the cost for preparation of the nitride catalysts. The *in-situ* transformation of the oxides led to higher catalyst surface areas and hence to higher activity compared to their nitride counterparts. The highest activity rate of 484 μmol-NH_3 g^{-1} h^{-1} was observed for cobalt molybdenum nitride, Co_3Mo_3N, produced *in situ* from an oxide precursor.

7.2 Future work

Since the quaternary based metal oxides and their nitride counterparts have demonstrated a significant catalytic performance for ammonia synthesis reaction, the applications of

complementary techniques such as neutron diffraction would be beneficial in order to better understand the chemical structures and the catalytic properties of these materials. Further developments are also required to achieve optimal materials for ammonia synthesis. Firstly, since the higher surface area could be one of the main factors linked to the observed catalytic performance in this work, further modifications on the particle size and surface area are required although the complex nature of molybdate structures. Secondly, the use of promoters like alkalis and the incorporation of Zn and Cr into the filled β-Mn and the η- 6 carbide type structures could be an efficient way to develop potential catalysts for ammonia synthesis.

Furthermore, it is viable to investigate the substituting effect of iron and tungsten metals by evaluation the activity of the starting materials for ammonia synthesis in order to elucidate whether the performance was due to one particular metal or all components are required. In this study, the horizontal tube furnace was used in the ammonolysis process. From engineering point of view a vertical ammonia flow direction is more preferable to allow a complete reaction between the gas and the precursor, and thereby lead to more homogenous materials. Therefore, using the vertical tube furnace could be a possible option in the future.

List of References

1 T. R. A. Denk, J. Mohn, C. Decock, D. Lewicka-Szczebak, E. Harris, K. Butterbach-Bahl, R. Kiese and B. Wolf, *Soil Biol. Biochem.*, 2017, **105**, 121–137.

2 B. Sciences, *Sci. York*, 2010, **39**, 378–386.

3 J. N. Galloway, J. D. Aber, J. W. Erisman, S. P. Seitzinger, R. W. Howarth, E. B. Cowling and B. J. Cosby, *Bioscience*, 2003, **53**, 341–356.

4 B. Gu, X. Ju, J. Chang, Y. Ge and P. M. Vitousek, *Proc. Natl. Acad. Sci. U. S. A.*, 2015, **112**, 8792–8797.

5 J. W. Erisman, M. A. Sutton, J. Galloway, Z. Klimont and W. Winiwarter, *Nat. Geosci.*, 2008, **1**, 636–639.

6 J. Brightling, *Johnson Matthey Technol. Rev.*, 2018, **62**, 32–47.

7 Food and Agriculture Organization of the United Nations, *World fertilizer trends and outlook to 2020*, Rome, 2017.

8 J. M. Modak, *Resonance*, 2002, **7**, 69–77.

9 V. Smil, *Ambio*, 2002, **31**, 126–31.

10 N. Alexandratos, *Expert Meet. How to Feed World 2050*, 2009, 1–32.

11 R. Sacks, *Aust. Fam. Physician*, 2001, **30**, 679–680.

12 D. E. Brown, T. Edmonds, R. W. Joyner, J. J. McCarroll and S. R. Tennison, *Catal. Letters*, 2014, **144**, 545–552.

13 A. Vojvodic, A. J. Medford, F. Studt, F. Abild-Pedersen, T. S. Khan, T. Bligaard and J. K. Nørskov, *Chem. Phys. Lett.*, 2014, **598**, 108–112.

14 H. Liu, *Chinese J. Catal.*, 2014, **35**, 1619–1640.

15 A. Mittasch and W. Frankenburger, *J. Chem. Educ.*, 1929, **6**, 2097–2098.

16 S. L. Foster, S. I. P. Bakovic, R. D. Duda, S. Maheshwari, R. D. Milton, S. D. Minteer, M. J. Janik, J. N. Renner and L. F. Greenlee, *Nat. Catal.*, 2018, **1**, 490–500.

17 M. Appl, *Ammonia, Methanol, Hydrogen, Carbon Monoxide: Modern Production Technologies*, CRU Publishing Ltd, London, UK, 1997.

18 M. Palys, A. McCormick, E. Cussler and P. Daoutidis, *Processes*, 2018, **6**, 91.

19 E. Worrell, L. Bernstein, J. Roy, L. Price and J. Harnisch, *Energy Effic.*, 2009, **2**, 109–123.

20 R. Schlögl, *Angew. Chemie - Int. Ed.*, 2003, **42**, 2004–2008.

21 P. Mars and D. W. Van Krevelen, *Chem. Eng. Sci*, 1954, **3**, 41–59.

22 Y. Abghoui, A. L. Garden, V. F. Hlynsson, S. Björgvinsdóttir, H. Ólafsdóttir and E. Skúlason, *Phys. Chem. Chem. Phys.*, 2015, **17**, 4909–4918.

23 S. T. Oyama and S. T. Oyama, *The chemistry of transition metal carbides and nitrides*, Blackie Academic & Professional, Glasgow, First., 1996.

24 S. K. R. Patil, N. S. Mangale, S. V. Khare and S. Marsillac, *Thin Solid Films*, 2008, **517**, 824–827.

25 J. G. Chen, *Chem. Rev.*, 1996, **96**, 1477–1498.

26 R. M. Fix, R. G. Gordon and D. M. Hoffman, *Chem. Mater.*, 1990, **2**, 235–241.

27 K. Watari, *J. Ceram. Soc. Japan*, 2001, **109**, S7–S16.

28 W. R. L. Lambrecht, M. S. Miao and P. Lukashev, *J. Appl. Phys.*, 2005, **97**, 1–4.

29 C. Giordano and M. Antonietti, *Nano Today*, 2011, **6**, 366–380.

30 M. -A. Nicolet, *Thin Solid Films*, 1978, **52**, 415–443.

31 R. B. Levy and M. Boudart, *Science (80-.).*, 1973, **181**, 547–549.

32 A. A. Levin, D. C. Meyer, M. Reibold, W. Kochmann, N. Pätzke and P. Paufler, *Cryst. Res. Technol.*, 2005, **40**, 905–916.

33 S. T. Oyama, *Catal. Today*, 1992, **15**, 179–200.

34 D. J. Ham and J. S. Lee, *Energies*, 2009, **2**, 873–899.

35 S. Zaman and K. J. Smith, *Catal. Rev. - Sci. Eng.*, 2012, **54**, 41–132.

36 M. J. Mayo, *Mater. Des.*, 1993, **14**, 323–329.

37 C. J. H. Jacobsen, *Chem. Commun.*, 2000, 1057–1058.

38 R. Kojima and K. ichi Aika, *Appl. Catal. A Gen.*, 2001, **218**, 121–128.

39 J. S. J. Hargreaves, *Appl. Petrochemical Res.*, 2014, **4**, 3–10.

40 N. Bion, F. Can, J. Cook, J. S. J. Hargreaves, A. L. Hector, W. Levason, A. R. McFarlane, M. Richard and K. Sardar, *Appl. Catal. A Gen.*, 2015, **504**, 44–50.

41 I. Alshibane, A. Daisley, J. S. J. Hargreaves, A. L. Hector, S. Laassiri, J. L. Rico and R. I. Smith, *ACS Sustain. Chem. Eng.*, 2017, **5**, 9214–9222.

42 S. Al Sobhi, N. Bion, J. S. J. Hargreaves, A. L. Hector, S. Laassiri, W. Levason, A. W. Lodge, A. R. Mcfarlane and C. Ritter, *Mater. Res. Bull.*, 2019, **118**, 110519.

43 S. F. Zaman, L. A. Jolaoso, S. Podila, A. A. Al-zahrani, Y. A. Alhamed, H. Driss, M. M. Daous and L. Petrov, *Int. J. Hydrogen Energy*, 2018, **43**, 1–7.

44 W.-F. Chen, J. T. Muckerman and E. Fujita, *Chem. Commun. (Camb).*, 2013, **49**, 8896–909.

45 G. S. Ranhotra, A. T. Bell and J. A. Reimer, *J. Catal.*, 1987, **108**, 40–49.

46 S. Ramanathan and S. T. Oyama, *J. Phys. Chem.*, 1995, **99**, 16365–16372.

47 M. K. K. Neylon, S. Choi, H. Kwon, K. E. E. Curry and L. T. T. Thompson, *Appl.*

Catal. A Gen., 1999, **183**, 253–263.

48 D. H. Gregory, *J. Chem. Soc. Dalt. Trans.*, 1999, 259–270.

49 S. T. Oyama, *The chemistry of transition metal carbides and nitrides*, Blackie Academic & Professional, Glasgow, First., 1996.

50 L. I. Johansson, *Surf. Sci. Rep.*, 1995, **21**, 177–250.

51 V. A. Gubanov, *Electronic structure of refractory carbides and nitrides*, Cambridge, New York, 1994.

52 E. Furimsky, *Appl. Catal. A Gen.*, 2003, **240**, 1–28.

53 Y. Zhong, X. H. Xia, F. Shi, J. Y. Zhan, J. P. Tu and H. J. Fan, *Adv. Sci.*, 2016, **3**, 1500286.

54 L. E. Toth, *Transition metal carbides and nitrides*, Academic Press, New York, 1971.

55 E. R. Jette and F. Foote, *J. Chem. Phys.*, 1935, **3**, 605–616.

56 B. Cao, J. C. Neuefeind, R. R. Adzic and P. G. Khalifah, *Inorg. Chem.*, 2015, **54**, 2128–2136.

57 P. S. Herle, M. S. Hegde, K. Sooryanarayana, T. N. Guru Row and G. N. Subbanna, *Inorg. Chem.*, 1998, **37**, 4128–4130.

58 T. J. Prior and P. D. Battle, *J. Solid State Chem.*, 2003, **172**, 138–147.

59 P. D. Battle, F. Grandjean, G. J. Long and S. E. Oldham, *J. Mater. Chem.*, 2007, **17**, 4785.

60 U. Eibenstein and W. Jung, *J. Solid State Chem.*, 1996, **133**, 21–24.

61 W. Jeitschko, I. I. Nowotny and F. Benesovsky, *Mh. Chem.*, 1964, **95**, 1212–1218.

62 J. A. M. Paddison, J. R. Stewart, P. Manuel, P. Courtois, G. J. McIntyire, B. D. Rainford and A. L. Goodwin, 2013, 5.

63 D. Bem, C. Gibson and H. Zur Loye, *Chem. Mater.*, 1993, **5**, 397–399.

64 S. K. Jackson, R. C. Layland and H. Loye, *J. Alloys Compd.*, 1999, **291**, 94–101.

65 J. G. Speight and M. Dekker, *Assess. Educ. Princ. Policy Pract.*, 2000, **7**, 271–284.

66 Y. Chu, Z. Wei, S. Yang, C. Li, Q. Xin and E. Min, *Appl. Catal. A Gen.*, 1999, **176**, 17–26.

67 G. M. Dolce, P. E. Savage and L. T. Thompson, *Energy & Fuels*, 1997, **11**, 668–675.

68 S. O. Masatoshi Nagai, Yosuke Goto, Atsushi Irisawa, *J. Catal.*, 2000, **191**, 128–137.

69 C. W. Colling, J.-G. Choi and L. T. Thompson, *J. Catal.*, 1996, **160**, 35–42.

70 C. W. Colling and L. T. Thompson, *J. Catal.*, 1994, **146**, 193–203.

71 R. Schlögl, *Angew. Chemie - Int. Ed.*, 2003, 42, 2004–2008.

72 L. Volpe and M. Boudart, *J. Solid State Chem.*, 1985, **59**, 332–347.

73 A. Mittasch and W. Frankenburg, *Adv. Catal.*, 1950, **2**, 81–104.

74 H. Wurfel, *The desulfurization of heavy oils and residua*, Marcel Dekker AG, New York, Second Edi., 1982, vol. 6.

75 J.-G. Choi, H. J. Lee and L. T. Thompson, *Appl. Surf. Sci.*, 1994, **78**, 299–307.

76 C. J. H. Jacobsen, S. Dahl, B. G. S. Clausen, S. Bahn, A. Logadottir and J. K. Nørskov, *J. Am. Chem. Soc.*, 2001, **123**, 8404–8405.

77 S. M. Hunter, D. McKay, R. I. Smith, J. S. J. Hargreaves and D. H. Gregory, *Chem. Mater.*, 2010, **22**, 2898–2907.

78 D. Mckay, J. S. J. Hargreaves, J. L. Rico, J. L. Rivera and X. L. Sun, *J. Solid State Chem.*, 2008, **181**, 325–333.

79 J. L. Rico, M. Albiter, J. Espino, J. S. J. Hargreaves, M. Ostroumov, L. I. Salcedo and K. Wilson, *J. Saudi Chem. Soc.*, 2012, **20**, 405–410.

80 B. G. Demczyk, J. G. Choi and L. T. Thompson, *Appl. Surf. Sci.*, 1994, **78**, 63–69.

81 S. Laassiri, C. D. Zeinalipour-Yazdi, C. R. A. Catlow and J. S. J. Hargreaves, *Catal. Today*, 2016, 4–11.

82 R. Kojima and K. Aika, *Appl. Catal. A Gen.*, 2001, **215**, 149–160.

83 J. S. J. Hargreaves and D. Mckay, *J. Mol. Catal. A Chem.*, 2009, **305**, 125–129.

84 S. M. Hunter, D. H. Gregory, J. S. J. Hargreaves, M. Richard, D. Duprez and N. Bion, *ACS Catal.*, 2013, **3**, 1719–1725.

85 R.S. Wise and E.J. Markel, *J. Catal.*, 1994, **145**, 344–355.

86 J. G. Choi, R. L. Curl and L. T. Thompson, *J. Catal.*, 1994, **146**, 218–227.

87 M. K. Neylon, S. K. Bej, C. A. Bennett and L. T. Thompson, *Appl. Catal. A Gen.*, 2002, **232**, 13–21.

88 Y. Zhang, Y. Li, R. Raval, C. Li, R. Zhai and Q. Xin, *J. Mol. Catal. a-Chemical*, 1998, **132**, 241–253.

89 S. Wang, X. Yu, Z. Lin, R. Zhang, D. He, J. Qin, J. Zhu, J. Han, L. Wang, H. K. Mao, J. Zhang and Y. Zhao, *Chem. Mater.*, 2012, **24**, 3023–3028.

90 A.-R. Ko, S.-B. Han, Y.-W. Lee and K.-W. Park, *Phys. Chem. Chem. Phys.*, 2011, **13**, 12705–12707.

91 R. Marchand, F. Tessier and F. J. DiSalvo, *J. Mater. Chem.*, 1999, **9**, 297–304.

92 K. S. Weil and P. N. Kumta, *Mater. Sci. Eng. B*, 1996, **38**, 109–117.

93 K. S. Weil and P. N. Kumta., *J. Alloys Compd.*, 1998, **265**, 96–103.

94 K. S. Weil and P. N. Kumta, *Acta Crystallogr. Sect. C Cryst. Struct. Commun.*, 1997, **53**, 1745–1748.

95 P. Krawiec, R. Narayan Panda, E. Kockrick, D. Geiger and S. Kaskel, *J. Solid State*

Chem., 2008, **181**, 935–942.

96 S. Alconchel, F. Sapiña, D. Beltrán and A. Beltrán, *J. Mater. Chem.*, 1999, **9**, 749–755.

97 A. Gomathi, *Mater. Res. Bull.*, 2007, **42**, 870–874.

98 R. Niewa and H. Jacobs, *Chem. Rev.*, 1996, **96**, 2053–2062.

99 Y. Chen, J. Shen and N. xian Chen, *Solid State Commun.*, 2009, **149**, 121–125.

100 D. S. Bem, C. M. LampeOnnerud, H. P. Olsen and H. C. zurLoye, *Inorg. Chem.*, 1996, **35**, 581–585.

101 R. N. Panda, G. Balaji, P. K. Pandey and N. S. Gajbhiye, *Hyperfine Interact.*, 2008, **184**, 245–250.

102 H. Zhang, Z. Zhao, C. Xu, A. Duan, W. Lin, H. Tian and I. E. Wachs, *Mater. Res. Bull.*, 2006, **41**, 2334–2340.

103 P. Subramanya Herle, *J. Mater. Chem.*, 1998, **8**, 1435–1440.

104 A. El-Himri, D. Marrero-López and P. Núñez, *J. Solid State Chem.*, 2004, **177**, 3219–3223.

105 T. J. Prior, D. Nguyen-Manh, V. J. Couper and P. D. Battle, *J. Phys. Condens. Matter*, 2004, **16**, 2273–2281.

106 T. J. Prior and P. D. Battle, *J. Mater. Chem.*, 2004, **14**, 3001–3007.

107 W. Yuhong, L. Wei, Z. Minghui, G. Naijia and T. Keyi, *Appl. Catal. A Gen.*, 2001, **215**, 39–45.

108 A. Kraupner, M. Antonietti, R. Palkovits, K. Schlicht and C. Giordano, *J. Mater. Chem.*, 2010, **20**, 6019–6022.

109 F. J. DiSalvo and S. J. Clarke, *Curr. Opin. Solid State Mater. Sci.*, 1996, **1**, 241–249.

110 P. G. Li, M. Lei, Z. B. Sun, L. Z. Cao, Y. F. Guo, X. Guo and W. H. Tang, *J. Alloys Compd.*, 2007, **430**, 237–240.

111 J. Choy and Y. Han, *J. Mater. Chem.*, 1997, **7**, 1815–1820.

112 N. G. Eror and H. U. Anderson, *Polymeric Precursor Synthesis of Ceramic Materials*, Materials Research Society, Pittsburg,PA, 1986, vol. 73.

113 M.P. Pechini, *U.S. Pat. nº 3,330.697*, 1967, 1–2.

114 J. Livage and C. Sanchez, *J. Non. Cryst. Solids*, 1992, **145**, 11–19.

115 A. E. Danks, S. R. Hall and Z. Schnepp, *Mater. Horizons*, 2016, **3**, 91–112.

116 A. V. Pashigreva, O. V. Klimov, G. A. Bukhtiyarova, M. A. Fedotov, D. I. Kochubey, Y. A. Chesalov, V. I. Zaikovskii, I. P. Prosvirin and A. S. Noskov, *The superior activity of the CoMo hydrotreating catalysts, prepared using citric acid: What's the*

reason?, Elsevier Masson SAS, 2010, vol. 175.

117 A. Katelnikovas, J. Barkauskas, F. Ivanauskas, A. Beganskiene and A. Kareiva, *J. Sol-Gel Sci. Technol.*, 2007, **41**, 193–201.

118 J. N. Lanlena, D. A. Cleary, E. C. C. And and N. F. Dean, *Inorganic Materials Synthesis and fabrication*, John Wiley & Sons, Inc., Hoboken, New Jersey, 2008.

119 P. Vaqueiro and M. A. López-Quintela, *Chem. Mater*, 1997, **9**, 2836–2841.

120 B. J. Hwang, R. Santhanam, D. G. Liu and Y. W. Tsai, *J. Power Sources*, 2001, **102**, 326–331.

121 K. A. Mishra, *Sol-gel Based Nanoceramic Materials:Preparation,Properties and Applications*, Springer, 2016.

122 K. D. Vernon-Parry, *III-Vs Rev.*, 2000, **13**, 40–44.

123 J. Goldstein, D. E. Newbury, P. Echlin, D. C. Joy, C. Fiori and E.Lifshin, *Scanning Electron Microscopy and X-Ray Microanalysis: A Text for Biologists, Materials Scientists, and Geologists*, Springer US, 2013.

124 R. J. Ross and E.D.R.Committee, *Microelectronics Failure Analysis: Desk Reference, Sixth Edition*, ASM International, 2011.

125 D. D. Vvedensky, *Surf. Interface Anal.*, 2001, **31**, 659–672.

126 M. Mühlbacher, *High-resolution characterization of TiN diffusion barrier layers, Licentiate Thesis No. 1720*, 2015.

127 Z. L. Wang, *J. Phys. Chem. B*, 2000, **104**, 1153–1175.

128 D. B. Williams and C. B. Carter, *Transition Electron Microscopy*, Plenum Press, New York, 1996.

129 M.Hosokawa, K.Nogi, M.Naito and T.Yokoyama, *Nanoparticles Technology Handbook*, Elsevier, Amsterdam, 2012.

130 H. M. Rietveld, *Acta Crystallogr.*, 1967, **22**, 151–152.

131 S. Brunauer, P. H. Emmett and E. Teller, *J. Am. Chem. Soc.*, 1938, **60**, 309.

132 A. W. Coast and J. P. Redfern, *Nature*, 1954, **88**, 1011–1012.

133 X. Liu and W. Yu, *J. Appl. Polym. Sci.*, 2006, **99**, 937–944.

134 S. R. Sandler, W. Karo, J.-A. Bonesteel and E. M. Pearce, *Polym. Synth. Charact.*, 1998, **1**, 108–119.

135 J. I. Langford, D. Louër and P. Scardi, *J. Appl. Crystallogr.*, 2000, **33**, 964–974.

136 C. R. Groom, I. J. Bruno, M. P. Lightfoot and S. C. Ward, *Acta Crystallogr. Sect. B Struct. Sci. Cryst. Eng. Mater.*, 2016, **72**, 171–179.

137 J. Faber and T. Fawcett, *Acta Crystallogr. Sect. B Struct. Sci.*, 2002, **58**, 325–332.

138 J. A. Kaduk, *Acta Crystallogr. Sect. B Struct. Sci.*, 2002, **58**, 370–379.

139 W. Clegg, *Crystal Structure determination*, Oxford University Press, New York, 1998.

140 W. L. Bragg, *Proc. R. Soc. London.*, 1913, **89**, 248–277.

141 A. K. Petford-Long and A. N. Chiaramonti, *Annu. Rev. Mater. Res.*, 2008, **38**, 559–584.

142 G. E. M. Jauncey, *Phys. Rev.*, 1922, **20**, 405–420.

143 N. C. Popa and D. Balzar, *J. Appl. Crystallogr.*, 2002, **35**, 338–346.

144 H. M. Rietveld, *J. Appl. Crystallogr.*, 1969, **2**, 65–71.

145 H. Z. Morawiec and H. M. D. Stróż, *Applied Crystallography: proceeeding of the XIX Conference: Kraków, Poland, 1-4 September 2003*, World Scientific, 2004.

146 R. Tilley, *Crystal and Crystal structure*, Weiley, Chichester, 2006.

147 C. Rocha, Á. Vieira and I. C. P. Margarit-mattos, 2014, **17**, 1356–1366.

148 R. A. Young, *The Rietveld Method*, Oxford University Press, New York, 1993.

149 W. I. F. David and K. Shankland, *Acta Crystallogr. Sect. A Found. Crystallogr.*, 2007, **64**, 52–64.

150 A. C. Larson and R. B. Von Dreele, *Structure*, 2004, **748**, 86–748.

151 A.Patterson, *Phys. Rev. B,* 1939, **56**, 978.

152 D. Mckay, PhD thesis, University of Glasgow, 2008.

153 D. Dorranian, L. Dejam and G. Mosayebian, *J. Theor. Appl. Phys.*, 2012, **6**, 13.

154 A. Razeghizadeh, M. Mahmoudi Ghalvandi, F. Sohilian and V. Rafee, *Phys. Chem. Res.*, 2017, **5**, 497–504.

155 G. Paniconi, Z. Stoeva, H. Doberstein, R. I. Smith, B. L. Gallagher and D. H. Gregory, *Solid State Sci.*, 2007, **9**, 907–913.

156 R. Juza, A. Rabenau and Z. Anorg, *Allg. Chem*, 1956, **285**, 212–220.

157 U. Zachwieja and H. Jacobs, *J.Less-common Met*, 1990, **161**, 175.

158 J. Choi and E. G. Gillan, *Inorg. Chem.*, 2005, **44**, 7385–7393.

159 A. Baiker and M. Maciejewski, *J. Chem. Soc. Faraday Trans. 1 Phys. Chem. Condens. Phases*, 1984, **80**, 2331–2341.

160 A. Alexander, PhD thesis, University of Glasgow, 2011.

161 P. Adamski, D. Moszyński, M. Nadziejko, A. Komorowska and A. Sarnecki, *Chem. Pap.*, 2019, **73**, 851–859.

162 *PDF-2 (Powder Diffr. File), 2012 release, Int. Cent. Diffr. Data, Swart. PA.*

163 B. H. Toby, *J. Appl. Crystallogr.*, 2001, **34**, 210–213.

164 *Inorg. Cryst. Struct. Database (ICSD, Fiz Karlsruhe) accessed via EPSRC-funded*

Natl. Chem. Database Serv. hosted by R. Soc. Chem.

165 S. Brunauer, P. H. Emmett and E. Teller, *J. Am. Chem. Soc.*, 1938, **60**, 309–319.

166 Y. Liu, J. Chen and M. D. Ryan, *Inorg. Chem.*, 1998, **37**, 425–431.

167 J. O. Conway and T. J. Prior, *J. Alloys Compd.*, 2019, **774**, 69–74.

168 K.S. Weil, P. N. Kumta. and J. Grins, *J. Solid State Chem.*, 1999, **146**, 22–35.

169 D.A. Fletcher, R.F. McMeeking and D. Parkin, *J. Chem. Inf. Comput. Sci*, 1996, **36**, 746.

170 T. Kawashima, E. Takayama-Muromachi and P. F. McMillan, *Phys. C Supercond. its Appl.*, 2007, **460-462 I**, 651–652.

171 H. M. Otte, *J. Appl. Phys.*, 1961, **32**, 1536–1546.

172 N. N. Greenwood and E. A. Earnshaw, *Chemistry of the Elements*, Butterworth-Heinemann, (2 nd Ed.)., 1997.

173 H. Ehrenberg, I. Svoboda, G. Wltschek, M. Wiesmann, F. Trouw, H. Weitzel and H. Fuess, *J. Magn. Magn. Mater.*, 1995, **150**, 371–376.

174 H. Sitepu, B. H. O. Connor and D. Li, *J. Appl. Crystallogr.*, 2005, **38**, 158–167.

175 E.M.McCarronIII and J.C.Calabrese, *J. Solid State Chem.*, 1991, **91**, 121–125.

176 A. C. Larson and R. B. Von Dreele, *Los Alamos Natl. Lab. Rep. LAUR*, 2000, 86–748.

177 A. Srifa, K. Okura, T. Okanishi, H. Muroyama, T. Matsui and K. Eguchi, *Catal. Sci. Technol.*, 2016, **6**, 7495–7504.

178 J. G. Choi, J. R. Brenner, C. W. Colling, B. G. Demczyk, J. L. Dunning and L. T. Thompson, *Catal. Today*, 1992, **15**, 201–222.

179 D. W. Kim, D. K. Lee and S. K. Ihm, *Korean J. Chem. Eng.*, 2002, **19**, 587–592.

180 L. Volpe and M. Boudart, *J. Phys. Chem.*, 1986, **90**, 4874–4877.

181 D. Mckay, D. H. Gregory, J. S. J. Hargreaves, S. M. Hunter and X. Sun, *Chem. Commun.*, 2007, **7**, 3051–3053.

182 R. Kojima and K. I. Aika, *Appl. Catal. A Gen.*, 2001, **219**, 141–147.

183 A. Boisen, S. Dahl and C. J. . Jacobsen, *J. Catal.*, 2002, **208**, 1–7.

184 F. Bozso, G. Ertl, M. Grunze and M. Weiss, *J. Catal.*, 1977, **49**, 18–41.

185 M. A. Sriram, K. S. Weil and P. N. Kumta, *Appl. Organomet. Chem.*, 1997, **11**, 163–179.

186 G. Cordier, P. Hohn, R. Kniep and A. Z. Rabenau, *Anorg. Allg. Chem.*, 1990, **591**, 58–66.

187 A. Gudat, R. Kniep, A. Rabenau, W. Bronger and U. Ruschewitz, *J.Less-common Met*, 1990, **161**, 31–36.

188 P. S. Herle, *J. Alloys Compd.*, 1995, **217**, 22–24.

189 T. J. Prior, S. E. Oldham, V. J. Couper and P. D. Battle, *Chem. Mater.*, 2005, **17**, 1867–1873.

190 S. E. Oldham, P. D. Battle, S. J. Blundell, M. L. Brooks, F. L. Pratt and T. J. Prior, *J. Mater. Chem.*, 2005, **15**, 3402–3408.

191 L. Wang, W. Xian, K. Zhang, W. Liu, H. Qin, Q. Zhou and Y. Qian, *Inorg. Chem. Front.*, 2017, **4**, 2055–2058.

192 R. N. Panda and N. S. Gajbhiye, *J. Alloys Compd.*, 1997, **256**, 102–107.

193 R. N. Panda and N. S. Gajbhiye, *J. Cryst. Growth*, 1998, **191**, 92–96.

194 D. S. Bern, H. P. Olsen and H. C. zur Loye, *Chem. Mater.*, 1995, **7**, 1824–1828.

195 S. Laassiri, C. D. Zeinalipour-Yazdi, C. R. A. Catlow and J. S. J. Hargreaves, *Appl. Catal. B Environ.*, 2018, **223**, 60–66.

196 S. M. Hunter, PhD thesis, University of Glagow, 2012.

197 W. Jung, T. Tschaplinski, L. Wang, J. Glazebrook and J. Greenberg, *Science (80-.).*, 2009, **324**, 89–91.

198 C. Shi, A. M. Zhu, X. F. Yang and C. T. Au, *Appl. Catal. A Gen.*, 2004, **276**, 223–230.

199 H. Jin, H. Zhang, J. Chen, S. Mao, Z. Jiang and Y. Wang, *J. Mater. Chem. A*, 2018, **6**, 10967–10975.

200 R. N. Panda, S. B. Dalavi and J. Theerthagiri, *Adsorpt. Sci. Technol.*, 2012, **30**, 345–354.

201 J. H. Kim and K. L. Kim, *Appl. Catal. A Gen.*, 1999, **181**, 103–111.

202 D. Choi and P. N. Kumta, *J. Am. Ceram. Soc.*, 2007, **90**, 3113–3120.

203 K. S. Weil and P. N. Kumta, *Acta Crystallogr. Sect. C Cryst. Struct. Commun.*, 1997, 53, 1745–1748.

204 J. D. Houmes, S. Deo and H.-C. Zur Loye, *J. Solid State Chem.*, 1997, **131**, 374–378.

205 R. P. Singh Gaur, *JOM*, 2006, **58**, 45–49.

206 S. Podila, S. F. Zaman, H. Driss, Y. A. Alhamed, A. A. Al-Zahrani and L. A. Petrov, *Catal. Sci. Technol.*, 2016, **6**, 1496–1506.

207 H. Wang, W. Li and M. Zhang, *Chem. Mater.*, 2005, **17**, 3262–3267.

208 L. Battery, *Int. J. Electrochem. Sci.*, 2016, **11**, 498–505.

209 U. M. García-Pérez, A. Martínez-De La Cruz and J. Peral, *Electrochim. Acta*, 2012, **81**, 227–232.

210 A. Rodriguez, S. Chaturvedi and J. C. Hanson, *J. Phys. Chem. B*, 1999, 770–781.

211 A. E. Reddy, T. Anitha, C. V. V. M. Gopi, S. S. Rao and H. Kim, *Dalt. Trans.*, 2018, 9057–9063.

212 M. Liu, L. Kong, C. Lu, X. Li, Y. Luo and L. Kang, *J. Mater. Chem. A*, 2013, **1**, 1380–1387.

213 D. Cai, D. Wang, B. Liu, Y. Wang, Y. Liu, L. Wang, H. Li, H. Huang, Q. Li and T. Wang, *Appl. Mater. Interfaces*, 2013, **5**, 12905–12910.

214 J. L. Brito and A. L. Barbosa, *J. Catal.*, 1997, **171**, 467–475.

215 S. Mani, V. Vediyappan, S. M. Chen, R. Madhu, V. Pitchaimani, J. Y. Chang and S. Bin Liu, *Sci. Rep.*, 2016, **6**, 2–9.

216 Y. Bi, H. Nie, D. Li, S. Zeng, Q. Yang and M. Li, *Chem. Commun.*, 2010, **46**, 7430–7432.

217 Y. Yoon, N. Fujikawa, W. Ueda and K. Lee, *Catal. Today*, 1995, **24**, 327–333.

218 S. Baoyi, X. Aiju and W. Jiang, *Integr. Ferroelectr.*, 2016, **171**, 16–22.

219 J. L. Brito, A. L. Barbosa, A. Albornoz, F. Severino and J. Laine, 1994, **26**, 329–337.

220 J. Chen, G. Zhao, Y. Chen, K. Rui, H. Mao and X. Dou, *Chem. Eur. J.*, 2019, **4**, 280–284.

221 J. Liao, D. Lu, G. Diao, X. Zhang, M. Zhao and H. Li, *ACS Sustain. Chem. Eng.*, 2018, **6**, 5843–5851.

222 Rafael Oliveira Paes de Lima and Marcelo da Silva Batista, *Int. J. ENERGY Environ.*, 2018, **9**, 71–76.

223 S. M. Alshehri, J. Ahmed, T. Ahamad, P. Arunachalam, T. Ahmad and A. Khan, *RSC Adv.*, 2017, **7**, 45615–45623.

224 S. M. Alshehri, J. Ahmed, A. M. Alzahrani and T. Ahamad, *New J. Chem.*, 2017, 8178–8186.

225 L. Niu, Z. Li, Y. Xu, J. Sun, W. Hong, X. Liu, J. Wang and S. Yang, *ACS Appl. Mater. Interfaces*, 2013, **5**, 8044–8052.

226 J. M. Quintana-Melgoza, J. Cruz-Reyes and M. Avalos-Borja, *Mater. Lett.*, 2001, **47**, 314–318.

227 M. N. Mancheva, R. S. Iordanova, D. G. Klissurski, G. T. Tyuliev and B. N. Kunev, *J. Phys. Chem. C*, 2007, **111**, 1101–1104.

228 J. Tian, Y. Xue, X. Yu, Y. Pei, H. Zhang and J. Wang, *RSC Adv.*, 2018, **8**, 41740–41748.

229 S. Rajagopal, D. Nataraj, O. Y. Khyzhun, Y. Djaoued, J. Robichaud and D. Mangalaraj, *J. Alloys Compd.*, 2010, **493**, 340–345.

230 L. Pan, L. Li and Y. Chen, *J. Sol-Gel Sci. Technol.*, 2013, **66**, 330–336.

231 L. Li, W. Chen, W. Luo, Z. Xiao, Y. Zhao, K. A. Owusu, Z. Liu, L. Zhou and L. Mai, *Energy Technol*, 2019, **1801160**, 1–7.

232 K. Park, S. Seo, H. Shim and D. Kim, *Nanoscale Res. Lett.*, 2012, **7:35**, 1–7.

233 S. J. Naik and A. V Salker, *Solid State Sci.*, 2010, **12**, 2065–2072.

234 A. P. De Moura, L. H. De Oliveira, I. L. V. Rosa, C. S. Xavier, P. N. Lisboa-Filho, M. S. Li, F. A. La Porta, E. Longo and J. A. Varela, *Sci. World J.*, 2015, **2015**, 8.

235 M. Q. Yu, L. X. Jiang and H. G. Yang, *Chem. Commun.*, 2015, **20**, 14361–14364.

236 W. Li, X. Wang, Y. Hu, L. Sun, C. Gao, C. Zhang, H. Liu and M. Duan, *Nanoscale Res. Lett.*, 2018, **13**, 1–10.

237 D. Errandonea and J. Ruiz-Fuertes, *Crystals*, 2018, **8**, 1–19.

238 H. Weitzel, *Zeitschrift für Krist.*, 1976, **144**, 238–258.

239 J. A. Rodriguez, J. C. Hanson, S. Chaturvedi and L. Joaquin, *Stud. Surf. Sci. Catal.*, 2000, 2795–2800.

240 D. Zagorac and J. C. Sch, *Cryst. Res. Technol.*, 2017, **52**, 4–9.

241 K. M. Rahulan, N. A. L. Flower, R. A. Sujatha, N. Padmanathan and C. Gopalakrishnan, *J. Mater. Sci. Mater. Electron.*, 2018, **29**, 1504–1509.

242 G. W. Smith, *Acta Crystallogr.*, 1965, **19**, 269.

243 C. Livage, A. Hynaux, J. Marrot, M. Nogues and G. Férey, *J. Mater. Chem.*, 2002, **12**, 1423–1425.

244 K. Eda, Y. Uno, N. Nagai, N. Sotani and M. S. Whittingham, *J. Solid State Chem.*, 2005, **178**, 2791–2797.

245 H. Emadi, B. T. Jahromi and A. N. Kharat, *J. Chem. Sci.*, 2017, **129**, 373–380.

246 A. W. Sleight, *Acta Crystallogr.*, 1972, **B28**, 2899–2902.

247 M. Wiesmann, H. Ehrenberg, G. Wltschek, P. Zinn, H. Weitzel and H. Fuess, *J. Magn. Magn. Mater.*, 1995, **150**, 0–3.

248 K. Eda, Y. Kato, Y. Ohshiro, T. Sugitani and M. S. Whittingham, *J. Solid State Chem.*, 2010, **183**, 1334–1339.

249 A. Maione and M. Devillers, *J. Solid State Chem.*, 2004, **177**, 2339–2349.

250 J. H. Ryu, S. M. Koo, J. W. Yoon, C. S. Lim and K. B. Shim, *Mater. Lett.*, 2006, **60**, 1702–1705.

251 D. Cai, B. Liu, D. Wang, Y. Liu, L. Wang, H. Li, Y. Wang, C. Wang, Q. Li and T. Wang, *Electrochim. Acta*, 2014, **115**, 358–363.

252 L. M. Madeira, M. F. Portela and C. Mazzocchia, *Catal. Rev. - Sci. Eng.*, 2004, **46**, 53–110.

253 M. C. Liu, L. Kang, L. Bin Kong, C. Lu, X. J. Ma, X. M. Li and Y. C. Luo, *RSC Adv.*, 2013, **3**, 6472–6478.

254 A. Alborzi and S. Khademolhoseini, *J. Mater. Sci. Mater. Electron.*, 2016, **27**, 3963–3967.

255 B. Moreno, E. Chinarro, M. T. Colomer and J. R. Jurado, *J. Phys. Chem. C*, 2010, **114**, 4251–4257.

256 B. Senthilkumar, K. V. Sankar, R. K. Selvan, M. Danielle and M. Manickam, *RSC Adv.*, 2013, **5635**, 352–357.

257 A. Kaddouri, R. Del Rosso, C. Mazzocchia, P. Gronchi and P. Céntola, *Catal. Letters*, 1999, **63**, 65–71.

258 J. S. J. Hargreaves and D. Mckay, *J. Mol. Catal. A Chem.*, 2009, **305**, 125–129.

259 R. Nava, B. Pawelec, J. Morales, R. A. Ortega and J. L. G. Fierro, *Microporous Mesoporous Mater.*, 2009, **118**, 189–201.

260 R. Kojima and K. I. Aika, *Appl. Catal. A Gen.*, 2001, **219**, 157–170.